

The *Chandra* Proposers' Observatory Guide

Prepared by:
Chandra X-ray Center
Chandra Project Science, MSFC
Chandra IPI Teams

Version 2.0
March 15, 2000

Contents

What's New for Cycle 2?	xix
0.1 Spacecraft	xix
0.2 ACIS	xix
0.3 HRC	xx
0.4 Observing Proposals	xx
0.5 NRA	xx
 I Technical Description	 1
1 Mission Overview	3
1.1 Program Organization	3
1.2 Unique Capabilities	3
1.3 Observatory Overview	4
1.4 Pointing Control and Aspect Determination(PCAD)	5
1.5 HRMA	5
1.6 Science Instrument Module (SIM)	6
1.6.1 Aimpoints	6
1.7 Ground System	6
1.8 Orbit	8
1.9 Particle Detector	8
1.10 ACIS	8
1.11 HRC	9
1.12 HETG	9
1.13 LETG	9
1.14 Effective Area Comparisons	10
1.15 Allocation of observing time	10
1.16 How to get information and help	10

2	Spacecraft, Telescope, Operations, & Mission Planning	13
2.1	Introduction	13
2.2	Spacecraft	13
2.3	Telescope System	15
2.4	Science Instrument Module (SIM)	17
2.4.1	SIM Motions	17
2.5	Electron Proton Helium Instrument (EPHIN)	19
2.6	Operations	19
2.6.1	Launch and On-orbit Verification	19
2.6.2	The Ground System	20
2.6.3	Commanding	21
2.6.4	Telemetry	21
2.6.5	SI Science Data	22
2.6.6	Event Timing and the Spacecraft Clock	22
2.7	Mission Planning	22
3	Offset Pointing, Visibility, and other Constraints	25
3.1	Introduction	25
3.2	Offset Pointing	25
3.3	Visibility	25
3.3.1	Radiation Belt Passages	27
3.3.2	Avoidances	27
3.3.3	Roll Angles	28
3.4	Constraints and Considerations	29
3.4.1	Instrument Constraints and Considerations	29
3.4.2	User-Imposed Constraints	29
4	High Resolution Mirror Assembly (HRMA)	31
4.1	Description and Physical Configuration	31
4.2	Calibration and Performance	33
4.2.1	Calibration and Model	33
4.2.2	HRMA Effective Area	34
4.2.3	Point-Spread-Function and Encircled Energy Fraction	34
4.2.4	Effective Area in Flight	42
4.3	Ghost Images	42
4.4	Effects of Aspect and Instrument Uncertainties	42
4.5	HRMA background material	46
4.5.1	Heritage	46
4.5.2	Exit cone angles	50
4.5.3	Sub-assembly Calibration	50

4.5.4	Operating Environment	50
4.6	References	51
5	Pointing Control and Aspect Determination System	53
5.1	Introduction	53
5.2	Physical configuration	53
5.2.1	ACA	54
5.2.2	Fiducial lights and Fiducial Transfer System	55
5.2.3	IRU	57
5.2.4	Momentum control – RWA and MUPS	58
5.3	Operating principles	58
5.4	Performance	59
5.5	Heritage	60
5.6	Special Characteristics	60
5.7	Calibration	60
5.7.1	Pre-launch calibration	60
5.7.2	Orbital activation and checkout calibration	61
5.7.3	On-orbit calibrations	61
5.8	Operations	63
5.8.1	PCAD modes	63
5.8.2	Operational constraints	63
5.8.3	Output data	63
5.9	Performing an Observation	65
5.9.1	Star acquisition	65
5.9.2	Science pointing scenarios	65
5.9.3	PCAD capabilities (advanced)	67
5.10	Ground Processing	68
5.10.1	Data products	69
5.10.2	Star catalog	69
6	ACIS: Advanced CCD Imaging Spectrometer	71
6.1	Introduction & Layout	71
6.2	Basic Principles	73
6.3	Event Grades	75
6.4	Aimpoints	77
6.5	Spatial Resolution & Encircled Energy	77
6.6	Dither	79
6.6.1	Gaps between the CCDs	81
6.7	Energy Resolution	81
6.8	Optical Blocking Filter & Optical Contamination	84

6.9	Quantum Efficiency and Effective Area	84
6.10	On-Orbit Background	89
6.10.1	The non X-ray background	89
6.10.2	The total background	91
6.10.3	Background variability	92
6.10.4	Background in Continuous Clocking Mode	94
6.11	Sensitivity	94
6.12	Operating Modes	97
6.12.1	Timed Exposure Mode	97
6.12.2	Frame Times - Full Frames	97
6.12.3	Frame Times & Subarrays	97
6.12.4	Trailed Images	97
6.12.5	Continuous Clocking Mode	98
6.13	Bias Maps	99
6.13.1	Telemetry Formats	99
6.14	Calibration	101
6.15	Hot Pixels and Columns	101
6.16	Anomalies	101
6.17	Pileup	103
6.17.1	Other consequences of pileup	103
6.17.2	Pileup Estimation	107
6.17.3	Reducing Pileup	109
6.18	Observing with ACIS- the input parameters	109
6.18.1	Required Parameters	110
6.18.2	Optional Parameters	111
6.18.3	Non-ACIS Parameters Relevant to an Observation with ACIS	112
6.19	Examples: Choosing the Instrument Parameters	112
6.19.1	Detection of a Faint Point Source	112
6.19.2	Pulse Phased Spectroscopy on a Bright Point Source in a Crowded Field	113
7	High Resolution Camera (HRC)	115
7.1	Introduction and Instrument Layout	115
7.2	Basic Principles	115
7.2.1	Aimpoints	120
7.3	Dither	122
7.4	Spatial Resolution & Encircled Energy	122
7.5	Energy Resolution	122
7.6	UV/Ion Shields	125

7.7	Quantum Efficiency and Effective Area	128
7.8	On-Orbit Background	131
7.8.1	HRC-I	131
7.8.2	HRC-S	132
7.8.3	Temporally Variable Background	133
7.9	Source Sensitivity	133
7.10	Instrument Anomalies	133
7.11	Calibration	133
7.12	Operational considerations and constraints	136
7.12.1	Total Count limits	136
7.12.2	Count rate limits	136
7.13	Output data	138
7.14	Observing with HRC - the input parameters	140
7.15	REFERENCES	140
8	HETG: <i>Chandra</i> High Energy Transmission Grating	145
8.1	Instrument Overview	145
8.1.1	Example of HETGS Observation	147
8.1.2	Scientific Objectives and Grating Heritage	148
8.1.3	HETGS Operating principles	148
8.1.4	HETG Physical Configuration	152
8.2	Instrument Characteristics	154
8.2.1	HETGS Effective Area	154
8.2.2	HETGS Line Response Function	167
8.2.3	Background	178
8.2.4	Absolute Wavelength	178
8.3	Calibration	178
8.3.1	Pre-launch Calibration	178
8.3.2	In Flight Calibration	179
8.4	HETG Operations	180
8.4.1	Operational Constraints	180
8.4.2	Output Data	180
8.4.3	Performance Monitoring, Health and Safety	181
8.4.4	Thermal response time	181
8.4.5	Observation frequency/duty cycle	181
8.4.6	Radiation Considerations	181
8.5	Observation Planning	182
8.5.1	Focal Plane Detector Considerations	182
8.5.2	Complications from multiple sources	183
8.5.3	Extended Sources and Spatial-Spectral Effects	185

8.5.4	Optimizing Detection of Isolated Emission Lines: Choice of Spectrometer	187
8.6	Example of Planning an observation	191
8.6.1	Counting rates from <i>PIMMS</i>	191
8.6.2	Choice of grating and detector	192
8.6.3	Choice of ACIS Mode	193
8.6.4	ACIS-S Gaps	193
8.6.5	Other Considerations	194
8.6.6	The Observing Proposal	194
8.7	Simulations with <i>MARX</i>	194
8.8	Document History	195
8.9	REFERENCES	197
9	LETG: Low Energy Transmission Grating	201
9.1	Instrument Description	201
9.1.1	Scientific Objectives	203
9.1.2	Heritage	203
9.1.3	Operating principles	203
9.1.4	Physical configuration	204
9.2	Calibration	209
9.2.1	Pre-launch Calibration	209
9.2.2	In Flight Calibration	209
9.3	LETGS Performance	210
9.3.1	Usage	210
9.3.2	Wavelength Coverage and Dispersion Relation	211
9.3.3	Resolving Power	213
9.3.4	Grating Efficiency	221
9.3.5	Effective Area	223
9.3.6	Background	228
9.3.7	Sample Data	234
9.4	Observation Planning	237
9.4.1	HRC-S, ACIS-S and HRC-I Detector Choices	237
9.4.2	Other Focal Plane Detector Considerations	244
9.4.3	General Considerations	246
9.5	Technical Feasibility	249
9.5.1	Simple Calculation of Exposure Times and Signal-to- Noise Ratio for Line and Continuum Sources	252
9.6	References	260

II	Policy, Planning, and Proposal Preparation	261
10	Observing Policy	263
10.1	<i>Chandra</i> observing policy	263
10.1.1	Introduction and scope	263
10.1.2	Applicable documents	263
10.1.3	Distribution of data	263
10.1.4	Target selection and phasing	265
10.1.5	Conflict resolution	265
10.1.6	Large Projects	265
10.1.7	Targets of Opportunity (TOOs)	266
10.1.8	GO time allocation	266
10.1.9	Director's Discretionary Time	266
10.2	Procedures concerning TOOs and DDT	267
10.2.1	Pre-proposed TOOs	267
10.2.2	Unanticipated TOOs	267
10.2.3	Directors Discretionary Time	268
10.3	Criteria for Completeness and Data Quality	268
10.3.1	Completeness	268
10.3.2	Data quality due to high background	269
10.3.3	Data quality - telemetry saturation due to x-ray sources	269
11	Tools for Assessing Feasibility	271
11.1	Purpose and Scope	271
11.2	Assessing Feasibility: the Methods	271
11.3	Estimating a Count Rate	272
11.3.1	<i>PIMMS</i>	272
11.4	Simulating Spectra	275
11.5	<i>XSPEC</i>	276
11.5.1	Functional Description	276
11.5.2	Accessing <i>XSPEC</i>	276
11.5.3	Stand-alone example	277
11.5.4	The Setup	277
11.6	<i>MARX</i>	284
11.6.1	What's New in Version 2.5?	284
11.6.2	Do you need <i>MARX</i> ?	285
11.6.3	Technical Description	285
11.6.4	Obtaining <i>MARX</i>	287
11.6.5	Obtaining help	287

12 Proposal Planning Tools	289
12.1 Overview of Proposal Planning Tools	289
12.2 Obtaining and Installing Command-line Versions	289
12.2.1 Sun-Solaris Executables	290
12.3 <i>ObsCat</i> – The <i>Chandra</i> Observation Catalog	291
12.3.1 Introduction	291
12.3.2 Running <i>ObsCat</i> over the WWW	291
12.4 WWW Target Information (non-Java).	295
12.5 <i>precess</i> - Astronomical Coordinate Conversion	297
12.5.1 Introduction	297
12.5.2 Running <i>precess</i> over the World Wide Web	297
12.5.3 Running <i>precess</i> in Command-line mode	299
12.5.4 Available coordinate systems	302
12.6 <i>colden</i> - Calculate Neutral Hydrogen Column Density	304
12.6.1 Introduction	304
12.6.2 Running <i>colden</i> over the World Wide Web	304
12.6.3 Running <i>colden</i> in Command-line mode	307
12.6.4 Supported Datasets	311
12.7 <i>dates</i> - Calendar Conversion Tool	311
12.7.1 Introduction	311
12.7.2 Running <i>dates</i> over the World Wide Web	311
12.7.3 Running <i>dates</i> in Command-line mode	313
12.7.4 Running <i>dates</i> on a file	315
12.7.5 Supported Calendars and Timescales	315
12.7.6 Zero Points - Command-Line only	317
12.7.7 Input Formats - Command-Line only	317
12.7.8 Setup Commands - Command Line Only	321
12.8 <i>ObsVis</i> – Observation Visualizer	322
12.8.1 Obtaining the <i>ObsVis</i> Software	322
12.8.2 Getting Started with <i>ObsVis</i>	323
12.8.3 Setting the Observing Parameters	327
12.8.4 Saving the <i>ObsVis</i> Output.	330
12.8.5 Known Bugs	330
13 Proposal Preparation and Submittal	331
13.1 Preparing the Proposal	331
13.2 Submitting a Proposal	333
13.2.1 WWW version	333
13.2.2 E-mail server	334

13.3	RPS Help: Specific Help for Fields of Cover and General	
	Pages	335
13.3.1	COVER PAGE	335
13.3.2	GENERAL FORM	340
13.4	RPS: Specific Help for Fields of TARGET FORM(S)	341
13.4.1	Parameters Required for All Targets, Regardless of	
	Instrument	341
13.4.2	HRC-S Parameters	347
13.4.3	ACIS Parameters	347
13.4.4	ACIS Required Parameters	347
13.4.5	ACIS Optional Custom Parameters:	349
13.5	RPS: Help for Fields for Target CONSTRAINTS	354
13.6	RPS: Help After Submitting: When You've Discovered A	
	Mistake	357
13.6.1	Mistake Discovered BEFORE the Proposal Deadline .	357
13.6.2	Mistake Discovered AFTER the Proposal Deadline . .	357
III	Appendices	359
A	Help and Contact Information	361
A.1	Contact Information	361
A.2	The <i>CXC</i> Website	361
A.3	The HelpDesk Form	362
A.4	Software Available for Proposers	362
A.5	Documents for Proposers	363
A.6	<i>CXC DO</i> Staff	363
B	Acronym List	365

List of Figures

1.1	The <i>Chandra</i> Observatory with certain subsystems labeled. LGA is an acronym for the Low Gain Antenna.	4
1.2	Arrangement of the ACIS and the HRC in the focal plane . .	7
1.3	Comparison of the on-axis effective areas of the HRMA/HRC-I, the HRMA/ACIS FI), and the HRMA/ACIS(BI) combinations	11
1.4	Comparison of the effective areas of the <i>Chandra</i> spectrometers	12
2.1	Major components of the telescope system	16
2.2	A schematic of the Science Instrument Module	18
3.1	Examples of offset pointing with ACIS	26
3.2	Example of offset pointing with HRC	26
3.3	<i>Chandra</i> average “visibility” (9/99-3/01)	28
4.1	The 4 nested HRMA mirror pairs and associated structures. .	32
4.2	The HRMA effective area versus energy	35
4.3	The HRMA effective area versus off-axis angle	36
4.4	The HRMA effective area as measured during the ground calibration	37
4.5	The fractional encircled energy as a function of angular radius calculated for an on-axis point-source	39
4.6	On-orbit performance prediction for encircled energy	40
4.7	Simulated on-axis HRMA/HRC-I on-axis images of mono-energetic point sources without aspect blurring	41
4.8	Radius of a circle enclosing 50% and 90% of the power [at 1.5 and 6.4 keV] as a function of off-axis angle. These curves apply to flat detectors (e.g. HRC-I or ACIS-S(S3)) which do not follow the curved focal plane	43
4.9	Simulated HRMA and HRMA/HRC-I images	44

4.10	Calculated image of a source 53' off-axis	45
4.11	The fractional encircled energy as a function of angular radius observed with the HRC-I in flight compared to model calculations for an on-axis point-source, including aspect and HRC-I effects	47
4.12	The fractional encircled energy as a function of angular radius observed with the HRC-S in flight compared to model calculations for an on-axis point-source, including aspect and HRC-I effects	48
4.13	The expected fractional encircled energy as a function of angular radius observed with the ACIS-S(S3) in flight for an on-axis point-source, including aspect and ACIS effects	49
5.1	Aspect camera assembly	55
5.2	Spectral response of the ACA CCD	56
5.3	Fiducial Transfer System	57
6.1	A schematic of the ACIS focal plane	72
6.2	Schematic ACIS Grade Calculator	76
6.3	Measured ACIS on-axis encircled energy versus radius	78
6.4	Contours of constant 50% encircled energy at 1.49 keV around the ACIS-I aimpoint	79
6.5	Contours of constant 50% encircled energy at 1.49 keV around the ACIS-S aimpoint	80
6.6	The ACIS pre-launch energy resolution versus energy	82
6.7	The energy resolution of the ACIS chips S3(BI) and I3(FI) versus row number	83
6.8	The quantum efficiency convolved with the appropriate optical blocking filter transmission of an average FI and the two BI chips as a function of energy	85
6.9	HRMA/ACIS effective area versus energy - log scale	86
6.10	HRMA/ACIS effective area versus energy - linear scale	87
6.11	Comparison of predicted and observed effective area versus off-axis angle	88
6.12	Enlarged view of an area of the FI chip I3 hit by a cosmic ray event	89
6.13	Energy spectra of the ACIS background with the HRMA doors closed - standard grades	90
6.14	Energy spectra of the ACIS background with the HRMA doors closed - grade 0	91

6.15	Fraction of ACIS background events as a function of grade from early-in-flight data for an FI chip (S2) (left) and a BI chip (S3) (right).	92
6.16	Background quiescent spectrum	93
6.17	ACIS background counting rate variability	94
6.18	Cumulative probability of background variability	95
6.19	Minimum detectable flux vs. exposure time	96
6.20	Examples of Subarrays	98
6.21	An Example of a Trailing Image	99
6.22	MARX simulations of the effects of pileup on spectral shape	102
6.23	Pileup Effects at a Single Energy	104
6.24	The Radial Distribution of the Core of the <i>PSF</i> for Different Incident Fluxes	106
6.25	Pileup Fraction versus Rate	108
7.1	A schematic of the HRC focal plane geometry	116
7.2	A schematic cross-section of the HRC-S MCP array	117
7.3	A schematic of the HRC Micro-channel-Plate detector	119
7.4	Schematic representation of the HRC position determination	121
7.5	Fractional encircled energy as a function of radius for an on-axis point source observed with the HRMA/HRC-I	123
7.6	HRMA/HRC-I Encircled energy as a function of source off-axis angle	124
7.7	The pulse height distributions versus x-ray energy	125
7.8	HRC-I UV/Ion shield transmission	126
7.9	HRC-S UV/Ion shield transmission	127
7.10	The HRC-I and the center section of the HRC-S UV/Ion shield effective area as a function of wavelength	129
7.11	The HRC-I and HRC-S MCP efficiencies as a function of energy	130
7.12	The predicted HRMA/HRC-I and HRMA/HRC-S effective area	131
7.13	HRC-I background variability	134
7.14	Predicted HRC minimum detectable flux against exposure time	135
8.1	HETGS Capella observation with typical location of spectra	149
8.2	HETGS Capella spectrum, MEG $m = -1$	150
8.3	Schematic layout of the HETGS	152
8.4	The Rowland geometry	153
8.5	The HETG support structure (HESS)	155
8.6	Cross-sections of the MEG and HEG membranes	156
8.7	The HETGS HEG predicted effective area	158

8.8	The HETGS HEG predicted effective area: linear scale	159
8.9	The HETGS MEG predicted effective area	160
8.10	The HETGS MEG predicted effective area: linear scale . . .	161
8.11	HRMA-HETG-ACIS-S combination first-order predicted ef- fective area	162
8.12	HEG and MEG efficiencies	164
8.13	HEG and MEG “Banana Plots”	165
8.14	HETGS pile-up and higher-order events	166
8.15	HETGS Zero-order and Frame-transfer Streak (Trailed Image)	170
8.16	HEG Line Response Functions	172
8.17	MEG Line Response Functions	173
8.18	HEG and MEG Resolving Power	174
8.19	HETGS spectral resolution: extended sources	176
8.20	HETG grating spectral resolution: off-axis	177
8.21	A ‘collision’ between two sources	184
8.22	spectral contamination caused by a second source	186
8.23	HETGS spatial-spectral effect example	187
8.24	The figure of merit for detecting isolated emission lines for the HETGS, LETG with HRC-S and for the LETG with ACIS-S	189
8.25	The figure of merit for detecting isolated emission lines for the HETGS, the LETG with the HRC-S, and the ACIS without either grating	190
8.26	A simulation of a 60 ksec HETGS observation of the elliptical galaxy NGC1399	195
8.27	A simulation of a HETGS spectrum of N132D	196
9.1	The LETG Grating Element Support Structure.	205
9.2	A detail of the LETG Grating Element Support Structure. .	205
9.3	Two grating modules in the LETG GESS.	206
9.4	A schematic picture of the LETG facet structure.	207
9.5	The HRC-S array elements and the Rowland circle.	208
9.6	LETG spectral resolving power.	215
9.7	LETG Zeroth-Order LRF.	216
9.8	LETGS Line Response Function	217
9.9	LETGS zeroth order profile goodness of fit vs. β	218
9.10	LETG spectral resolving power for extended sources.	219
9.11	LETG spectral resolving power for off-axis sources.	220
9.12	LETG grating efficiency.	222
9.13	LETG+HRC-S Cross-dispersion and Extraction window . . .	225
9.14	LETGS 0th-order effective area	226

9.15	LETGS 1st-order effective area.	227
9.16	LETG/HRC-S effective area for higher orders.	229
9.17	LETG/HRC-S/LESF effective area for higher orders.	230
9.18	LETG/ACIS-S effective area for higher orders.	231
9.19	LETG+HRC-S background	233
9.20	HRC-S detector image of LETGS observation of Capella . . .	235
9.21	Detail of LETG/HRC-S Capella image	236
9.22	HRC-S/LETG image of Capella positive order dispersion . .	238
9.23	Extracted Capella spectrum	239
9.24	Sirius AB, zeroth order image	240
9.25	ISM Transmittance in LETGS bandpass	250
9.26	The “moderate” LETG+HRC-S total background count rate	254
9.27	The first order spectrum for an 80 ksec observation of the AGN NGC5548.	258
9.28	MARX simulation of spectra showing the effect of source extent.	259
11.1	WWW version of <i>PIMMS</i>	273
11.2	The simulated continuum spectrum for NGC 4151	282
11.3	<i>MARX</i> simulation of the CTI-induced variation in CCD spec- tral resolution	286
12.1	WWW page of the <i>ObsCat</i> tool	292
12.2	WWW list from the <i>ObsCat</i> tool	293
12.3	WWW detail page of the <i>ObsCat</i> tool	294
12.4	WWW non-Java search page	296
12.5	<i>precess</i> Interface	298
12.6	<i>colden</i> Interface	305
12.7	<i>ObsVis</i> target form.	324
12.8	<i>ObsVis</i> Roll and Visibility Plot for NGC4258. Visibility is shown by the (blue) line and the range of allowed roll angle by the (red) vertical points.	325
12.9	<i>ObsVis</i> Digital Sky Survey (DSS) image with ACIS-I (the default) FOV superposed for NGC4258. The image has been zoomed outwards by two steps using <i>ds9</i> to show the full ACIS-I plus ACIS-S FOV.	326
12.10	<i>ObsVis</i> Dates Dialog, accessed by selecting <i>Start/End Dates</i> in the <i>Options</i> menu of the main <i>ObsVis</i> GUI.	328
12.11	<i>ObsVis</i> Parameters Dialog, accessed by selecting <i>Parameters</i> in the <i>Options</i> menu of the main <i>ObsVis</i> GUI.	329

List of Tables

2.1	Spacecraft Parameters	14
4.1	<i>Chandra</i> HRMA Characteristics	33
4.2	HRMA Encircled Energy Performance	38
4.3	Exit cone angles for each hyperboloid.	50
5.1	Aspect System Requirements and Performance	59
5.2	PCAD modes	64
5.3	Default dither parameters	66
5.4	ACA photometric accuracy	68
5.5	Aspect pipeline data products	70
6.1	Table of ACIS Characteristics	74
6.2	ACIS and <i>ASCA</i> Grades	76
6.3	Nominal Optical Blocking Filter Composition and Thicknesses	84
6.4	Approximate on-orbit standard grade background counting rates with ACIS positioned at the ACIS-I aimpoint.	92
6.5	Approximate on-orbit standard grade background counting rates with ACIS positioned at the ACIS-S aimpoint and the HETG in position.	93
6.6	Typical total quiescent background rates by chip type	93
6.7	Telemetry Saturation Limits	100
6.8	<i>ASCA</i> -Grade Distributions at 1.5keV for Different Incident Fluxes	105
7.1	HRC Parameters	118
7.2	HRC Event Data Format	140
8.1	HETG(S) Parameters	146
8.2	Table of HETGS Gap Locations	168
8.3	HETGS Calibration Observations	180

8.4	<i>PIMMS</i> results for example HETGS observation	193
9.1	LETGS Parameters	202
9.2	Planned LETGS Calibration Observations	210
9.3	LETG Position-Dependent Features	213
9.4	Absorption Edges	224
12.1	Summary Proposal Tools	289
13.1	Reccomended SIM-Z offsets	344
13.2	Valid SIM-Z values by detector	345
13.3	Standard Subarrays	350

What's New for Cycle 2?

Here we summarize changes to the *Chandra* X-Ray Observatory (*CXO* or *Chandra*) that have taken place since the *NASA* Research Announcement (NRA) for Cycle 1 was released. The material here assumes a certain familiarity with the *Chandra* Project and is intended purely as an update for users who may have had some previous involvement. All new material has been included in the NRA and/or this document.

0.1 Spacecraft

- The sign convention used in specifying target offsets has changed. See Chapter 3 and also 6.4.

0.2 ACIS

- The front-illuminated CCDs now exhibit position-dependent energy resolution (and increased charge transfer inefficiency) as a result of damage due to exposure to low energy protons early in the mission. The energy resolution is at/near pre-launch values at the edge closest to the readout. The back-illuminated CCDs were unaffected. Details are to be found in Chapter 6 in Section 6.7.
- The background counting rates in the CCDs exhibit flares from time to time. Details are in Section 6.10 and at (<http://asc.harvard.edu>) – click “Calibration”, then “ACIS”, and then “Particle Background”. Even when there is no flaring, the quiescent background rates are (~ 2) times higher than assumed for Cycle 1.
- The aimpoint on S3 (the on-axis BI CCD of ACIS-S) is at the boundary between two chip nodes (each ACIS chip uses 4 amplifiers, one for each node, or quadrant). The observatory dither deliberately spreads

point source data over the two nodes, each with different amplifier characteristics. To minimize the importance and impact of the relative calibration between nodes, we now add a -20 arcsec Y-offset to S3 observations. The 20 arcsecond offset has very small impact on image quality – see Chapter 4.

- Several new ACIS operating modes have been made available, including reporting of 3x3 event islands in the continuous clocking (CC) mode. It is also now possible to request different windows for different CCDs (See Section 6.18.2.)

0.3 HRC

- The HRC-S background is much higher than anticipated because of an error in timing between the anticoincidence shield and the detector electronics. To avoid complete saturation of the telemetry by the high background, only the data from a subsection of the detector is being sent to the ground. The subsection spans the full length of the HRC-S to accommodate the LETG-dispersed spectra. See Chapter 7.
- Because of the high HRC-S background and methods of dealing with it, the high energy suppression filter (unsupported during Cycle 1) is no longer available for use.

0.4 Observing Proposals

- Proposal submission must be via the Remote Proposal System.
- Starting with Cycle 2, proposal submission will be fully electronic including science justification and figures.
- Proposers can now request off-nominal Z-displacement of instruments.

0.5 NRA

- Large Projects (>300 ksec) are encouraged: At least $\sim 20\%$ of the available observing time awarded during NRA 2 will be allocated to Large Projects, subject to reasonable standards of scientific merit. See Chapter 10 for details

- Director's Discretionary Time has been made available. Director's time is limited at 5% of the total time. See Chapter 10 and also Chapter 12 for how to apply.

Part I

Technical Description

Chapter 1

Mission Overview

The *Chandra* X-Ray Observatory (*CXO*), formerly known as the Advanced X-ray Astrophysics Facility (*AXAF*), combines an efficient high-resolution ($\leq 1/2$ arcsecond) X-ray telescope with a suite of advanced imaging and spectroscopic instruments. The Observatory was successfully launched by *NASA*'s Space Shuttle Columbia on July 9, 1999, with Col. Eileen Collins commanding. Subsequently an Inertial Upper Stage and *Chandra*'s Internal Propulsion System placed the Observatory in a high elliptical orbit. *Chandra* is the X-Ray component of *NASA*'s four Great Observatories. The other components are the Hubble Space Telescope, the Compton Gamma-Ray Observatory and the yet-to-be launched Space Infra-Red Telescope Facility.

1.1 Program Organization

The *Chandra* Project is managed by *NASA*'s Marshall Space Flight Center. The Project Scientist is Martin C. Weisskopf. Day-to-day responsibility for *Chandra* science operations lies with the Chandra X-ray Center (*CXC*), Harvey Tananbaum, Director. The *CXC* is located at the Cambridge, Massachusetts facilities of the Smithsonian Astrophysical Observatory (*SAO*) and the Massachusetts Institute of Technology (*MIT*). The *Chandra* Operations Control Center (*OCC*) is also located in Cambridge. The *CXC* uses the *OCC* to operate the Observatory for *NASA*.

1.2 Unique Capabilities

Chandra was designed to provide order-of-magnitude advances over previous X-ray astronomy missions with regards to spatial and spectral resolution.

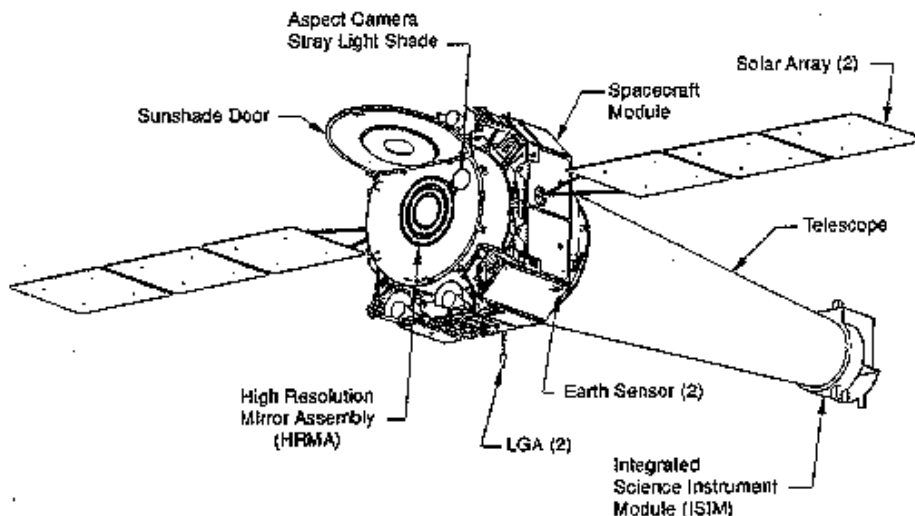


Figure 1.1: The *Chandra* Observatory with certain subsystems labeled. LGA is an acronym for the Low Gain Antenna.

The High Resolution Mirror Assembly (HRMA) produces images with a half-power diameter (HPD) of the point spread function (*PSF*) of < 0.5 arcsec. Both grating systems – the Low Energy Transmission Grating (LETG) and the High Energy Transmission Grating (HETG) – offer resolving powers well in excess of 500 over much of their bandwidth which, together, cover the range from ≤ 0.1 to 10 keV.

1.3 Observatory Overview

An outline drawing of the *Chandra* X-ray Observatory is shown in Figure 1.1. *Chandra* consists of a spacecraft and a telescope/science-instrument payload. The spacecraft provides power; communications, and command, and data management; pointing control and aspect determination. The principal elements of the observatory that will be discussed in this document are:

- The Aspect System (Chapter 5)
- The High Resolution Mirror Assembly (HRMA)(Chapter 4)
- The Focal-plane Science Instruments (SIs):

- The High Resolution Camera (HRC)(Chapter 7)
- The Advanced CCD Imaging Spectrometer (ACIS)(Chapter 6)
- The Objective Transmission Gratings:
 - High Energy Transmission Grating (HETG)(Chapter 8)
 - Low Energy Transmission Grating (LETG)(Chapter 9)

These and related elements of the *Chandra* Project are introduced briefly in the remainder of this chapter.

1.4 Pointing Control and Aspect Determination(PCAD)

The PCAD system controls the pointing and dithering of the observatory and provides the data from which both the relative and absolute aspect are determined. Dithering is imposed in order to spread the instantaneous image over many different pixels of the focal plane detector in order to smooth out pixel-to-pixel variations. The dither pattern is a Lissajous figure (and can be seen quite clearly in the un-aspect corrected data from bright point sources). The amplitude, phase, and velocity depend on which instrument (ACIS or HRC) is in the focal plane.

Key elements of the PCAD system are the set of redundant gyroscopes, momentum wheels, and an aspect system consisting of a four inch optical telescope with (redundant) CCD detector. The aspect camera simultaneously images a fiducial light pattern produced by light emitting diodes placed around the focal-plane instruments along with the flux from up to five bright stars that may be in the aspect camera's field-of-view. An interesting consequence is that the user may request that one of the targets of the aspect camera be at the location of the x-ray target. For bright optical counterparts, this option allows real-time optical monitoring albeit at the price of a reduced-accuracy aspect solution – see Chapter 5 for further details.

1.5 HRMA

The HRMA consists of a nested set of four paraboloid-hyperboloid (Wolter-1) grazing-incidence X-ray mirror pairs, with the largest having a diameter of 1.2 m (twice that of the *Einstein* Observatory). The focal length is 10m.

The mirror glass was obtained from Schott Glasswerke; grinding and polishing was performed at Hughes Danbury Optical Systems; coating at Optical Coating Laboratory; and the mirror alignment and mounting at Eastman-Kodak Co. The mirrors weigh about 1000kg. Details of the HRMA and its performance are presented in Chapter 4.

The *Chandra* Telescope Scientist is Leon Van Speybroeck, of the Smithsonian Astrophysical Observatory.

1.6 Science Instrument Module (SIM)

The Science Instrument Module consists of the special hardware that provides mechanical and thermal interfaces to the focal-plane scientific instruments (SIs). The most critical functions from an observer's viewpoint are the capability to adjust the telescope focal length and the ability to move the instruments along an axis orthogonal to the optical axis.

The SIM houses the two focal instruments - the ACIS and the HRC. Each of these have two principal components - HRC-I and S and ACIS-I and S. The focal plane instrument layout is shown in Figure 1.2. The SIM moves in both the X-axis (focus) and the Z-axis (instrument and aimpoint(1.6.1) selection). Note that the Y-Axis parallels the dispersion direction of the gratings.

1.6.1 Aimpoints

The aimpoint is simply the position on the detector where the imaged flux from an on-axis point source will appear. The aimpoints are discussed in detail in the Chapters about each instrument and in Chapter 3.

1.7 Ground System

The ground system consists of the *Chandra* X-ray Center (*CXC*) and the Operations Control Center (*OCC*) in Cambridge, MA, the Engineering Support Center (ESC) at *MSFC*, and various *NASA* communications systems including the Deep Space Network operated for *NASA* by the Jet Propulsion Laboratory. See Section 2.6.2 for details.

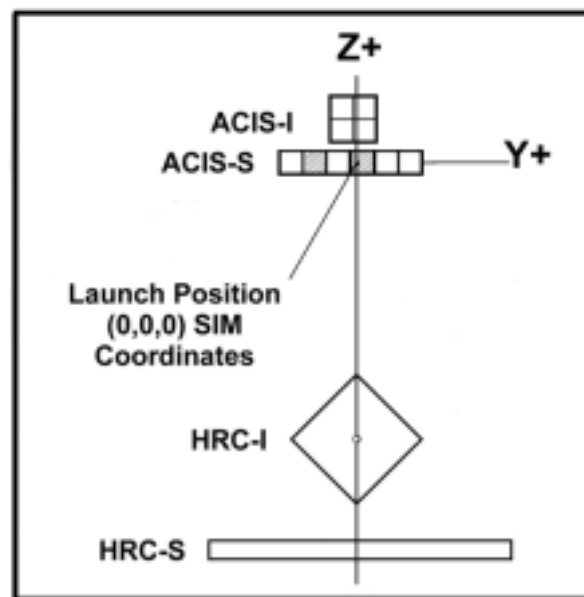


Figure 1.2: Arrangement of the ACIS and the HRC in the focal plane. The view is along the axis of the telescope from the direction of the mirrors. For reference, the two back-illuminated ACIS-S chips are shaded. SIM motion can be used to place the aimpoint at any point on the vertical solid line.

1.8 Orbit

The *Chandra* orbit is highly elliptical and varies with time. As of November 1999 the apogee was $\sim 138,800$ km and the perigee was $\sim 10,100$ km. The apogee and perigee are drawing closer to each other and will continue to do so for about 5 years (at a rate of a few thousand km/year) when the trend will reverse. The orbit allows for reasonably high observing efficiency as the satellite spends most of the time well above the radiation belts ($\geq 75\%$) and long continuous observations (≥ 170 ksec) are made possible by the orbital period of 63.5h.

1.9 Particle Detector

There is a particle detector mounted near the telescope, called the Electron, Proton, Helium INstrument (EPHIN) (see 2.5). This detector is used to monitor the local charged particle environment as part of the scheme to protect the focal-plane instruments from particle radiation damage. Data taken during an observation are available to the observer.

The Co-Principal Investigators of the EPHIN instrument are Drs. Reinhold Muller-Mellin and Hoarst Kunow of the University of Kiel, Germany.

1.10 ACIS

ACIS is comprised of two CCD arrays, a 4-chip array, ACIS-I; and a 6-chip array, ACIS-S. The CCDs are flat, but the chips in each array are positioned (tilted) to approximate the relevant focal surface: that of the HRMA for ACIS-I and that of the HETG Rowland circle for ACIS-S. ACIS-I was designed for CCD imaging and spectrometry; ACIS-S can be used both for CCD imaging spectrometry and also for high-resolution spectroscopy in conjunction with the HETG grating.

There are two types of CCD chips. ACIS-I is comprised of front-illuminated (FI) CCDs. ACIS-S is comprised of 4 FI and 2 back-illuminated (BI) CCDs, one of which is at the best focus position. The BI CCDs response extends to lower energies than the FI CCDs and the energy resolution is mostly independent of position. The FI CCD response is more efficient at higher energies but the energy resolution (currently) varies with position due to radiation damage caused by protons reflecting through the telescope during radiation-zone passages in the early part of the mission. Details in Chapter 6.

The Principal Investigator is Prof. Gordon Garmire of the Pennsylvania State University.

1.11 HRC

The HRC is comprised of two microchannel plate (MCP) imaging detectors: the HRC-I designed for wide-field imaging; and, HRC-S designed to serve as a readout for the LETG. The HRC-I is placed at right angles to the optical axis, tangent to the focal surface. The HRC-S is made of three flat elements, the outer two of which are tilted to approximate the LETG Rowland circle. The HRC detectors have the highest spatial resolution on *Chandra*, matching the HRMA point spread function most closely. The HRC detectors also offer the fastest time resolution ($16\mu\text{s}$). Details concerning the HRC are in Chapter 7.

The Instrument Principal Investigator is Dr. Stephen Murray of the Smithsonian Astrophysical Observatory.

1.12 HETG

The HETG, when operated with the HRMA and the ACIS-S, forms the High-Energy Transmission Grating Spectrometer (HETGS) for high resolution spectroscopy. The HETGS achieves resolving power ($E/\Delta E$) up to 1000 in the band between 0.4 keV and 10.0 keV. The HETG is comprised of two grating assemblies – the High Energy Grating (HEG) and the Medium Energy Grating (MEG) – on a single structure that can, by command, be placed in the optical path just behind the HRMA. The HEG intercepts X-rays from only the two inner mirror shells and the MEG intercepts X-rays from only the two outer mirror shells. The HEG and MEG dispersion directions are offset by 10 degrees so the two patterns can be easily distinguished. Details are presented in Chapter 8.

The Instrument Principal Investigator for the HETG is Prof. Claude Canizares, of the *MIT* Center for Space Research.

1.13 LETG

The LETG when operated with the HRC-S, forms the Low Energy Transmission Grating Spectrometer (LETGS). The LETGS provides the highest spectral resolution on *Chandra* at low (0.08 - 0.2 keV) energies. The LETG is comprised of a single grating assembly that, on command, can be placed in

the optical path behind the HRMA. The LETG grating facets intercept and disperse the flux from all of the HRMA mirror shells. Details are given in Chapter 9.

The LETG was developed at the Laboratory for Space Research in Utrecht, the Netherlands in collaboration with the Max-Planck-Institut für Extraterrestrische Physik in Garching, Germany. The Instrument Principal Investigator is Dr. Albert Brinkman of the Laboratory for Space Research.

1.14 Effective Area Comparisons

The effective areas of the imaging instruments are shown in Figure 1.3. A comparison of the effective areas of the grating spectrometers are shown in Figure 1.4. Note that the data from the HEG and MEG are obtained simultaneously. The comparisons shown here are based on the most recent calibration at the time of issuance of this document and are subject to revision. The proposer is urged to read the detailed material in the appropriate chapters and examine the *CXC* web (see 1.16) site for updates.

1.15 Allocation of observing time

Observing time is awarded through the *NASA* proposal and peer review process. The prospective user must submit a proposal in which the observation is described and justified in terms of the expected results. The proposer must also show that the observation is well suited to *Chandra* and that it is technically feasible.

1.16 How to get information and help

The *CXC* WWW page (<http://asc.harvard.edu>) provides access to most documents, proposal preparation tools, and proposal submission software. Many documents are also available in printed form by request through the *CXC* HelpDesk or by writing to *Chandra* Directors Office, Mail stop 4, 60 Garden St., Cambridge, MA 02138. The *CXC* web page provides a “HelpDesk ” for communicating specific questions and requests concerning all user aspects of *CXO*. Details of the HelpDesk and *CXC* webpages can be found in Chapter A.

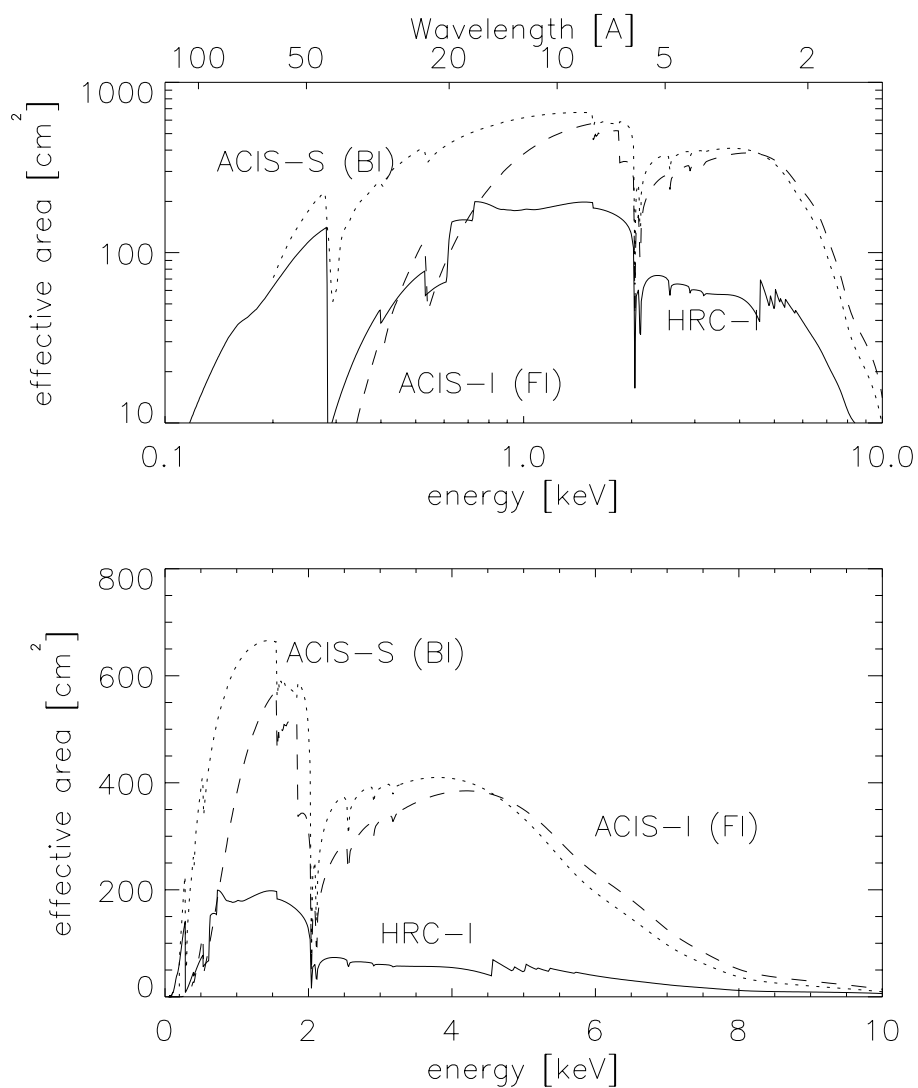


Figure 1.3: Comparison of the on-axis effective areas for observing a point source (integrated over PSF) of the HRMA/HRC-I, the HRMA/ACIS(FI), and the HRMA/ACIS(BI) combinations.

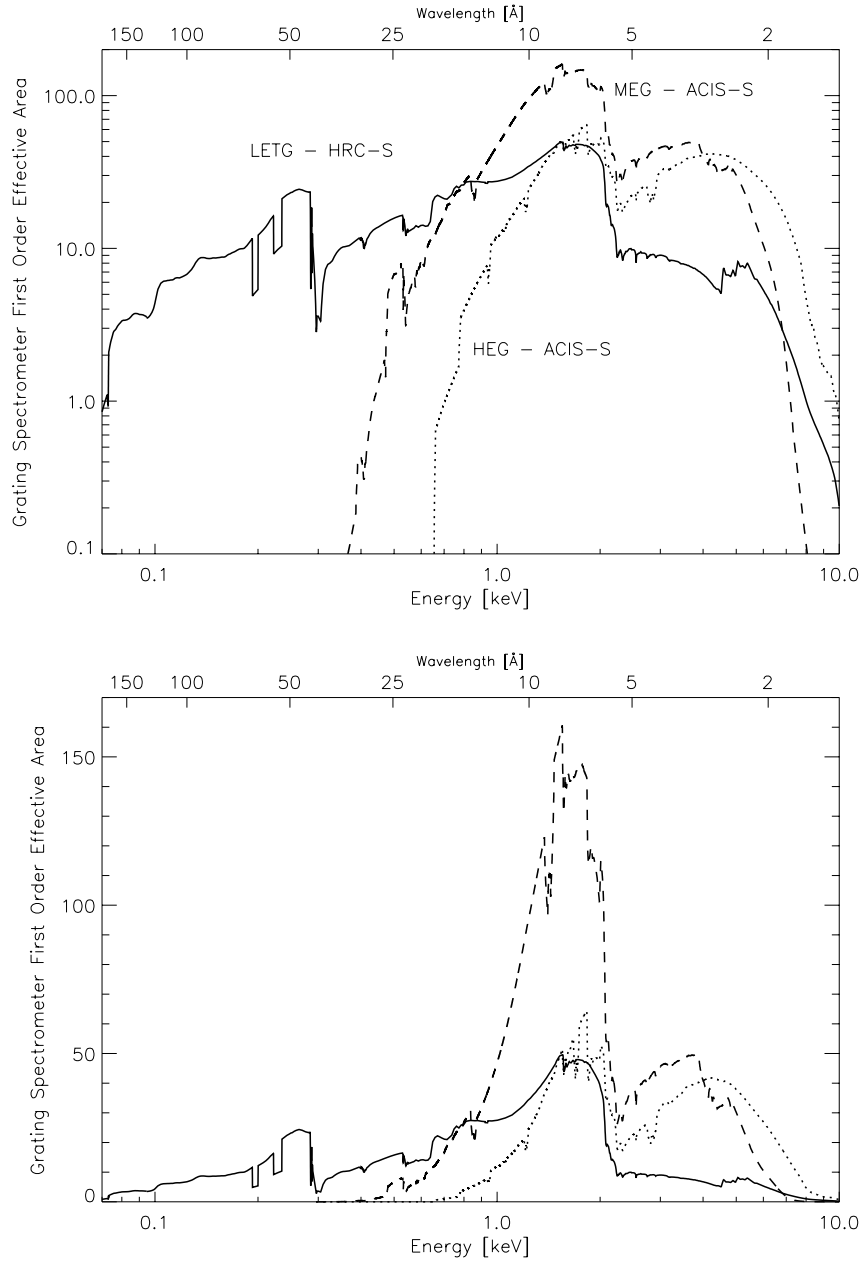


Figure 1.4: Comparison of the first-order effective areas in cm^2 (integrated over the line spread function) of the MEG and HEG and LETG spectrometers. The (+/−) first orders of the diffracted spectrum have been added.

Chapter 2

Spacecraft, Telescope, Operations, & Mission Planning

2.1 Introduction

In this chapter we provide a brief overview of the spacecraft, the telescope system including the Science Instrument Module (SIM), operations, and mission planning.

A number of observatory parameters are given in Table 2.1.

2.2 Spacecraft

An outline drawing of the Observatory was shown in Figure 1.1. The spacecraft equipment panels are mounted to, and supported by, a central cylindrical structure. The rear of the spacecraft attaches to the telescope system.

The spacecraft includes six subsystems:

1. **Structures and Mechanical** Subsystem. This subsystem includes all spacecraft structures, mechanisms (both mechanical and electro-mechanical), and structural interfaces with the Space Shuttle. Mechanisms, such as those required for the sunshade door, are also part of this subsystem.
2. **Thermal Control** Subsystem. Thermal control is primarily passive, using thermal coatings and multi-layer insulation blankets. On-board-computer-controlled electrical heaters augment these passive elements

Table 2.1: Spacecraft Parameters

<i>Chandra</i> “dry” weight (incl. reserve)	4790 kg
Loaded Propellant	969 kg
Electrical Power	3 NiH ₂ 30 Amp-hr batteries Two 3-panel solar arrays
Nominal Operating Power	2034 W (TBR)
Optical bench length	~ 10 meters
SIM focus adjustment range	±0.4 inches
SIM focus adjustment accuracy	±0.0005 inches
SIM Z-position adjustment repeatability	±0.005 inches
Solid-state recorder capacity	1.8 Gb each of 2
On-board command storage	5400 command words
Nominal command storage period	72 hours
Observatory telemetry data-rate	32 kbps
Telemetry playback downlink rates	1024, 512 and 256 kbps
Nominal ground contact periods	45 to 75 minutes per 8 hours
SI telemetry rate	24 kbps
Telemetry format	1 major frame = 32.8 seconds = 128 minor frames
Clock error	< 100 μ s
Clock stability	1:10 ⁹ per day
Clock frequency	1.024 MHz

to maintain sensitive items such as the HRMA at nearly constant temperature.

3. **Electrical and Power Subsystem.** This subsystem includes all hardware necessary to generate, condition, and store electrical energy. Power is generated by solar cells mounted on two solar array wings (three panels each), sized to provide a 15% end-of-life power margin. Electrical power is stored in three, NiH_2 , 30-Ampere-hour batteries. Battery sizing requires non-critical components, including science instruments, to be powered down during times when either the earth or the moon (partially or completely) blocks the sun. These eclipses occur infrequently due to the particular nature of the *Chandra* orbit.
4. **Communication, Command, and Data Management (CCDM) Subsystem.** This subsystem includes all the equipment necessary to provide ranging, modulation, and demodulation of radio frequency transmission of commands and data to and from the Deep Space Network NASA Communication System. The CCDM includes two low gain antennas, providing omnidirectional communications, an on-board computer (OBC), a serial digital data bus for communication with other spacecraft components, the spacecraft clock, and a telemetry formatter which provides several different formats.
5. **Pointing Control and Aspect Determination (PCAD) Subsystem.** This subsystem includes the hardware and control algorithms for attitude determination and for attitude and solar array control. The solar arrays can be rotated about one axis. The PCAD subsystem also includes hardware for safing the observatory. Specific details of the the PCAD subsystem especially relevant to scientific performance are discussed in Chapter 5.
6. **Integral Propulsion Subsystem.** This subsystem contains thrusters and fuel for control of the orbit and spacecraft orientation. The portion of the system used for orbital adjustment was disabled once the final orbit was achieved for reasons of safety to the observatory. There is enough fuel available to support more than 10 years of operation.

2.3 Telescope System

The principal elements of the telescope system are the HRMA (Chapter 4), and an optical bench. A schematic is shown in Figure 2.1. The HRMA,

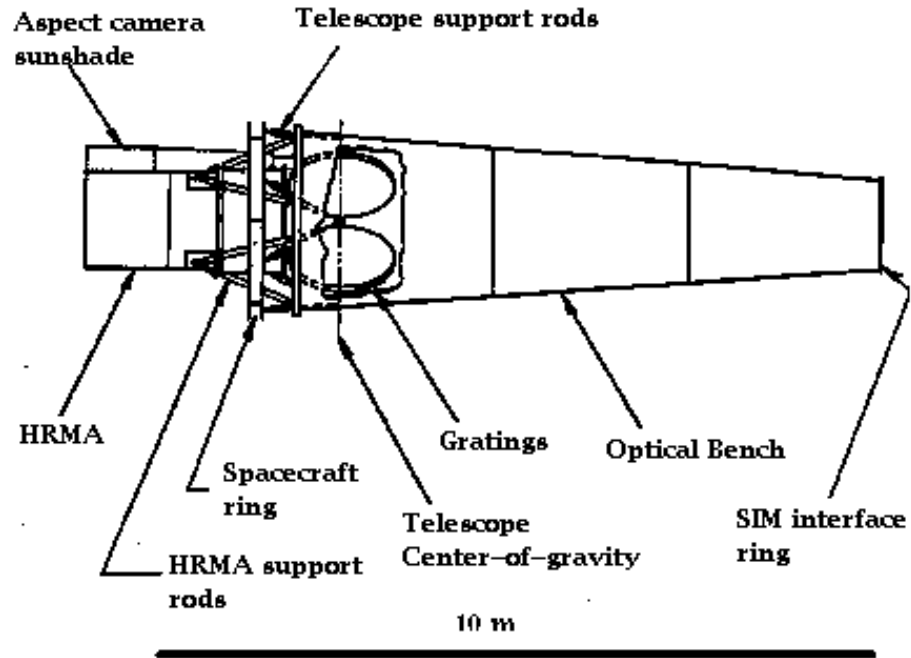


Figure 2.1: Major components of the telescope system.

comprised of four concentric grazing incidence x-ray telescopes, focuses x-rays on the selected detector located in the Science Instrument Module (2.4).

The telescope system includes:

1. High Resolution Mirror Assembly
2. Optical Bench Assembly
3. Spacecraft Support Structure Assembly
4. Fiducial Transfer Optical Components
5. Spacecraft to Telescope Support Struts
6. Forward and Aft HRMA Contamination Covers
7. Magnetic Baffle Assembly
8. Stovepipe Baffle

The Optical Bench Assembly is primarily the long composite structure separating the HRMA from the SIM. The Spacecraft Support Structure Assembly includes the ring to which the spacecraft is mounted. The Fiducial Transfer Assembly Optical Components are discussed in Chapter 5. The Spacecraft to Telescope support struts are self explanatory and are shown in Figure 2.1. The forward and aft contamination covers were opened on-orbit and cannot be closed. The forward contamination cover also serves as the sun-shade.

The magnetic baffle assembly was designed to prevent low energy (up to about ~ 100 keV) electrons (reflecting through the x-ray optics) from reaching the focal plane. More details as to these baffles may be found at

<http://wwwastro.msfc.nasa.gov/xray/magbroom/>
and
<http://wwwastro.msfc.nasa.gov/ACIS/>

The stovepipe baffle, located inside the optical bench and at the entrance to the SIM, includes tantalum coated plates to prevent x-rays, other than those passing through the telescope, from reaching the focal plane. There are several such baffles inside the optical bench. Details of the baffles may be found at:

<http://wwwastro.msfc.nasa.gov/xray/x-shield/x-shield.html>

2.4 Science Instrument Module (SIM)

The SIM, shown schematically in Figure 2.2, is a movable bench on which the focal-plane x-ray detectors are mounted. Kinematic mounts (flexures) and thermal isolation are provided between the SIM and the telescope optical bench. A graphite epoxy support structure houses the translation stage on which the instruments are mounted.

2.4.1 SIM Motions

The focal plane instruments are positioned by the SIMZ-axis translation stage with a repeatability to ± 0.005 inches over a translation range of 20 inches. The SIM X-axis motion sets the focus to an accuracy of ± 0.0005 inches over a range of 0.8 inches. The fine-focus adjustment step is 0.00005 inches.

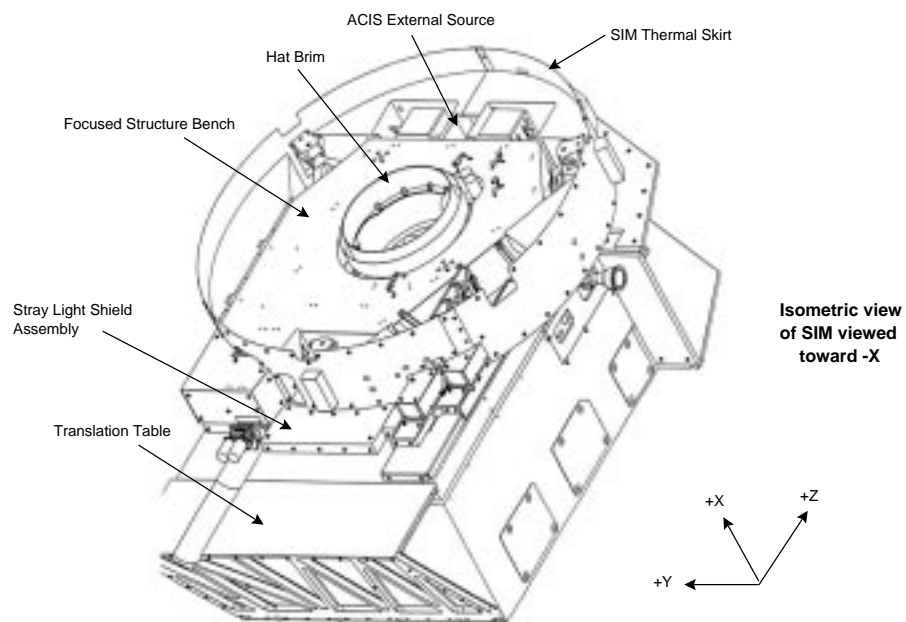


Figure 2.2: A schematic of the Science Instrument Module.

2.5 Electron Proton Helium Instrument (EPHIN)

The local particle radiation environment is monitored by the EPHIN detector. EPHIN consists of an array of 5 silicon detectors with anti-coincidence. The instrument is sensitive to electrons in the energy range 150 keV - 5 MeV, and protons/helium isotopes in the energy range 5 - 49 MeV/nucleon. The field of view is 83 degrees and the instrument is mounted near the HRMA. EPHIN data rates are monitored by the OBC, which activates commands to safe the ACIS and HRC during periods of high radiation such as a solar flare.

The forerunner of the *Chandra*-EPHIN was flown on the SOHO satellite. Information is available at

http://ifkki.kernphysik.uni-kiel.de/soho/ephin_e.html

The EPHIN instrument was built by the Institut für Experimentelle und Angewandte Physik Extraterrestrische Physik at the University of Kiel, Germany. Drs. Reinhold Müller-Mellin and Horst Kunow are the Co-Principal Investigators.

2.6 Operations

2.6.1 Launch and On-orbit Verification

Chandra was launched on board the Space Shuttle Columbia from the Kennedy Space Center in Florida on July 23, 1999 at 12:31:00:04 a.m. EDT. The Observatory was deployed from the Space Shuttle a few hours later at 8:45 a.m. EDT. Two burns of the IUS (Inertial Upper Stage) took place an hour after *Chandra* was released. A series of five burns of the Integral Propulsion System (IPS) over the period July 24-Aug 7 took *Chandra* to its final orbit.

Once in final orbit, the Orbital Activation and Checkout (OAC) phase started. During this time, all systems were brought on-line and numerous calibrations were performed. The data from these calibrations are publicly available through the *Chandra* web site. Potential proposers are encouraged to download some of the calibration data to gain experience with *Chandra*.

Originally, it was planned to devote approximately 60 days to OAC followed by 30 days of the guaranteed time observations. However, after the contamination covers on the HRMA were opened, and after a few passages through the radiation belts under this condition, the front-illuminated

ACIS CCDs showed signs of increased, and spatially-dependent, energy resolution together with increased charge transfer inefficiency (CTI), consistent with radiation damage. Steps were successfully taken to prevent further damage (see Chapter 6). Due to this situation, and because of uncertainties of the long term stability of the FI chips at that time, additional ACIS calibrations were performed and emphasis was placed on observations requiring the use of the FI CCDs. Note that the back-illuminated CCDs were unaffected, and the situation is now stable in that no further degradation is taking place. Normal Operations started in late November.

2.6.2 The Ground System

The *Chandra* “Ground System” is comprised of facilities required to operate the spacecraft, receive and analyze the spacecraft telemetry and provide scientific support to the user community. The ground system includes the following elements:

Deep Space Network (DSN). The DSN is used for communicating commands to the spacecraft and receiving telemetry.

NASA Communications (NASCOM). NASCOM provides communications links between the DSN and the OCC and between the OCC and other ground facilities.

Operations and Control Center (OCC) is responsible for operating the observatory. This includes activities such as preparing command loads, processing telemetry, attitude determination, monitoring health and safety, etc. OCC personnel utilize two major software environments, the Online System (ONLS) and the Offline System (OFLS). The ONLS deals primarily with real-time operations such as receiving telemetry and sending commands through the DSN. The OFLS deals with functions such as mission planning and supporting engineering analysis.

Software Maintenance Facility (SMF). The SMF which maintains the flight software is operated by TRW and is located at their facilities in Redondo Beach, California.

***Chandra* Science Center (CXC).** The *CXC* is the focal point for service to the scientific community. The *CXC* supports NASA in preparing technical material for NASA Research Announcements and providing technical assistance for conducting peer reviews. The *CXC* assists prospective observers in developing proposals, generates an observing

plan from the proposals that are selected, and carries out certain data processing to supply data products to observers. The *CXC* performs on-orbit calibration and maintains the calibration data-base, produce response functions, etc. The *CXC* is also responsible for providing limited assistance to observers, including software, for analyzing data. The *CXC* is also responsible for archiving *Chandra* data.

2.6.3 Commanding

All normal *Chandra* operations are preplanned. The OFLS divides the weekly mission schedule into approximately one day segments and generates spacecraft and instrument commands to be executed that day. Once a day, this command load is uplinked to the spacecraft and stored. Three consecutive daily segments are loaded to assure autonomous operation for 72 hours. Stored command loads can be interrupted if necessary, and updated either because of an emergency or to accommodate Targets of Opportunity. The interruption process may require up to 24 hours to complete depending on numerous factors including the availability of ground contact. In a true emergency, ground contact can always be scheduled.

2.6.4 Telemetry

The telemetry is formatted into major frames and minor frames -a major frame lasts 32.8 seconds and includes 128 minor frames. Each minor frame contains 1019 bytes of science and engineering data plus a 6 byte header (yes - 1025, not 1024, total bytes!) that includes a 3-byte minor frame counter – the Virtual Channel Data Unit (VCDU) counter – which resets every 49.8 days.

During normal science operations, telemetry data is generated on the Observatory at a rate of 32 kbps, of which 24 kbps are devoted to the “science stream” data from one of the focal plane instruments and the remainder allocated to other systems, including 0.5 kbs to the “next-in-line” instrument. The data is recorded on one of two solid state recorders for subsequent transmission to the ground. Each solid state recorder has a capacity of 1.8 Gbits equivalent to 16 hours of operation.

The recorded data are transmitted through one of the low gain antennas to the ground at 1024 kbps, (or 512 kbps, or 256 kbps) during scheduled Deep Space Network contacts every eight hours. Contacts last typically from 45-75 minutes. The ground stations, in turn, transmit the data to JPL which then transmits the data to the OCC.

2.6.5 SI Science Data

There are individual telemetry formats for HRC and ACIS data. The 24 kbps data is collected by the CCDM subsystem from each instrument as a sequence of 8-bit serial-digital words through a Remote Command and Telemetry Unit (RCTU). An additional small amount of housekeeping telemetry is always collected from each instrument independent of the selected format.

2.6.6 Event Timing and the Spacecraft Clock

The CCDM subsystem provides prime and redundant 1.024 MHz clocks, and the $(1/1.024\mu\text{s})$ pulses are utilized by the two focal plane instruments for timing. Each instrument has electronics that counts the elapsed time since the beginning of the current telemetry major frame. The time of events recorded on *Chandra* are given in Terrestrial Time (TT) which differs from UTC by about a minute. (See <http://tycho.usno.navy.mil/systime.html> for a discussion.) The accuracy of the time relationship is 100 microseconds. The spacecraft clock is stable to better than one part in 10^9 per day.

2.7 Mission Planning

The structure of *Chandra* scheduling is derived from the desire for efficiency as part of the process of maximizing the scientific return at the same time minimizing risk to the spacecraft. Annually, the process ingests a list of targets and associated observing information from the calibration program, guaranteed time observations, and successful proposals submitted in response to a NASA NRA. A Science Plan is developed from this list with the aid of the Spike scheduling software, originally developed for use with the Hubble Space Telescope and modified for *Chandra*. The Spike routine places all available targets into various one week segments during which sky-viewing constraints (e.g., sun avoidance) and any user-imposed constraints such as time or roll angle can be satisfied. Unconstrained observations are kept in a pool of targets to help fill in the weekly schedule.

The next step in the process is to forward a one month interval of the Science Plan to the Flight Operations Team (FOT), which constructs a detailed weekly operation plan for use several weeks in the future. Oversubscription of targets allows the FOT, using the Mission Planning and Scheduling software, to construct the detailed schedule. Priorities are set so that all of the constrained observations (which must be accomplished) and a subset of the unconstrained targets are used in creating the most observatory-efficient

schedule. The *CXC* keeps track of unscheduled targets and updates the pool accordingly. The Science Plan is available to observer's on the *CXC* [www](#) site.

Chapter 3

Offset Pointing, Visibility, and other Constraints

3.1 Introduction

This chapter gathers together several topics pertaining to observation planning, irrespective of focal-plane instrument and grating configuration, to serve as additional guidelines for preparing proposals. Most all of these topics are automatically addressed by the observation visualizer software discussed in Chapter 12. The intention here is to familiarize the user with these issues.

3.2 Offset Pointing

The offset pointing convention for *Chandra* is that a negative offset of a coordinate moves the image to more positive values of the coordinate and vice-versa. Example of offset pointings of the ACIS instrument are shown in Figure 3.1. Examples using the HRC are shown in Figure 3.2.

3.3 Visibility

There are a number of factors that limit the precise time when observations can be performed.

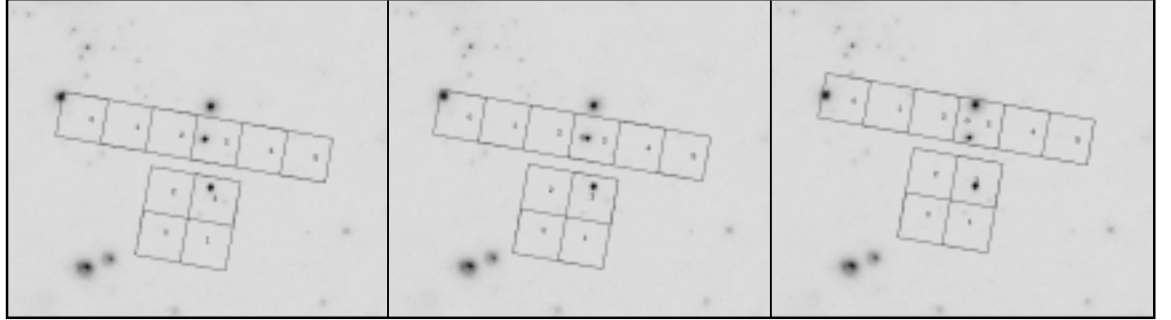


Figure 3.1: Examples of offset pointing with ACIS. North is up, and East is to the left. Roll is measured positive, West of North. The roll angle shown is 10° . Left Panel: The target, a bright x-ray source, is placed at the ACIS-S nominal aimpoint with (Y,Z) offset of (0,0) arcmin. In the Center Panel the offset is (-1,0). In the Right Panel the offset is (-1,-3). Note the small circle at the location of the ACIS-S aimpoint.

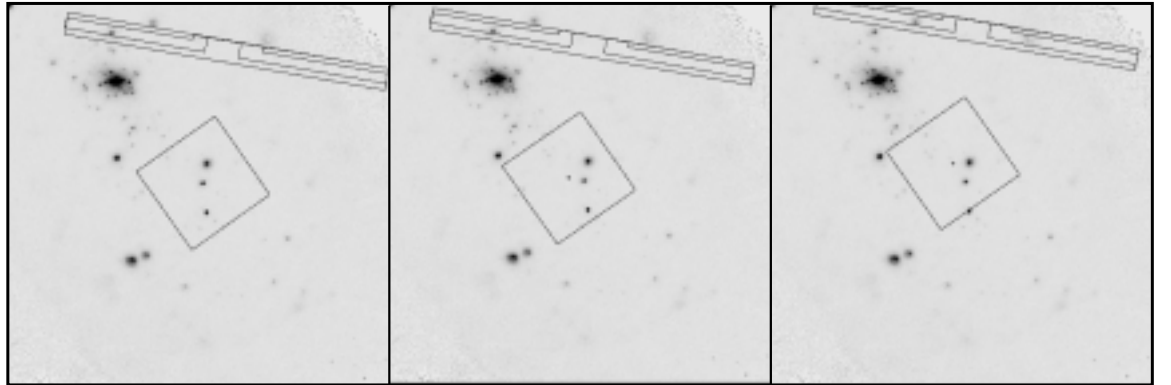


Figure 3.2: Example of offset pointing with HRC. North is up, and East is to the left. Roll is measured positive, west of north. The roll angle shown is 10° . Left Panel: The target, a bright x-ray source is placed at the HRC-I nominal aimpoint with (Y,Z) offset of (0,0) arcmin. Center Panel: the offset is (-5,0). Right Panel: the offset is (-5,-5)//Note the small dot at the location of the HRC-I aimpoint.

3.3.1 Radiation Belt Passages

High particle-radiation levels are encountered as the Observatory approaches perigee. Data acquisition ceases whenever certain particle-radiation thresholds are exceeded. A working number for the altitude at which this takes place is about 60,000 km. Cessation of observations and protection of the instruments in regions of high radiation results in approximately 25% of the 63.5 hour *Chandra* orbit being unusable.

3.3.2 Avoidances

There are two soft (can be overridden), and one hard (cannot be overridden) avoidances:

1. Sun avoidance – cannot be overridden – viewing is restricted to angles larger than 45 degrees from the limb of the Sun. This restriction makes about 15% of the sky inaccessible on any given date, but no part of the sky is ever inaccessible for more than 3 months.
2. Moon avoidance – viewing is restricted to angles larger than 6 degrees from the limb of the Moon. This restriction makes less than 1% of the sky inaccessible at any time. This avoidance can be waived, but at the price of a reduced-accuracy aspect solution (see Chapter 5).
3. Bright Earth avoidance – viewing is restricted to angles larger than 20 degrees from the limb of the bright Earth. This restriction makes less than 10% of the sky inaccessible at any time, but there are certain regions which can only be viewed, continuously, for up to about 30 ks. The avoidance can be waived, but at the price of a reduced-accuracy aspect solution (see Chapter 5).

The combination of these avoidances implies that 80 to 85% of the sky is accessible for viewing at any time. The exact value depends on the relative positions of the Sun, Earth, and Moon as seen from *Chandra*.

Figure 3.3 illustrates the point that the Earth avoidance region is nearly stationary in equatorial coordinates. This is a consequence of the high orbit and exacerbated by radiation belt passages: For the nominal orbit (inclination 28.5 degrees, right ascension of the ascending node 200 degrees, and argument of perigee 270 degrees), the region near $RA \sim 110^\circ$, $DEC \sim -30^\circ$ lies within the earth avoidance zone and continuous observations in this region are limited to < 30 ks duration. This partially blocked region will move

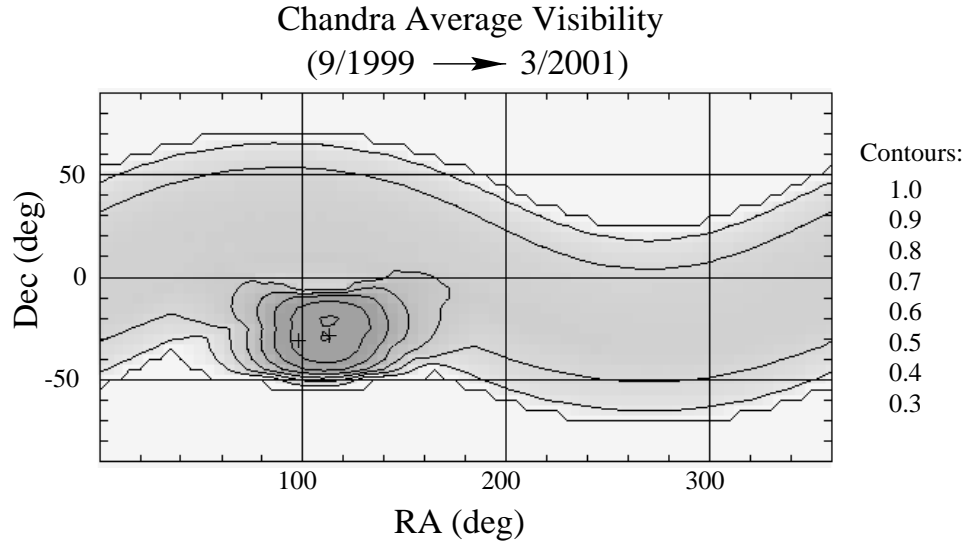


Figure 3.3: The *Chandra* visibility showing contours of fractional visibility averaged over an 18-month interval. A value of 1.0 indicates that observations in this region are interrupted *only* by passes near perigee into the radiation belts, a value of 0.9 indicates that observations are available 90% of the time, etc. The center of the area of lowest visibility is marked by the two + symbols; the one at higher RA is for 7/99, the other is for 3/01.

only several degrees per year, as indicated, reflecting the evolution of the orbital elements.

3.3.3 Roll Angles

The spacecraft and instruments were designed to take advantage of the Observatory having a hot and a cold side. Thus, the spacecraft is preferentially oriented with the Sun on the $-Z$ side of the $X-Y$ plane, where $+X$ is in the viewing direction, the Y -axis is parallel to the solar panel axes, and $+Z$ is in the direction of the ACIS radiator (see Figure 1.1). In this orientation there is only one “roll angle” (rotation about the viewing- or X -axis - positive west of north) for which the solar panels can be rotated so that they are directly viewing the sun - the nominal roll angle. Small deviations (\sim degrees) from the nominal roll angle are allowed which depend on the efficiency of the solar panel and the “beta angle” - the angle between the target and the sun. The roll-angle constraint imposes further visibility restrictions. These can also be evaluated with the *ObsVis* tool.

3.4 Constraints and Considerations

The instrument constraints are discussed in the appropriate Chapters and user-imposed constraints are discussed in the instructions for completing the RPS form. We summarize these here. Please examine the relevant Chapters for details.

3.4.1 Instrument Constraints and Considerations

- The HRC has a brightness limit which limits the flux per microchannel plate pore.
- The HRC has a telemetry limit. Exceeding this limit, amongst other consequences, reduces observing efficiency.
- The HRC has linearity limits. Exceeding these limits voids the effective area calibrations.
- The ACIS has a telemetry limit. Exceeding this limit, amongst other consequences, reduces observing efficiency.
- The ACIS is subject to the effects of pulse pileup. Dealing with this effect requires careful planning of the observation.

3.4.2 User-Imposed Constraints

Chandra users may need to specify a number of observing constraints particular to their observations. In general, the specification of a user-imposed constraint decreases the efficiency of the observatory and therefore should be well justified in the proposal. Note that only a limited fraction ($\leq 25\%$) of constrained observations can be accommodated. User imposed constraints are

- Time Constraints:**
1. Time Windows – specific time intervals in which observation must be scheduled. Such constraints are primarily for use in coordinated observing campaigns or for arranging an observation to coincide with some time-critical aspect of the target.
 2. Monitoring Intervals – for observing a target at semi-regular intervals for a specified duration.

3. Ordering of observations – specifying that a set of observations be carried out in a particular order (with or without a range in allowed delays between the end of the first observations and the beginning of the second, third, etc.).
4. Continuity of observation – specifying that an observation may not be interrupted (up to 170 ks).

Roll Constraints: – specifying a particular roll angle and tolerance.

Chapter 4

High Resolution Mirror Assembly (HRMA)

4.1 Description and Physical Configuration

The *Chandra* telescope consists of 4 pairs of concentric thin-walled, grazing-incidence Wolter Type-I mirrors. [X-ray optics are reviewed by B. Aschenbach (1985).] The front mirror of each pair is a paraboloid (P_n) and the back a hyperboloid (H_n). The eight mirrors were fabricated from Zerodur glass, polished, and coated with iridium on a binding layer of chromium.

The High Resolution Mirror Assembly (HRMA), shown schematically in Figure 4.1, contains the nested mirrors, center, forward and aft aperture plates, baffles, inner and outer cylinders, mounts, pre- and postcollimators, fiducial light transfer components, mirror support sleeves, forward and aft contamination covers, flux contamination monitors, and thermal control hardware. The outer mirror pair is number 1, and, progressing inwards, 3, 4, and 6. (The original design had six mirror pairs; numbers 2 and 5 were eliminated.) The pair diameters range from about 0.65 to 1.23 meters. The distance from the center of the Central Aperture Plate (CAP) separating the paraboloid and hyperboloid mirrors to the Gaussian focal point is 10.0548 meters, with each mirror pair varying slightly about this value. (Note that this distance is close to, but not exactly, the focal length.) Some other characteristics are given in Table 4.1 and in section 4.5

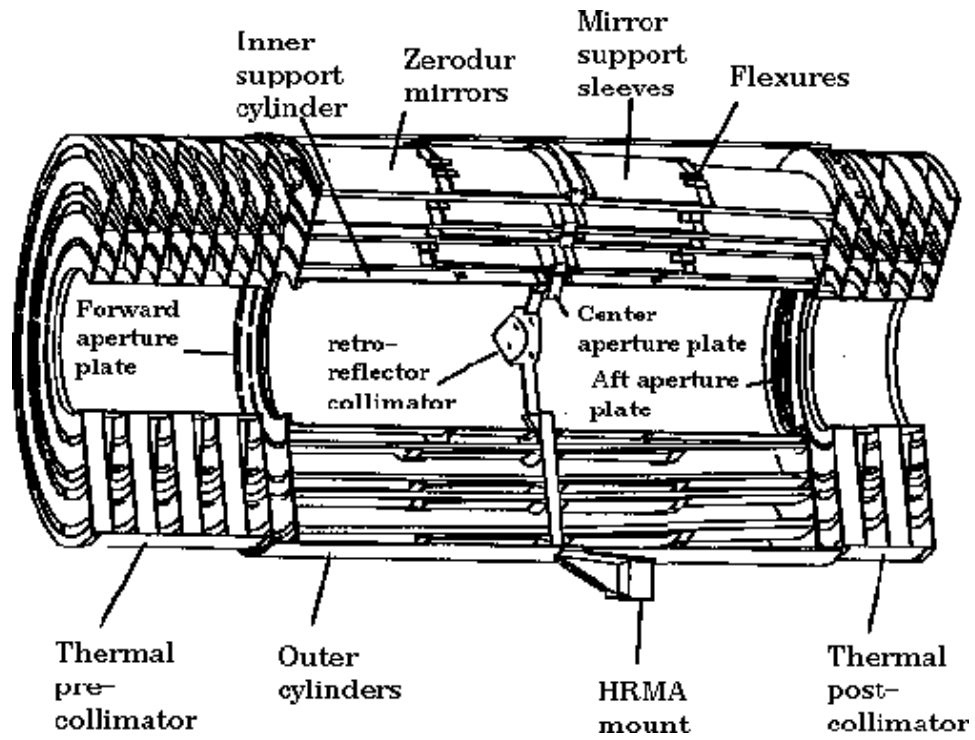


Figure 4.1: The 4 nested HRMA mirror pairs and associated structures.

Table 4.1: *Chandra* HRMA Characteristics

HRMA	
Optics	Wolter Type-I
Mirror coatings	Iridium
Nominal coating thickness	330 Å
Mirror outer diameters (1, 3, 4, 6)	1.23, 0.99, 0.87, 0.65 m
Mirror lengths (P_n or H_n)	84 cm
Total length (pre-collimator to post-collimator)	276 cm
Unobscured clear aperture	1145 cm ²
HRMA mass	1484 kg
Focal length	10.066 m
Plate scale	48.8 $\mu\text{m arcsec}^{-1}$
PSF FWHM (with detector)	0.5 arcsec
Effective area:	
@ 0.25 keV	800 cm ²
@ 5.0 keV	400 cm ²
@ 8.0 keV	100 cm ²
Ghost-free field of view	30 arcmin dia

4.2 Calibration and Performance

4.2.1 Calibration and Model

VanSpeybroeck (1997), Weisskopf (1997), and Zhao et al. (1997), describe the ground calibration of the HRMA and present some preliminary results. During these tests, the mirror assembly was mounted horizontally in a vacuum chamber and irradiated with X-rays from a source located at a distance of approximately 500 meters. The data taken in the XRCF (the X-Ray Calibration Facility at MSFC) include the effective areas and image distributions as a function of incident energy and angle. The mirror performance during these tests differs from that expected in space because of gravity distortions and the finite source size and distance; consequently, the calibration data cannot be directly compared to flight observations. The approach taken was to develop a model based upon surface and assembly measurements taken before the X-ray calibration activity. The X-ray calibration data then were used to validate this model and to make minor adjustments in model parameters to achieve satisfactory agreement with the observations. Further minor modifications were made as a result of flight experience.

The HRMA characteristics illustrated in this chapter were generated

by a ray-trace program using this model. Note that this chapter typically gives characteristics of the HRMA only; unless otherwise indicated, blurring caused by the detector and the aspect solution is *not* included. These effects are *very* important for on-axis sources, and are included in the instrument chapters. See also section 4.4.

4.2.2 HRMA Effective Area

The unobscured geometric clear aperture of the HRMA is 1145 cm^2 , which is about 0.1% of the full aperture's area [$\pi(1200/2)^2 = 1.1 \times 10^6 \text{ cm}^2$]. The obstruction of the HRMA clear aperture by supporting struts is less than 10%. Since reflectivity depends on energy as well as grazing angle, the HRMA throughput varies with x-ray energy.

Figure 4.2 shows the dependence of effective area on energy for each mirror pair and for the HRMA. Figure 4.3 shows the effects of off-axis vignetting on the effective area for various energies; the plotted results are averages over the azimuthal angle.

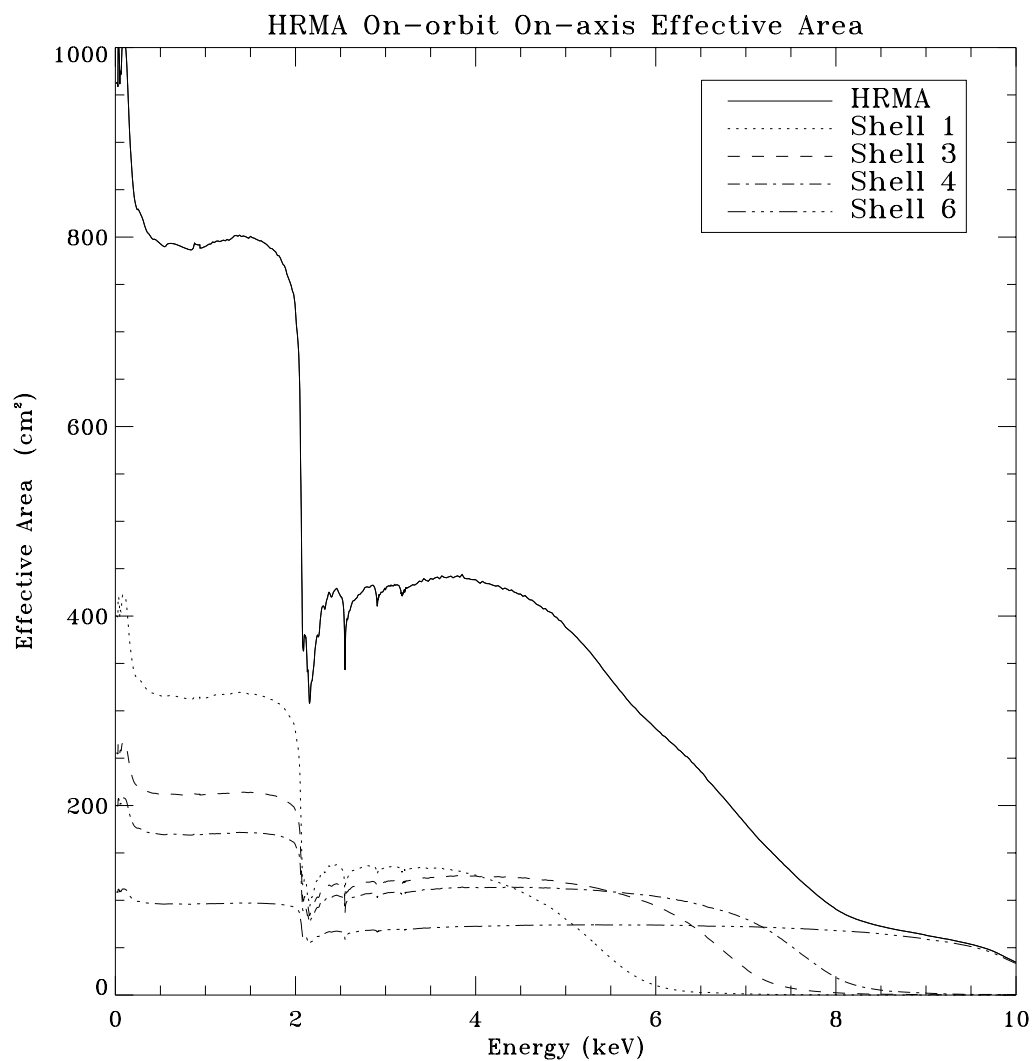
The above predictions are based upon the mirror model discussed previously and scaled by the HRMA ground calibration data. The agreement between the effective area predicted for the ground calibration using this model and the actual measurement, as well as the scaling function used for the on-orbit prediction, are shown in Figure 4.4.

4.2.3 Point-Spread-Function and Encircled Energy Fraction

The *Chandra* HRMA point-spread function (PSF) has been simulated with numerical ray-trace calculations based upon the model previously discussed. A most useful parameter is the encircled energy fraction (the two-dimensional integral of the PSF) as a function of radius from the image center. The PSF and the encircled energy fraction for a given radius depend upon off-axis angle and energy. The PSF broadens, and the encircled energy fraction decreases, as the off-axis angle increases because of mirror aberrations. The performance also degrades as the X-ray energy increases because of larger X-ray scattering.

On-axis Response

Figure 4.5 shows the encircled energy fraction as a function of image radius for on-axis rays and for different energies. The resulting increase in image size with energy is apparent. The fraction contained within one and ten



Zhao/SAO 23Feb00

Figure 4.2: The HRMA effective area versus energy. The total predicted on-orbit effective area and contributions of each $P_n - H_n$ pair are shown on a linear scale. The structure near 2 keV is due to the iridium M-edge.

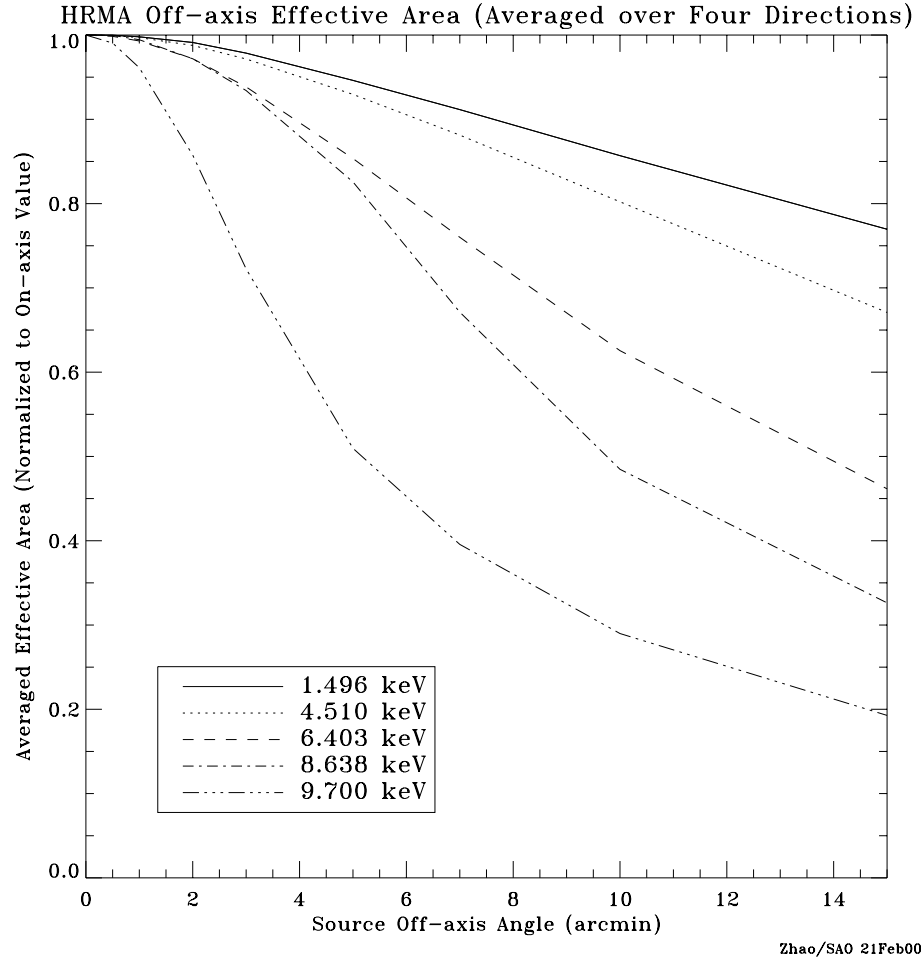


Figure 4.3: The HRMA effective area versus off-axis angle, averaged over azimuth, for selected energies, normalized to the on-axis area for that energy.

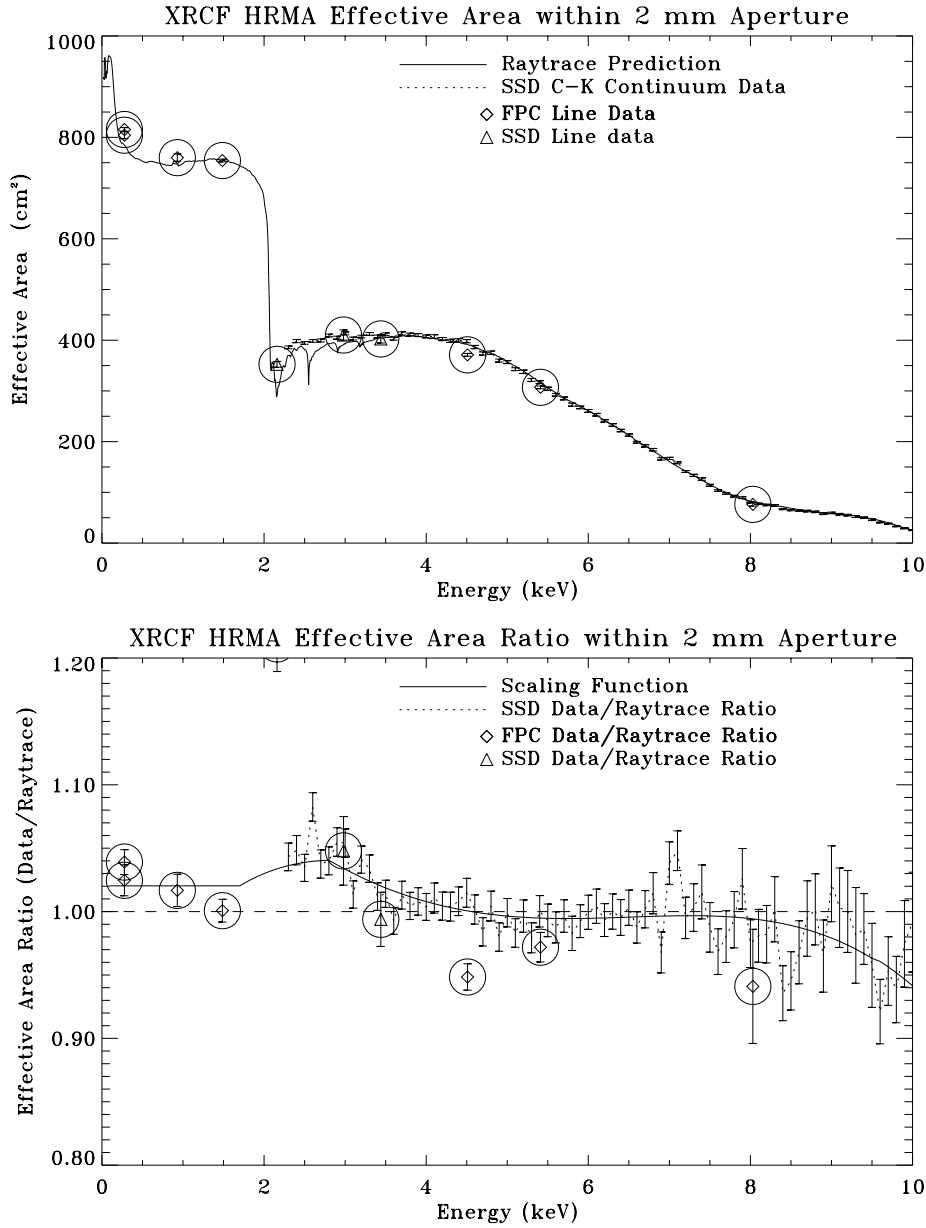


Figure 4.4: The HRMA effective area versus energy as measured during the ground calibration. The solid line in the upper plot is the raytrace prediction and data points are shown for a continuum and 2 sets of line sources. The contributions from all 4 mirrors are included. The lower curve shows deviation of measurements from the raytrace prediction.

Table 4.2: HRMA Encircled Energy Performance

X-ray:		Encircled Energy Fraction	
E	λ	Diameter	
kev	\AA	1''	10''
0.1085	114.2712	0.7954	0.9979
0.1833	67.6401	0.7937	0.9955
0.2770	44.7597	0.7906	0.9929
0.5230	23.7064	0.7817	0.9871
0.9297	13.3359	0.7650	0.9780
1.4967	8.2838	0.7436	0.9739
2.0424	6.0706	0.7261	0.9674
2.9843	4.1545	0.6960	0.9560
3.4440	3.6000	0.6808	0.9479
4.5108	2.7486	0.6510	0.9319
5.4147	2.2898	0.6426	0.9300
6.4038	1.9361	0.6365	0.9344
8.0478	1.5406	0.5457	0.9185
8.6389	1.4352	0.5256	0.9151
10.0000	1.2398	0.4971	0.8954

arc seconds diameters for on-axis rays is shown as a function of energy in Figure 4.6 and in Table 4.2.

Pre-flight measurements and also images taken at the XRCF show that there is a slight ($\approx 500\mu\text{m}$) offset between the optical axes of the paraboloids and hyperboloids, and that pair 6 is slightly tilted with respect to the other three. Consequently, the image from mirror pair 6 is not as symmetrical as the images from the other shells. The effect of this asymmetry on images depends on energy because of the different relative contribution of mirror pair 6.

Figure 4.7 shows simulated HRMA/HRC-I images at four energies. The effect of the mirror pair 6 alignment errors can be seen in the 8.6 keV image; note that the core of this image is not centered in the distribution. This 0.2'' effect is not important compared to other sources of image degradation encountered in flight such as uncertainties in the aspect solution.

Off-axis Response

The PSF broadens for off-axis sources, and there is considerable distortion in the image even for a perfect mirror set. This distortion is due to the

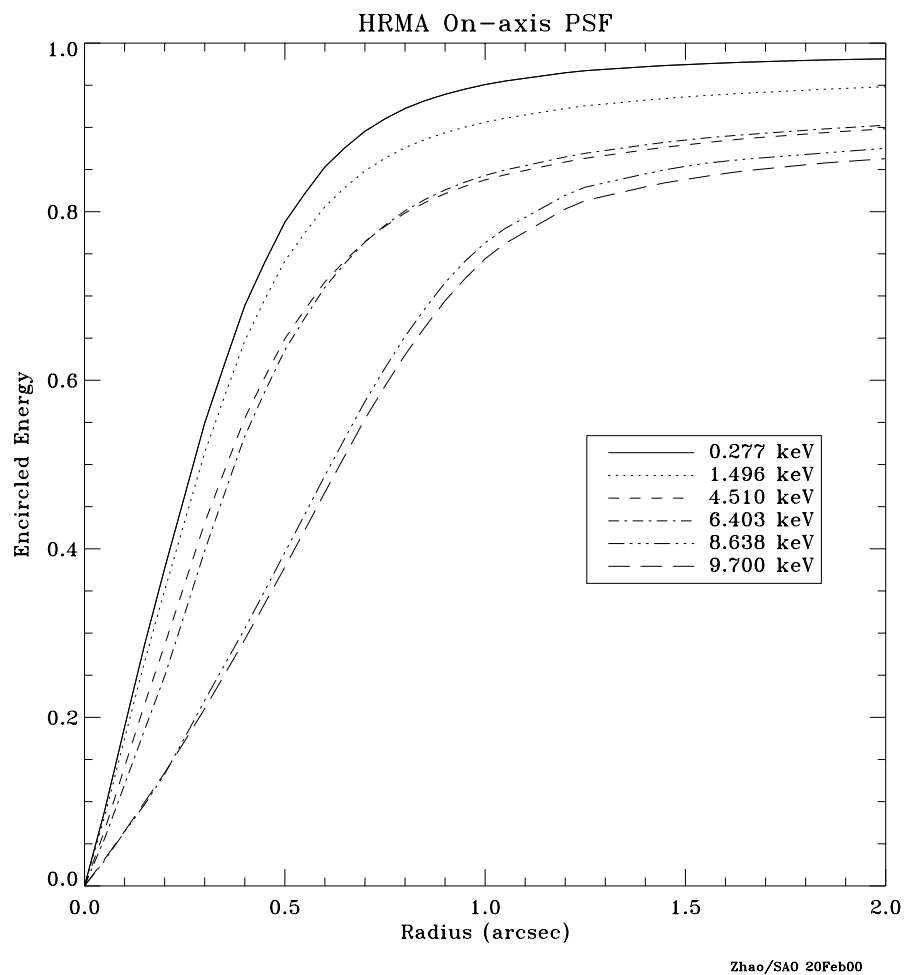


Figure 4.5: The fractional encircled energy as a function of angular radius calculated for an on-axis point-source, at selected X-ray energies. The curves are the combined response of the four nested mirror pairs.

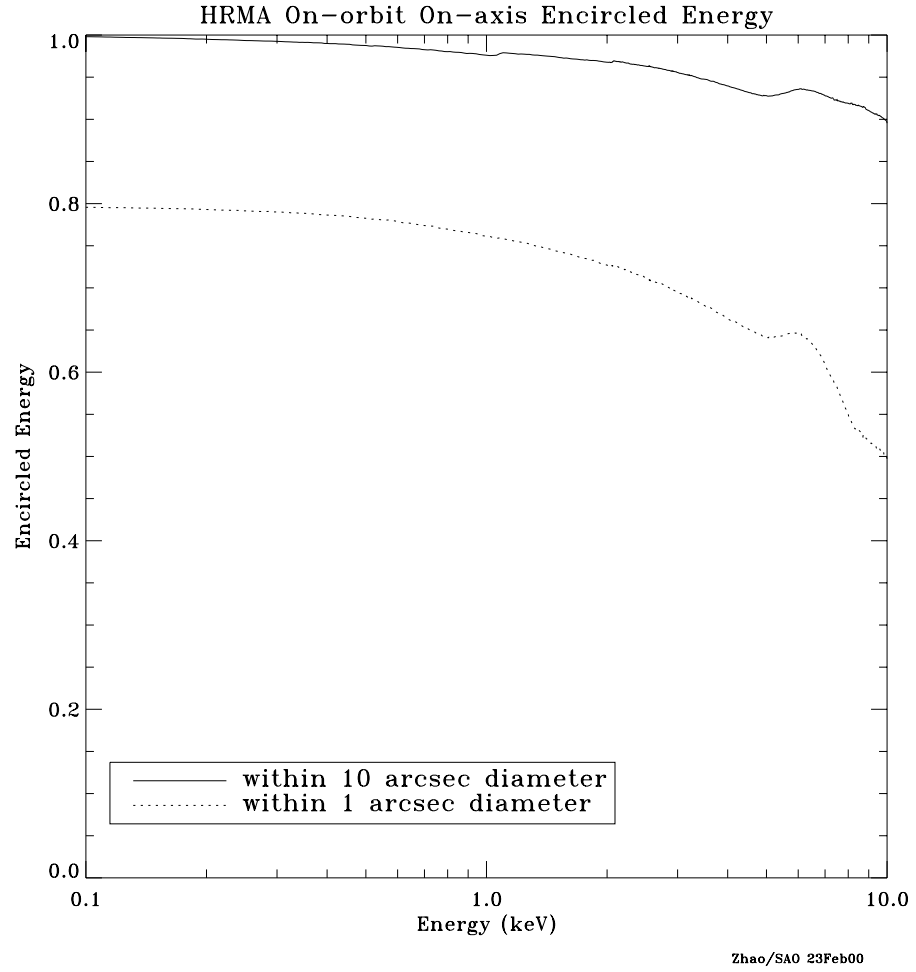


Figure 4.6: On-orbit performance prediction for encircled energy, calculated from model derived from ground-based calibration data.

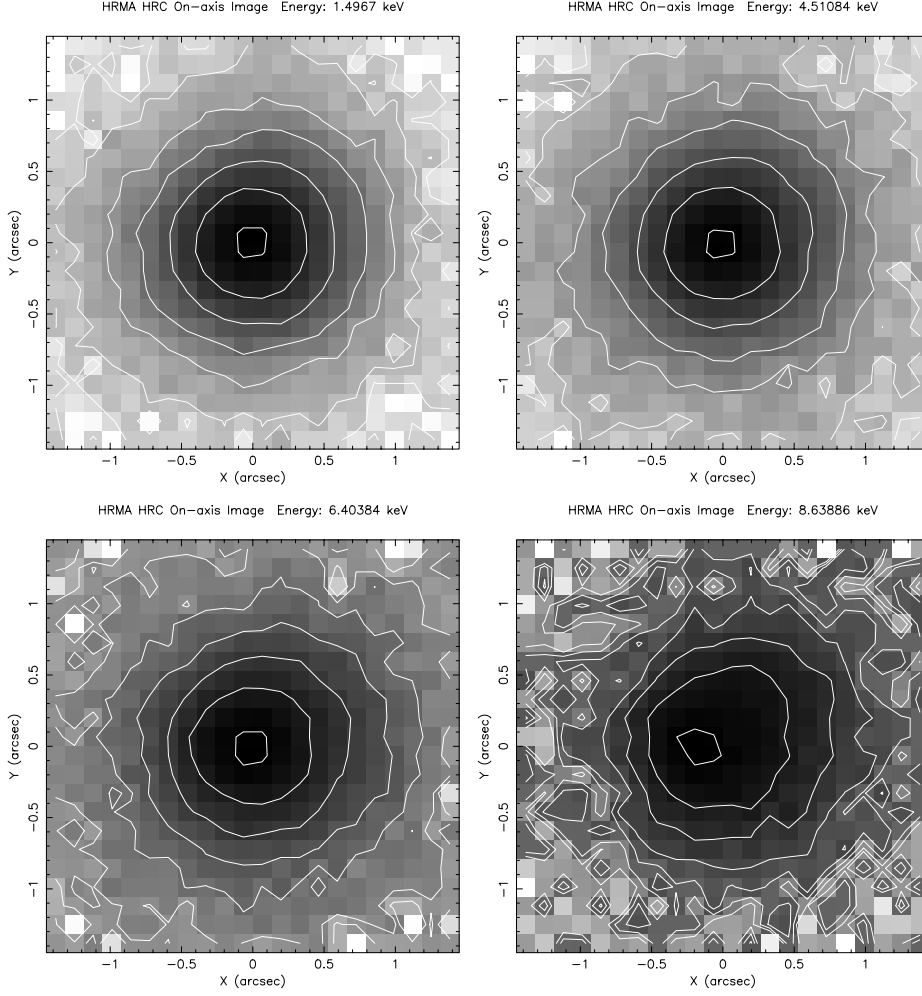


Figure 4.7: Simulated on-axis HRMA/HRC-I on-axis images of mono-energetic point sources without aspect blurring. Energies (reading like a book) are 1.49, 4.51, 6.40, and 8.63 keV. Surface brightness contours are logarithmic and spaced in factors of 3. The innermost contour is at 90% of the peak brightness. The 8.6 keV image core is off-center due to the shell 6 misalignment. Each panel is $3''$ square.

aberrations of Wolter type I optics and to the different focal surfaces for the four mirror pairs. The increase in image size with off-axis angle is greatest for the inner shell, and hence is larger for higher X-ray energies. Figure 4.8 shows the dependence of encircled energy radii on off-axis angle.

Figure 4.9 contains simulated HRMA images of point sources 5' and 10' off-axis, at the flat HRC-I surface. At 10' off-axis the separation between the flat detector surface and the curved focal surface is significant. Cusps in the HRMA images are due to a slight misalignment of the parabolic and hyperbolic mirrors.

4.2.4 Effective Area in Flight

There was a concern that the effective areas might change between ground calibration and flight due to accumulation of contaminants or degradation of the reflecting surfaces. A Flux Contamination Monitor (FCM) was added to evaluate these effects. The FCM consisted of radioactive sources embedded in the forward contamination cover. The ACIS response to these sources was measured in the XRCF at the end of ground calibration, and again in orbit before the forward contamination cover was removed. No change in performance was detected.

The FCM is described in Elsner et al., 1994. The *Chandra* detectors are not exposed to the FCM now that the forward contamination cover has been opened.

4.3 Ghost Images

Baffles prevent non-reflected or singly reflected rays from impinging on the focal plane within the central 29' diameter of the field of view. Outside of this region, however, singly reflected rays from strong off-axis sources may appear. Figure 4.10 shows a simulated ghost image in which the off-axis angle was chosen to give the closest approach of singly-reflected rays to the focal point. In this situation, the outermost ray could extend into the HRC field of view. The area extending from the optical axis to a diameter of about 29' is free from ghost images.

4.4 Effects of Aspect and Instrument Uncertainties

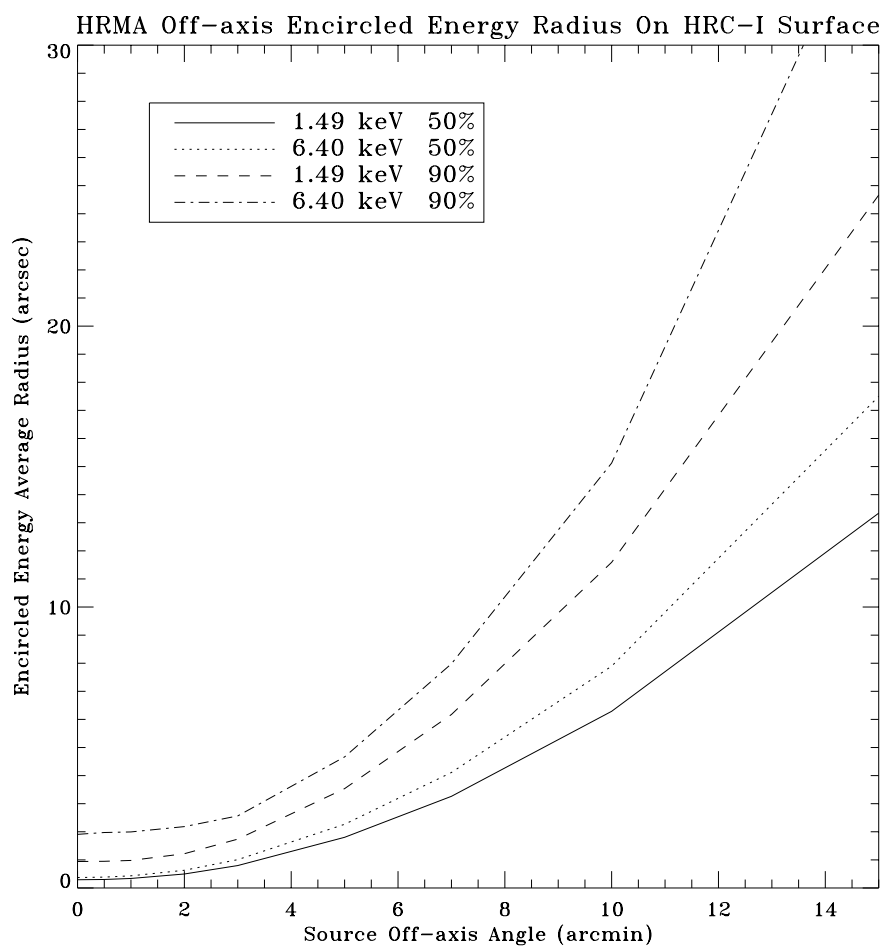


Figure 4.8: Radius of a circle enclosing 50% and 90% of the power [at 1.5 and 6.4 keV] as a function of off-axis angle. These curves apply to flat detectors (e.g. HRC-I or ACIS-S(S3)) which do not follow the curved focal plane

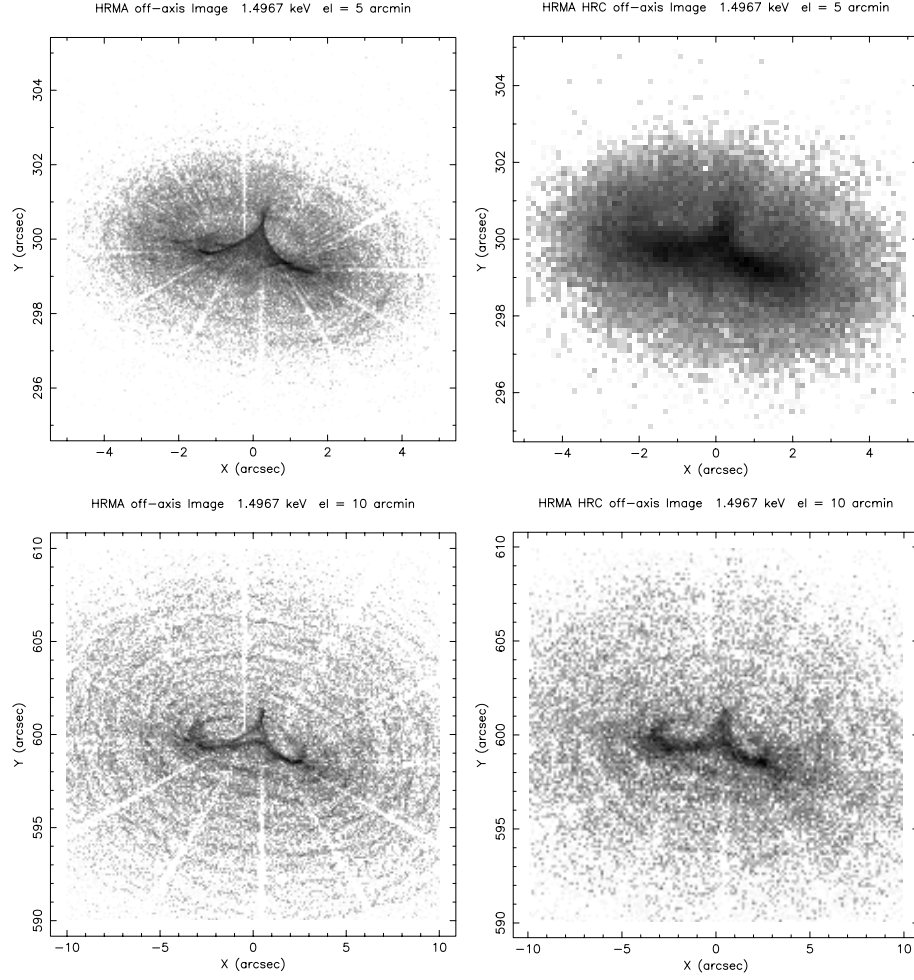


Figure 4.9: Simulated 1.49 keV images, for the HRMA only (at left) and the HRMA HRC-I combination (at right), of a point source 5' (at top) and 10' (at bottom) off-axis. Panels are 11'' and 22'' square, respectively, much larger than the panels in figure 4.7. Spokes in the images are due to shadowing by mirror support struts. The 10' off-axis images include some rays slightly outside of the figures.

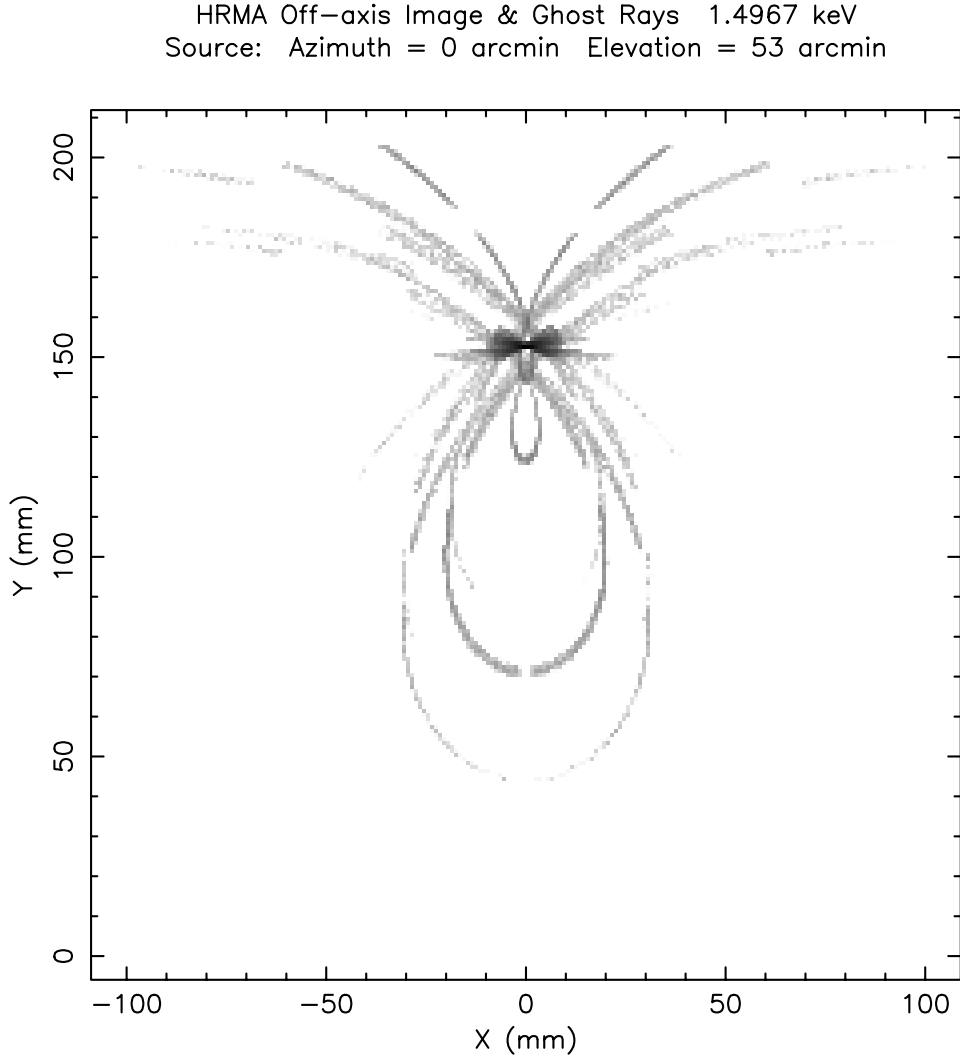


Figure 4.10: Calculated image of a source on the HRC-I at 53' off-axis. The aimpoint is at position (0,0) at bottom center of the figure. The horizontally elongated bright region at (0,150) is the image produced by doubly reflected rays. The other curved lines in the figure are due to single reflections from different mirror segments. These lines comprise the “ghost image”. If the HRC-I detector were centered on (0,0) with diagonal vertical, the upper corner of the field would be at (0,64)

The HRMA performance discussed in the previous sections will be slightly degraded by uncertainties in the aspect solution and the details of the imaging detector spatial response function. The ground software system also deliberately adds a small random position error to reduce image artifacts which result from instrument and data system integer location values. These effects are illustrated for the HRC-I and HRC-S instruments in Figures 4.11 and 4.12 respectively. These figures also show the fractional encircled energy as a function of radius actually observed in flight compared to model calculations at 0.277 and 6.403 keV. A ± 0.4 arcsec aspect error was included in the model calculations. The agreement between the observations and the lower energy model predicted curve is quite good. The HRC efficiency and typical spectral photon number densities both decrease with energy, so the higher energy response curve would not be expected for most sources.

Similar calculations have been performed for the ACIS-S(S-3) over a wider range of energies; the results are shown in Figure 4.13. The simulation accounted for the typical spacecraft jitter, so the location of the instrument pixel boundaries has little effect. There is, however, a small effect of the location of the source compared to the data system pixel boundaries. These particular calculations were performed for a point source centered on the boundary between two data system pixels. The ACIS-I instrument response is similar.

The curves of this section, Figures 4.11, 4.12, and 4.13 may be compared with Figure 4.5 to estimate the image performance degradation due to non-HRMA effects.

4.5 HRMA background material

4.5.1 Heritage

The *Chandra* mirrors represent a logical progression from those of the Einstein (HEAO-2) (Giacconi et al. 1979) and ROSAT (Trümper 1983; Aschenbach 1991) missions. Each of these previous X-ray observatories utilized nested Wolter Type-I optics with about 4 arcsec angular resolution. The Einstein mirror assembly had considerably less geometric area than *Chandra*, while ROSAT had comparable area (1100 cm^2) at low energies ($< 1 \text{ keV}$).

The Validation Engineering Test Article-I (VETA-I) was constructed to verify the technology required for the spatial resolution of *Chandra*. VETA-I contained the P_1H_1 proto-flight mirror shells constructed to final tolerances,

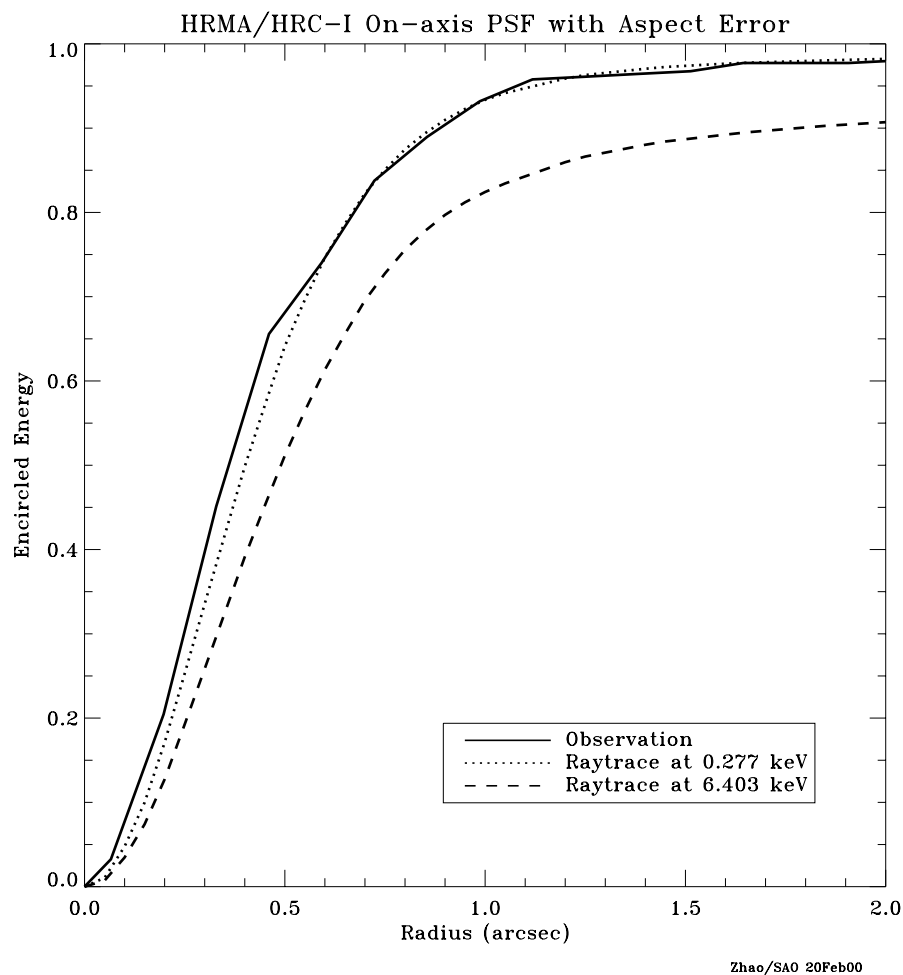
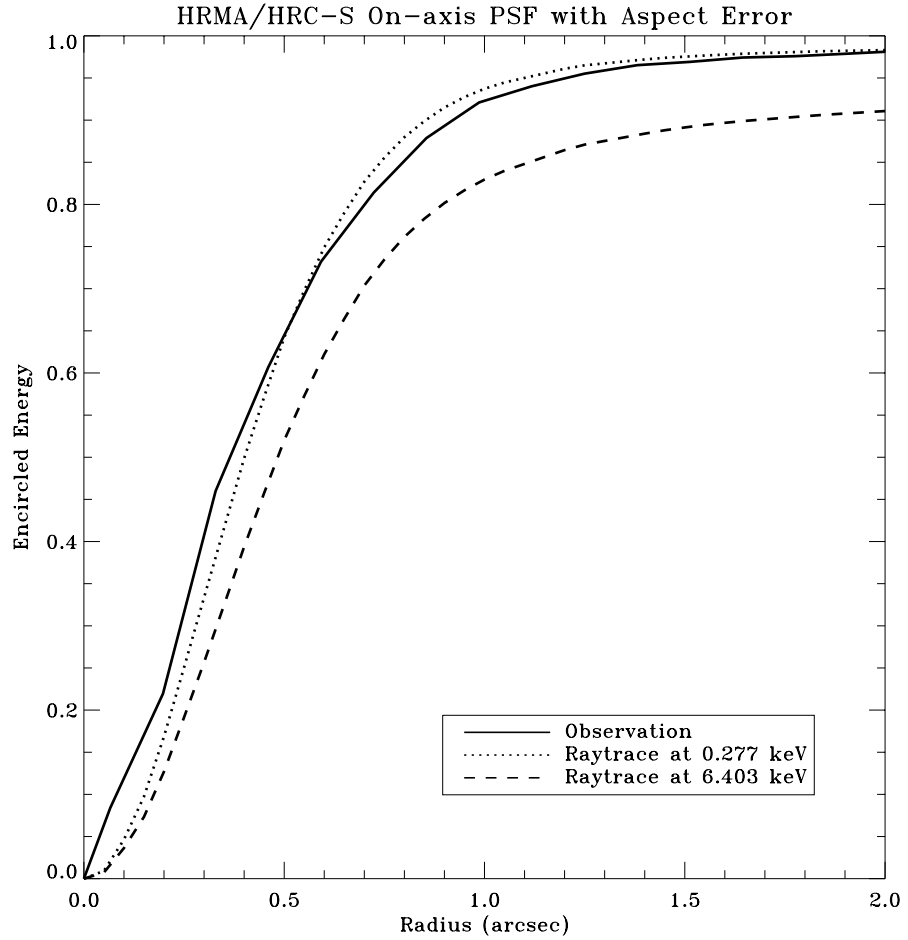


Figure 4.11: The fractional encircled energy as a function of angular radius observed in flight compared to model calculations for an on-axis point-source at selected X-ray energies. The curves are the combined response of the four nested mirror pairs, typical aspect uncertainties, and the HRC-I response function.



Zhao/SAO 20Feb00

Figure 4.12: The fractional encircled energy as a function of angular radius observed in flight compared to model calculations for an on-axis point-source at selected X-ray energies. The curves are the combined response of the four nested mirror pairs, typical aspect uncertainties, and the HRC-S response function.

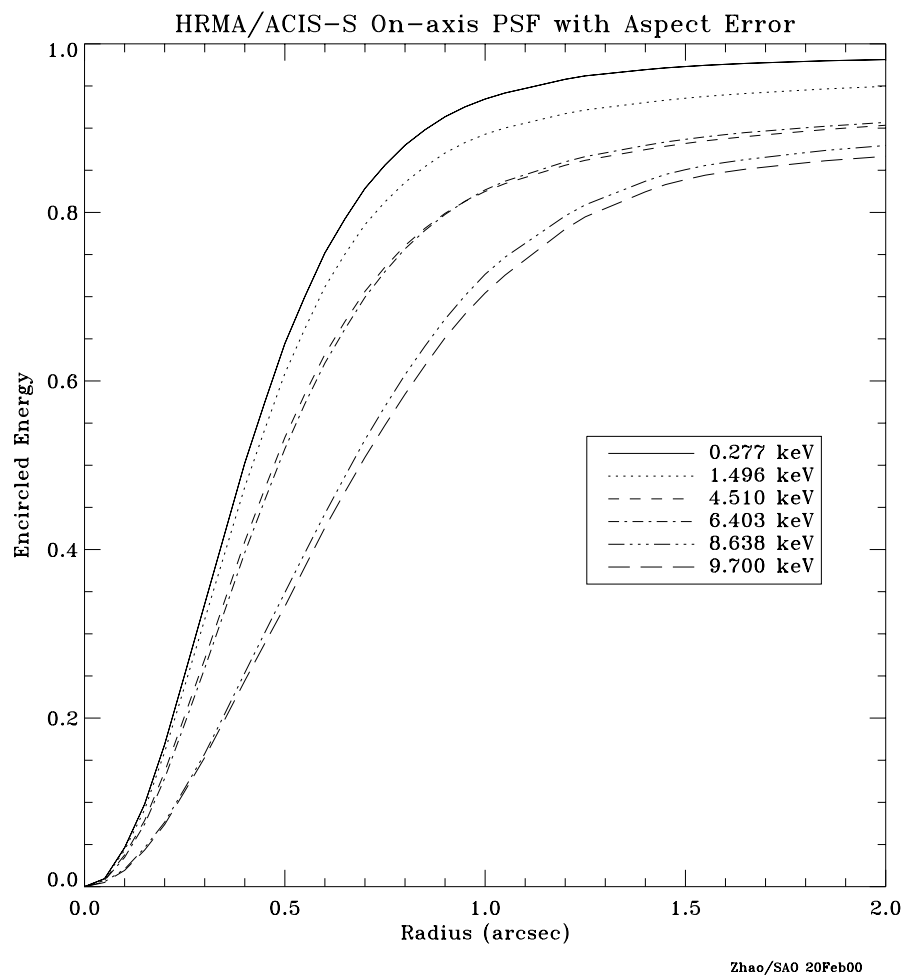


Figure 4.13: The fractional encircled energy as a function of angular radius expected for in flight ACIS-S(S3) measurements for an on-axis point-source at selected X-ray energies. The curves are the combined response of the four nested mirror pairs, typical aspect uncertainties, and the ACIS response function.

Hyperboloid	θ_c		θ_d	
	[rad]	[deg]	[rad]	[deg]
1	0.05961	3.42	0.06115	3.50
3	0.04795	2.75	0.04923	2.82
4	0.04223	2.42	0.04237	2.49
6	0.03144	1.80	0.03232	1.90

Table 4.3: Exit cone angles for each hyperboloid.

but uncoated and with ends uncut. The VETA-I tests included the image full-width-half-maximum, encircled energy, effective area, and ring focus properties (for azimuthal and low spatial-frequency figure). Many of the results of these tests appear in SPIE Proceedings 1742, e.g. Hughes et al. 1992. Zhao et al. 1993, give a good overview of the VETA tests. A series of papers in SPIE Proceedings 3113, e.g. Zhao et al. 1997, report on the XRCF calibration of the HRMA assembly.

4.5.2 Exit cone angles

An annular on-axis beam enters each mirror pair, is reflected from paraboloids and hyperboloids and exits to converge to a focus. The angle θ between the direction of the reflected ray and the optical axis lies between two angles θ_c and θ_d ; these limits are listed in Table 4.3.

4.5.3 Sub-assembly Calibration

Extensive measurements of the mirror shapes and of the surface characteristics were made at Hughes-Danbury Optical Systems (HDOS) during fabrication of the mirror segments and during assembly at Eastman-Kodak Co. HRMA throughput depends critically on the coating of the individual mirror elements carried out at Optical Coating Laboratory, Santa Rosa, California. Mirror flats were present in the coating chamber and coated with iridium at the same time as the HRMA mirror elements. Reflectivity of X-rays from these witness flats was measured, and some results have been described in the 1997 July/Aug SPIE meeting proceedings.

4.5.4 Operating Environment

Insulation and heaters maintain the HRMA temperature at 70° Fahrenheit to minimize changes from the assembly and alignment environments.

4.6 References

- Aschenbach, B., 1985, Rep. Prog. Phys, 48, 579.
Aschenbach, B., 1991, Rev. Mod. Astron. 4, 173.
Edgar, R.J. , 1997, SPIE Proceedings, 3113, 124.
Elsner, R.F, et al, 1998, SPIE Proceedings, 3444, 177.
Gaetz, T.J., et al, 1997, SPIE Proceedings, 3113, 77.
Giacconi, R., et al., 1979, Ap.J. 230, 540.
Graessle, D. E., et al, 1998, SPIE Proceedings, 3444, 140.
Henke, B.L., et. al., 1993, Atomic Data and Nuclear Data Tables 54, 181.
Hughes, J.P., et al., 1992, SPIE Proceedings, 1742, 152.
Kolodziejczak, J.J., et al, 1997, SPIE Proceedings, 3113, 65.
O'Dell, S.L. and Weisskopf, M.C., 1998, SPIE Proceedings, 3444, 2.
Olds, C.R. and Reese, R.P., 1998, SPIE Proceedings, 3356, 910.
Trümper, J., 1983, Adv. Space Res. 2(4), 241.
Van Speybroeck, L., et al, 1997, SPIE Proceedings, 3113, 89.
Weisskopf, M.C. and O'DELL, S.L., 1997, SPIE Proceedings, 3113, 2.
Zhao, P. and Van Speybroeck, L., et al, 1995, SPIE Proceedings, 2515, 391.
Zhao, P., et al, 1993, SPIE Proceedings, 2011, 59.
Zhao, P., et al, 1997, SPIE Proceedings, 3113, 106.
Zhao, P., et al, 1998, SPIE Proceedings, 3444, 234.

Calibration reports can also be found at the MSFC AXAF calibration page
<http://wwwastro.msfc.nasa.gov/xray/xraycal>

Postscript copies of various aspects of the HRMA calibration can be obtained from the *CXC* HRMA Calibration Group
<http://hea-www.harvard.edu/MST/simul/xrcf/report/index.html>

Chapter 5

Pointing Control and Aspect Determination System

5.1 Introduction

The total system of sensors and control hardware that is used to point the observatory, maintain the stability, and provide data for determining where the observatory had been pointing is called the Pointing Control and Aspect Determination (PCAD) system. Unlike the Hubble Space Telescope, *Chandra* pointing requirements are much less stringent. This is because *Chandra* detectors are essentially single-photon counters and as long as one knows where the spacecraft was pointing when each photon was detected, it is possible to determine the celestial location. The mapping of photon positions from detector to relative and absolute positions on the sky is often referred to as “image reconstruction”.

In this chapter we briefly discuss the hardware that comprises the PCAD system and how it is used.

5.2 Physical configuration

The main components of the PCAD system are:

Aspect camera assembly (ACA) – 11.2 cm optical telescope, stray light shade, two CCD detectors (primary and redundant), and two sets of electronics

Inertial reference units (IRU) – Two IRUs, each containing two 2-axis gyroscopes.

Fiducial light assemblies (FLA) – LEDs mounted near each science instrument (SI) detector which are imaged in the ACA via the FTS

Fiducial transfer system (FTS) – The FTS directs light from the fid lights to the ACA, via the retroreflector collimator (RRC) mounted at the HRMA center, and a periscope

Coarse sun sensor (CSS) – All-sky coverage of the sun

Fine sun sensor (FSS) – 50 degree FOV and 0.02 degree accuracy

Earth sensor assembly (ESA) – Conical scanning sensor, used during the orbital insertion phase of the mission

Reaction wheel assembly (RWA) – 6 momentum wheels which change spacecraft attitude

Momentum unloading propulsion system (MUPS) – Liquid fuel thrusters which allow RWA momentum unloading

Reaction control system (RCS) – Thrusters which change spacecraft attitude

Since data from the CSS, FSS, and ESA are not normally used in the processing of science observations these are not discussed. However, in the unlikely event of a complete failure of the ACA, we would attempt to use CSS and FSS data.

5.2.1 ACA

The aspect camera assembly (Figure 5.1) includes a sunshade (~ 2.5 m long, ~ 55 cm in diameter), a 11.2 cm, F/9 Ritchey-Chretien optical telescope, and light-sensitive CCD detector(s). This assembly and its related components are mounted on the side of the HRMA. The camera's field of view is 1.4×1.4 deg and the sun-shade is designed to protect the instrument from the light from the Sun, Earth and Moon, with protection angles of 45, 20 and 6 deg, respectively.

The aspect camera focal plane detector is a 1024×1024 Tektronix CCD chip, with 24×24 micron ($5 \times 5''$) pixels, covering the spectral band between 4000 and 9000 Å. The CCD chip is deliberately out of focus (point source FWHM = 9 arcsec) to spread the star images over several pixels in order to increase accuracy of the centering algorithm, and to reduce variation in

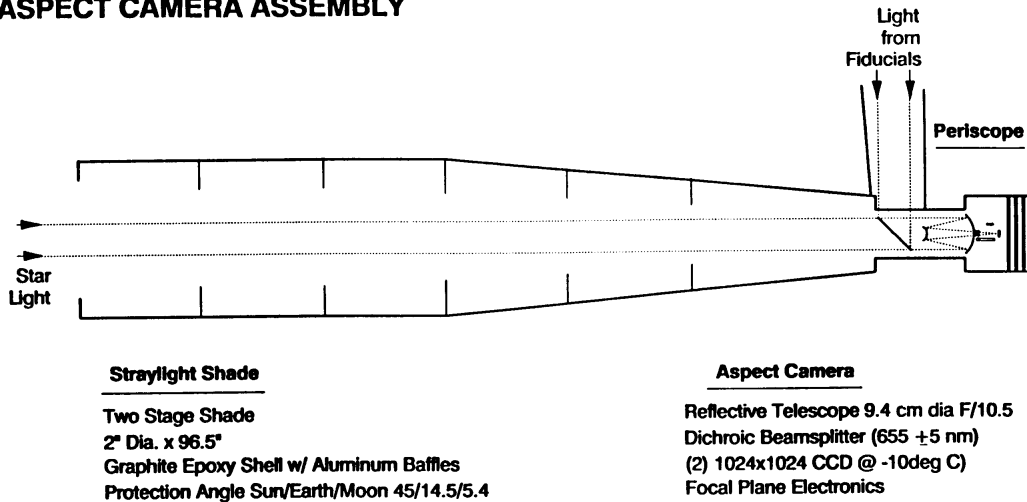
ASPECT CAMERA ASSEMBLY

Figure 5.1: Aspect camera assembly

the point response function over the field of view. There is a spare identical CCD chip, which can be illuminated by activating a rotating mirror.

The ACA electronics tracks a small pixel region (either 4×4 , 6×6 , or 8×8 pixels) around the fiducial light and star images. There are a total of eight such image slots available for tracking. Typically five guide stars and three fiducial lights (section 5.2.2 are being tracked. The average background level is subtracted on-board, and image centroids are calculated by a weighted-mean algorithm. The image centroids and fluxes are used on-board by the PCAD, and are also telemetered to the ground along with the raw pixel data.

The spectral response of the CCD detector (Figure 5.2) is such that faint cool stars (e.g. type N0), with visual magnitudes lower than the limit of the Guide Star Catalog (i.e., 13) can produce large numbers of counts. These so-called “spoiler stars” are detected as part of the on-ground aspect “pipeline” data processing, and subsequent centroiding removes any bias that the spoilers may have introduced.

5.2.2 Fiducial lights and Fiducial Transfer System

Surrounding each of the SI detectors is a set of fiducial Light Emitting Diodes. Each fiducial light produces a collimated beam at 635 nm which is

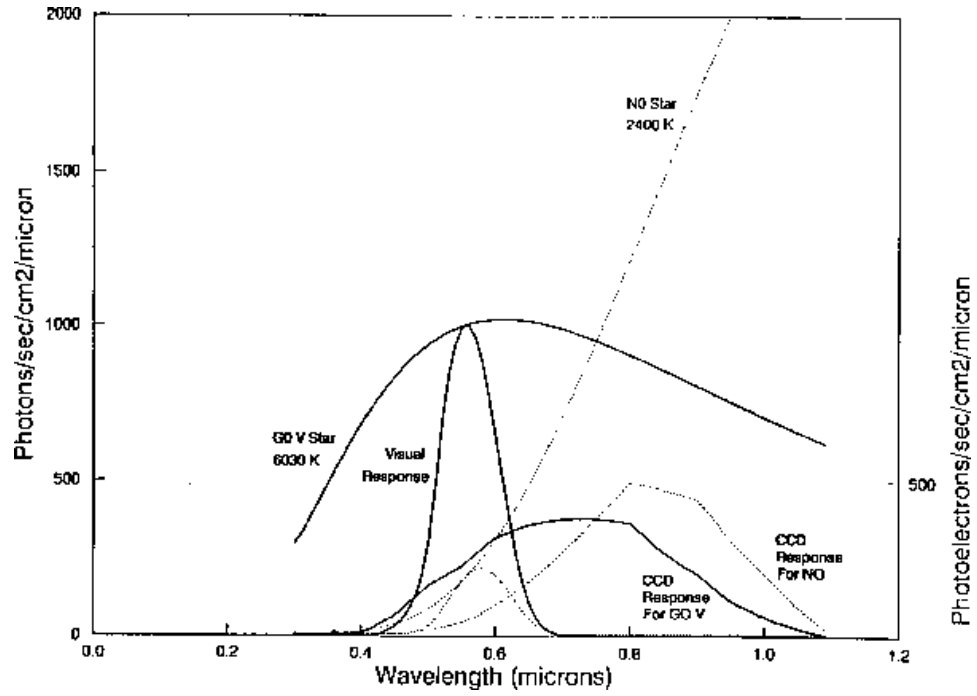


Figure 5.2: Spectral response of the ACA CCD. The same signal-to-noise is achieved for a V=11.7 magnitude N0 star as for a V=10 magnitude G0V star. Also shown are the spectra and the standard visual response for the two stars.

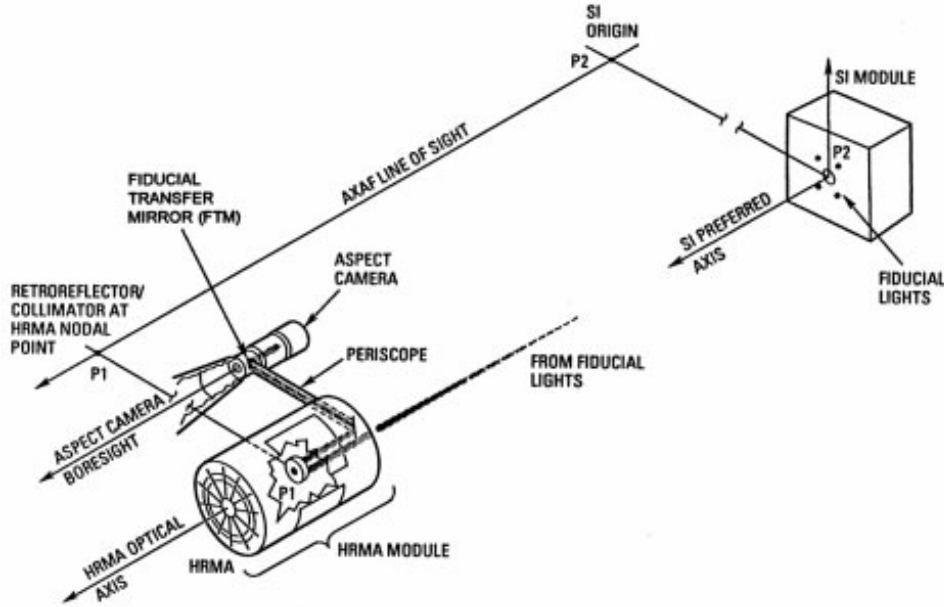


Figure 5.3: Fiducial Transfer System

imaged onto the ACA CCD via the RRC, the periscope, and the fiducial transfer mirror (Figure 5.3). The images of the fiducial lights are used to locate the instrument position relative to the HRMA nodal axis and the guide stars.

5.2.3 IRU

Two Inertial Reference Units (IRU) are located in the front of the observatory on the side of the HRMA. Each IRU contains two gyros, each of which measures an angular rate about 2 gyro axes. This gives a total of eight gyro channels. Data from four of the eight channels can be read out at one time. The gyros are arranged within the IRUs and the IRUs are oriented such that all 8 axes are in different directions and no three axes lie in the same plane. The gyros output pulses represent incremental rotation angles. In high-rate mode, each pulse nominally represents $0.75''$, while in low-rate mode (used during all normal spacecraft operations) each pulse represents

nominally $0.02''$.

5.2.4 Momentum control – RWA and MUPS

Control of the spacecraft momentum is required both for maneuvers and to maintain stable attitude during science observations. Momentum control is primarily accomplished using 6 Teldix RDR-68 reaction wheel units mounted in a pyramidal configuration. During observing, with the spacecraft attitude constant apart from dither, external torques on the spacecraft (e.g. gravity gradient, magnetic) will cause a buildup of momentum in the RWA. Momentum is then unloaded by firing the MUPS and simultaneously spinning down the reaction wheels.

5.3 Operating principles

The *Chandra* aspect system serves two primary purposes: on-board spacecraft pointing control and aspect determination and post-facto ground aspect determination, used in X-ray image reconstruction and celestial location.

The PCAD system has 9 operational modes (6 normal and 3 safe modes) which use different combinations of sensor inputs and control mechanisms to control the spacecraft and ensure its safety. These modes are described in Section 5.8.1. In the normal science pointing mode, the PCAD system uses sensor data from the ACA and IRUs, and control torques from the RWAs, to keep the X-ray target within $\sim 30''$ of the telescope boresight. This is done using a Kalman filter which optimally combines ACA star centroids (typically 5) and angular displacement data from two 2-axis gyroscopes. On short time scales (\sim seconds) the spacecraft motion solution is dominated by the gyroscope data, while on longer timescales it is the star centroids that determine the solution.

The post-facto aspect determination is done on the ground and uses more sophisticated processing and better calibration data to produce a more accurate aspect solution. The suite of *CXC* tools to perform this processing is called the aspect pipeline. The key improvements over PCAD aspect come from better image centroiding and using Kalman smoothing (which uses all available data over the observation period – as opposed to historical data). In addition, the aspect pipeline folds in the position of the focal-plane instrument.

Table 5.1: Aspect System Requirements and Performance

Description	Requirement	Actual	References
Absolute celestial pointing	30.0'' (99.0%, radial)	3.0''	<i>Chandra</i> PRD, SE31 §6.3
PCAD 10 sec pointing stability	0.25'' (RMS, 1-axis)	0.043'' (pitch) 0.030'' (yaw)	<i>Chandra</i> PRD, SE31 §6.4.1.1.2
Image reconstruction	0.5'' (RMS diameter)	0.3''	<i>Chandra</i> PRD, SE31 §4.3
Celestial location	1.0'' (RMS radius)	0.76''	<i>Chandra</i> PRD, SE31 §4.4

5.4 Performance

The important PCAD system performance parameters and a comparison to the original requirements are shown in Table 5.1. Absolute celestial pointing refers to the accuracy with which the *Chandra* line of sight (the line connecting the nominal aimpoint and the HRMA node) can be pointed toward a particular target location on the sky, and is about 3'' in radius. Note that this is based on a small sample of (ACIS-S) observations taken prior to the release of this document.

The PCAD 10-second pointing stability requirement specifies that in 95% of 10 sec intervals, the RMS attitude control error (1-axis) shall be less than 0.25''. Systematic offsets are not included in this term. This requirement applies during dithered observations as well, but the dither cancels (to first order) and is not part of the attitude control error since the commanded and true attitude both contain the dither.

The image reconstruction requirement states that if the resolution and focus of the HRMA, SIs, and locations of reference stars, were perfect, the reconstructed image of an X-ray point source, anywhere within the central 5 arcminute radius field of view, will have an RMS diameter spread of less than 0.5''. The typical performance has been 0.3'', there have been exceptions.

The celestial location requirement specifies that a reconstructed image can be placed on the celestial sphere to an accuracy of 1.0'' (RMS) radius relative to the reference star locations. The current measured performance for celestial location accuracy is approximately 0.8'' RMS radius. As various errors have been found from time-to-time, the user is urged to check for cautions and updates on the *CXC* web page.

5.5 Heritage

The *Chandra* aspect camera design is based on the Ball CT-601 star tracker, which is currently operating on the XTE mission. The *Chandra* IRUs are nearly identical to the SKIRU V IRUs, some 70 of which have been built by the manufacturer - Kearfott. These IRUs are similar to those used on CGRO.

5.6 Special Characteristics

The ACA CCD detectors will degrade in performance due to radiation damage (as for ACIS). This will produce an increase in dark current, read noise, and charge transfer inefficiency (CTI). The first two factors increase centroiding uncertainty, while CTI produces systematic centroid shifts. The CTI-induced shifts can, to some extent, be removed by on-orbit calibration (Section 5.7.3).

Contamination buildup on the CCD surface is expected to result in a mean throughput loss of 9% by EOL, which is within margin. However, the calculation of this number is complicated, and the actual degradation may differ. Furthermore, it is difficult to predict the uniformity of the contaminants. Non-uniform contamination would especially impact the star centroiding accuracy, and hence degrade the accuracy of the aspect solution. The buildup of contaminants is tracked by a trending analysis of expected versus observed star brightnesses. Non-uniform contamination (and other effects) are searched for by trending analysis of the aspect accuracy and looking for anomalous changes. In the event that the 0.5" image reconstruction requirement (Section 5.4) cannot be maintained in the future, we will consider "baking-out" the CCD on-orbit. In this procedure the current on the CCD thermo-electric cooler is reversed so as to *heat* the device to approximately 30 C for a period of several hours. After bake-out the CCD would be returned to its nominal operating temperature of -10 degrees centigrade.

5.7 Calibration

5.7.1 Pre-launch calibration

IRU component testing at Kearfott provided calibration data necessary for accurate maneuvers and for deriving the aspect solution. The key parameters are the scale factor (arcsec/gyro pulse) and the drift rate stability parameters. The stability parameters specify how quickly the gyro readout

random-walks away from the true angular displacement. These terms limit the aspect solution accuracy during gyro hold observations (Section 5.9.2).

ACA component testing at Ball provided calibration data necessary for on-orbit pointing control and for post-facto ground processing. On-orbit, the ACA uses CCD gain factors, the plate scale factor, and temperature dependent field distortion coefficients to provide the control system with star positions and brightnesses. In ground processing, the *CXC* aspect pipeline makes use of those calibration data as well as CCD read noise, flat-field maps, dark current maps, and the camera PSF in order to accurately determine star positions.

5.7.2 Orbital activation and checkout calibration

Orbital activation and checkout of the PCAD occurred during the first 30 or so days of the *Chandra* mission. During the first phase of OAC, before the HRMA sunshade door was opened it was possible to use the ACA to observe the fiducial lights (period 1). After the sunshade door was opened it was possible to fully check the aspect camera using star light (period 2).

Chandra activation produced the following aspect system calibration data:

- Bias, alignment, scale factor of the CSS and FSS (period 1)
- Coarse gyro bias (period 1)
- ACA CCD dark current map (periods 1 and 2)
- Fiducial light intensity, image, and centroid at nominal voltage (periods 1 and 2)
- IRU bias, alignment, scale factor (period 2)
- ACA alignment and field distortion coefficients (period 2)

5.7.3 On-orbit calibrations

During the *Chandra* science mission, aspect system components will require on-orbit calibration to compensate for alignment or scale factor drifts, and ACA CCD degradation due to cosmic radiation. The IRU calibration coefficients are updated infrequently based on cumulative science and data taken during slews. The following ACA calibrations are performed, as-needed, based on the trending analyses of aspect solution data.

Dark current

Cosmic radiation damage will produce an increase in the mean CCD dark current as well as the dark current non-uniformity (i.e., pixel-to-pixel variations). If uncalibrated, the latter term can degrade aspect solution accuracy by up to $0.1''$ (image reconstruction RMS diameter). During OAC, dark current calibrations were performed shortly before and after sun-shade door opening. These indicated a substantial increase in the number of “warm” CCD pixels (due to radiation damage), relative to ground testing, however, as was shown in Table 5.1 there has been no impact on performance. Dark current calibrations will be performed several times per year.

Because the ACA has no shutter, a dark current calibration must be done with *Chandra* pointing at a star field which is as free from optical sources as possible. Furthermore, in order to minimize dark current accumulation during the CCD readout, only a small portion (typically 128 rows) of the CCD is actually digitized after each 30 second integration. A minimum of three full-frame CCD maps are collected, each with slight pointing offsets in order to allow removal of field stars. The entire calibration procedure takes between 30 minutes and 2 hours, depending on the number of repeats, integration time, and number of rows per integration.

Charge transfer inefficiency (CTI)

Radiation damage degrades the efficiency with which charge is transferred in the CCD by introducing dislocations in the semiconductor which trap electrons and prevent their transfer. The most important consequence is a “streaking” or “trailing” of star images along the readout column(s), which can introduce systematic centroid shifts. These shifts depend primarily on CCD transfer distance to the readout and star magnitude.

The procedure for calibrating the mean CTI is to dither a faint star across the CCD quadrant boundary and observe the discontinuity in centroid (the CCD is divided electrically into four quadrants).

Field distortion

The precise mapping from ACA CCD pixel position to angle relative to the ACA boresight is done with the “ACA field distortion polynomial”. This includes linear plate scale factors as well as non-linear temperature-dependent terms. In order to verify that no mechanical shift in the ACA had occurred during launch, a field distortion calibration was performed during the orbital activation and checkout phase. A mechanical shift would

result in degraded celestial location accuracy, but the on-orbit calibration revealed no shift.

The calibration was done by observing a dense field of stars with the spacecraft in normal pointing mode. Two reference stars were observed continuously, while sets of 4 stars each were observed for 100 seconds. The calibration was completed after observing 64 stars over the ACA field of view, taking roughly 60 minutes. There are currently no plans to repeat this calibration.

5.8 Operations

5.8.1 PCAD modes

The PCAD system has 9 operational modes (6 normal and 3 safe) which use different combinations of sensor inputs and control mechanisms to control the spacecraft and ensure its safety. These modes are listed in Table 5.2. Normal science observations are carried out in Normal Pointing Mode (NPM), while slews between targets are done in Normal Maneuver Mode (NMM).

5.8.2 Operational constraints

The ACA will meet performance requirements when the ACA line of sight is separated from: the Sun by 45 degrees or more; the limb of the bright Earth by 20 degrees or more; and the dark Earth or Moon by 6 degrees or more. If these restrictions are violated, the star images may be swamped by scattered background light, with resulting noise on star position that exceeds the $0.360''$ requirement ($1\text{-}\sigma$, 1-axis).

5.8.3 Output data

The important output data from the ACA are the scaled raw pixel intensities in a region (4×4 , 6×6 , or 8×8 pixel) centered on the star and fiducial light images. These data are placed in the engineering portion of the telemetry stream, which is normally allocated 8 kbit s^{-1} . During an ACA dark current calibration (Section 5.7.3), *Chandra* utilizes a 512 kbit s^{-1} telemetry mode (in real-time contact) to enable read-out of the entire CCD (1024×1024 pixels). The key data words in telemetry from the IRU are the 4 accumulated gyro counts (32 bits every 0.256 sec).

Table 5.2: PCAD modes

Mode	Sensors	Control	Description
Standby	—	—	OBC commands to RWA, RCS, and SADA disabled, for initial deployment, subsystem checkout, etc.
Normal Pointing	IRU, ACA	RWA	Point at science target, with optional dither
Normal Maneuver	IRU	RWA	Slew between targets at peak rate of 2° per minute
Normal Sun	IRU, CSS, FSS	RWA	Acquire sun and hold spacecraft -Z axis and solar arrays to the sun
Powered Flight	IRU	RCS	Control <i>Chandra</i> during Liquid Apogee Engine burns
RCS Maneuver	IRU	RCS	Control <i>Chandra</i> using the RCS
Safe Sun	IRU, CSS, FSS	RWA	Safe mode: acquire sun and hold spacecraft -Z axis and solar arrays to the sun
Derived Rate Safe Sun	IRU, CSS, FSS	RWA	Similar to Safe Sun Mode, but using only one gyro (two axes) plus sun sensor data
RCS Safe Sun	IRU, CSS, FSS	RCS	Same as Safe Sun Mode, but using RCS instead of RWA for control

5.9 Performing an Observation

5.9.1 Star acquisition

After maneuvering at a rate of up to $2^\circ/\text{minute}$ to a new celestial location using gyroscope data and the reaction wheels, *Chandra* begins the star acquisition sequence, a process which takes from 6 to 10 minutes. First the OBC commands the ACA to search for up to 8 acquisition stars, which are selected to be as isolated from nearby stars as possible. The search region size is based on the angular size of the slew, which corresponds to the expected uncertainty in attitude. If two or more acquisition stars are found, an attitude update is performed using the best (brightest) pair of stars. This provides pointing knowledge to $3''$ (3σ per axis). Next the guide star search begins. Depending on the particular star field configuration, the star selection algorithm may choose guide stars which are the same as the acquisition stars. In this case the acquisition time is somewhat reduced. When at least two guide stars have been acquired and pointing control errors converge, the on-board Kalman filtering is activated and the transition to Normal Point Mode is made, at which point sensing of the fiducial lights begins.

5.9.2 Science pointing scenarios

The on-board PCAD system is flexible and allows several different *Chandra* science pointing scenarios, described in the following sections.

NPM dither

The large majority of observations are performed using Normal Point Mode, with dither selected. In this case the *Chandra* line-of-sight will be commanded through a Lissajous pattern. Dithering distributes photons over many detector elements (microchannel pores or CCD pixels) and serves several purposes: reduces uncertainty due to pixel to pixel variation in quantum efficiency (QE); allows sub-sampling of the image; and, in the case of the HRC, distributes the total exposure over many microchannel pores - useful since the QE of a pore degrades slowly with exposure to photons. The dither pattern parameters are amplitude, phase, and period for two axes. Each of the six parameters is separately commandable and differ for the two different instruments (See Chapters 6 and 7). The default values for these parameters are given in Table 5.3. The minimum dither rate required to maintain the health of the HRC is $0.02''/\text{sec}$, and the maximum rate tolerated by PCAD to maintain pointing stability is $0.1''/\text{sec}$.

Table 5.3: Default dither parameters

Parameter	Value	Comment
Phase (pitch)	0.0 rad	
Phase (yaw)	0.0 rad	
Amplitude (pitch)	8.0 arcsec	16 arcsec peak-to-peak
Amplitude (yaw)	8.0 arcsec	
Period (pitch)	706.96 sec	
Period (yaw)	999.96 sec	

NPM steady

This mode is identical to NPN dither, but without the dither.

Pointing at solar system objects

Observations of moving solar system objects are done using a sequence of pointed observations, with the object moving through the field of view during each dwell period. Except in special circumstances, each pointing is selected so that the object remains within $5'$ of the *Chandra* line-of-sight. Most solar system objects move slowly enough so that a single pointed observation will suffice.

Raster scan

Survey scans of regions larger than the instrument field of view are specified simply with a list of target coordinates giving the field centers. The fields can optionally overlap, depending on the science requirements of the survey.

Offset and gyro hold

In special circumstances it will be necessary to perform observations without tracking guide stars. It may occur that a field has no suitable guide stars, although the *CXC* mission planning group has found no such fields to date. A more likely situation is that a very bright object, such as the Earth or Moon, saturates the ACA CCD and precludes tracking stars. In this case *Chandra* will first be maneuvered to a nearby pointing which has guide stars to establish fine attitude and a gyro bias estimate. A dwell time of approximately 25 minutes is needed to calibrate the bias estimate, which is the dominant term in the drift equation below. *Chandra* will then be

maneuvered to the target. The default automatic transition to NPM will be disabled, and the spacecraft will hold on the target attitude in NMM.

While holding on gyros only, the spacecraft attitude will drift due to noise in the gyros, which results in an aspect solution error. The variance of the angle drift for each gyro axis, in time t , is given by

$$\sigma^2 = \sigma_b^2 t^2 + \sigma_v^2 t + \sigma_u^2 t^3 / 3$$

Ground test data for gyro noise parameters indicate worst case values of $\sigma_u = 1.5 \times 10^{-5}$ arcsec sec^{-3/2} and $\sigma_v = 0.026$ arcsec sec^{-1/2}. Analysis of the residual Kalman filter bias estimate gives $\sigma_b = 0.002$ arcsec sec⁻¹. This results in 1- σ angle drift errors of: 0.3'' for 0.1 ksec; 2.2'' for 1 ksec; 11'' for 5 ksec; and 22'' for 10 ksec. After a maximum of 5 ksec, *Chandra* will be maneuvered back to the nearby field with guide stars in order to re-establish fine attitude and update the gyro drift rate.

5.9.3 PCAD capabilities (advanced)

Nudge mode

The nudge mode capability of PCAD is a way of performing small maneuvers (< 30'). In the normal method of maneuvering, the spacecraft transitions to NMM, slews, and then re-acquires stars. In nudge mode, a new target position (quaternion) is commanded and the on-board software maneuvers to the new attitude at a peak rate of 2''/sec, without leaving NPM or losing track on the aspect guide stars. In this way an accurate aspect solution can be generated during the maneuver, the X-ray images can be reconstructed, and the overhead of re-acquiring guide stars is eliminated.

This capability is not currently available for normal science observations, and small maneuvers are performed via the usual transition to NMM. Subsequent releases of the ground mission planning software may support nudge mode maneuvers in the future.

Monitor star photometry

The ACA has the capability to devote one or more of the eight image slots to "monitor" particular sky locations. This allows simultaneous optical photometry of one or more X-ray targets in the field of view. These optical sources can be fainter than the ACA guide star limit of $m_{ACA} = 10.2$ mag. The bright-end limit for monitor star photometry is $m_{ACA} = 6.2$ mag. However, since there are a fixed number of image slots, devoting a slot to photometry instead of tracking a guide star results in a degradation of the image

Table 5.4: ACA photometric accuracy

m_{ACA}	T_{int} (sec)	Signal-to-Noise
12.5	2.0	9
12.5	10.0	20
12.5	200.0	70
15.0	2.0	~ 1
15.0	10.0	3
15.0	200.0	7

reconstruction and celestial location accuracy (Section 5.4). Using a monitor slot represents a 15 - 25% increase in the RMS diameter, depending on the particular guide star configuration. For two monitor slots, the increase is about 50 - 60%. The photometric accuracy which can be achieved depends primarily on the star magnitude, integration time, CCD dark current, CCD read noise, sky background, and the CCD dark current uncertainty. The final term ultimately limits the photometric accuracy at the faint end, and results from uncalibrated pixel-to-pixel changes in dark current due to radiation damage. Table 5.4 lists estimates of the achievable signal to noise for end-of-life CCD parameters. The zero instrument magnitude is defined as the Aspect Camera response to a zero magnitude star of spectral class G0V. The conversion from V and B magnitude to ACA instrument magnitude, based on flight data, is given approximately by

$$m_{ACA} = V + 0.355 - 0.022(B - V) - 0.442(B - V)^2$$

5.10 Ground Processing

For each science observation, the aspect system data described in Section 5.8.3 are telemetered to the ground to allow post-facto aspect determination by the *CXC* aspect pipeline, as part of the standard *CXC* data processing pipeline. The important components of the pipeline are:

Gyro process: Filter gyro data, gap-fill, and calculate raw spacecraft angular rate

ACA process: Filter bad pixels, make CCD-level corrections (e.g. dark current), find spoiler stars, centroid, make camera-level corrections, convert to angle

Kalman filter and smooth: Optimally combine ACA and gyro data to determine ACA celestial location and image motion

Combine ACA and fids: Derive fid light solution, and combine with ACA solution, to generate image motion and celestial location at the focal plane science instrument.

5.10.1 Data products

The data products which are produced by the aspect solution pipeline are listed in Table 5.5. Key data elements include: IRU accumulated counts; raw pixel data for 8 images; observed magnitudes, pixel positions of the aspect stars and fiducial lights versus time; and aspect solution versus time.

Note that the solutions from two independent algorithms, Kalman filtering and the “photographic method” (ala Einstein satellite aspect), are calculated. In each case the star data are used to determine the RA, Dec, and roll (and corresponding uncertainties) of the HRMA axis as a function of time. The fid light images are used to track any drift of the SIM away from the nominal position. One cause of such drift is thermal warping of the optical bench assembly. The Kalman filtering routines also calculate an optimal estimate of the gyro bias rate as a function of time.

5.10.2 Star catalog

The Aspect system uses the AGASC (AXAF Guide and Aspect Star Catalog). The AGASC was prepared by the CXC Mission Planning group, and is a compilation of the Hubble Guide Star Catalog, the Positions and Proper Motion Catalog and the Tycho Output Catalog.

Document history

- Feb. 00 — revised by T. Aldcroft
- Dec. 99 — revised by Andrea Prestwich
- Sep. 97 — revised by T. Aldcroft, A. Prestwich
- Aug. 97 — revised by T. Aldcroft
- Aug. 96 — revised by T. Aldcroft
- Oct. 92 — reviewed by D. Schwartz

Table 5.5: Aspect pipeline data products

Product	Description
ASPSOL	Final aspect solution with errors
ASPQUAL	Aspect solution quality indicators
AIPROPS	Aspect Intervals
ACACAL	ACA calibration data from ODB and CALDB
GSPROPS	Guide star properties, both from the AXAF Guide and Acquisition Star Catalog, and as actually observed with the ACA
FIDPROPS	Fiducial light properties, as commanded and as observed
ACADATA	Aspect camera telemetry (including ACA housekeeping), and images after CCD-level correction
ACACENT	Image centroids and associated fit statistics
GYROCAL	Gyro calibration data from ODB and CALDB
GYRODATA	Gyro raw and gap-filled, filtered data
KALMAN	Intermediate and final data in Kalman filter and smoother

Chapter 6

ACIS: Advanced CCD Imaging Spectrometer

6.1 Introduction & Layout

The Advanced CCD Imaging Spectrometer (ACIS) offers the capability to simultaneously acquire high-resolution images and moderate resolution spectra. The instrument can also be used in conjunction with the High Energy Transmission Grating (HETG) to obtain very high resolution spectra (Chapter 8).

ACIS contains 10 planar, 1024 x 1024 pixel CCD s (Figure 6.1); four arranged in a 2x2 array (ACIS-I) used for imaging, and six arranged in a 1x6 array (ACIS-S) used either for imaging or as a grating readout. Two CCDs are back-illuminated (BI) and eight are front-illuminated (FI). The response of the BI devices extends to energies below that accessible to the FI chips. The chip-average energy resolution of the BI devices is, currently, better than that of the FI devices. Any combination of up to 6 CCDs may be operated simultaneously. Operating six chips increases the chances of serendipitous science but at the price of increased total background counting rate and therefore a somewhat enhanced probability of saturating telemetry.

The Instrument Principal Investigator for ACIS is Prof. Gordon Garmire (Pennsylvania State University). ACIS was developed by a collaboration between Penn State, the *MIT* Center for Space Research and the Jet Propulsion Laboratory, and was built by Lockheed Martin and *MIT*. The *MIT* effort was led by Dr. George Ricker. The CCDs were developed by *MIT*'s Lincoln Laboratory.

ACIS is a complex instrument having many different characteristics and

ACIS FLIGHT FOCAL PLANE

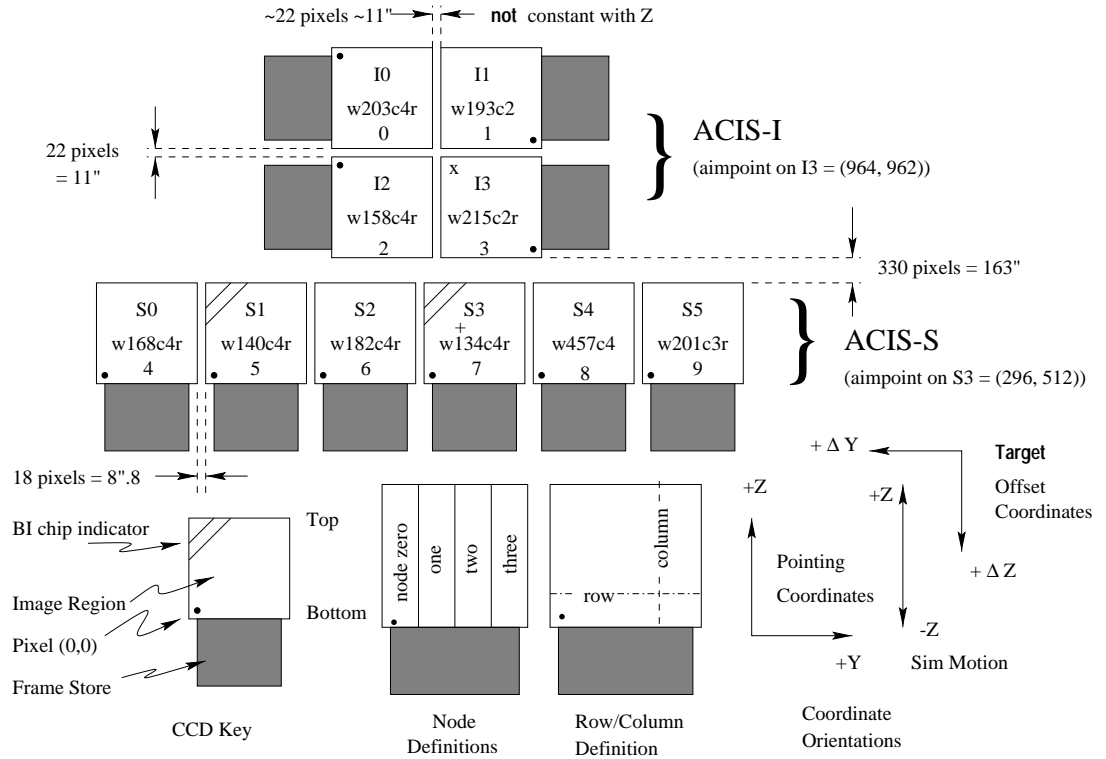


Figure 6.1: A schematic drawing of the ACIS focal plane; insight to the terminology is given in the lower left. Note the nominal aimpoints: on S3 (the '+') and on I3 (the 'x'). Note the also the differences in the orientation of the I and S chips, important when using Subarrays (Section 6.12.3). Note the (Y, Z) coordinate system and the target offset convention (see Chapter 3) as well as the SIM motion (+/-Z). The view is along the optical axis, from the source towards the detectors, (-X). The numerous ways to refer to a particular CCD are indicated: chip letter+number, chip serial number, and ACIS chip number. The node numbering scheme is illustrated lower center.

operating modes. Radiation damage suffered by the FI chips has had a negative impact on their energy resolution – the BI devices were not impacted – thus altering the basic considerations as to how to make best use of the instrument. We will review the tradeoffs elsewhere in this Chapter. The situation with regards to the energy resolution of the FI devices is somewhat fluid and potential methods of improving the energy resolution are being studied. Users are encouraged to look for updates at the *CXC* web site.

Many of the characteristics of the ACIS instrument are summarized in Table 6.1.

6.2 Basic Principles

A CCD is a solid-state electronic device composed primarily of silicon. A “gate” structure on one surface defines the pixel boundaries by alternating voltages on three electrodes spanning a pixel. The silicon in the active (depletion) region (the region below the gates wherein most of the absorption takes place) has an applied electric field so that charge moves quickly to the gate surface. The gates allow confined charge to be passed down a “bucket brigade” (the buried channel) of pixels in parallel to a serial readout at one edge by appropriately varying (“clocking”) the voltages in the gates.

The ACIS front-illuminated CCDs have the gate structures facing the incident X-ray beam. Two of the chips on the ACIS-S array (S1 and S3) have had treatments applied to the back sides of the chips, removing insensitive, undepleted, bulk silicon material and leaving the photo-sensitive depletion region exposed. These are the BI chips and are deployed with the back side facing the HRMA.

Photoelectric absorption of an X-ray in silicon results in the liberation of a proportional number of electrons (an average of one electron-hole pair for each 3.7 eV of photon energy absorbed). Immediately after the photoelectric interaction, the charge is confined by electric fields to a small volume near the interaction site. Charge in an FI device can also be liberated below the depletion region (in an inactive substrate) from where it diffuses into the depletion region. This charge may easily appear in two or more pixels.

Good spectral resolution depends upon an accurate determination of the total charge deposited by a single photon. This in turn depends upon the fraction of charge collected, the fraction of charge lost in transfer from pixel to pixel during read-out, and the ability of the readout amplifiers to measure the charge. Spectral resolution also depends on read noise and the off-chip analog processing electronics. The ACIS CCDs have readout noise

Focal plane arrays:	
I-array	4 CCDs placed to lie tangent to the focal surface
S-array	6 CCDs in a linear array tangent to the grating Rowland circle
CCD format	1024 by 1024 pixels
Pixel size	24.0 microns (0.492 ± 0.0001 arcsec)
Array size	16.9 by 16.9 arcmin ACIS-I 8.3 by 50.6 arcmin ACIS-S
On-axis effective Area	110 cm^2 @ 0.5 keV (FI)
(integrated over the <i>PSF</i>	600 cm^2 @ 1.5 keV (FI)
to >99% encircled energy)	40 cm^2 @ 8.0 keV (FI)
Quantum efficiency	> 80% between 3.0 and 5.0 keV
(frontside illumination)	> 30% between 0.8 and 8.0 keV
Quantum efficiency	> 80% between 0.8 and 6.5 keV
(backside illumination)	> 30% between 0.3 and 8.0 keV
Charge transfer inefficiency	FI: $\sim 2 \times 10^{-4}$; BI: $\sim 1 \times 10^{-5}$
System noise	$< \sim 2$ electrons (rms) per pixel
Max readout-rate per channel	~ 100 kpix/sec
Number of parallel signal channels	4 nodes per CCD
Pulse-height encoding	12 bits/pixel
Event threshold	FI: 38 ADU (~ 140 eV) BI: 20 ADU (~ 70 eV)
Split threshold	13 ADU
Max internal data-rate	6.4 Mbs ($100 \text{ kbs} \times 4 \times 16$)
Output data-rate	24 kb per sec
Minimum row readout time	2.8 ms
Nominal frame time	3.2 sec (full frame)
Allowable frame times	0.2 to 10.0 s
Frame transfer time	41 μsec (full frame)
Point-source sensitivity	$4 \times 10^{-15} \text{ ergs cm}^{-2} \text{ s}^{-1}$ in 10^4 s (0.4-6.0 keV)
Detector operating temperature	-90 to -120°C

Table 6.1: ACIS Characteristics

less than 2 electrons RMS. Total system noise for the 40 ACIS signal chains (4 nodes/CCD) ranges from 2 to 3 electrons (rms) and is dominated by off-chip analog processing electronics.

The CCDs have an “active” or imaging section (see Figure 6.1) which is exposed to the incident radiation and a shielded “frame store” region. A typical mode of the ACIS CCD operation is: (1) the active region is exposed for a fixed amount of time (full frame ~ 3.2 s); (2) at the end of the exposure the charge in the active region is quickly (~ 40 ms) transferred into the frame store; (3) the next exposure begins; (4) simultaneously, the data in the frame store region is passed to a local processor which, after removing bias (the amount of charge in a pixel in the absence of any X-ray induced signal), identifies the position and amplitude of any “events” according to a number of criteria depending on the precise operating mode. These criteria always require a local maximum in the charge distribution above the event threshold (see Table 6.1). The position and the amount of charge collected, together with similar data for a limited region containing and surrounding the pixel are classified (“graded”) and then passed into the telemetry stream.

6.3 Event Grades

During the first step in the algorithm for detecting X-ray events, the on-board processing examines every pixel in the full CCD image (even in the continuous clocking mode (section 6.12.5) and selects as events regions with bias-subtracted pixel values that both exceed the event threshold and are greater than all of the touching or neighboring pixels (i.e., a local maximum). The surrounding 3x3 neighboring pixels are then compared to the bias-subtracted split-event threshold; those that are above the threshold establish the pixel pattern. On the basis of this pattern, the event is assigned a grade. Depending on the grade, the data are then included in the telemetry. On-board suppression of certain grades is used to limit the telemetry bandwidth devoted to background events (see section 6.10.1).

The grade of an event is thus a code that identifies which pixels, within the three pixel-by-three pixel island centered on the local charge maximum, are above certain amplitude thresholds. The thresholds are listed in Table 6.1. Note that the local maximum threshold differs for the FI and the BI CCD. A Rosetta Stone to help one understand the ACIS grade assignments is shown in Figure 6.2, and the relationship to the *ASCA* grading scheme is given in Table 6.2

32	64	128
8	0	16
1	2	4

Figure 6.2: Schematic for determining the grade of an event. The grade is determined by summing the numbers for those pixels that are above their thresholds. For example, an event that caused all pixels to exceed their threshold is grade 255. A single pixel event is grade 0.

Table 6.2: ACIS and ASCA Grades		
ACIS Grades	ASCA Grade	Description
0	0	Single pixel events
64 65 68 69	2	Vertical Split Up
2 34 130 162	2	Vertical Split Down
16 17 48 49	4/3	Horizontal Split Right
8 12 136 140	3/4	Horizontal Split Left
72 76 104 108	6	“L” & Quad, upper left
10 11 138 139	6	“L” & Quad, down left
18 22 50 54	6	“L” & Quad, down right
80 81 208 209	6	“L” & Quad, up right
1 4 5 32 128	1	Diagonal Split
33 36 37 129		
132 133 160 161		
164 165		
3 6 9 20 40	5	“L”-shaped split with corners
96 144 192 13 21		
35 38 44 52 53		
97 100 101 131		
134 137 141 145		
163 166 168 172		
176 177 193 196		
197		
24	7	3-pixel horizontal split
66		3-pixel vertical split
255		All pixels
all others		

It is important to understand that most, if not all, calibrations of ACIS are based on a specific subset of ACIS grades. This “standard” set comprises *ASCA* grades 0,2,3,4, and 6 – G(02346). In the absence of pileup, this particular grade selection appears to optimize the signal-to-background ratio, but this conclusion depends on the detailed spectral properties of the source. Further, most of the scientifically important characteristics of ACIS (effective area, sensitivity, point spread function, energy resolution, etc.) are grade- and energy-dependent.

6.4 Aimpoints

Aimpoints are the nominal positions on the ACIS where the flux from an on-axis point source is placed. There are two nominal aimpoints, indicated in Figure 6.1 - one on the corner of I3 on the ACIS-I array (the ACIS-I aimpoint), and one near the boundary between nodes 0 and 1 on S3 of the ACIS-S array (the ACIS-S aimpoint). Contours of constant encircled energy are shown relative to these aimpoints in Figures 6.4 and 6.5. If required, other aimpoints can be selected along the Z-axis.

It is important to note that it has become standard practice for the *CXC* to offset point all ACIS-S observations with the aimpoint shifted by a small amount (-20 arcsec in Y - see Figure 6.1) in order to assure that the dithered flux from a (now almost) on-axis point source is placed entirely on a single node (node 1) of the S3 CCD. This was done both to simplify and improve the analysis of data from a point source by avoiding to have to deal with the response functions from two nodes. The shift has a negligible impact on image quality because the diameter of the circle, for which >90% of the encircled energy lies within $2''$, is $\sim 2'.4$.

6.5 Spatial Resolution & Encircled Energy

The spatial resolution for on-axis imaging with ACIS is limited by the physical size of the CCD pixels ($24.0 \mu\text{m}$ square ~ 0.492 arcsec) and not the HRMA. This limitation applies irregardless of whether the aimpoint is selected to be the nominal point on I3 or S3 (Figure 6.1). Approximately 90% of the encircled energy lies within 4 pixels (2 arcsec) of the center pixel at 1.49 keV and within 5 pixels (2.5 arcsec) at 6.4 keV. Figure 6.3 shows an

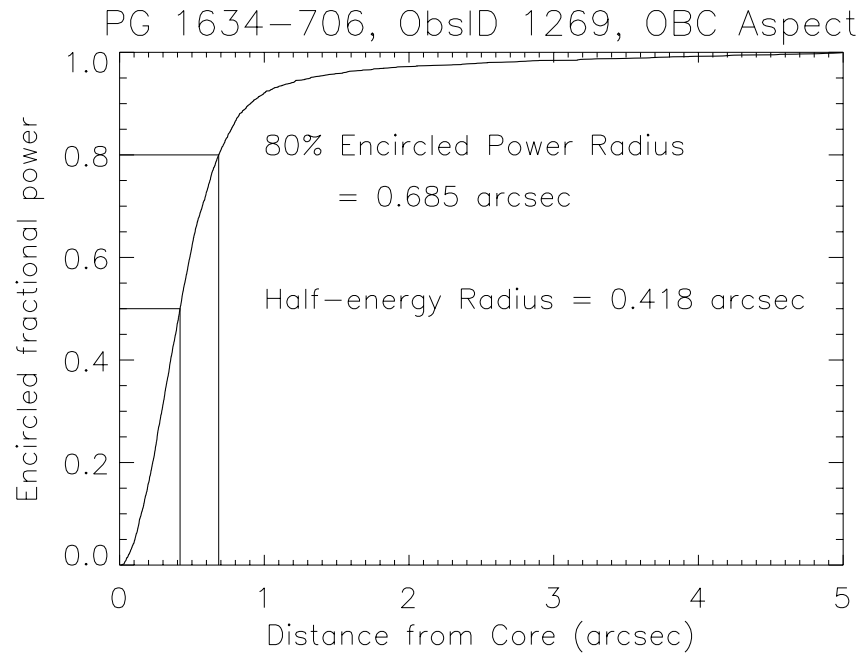


Figure 6.3: The on-orbit encircled broad-band energy versus radius for an ACIS observation of point source PG1634-706. The effective energy is 1 keV.

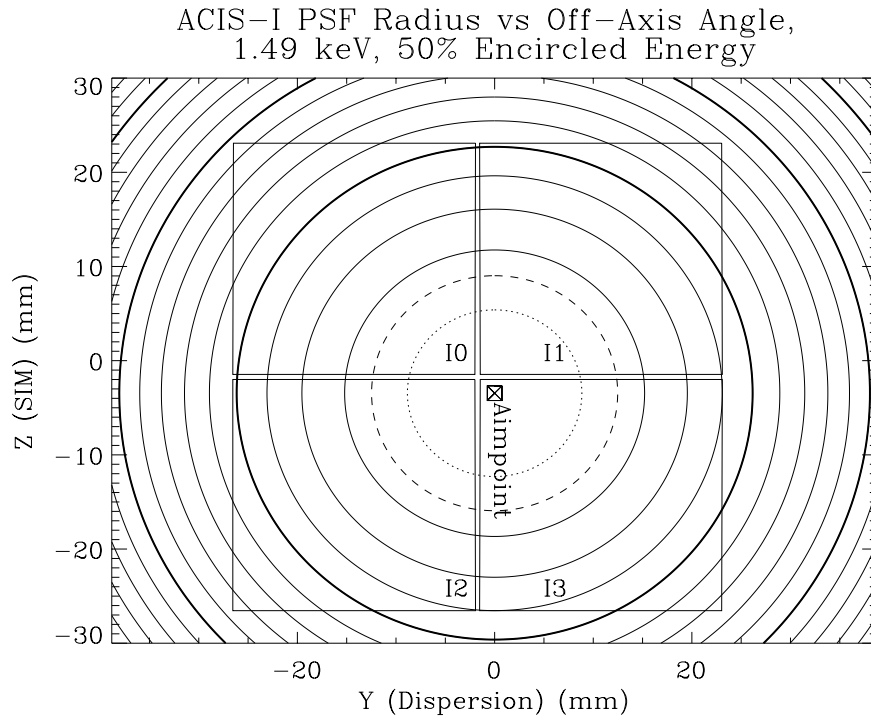


Figure 6.4: Contours of constant 50% encircled energy at 1.49 keV relative to the ACIS-I aimpoint on I3. The dotted line is 1 arcsec, the dashed line is 1.5 arcsec. The remainder are 1 arcsec intervals. The solid lines highlight the 5, 10, and 15 arcsec contours.

in-flight calibration. There is no evidence for any differences in data taken with either S3 or I3 at the nominal focus.

Off-axis, the departure of the CCD layout from the ideal focal surface and the increase of the HRMA *PSF* with off-axis angle become dominating factors. Since the ideal focal surface depends on energy, observers, for whom such considerations may be important, are urged to make use of the MARX simulator to study the impact on their observation.

6.6 Dither

Unless specially requested, the spacecraft is dithered during all observations. The dither pattern is a Lissajous figure. For observations with ACIS, the dither pattern spans 16 arcsec peak to peak. The dither serves two purposes:

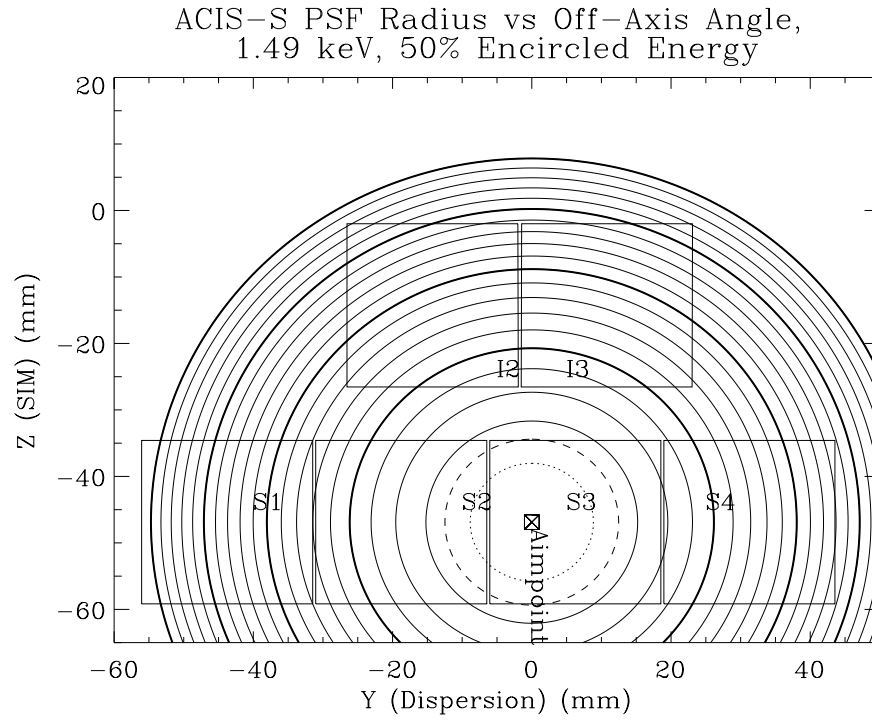


Figure 6.5: Contours of constant 50% encircled energy at 1.49 keV relative to the ACIS-S aimpoint on S3. The dotted line is 1 arcsec, the dashed line is 1.5 arcsec. The remainder are 1 arcsec intervals. The solid lines highlight the 5, 10, and 15 arcsec contours.

(1) to provide some exposure in the gaps between the CCD, and; (2) to smooth out pixel-to-pixel variations in the response. The dither is removed during high-level ground processing of the data. Obviously the exposure time in the gaps between chips will be less than that for the remainder of the field.

6.6.1 Gaps between the CCDs

The approximate sizes of the various gaps between chips are shown in Figure 6.1. Note that the Y-gaps in the ACIS-I array vary with Z due to the way the CCDs are tilted.

6.7 Energy Resolution

The ACIS FI CCDs originally approached the theoretical limit for the energy resolution at almost all energies, while the BI CCDs exhibited poorer resolution. The prelaunch energy resolution as a function of energy is shown in Figure 6.6. Subsequent to launch and orbital activation, *the energy resolution of the FI CCDs has become a function of the row number*, being near pre-launch values close to the frame store region and substantially degraded in the farthest row. An illustration of the dependence on row is shown in Figure 6.7.

We believe that the damage was caused by low energy protons, encountered during radiation belt passages and reflecting off the x-ray telescope onto the focal plane. Subsequent to the discovery of the degradation, operational procedures were changed, the ACIS is not left at the focal position during radiation belt passages. (The HRC is left at the focal position, but with door partially closed for protection.) Since this procedure was initiated, no further degradation in performance has been encountered. The BI CCDs were not impacted and this result is consistent with the proton-damage scenario – it is far more difficult for low-energy protons from the direction of the HRMA to deposit their energy in the buried channels of the BI devices, since the channels are near the gates and the gates face in the direction opposite to the HRMA. Thus the energy resolution for the two BI devices remains at their prelaunch values. The position-dependent energy resolution of the FI chips depends significantly on the ACIS operating temperature. Since activation, the ACIS operating temperature has been lowered in steps, based on considerations of molecular contamination, and is now set at the lowest temperature thought safely achievable ($\sim -120^\circ\text{C}$).

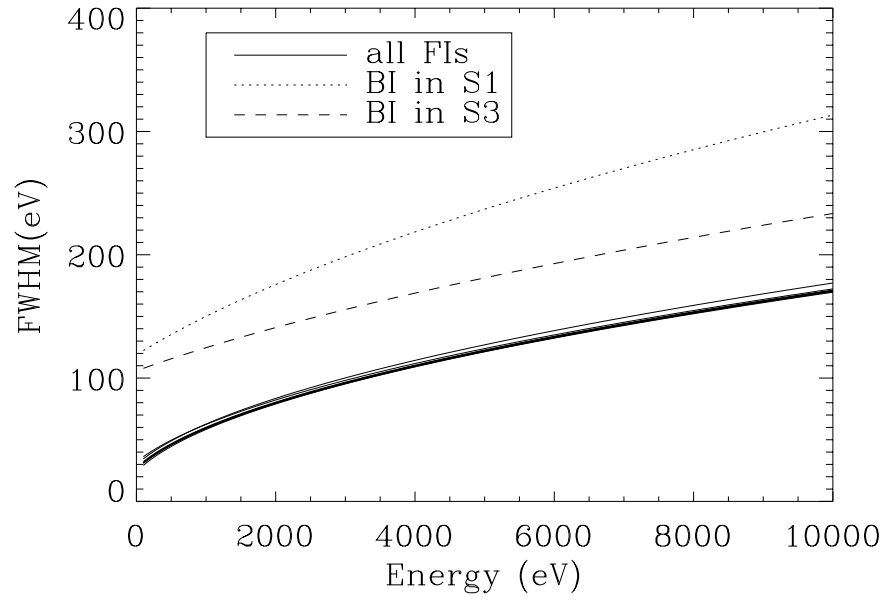


Figure 6.6: The ACIS prelaunch energy resolution as a function of energy. (Source: *CXC* Calibration group).

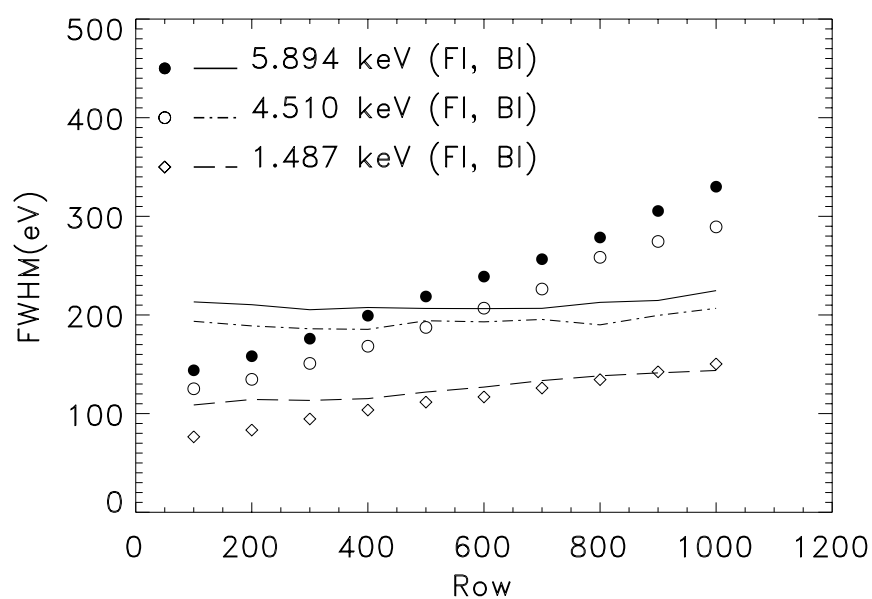


Figure 6.7: The energy resolution of S3 and I3 as a function of row number. These data were taken at -120°C . Note that these curves are representative of the variation - but they do not account for the row-dependent gain variation which also increases the energy resolution by about 10-15%, especially for the larger row numbers.

Table 6.3: Nominal Optical Blocking Filter Composition and Thicknesses

ACIS-I	Al/Polyimide/Al	1200Å	2000Å	400Å
ACIS-S	Al/Polyimide/Al	1000Å	2000Å	300Å

6.8 Optical Blocking Filter & Optical Contamination

Optical blocking filters (OBFs) are placed just over the CCDs between the chips and the HRMA. The filters are composed of polyimide (a polycarbonate plastic) sandwiched between two thin layers of aluminum. The nominal thicknesses of these components for the two arrays are given in Table 6.3. Details of the calibration of these filters may be found in the ACIS calibration report at

http://www.astro.psu.edu/xray/docs/cal_report/

The threshold for optical contamination is, unfortunately, subject to some uncertainty. The threshold for detectable visible light contamination on the ACIS-S array, for cool ($T < 5000\text{k}$) stars, is $V=5.3$ for the nominal 3.2 second exposure or $V=3.0$ for a 0.4s, 1/8 chip subarray. The thresholds are about 2 magnitudes brighter for the ACIS-I array. Recent observations, however, have placed these considerations into question, more so for ACIS-S than for ACIS-I. A safety margin of three additional magnitudes for ACIS-S is considered prudent. The user is urged to check the *CXC* web site for updates.

6.9 Quantum Efficiency and Effective Area

The quantum efficiencies for the ACIS CCDs for the standard grade set, including the optical blocking filters, are shown in Figure 6.8. Note that the quantum efficiency for the FI chips varies somewhat with row number (not shown), and decreases by $\sim 5\text{-}15\%$ farthest from the readout at energies above 4 keV. The variation with row number for the BI chips is much smaller.

The combined HRMA/ACIS on-axis effective areas are shown in Figures 6.9 (log energy scale) and 6.10 (linear energy scale). The calculations are for a point source and 20 arcsec diameter detection cell.

Figure 6.11 shows the vignetting at several off-axis angles using flight data.

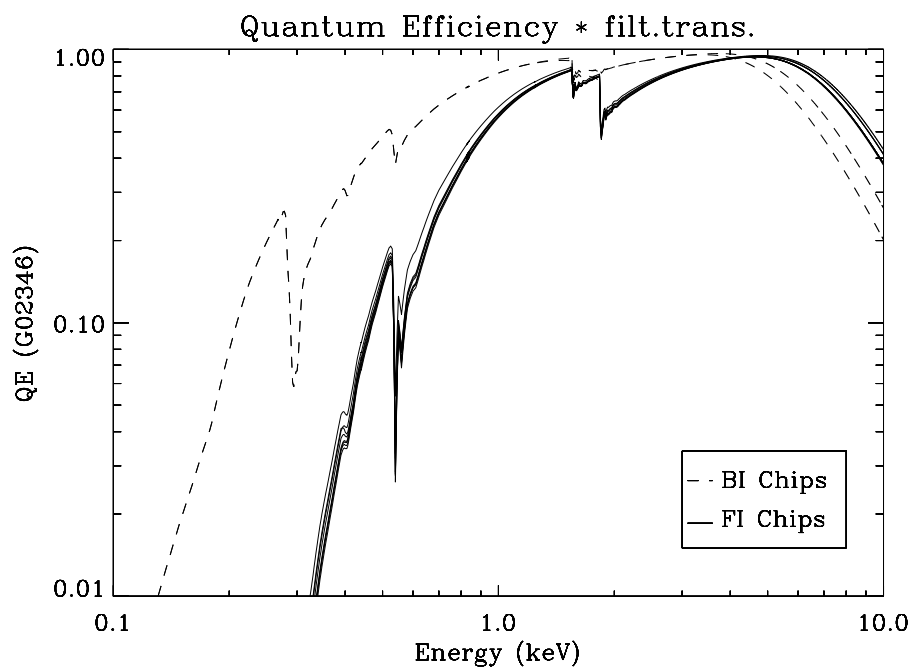


Figure 6.8: The quantum efficiency, convolved with the transmission of the appropriate optical blocking filter, of the FI CCDs (from a row nearest the readout) and the two BI CCDs as a function of energy. S3 is somewhat thicker, hence more efficient, than S1.

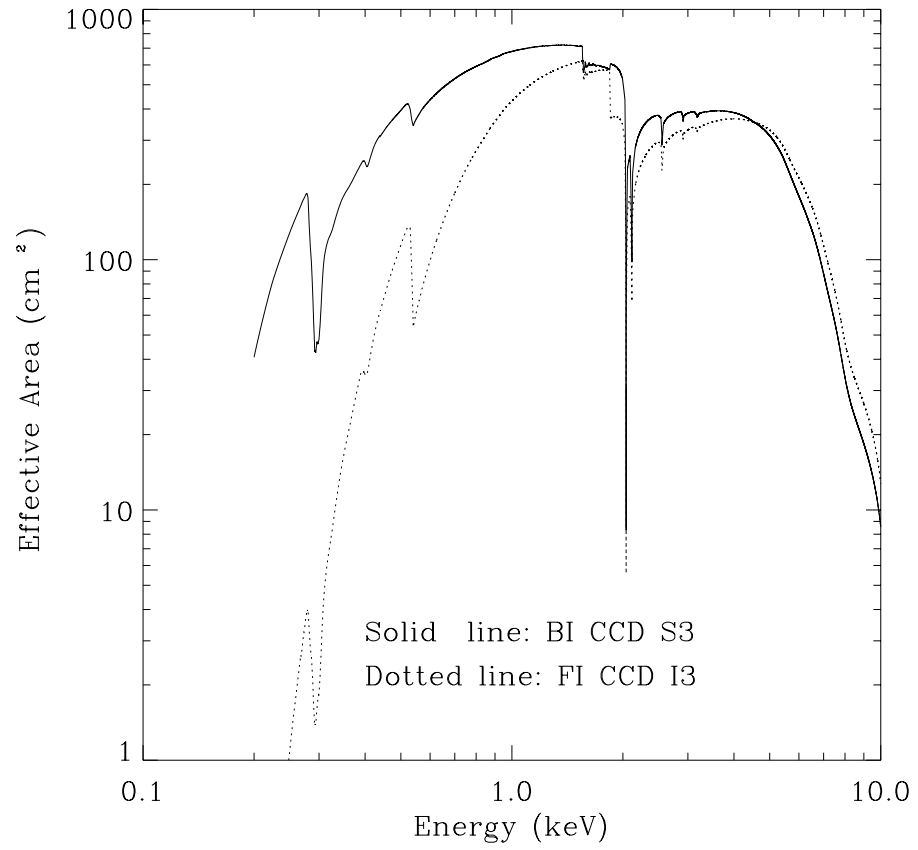


Figure 6.9: The HRMA/ACIS predicted effective versus the energy on a log scale. The dashed line is for the FI CCD I3, and the solid line is for the BI CCD S3.

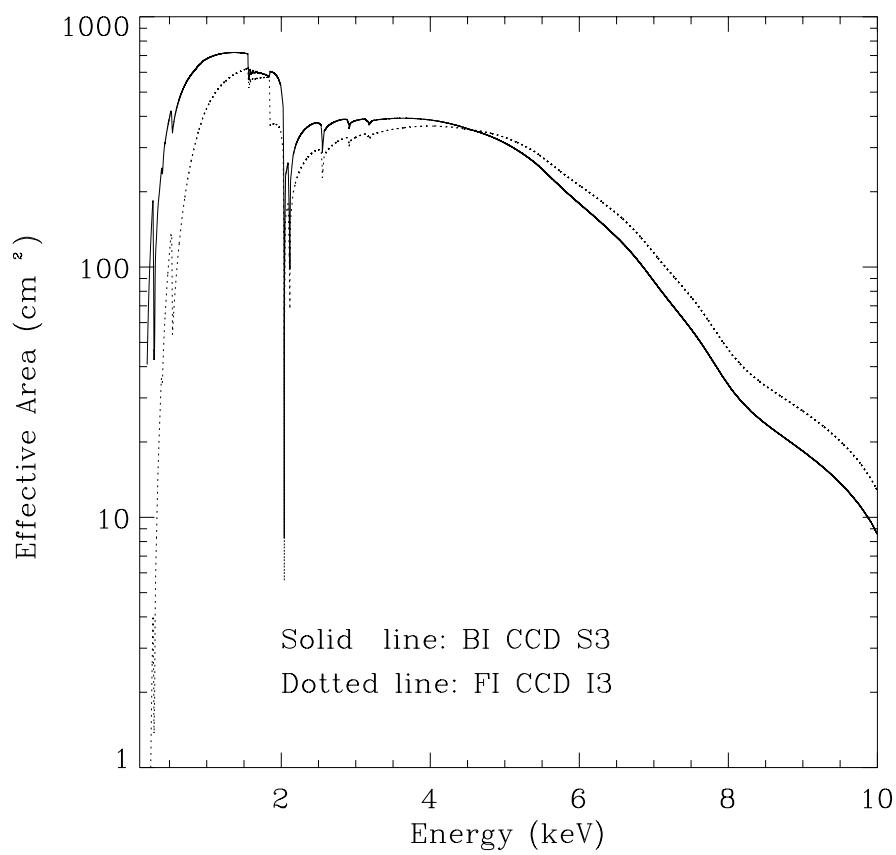


Figure 6.10: The HRMA/ACIS predicted effective versus the energy. The dashed line is for the FI CCD I3, and the solid line is for the BI CCD S3.

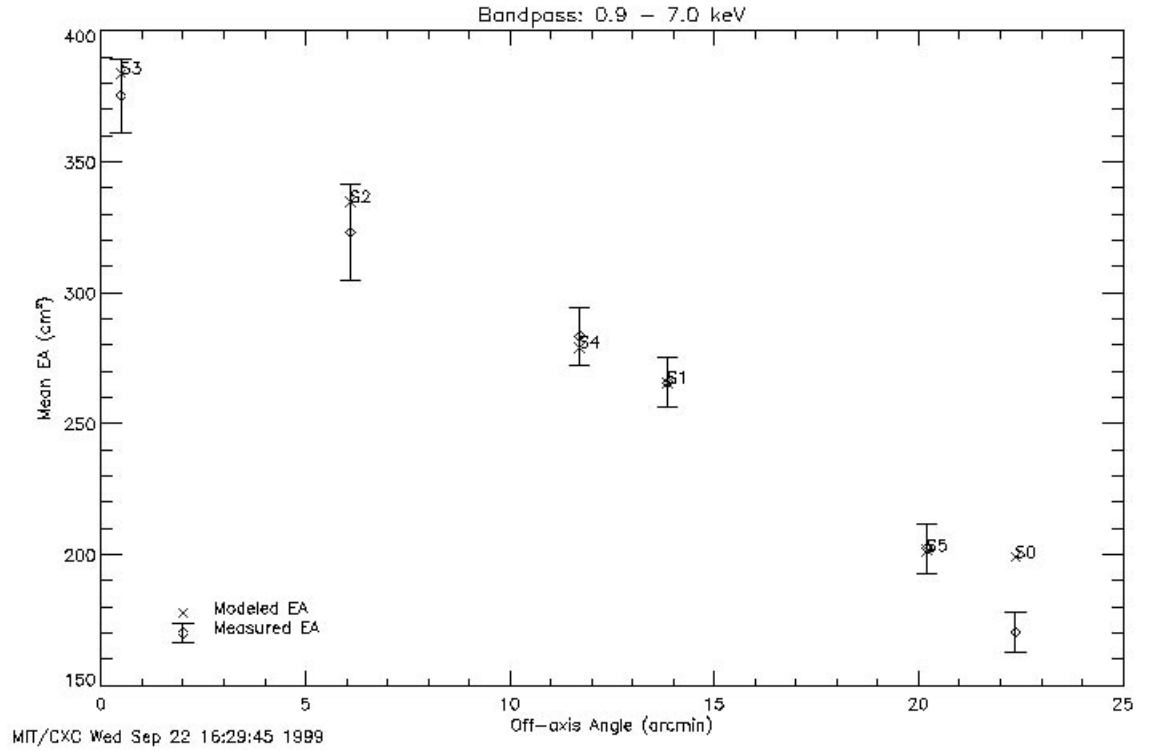


Figure 6.11: A comparison of the predicted and observed effective area (0.9–7.0 keV) versus off-axis angle for flux at the center of each chip of the ACIS-S array. Standard grades.

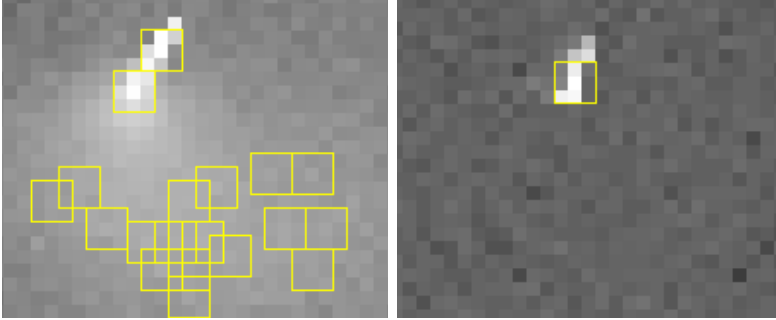


Figure 6.12: Enlarged view of an area of a FI chip I3 (left) and a BI chip (right) after being struck by a charged particle. There is far more “bloom-ing” in the FI image since the chip is thicker. The overlaid 3x3 detection cells indicate that the particle impact on the FI chip produced a number of events, most of which end up as *ASCA* Grade 7, and are thus rejected with high efficiency. The equivalent event in the BI chip, is much more difficult to distinguish from an ordinary x-ray interaction, and hence the rejection efficiency is lower.

6.10 On-Orbit Background

There are three components to the on-orbit background. The first is that due to the diffuse X-ray background (most of which may resolve into discrete sources during an observation with *Chandra*). The second component is commonly referred to as the charged particle background. This latter arises both from charged particles, photon, and other neutral particle interactions that ultimately deposit energy in the instrument. The third component depends on the flux from the very objects under observation and is a consequence of the “trailing” of the image discussed in Section 6.12.4. Strictly speaking, this last component is only “background” to the extent that one doesn’t recognize that it is signal.

The background rates differ between the BI and the FI chips, in part because of differences in the efficiency for identifying charged particle interactions. Figure 6.12 illustrates why.

6.10.1 The non X-ray background

An excellent measure of the major portion of the non-X-ray background was obtained during orbital activation (OBSIDs 62704-62710). The door to ACIS was open, but both the forward and aft HRMA contamination covers

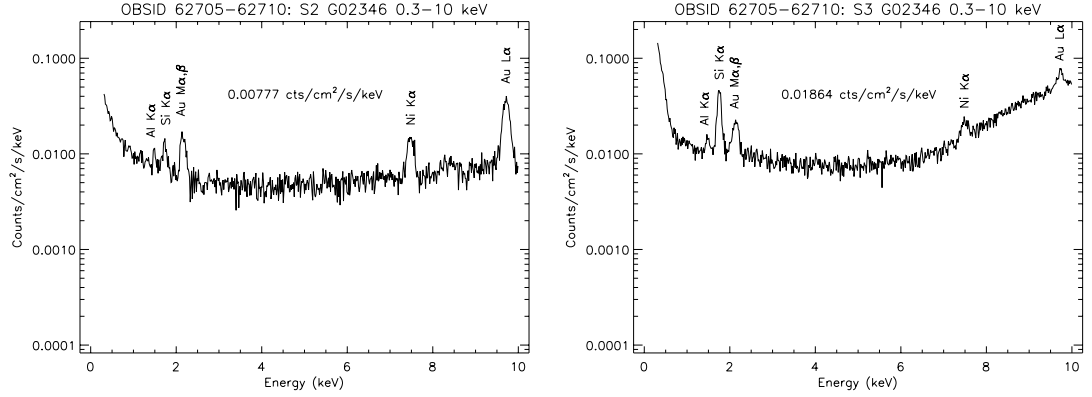


Figure 6.13: Energy spectra of the ACIS background (standard grades) with the HRMA doors closed. For a FI chip S2 (left) and a BI chip S3 (right). Line features are due to fluorescence of material in the telescope and focal plane.

were closed. Thus none of the ACIS -detected events were from X-rays that passed through the telescope. We note that these data were taken with ACIS operating at a temperature of -90°C , and that the energy resolution of the FI chips had not, as yet, degraded.

Figure 6.13 shows the filtered (G02346) energy spectrum obtained with an FI chip (S2) and a BI chip (S3). The FI-chip spectrum is flat from ~ 2 to 9 keV, whereas the BI-chip spectrum rises above ~ 6 keV. Note also the steep rise in both spectra below ~ 0.5 keV, especially for the BI device. *It should be emphasized that, in certain bandpasses, these background rates in the two types of CCDs are almost equal as shown in Tables 6.4 and 6.5.* Figure 6.13 also shows the corresponding spectra when only grade 0 events are considered. With this filtering, the non-x-ray background that does not pass through the telescope *is lower in the BI chip* over much of the spectral range. This may be exploited for certain experiments, but the user should bear in mind that the effective area for grade-0 events is not the same as that for G02346.

The grade distributions of the non-X-ray background for the two types of CCDs are shown in Figure 6.15. About 93% of the non-x-ray background events in the FI chip (S2) fall into just 12 ACIS grades (93.7% - all events; 97.7% - 0.3-10 keV). In contrast, these same 12 grades account for just 28% (all events) or 49% (0.3-10 keV) of the background in the BI chip (S3). Based on these data, events from grades 24, 66, 107, 214, and 255

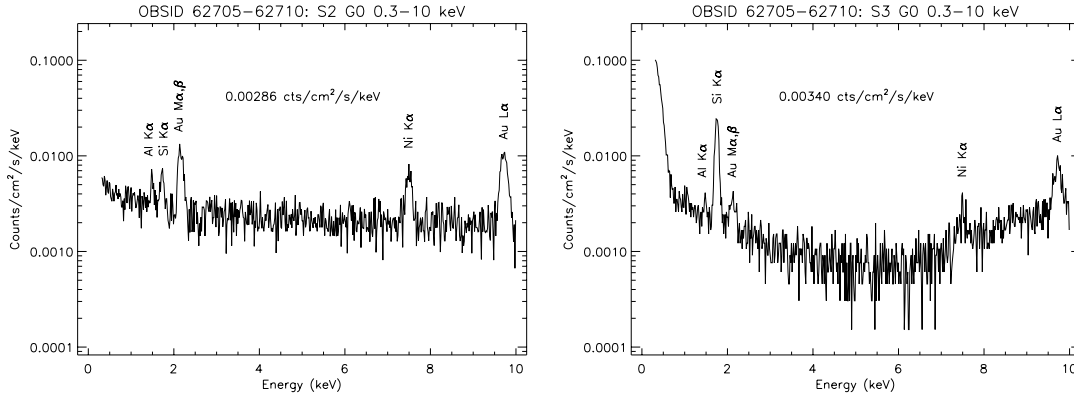


Figure 6.14: Energy spectra of the ACIS background (grade 0) with the HRMA doors closed. For a FI chip S2 (left) and a BI chip S3 (right). Line features are due to fluorescence of material in the telescope and focal plane.

are (currently) routinely discarded on-board. The user needs to be aware that only the total rate of the discarded events is available in the data stream, and that all other knowledge of the details of the discarded events is lost. Subsequent to these measurements, the CCD temperature has been lowered, the FI devices suffered the effects of the radiation damage, and the cosmic X-ray background is present. Despite these changes, the background is still dominated by the same grades although the detailed distribution has changed.

6.10.2 The total background

Once the HRMA doors were opened, two more components to the background come into play. The first is the diffuse X-ray background which, for moderately long (~ 100 ks) observations will be mostly resolved into discrete sources, but, nevertheless, contributes to the overall counting rate. The second is due to any charged particles that may reflect from the telescope and have sufficient momentum so as not to be diverted from the focal plane by the magnets included in the observatory for that purpose. Figure 6.16 shows a representative “quiescent” background spectra for both types of CCDs taken after the doors were opened and with no bright sources in the field. The total background counting rates in various energy bands and for the standard grades are given in Tables 6.4 and 6.5. These tables should be considered for sensitivity calculations. The total background counting rates

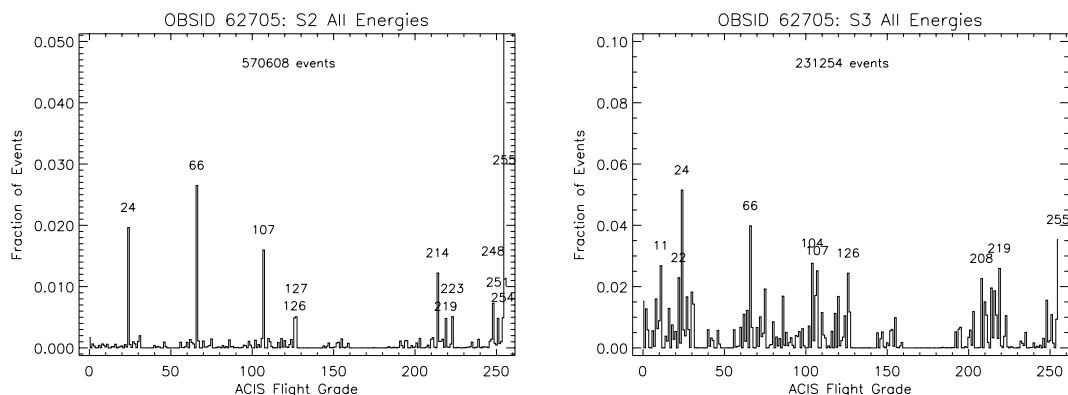


Figure 6.15: Fraction of ACIS background events as a function of grade from early-in-flight data for an FI chip (S2) (left) and a BI chip (S3) (right).

Table 6.4: Approximate on-orbit standard grade background counting rates with ACIS positioned at the ACIS-I aimpoint.

	Bkgrd rates (cts/sec)					
Energy Band (keV)	I0	I1	I2	I3	S2	S3
0.3-10	0.31	0.31	0.31	0.29	0.32	0.89
0.5-2	0.07	0.07	0.07	0.07	0.07	0.17
0.5-7	0.19	0.19	0.19	0.18	0.20	0.40
5.0-10	0.15	0.15	0.15	0.14	0.15	0.51

for each type of chip, important when considering telemetry saturation, are given in Table 6.6.

6.10.3 Background variability

In general the background counting rates are stable during an observation. Occasionally, however, there are significant variations, especially in the BI chips as illustrated in Figure 6.17. A early measure (August 1999) showing the frequency of such variations when compared to more the more quiescent level is shown in Figure 6.18. The user should note the finite probability that the counting rate in the BI CCDs can significantly increase in these circumstances, and thus possibly saturate telemetry – hence the advice to avoid turning on the BI chip(s) unless, of course, necessary for

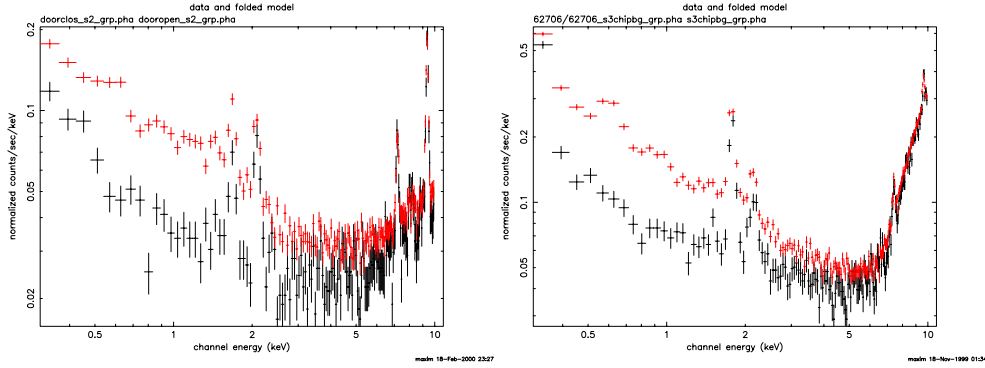


Figure 6.16: ACIS quiescent background spectrum for an FI CCD (s2) (left) and a BI CCD (S3)(right). The lower curve shows the spectrum before the HRMA doors were opened; the upper curve after. Both curves have G02346 filtering.

Table 6.5: Approximate on-orbit standard grade background counting rates with ACIS positioned at the ACIS-S aimpoint and the HETG in position.

Energy Band (keV)	Bkgrd rates (cts/sec)					
	S0	S1	S2	S3	S4	S5
0.3-10	0.27	1.55	0.38	1.03	1.13	0.33
0.5-2	0.07	0.18	0.10	0.18	0.57	0.08
0.5-7	0.19	0.51	0.26	0.53	0.77	0.21
5.0-10	0.10	1.08	0.16	0.56	0.16	0.15

Table 6.6: Typical total quiescent background rates by chip type

Type	Chip	Rate (cts s ⁻¹)	
		0.0 < E < 10.0 keV	all E
BI	S3	3.6	10.5
FI	S2	8.1	9.4

[†] See Figure 6.18 for an estimate of the probability that the actual background exceeds the quiescent value.

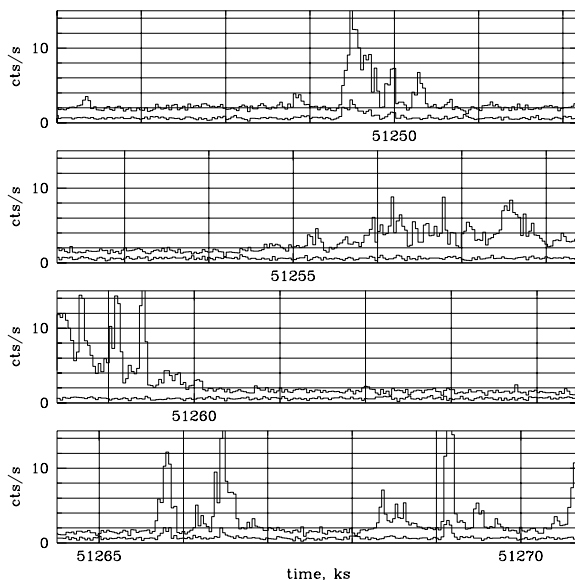


Figure 6.17: The ACIS background counting rate versus time - BI chip (S3; top curve) and an FI chip (I2; bottom curve). These are for the standard grades and the band from 0.3 - 10 keV.

accomplishing the scientific particular objective.

6.10.4 Background in Continuous Clocking Mode

Apart from compressing the data into one dimension (Section 6.12.5), there is essentially no difference in the total background in this mode. The background per-sky-pixel, however, will be 1024 times larger, since the sky-pixel is now 1×1024 ACIS pixels.

6.11 Sensitivity

The ACIS sensitivity for detecting a point source, on axis, during times of quiescent background is approximately 2×10^{-14} ergs $\text{cm}^{-2} \text{s}^{-1}$ in a 10 ks exposure in the 0.4–6.0 keV band. Necessarily, the sensitivity is a function of energy and depends on which CCD FI(I3) or BI(S3) is selected. Figure 6.19 shows the minimum detectable flux, for a point source and a $20''$ -diameter extended source for different choices of spectral parameters.

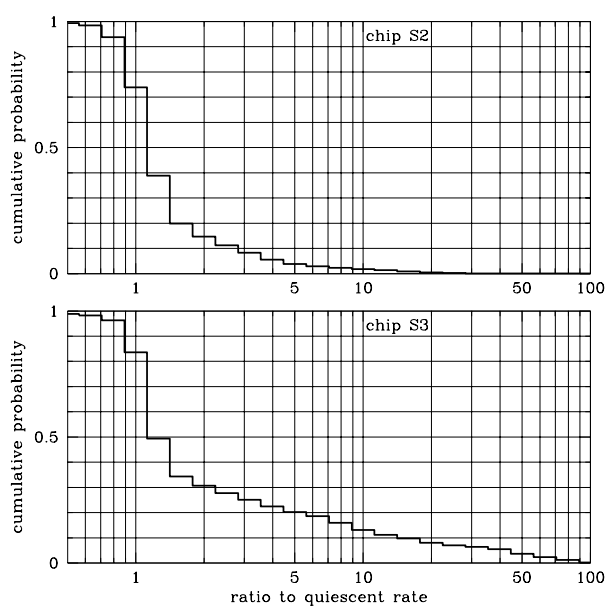


Figure 6.18: An estimate of the cumulative probability that the ratio of the background counting rate to the quiescent background counting rate is larger than a given value. Upper curve for a representative FI chip - S2, and the lower curve for a representative BI chip - S3.

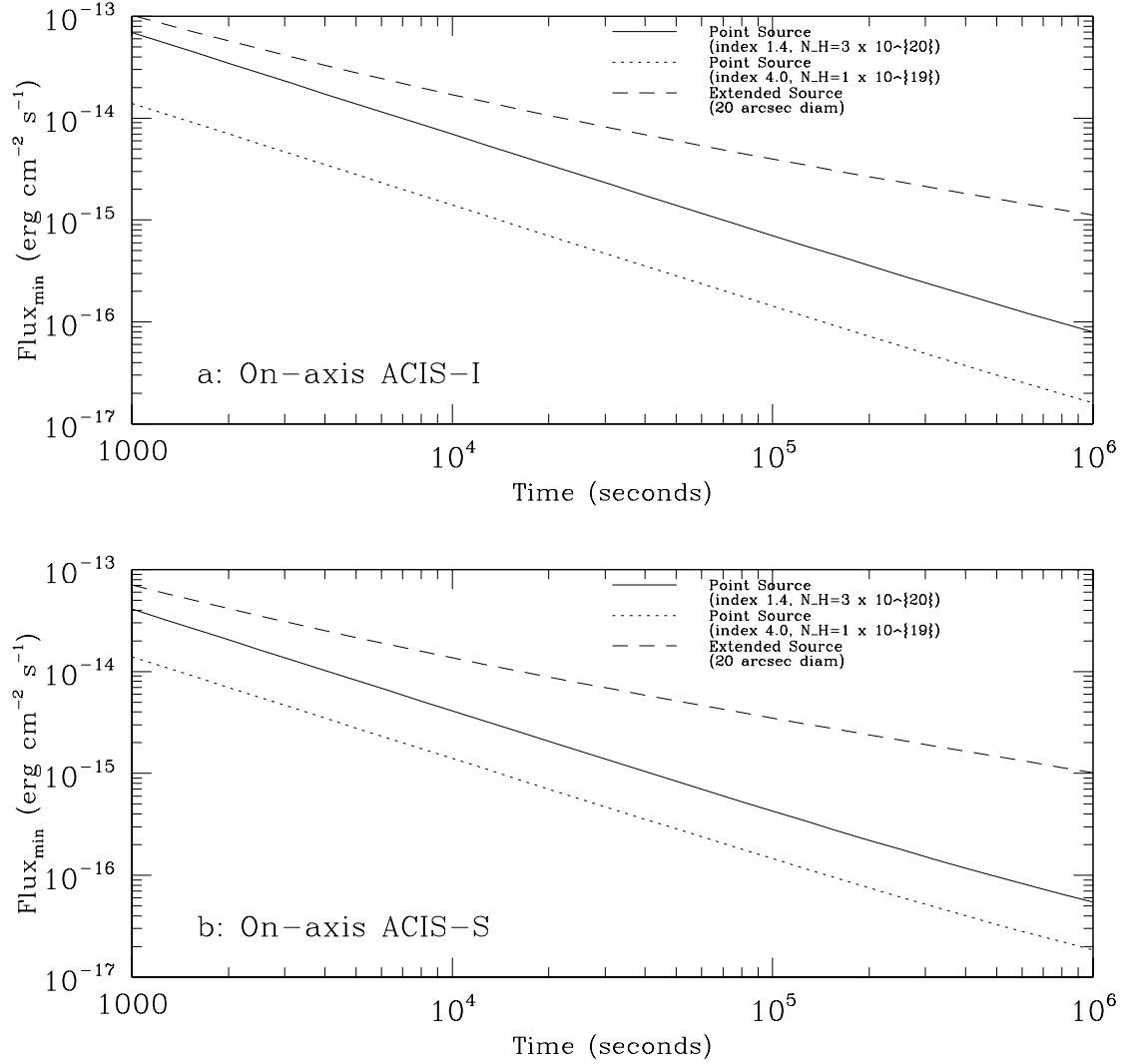


Figure 6.19: The minimum detectable flux as a function of exposure time for an on-axis observation of a point source using an FI chip (top) and a BI chip (bottom). The calculation assumes a 3σ 2-10 keV absorbed *flux* detection criterion in a 5x5 pixel detection cell and *no* pileup. The power law index is a photon index. The extended source spectrum assumed the -1.4 index power law and corresponding column.

6.12 Operating Modes

6.12.1 Timed Exposure Mode

A timed exposure refers to the mode of operation wherein a CCD collects data (integrates) for a preselected amount of time - the Frame Time. Once this time interval has passed, the charge from the 1024 x 1024 active region is quickly (~ 40 msec) transferred to the framestore region and subsequently read out through (nominally) 1024 serial registers.

6.12.2 Frame Times - Full Frames

Frame times are selectable within a range of values spanning the time interval from 0.2 to 10.0 seconds. If the data from the entire CCD are utilized (full frame) then *the nominal (and optimal) frame time is 3.2s*. Selecting a frame time *shorter* than the nominal value (e.g. to decrease the probability of pileup - section 6.17 - has the consequence that there will be a time during which *no* data are taken, as 3.2s are required for the process regardless of the frame time. The fraction of time during which no data are taken is simply the ratio of the selected frame time to the nominal frame time - e.g. 0.2/3.2 if 0.2 sec was the choice. We note, strictly speaking, the full-frame time depends on how many CCD s are on - see the equation in section 6.12.3 - but the differences are very small.

6.12.3 Frame Times & Subarrays

It is also possible for one to select a *subarray* - a restricted region of the CCD in which data will be taken. A subarray is fully determined by specifying the number of rows separating the subarray from the framestore region (q) and the number of rows in the subarray (n). Examples of subarrays are shown in Figure 6.20. The nominal frame time for a subarray depends on (q), (n), and the total number of CCDs that are activated (m). The nominal frame time is given by:

$$T(msec) = 41 \times m + 2.84 \times n + 5.2 + 0.040 \times (m \times q).$$

As with full frames (section 6.12.2), selecting a frame time less than the optimum results in loss of data.

6.12.4 Trailed Images

It takes 40 μ sec to transfer the charge from one row to another during the process of moving the charge from the active region to the framestore region.

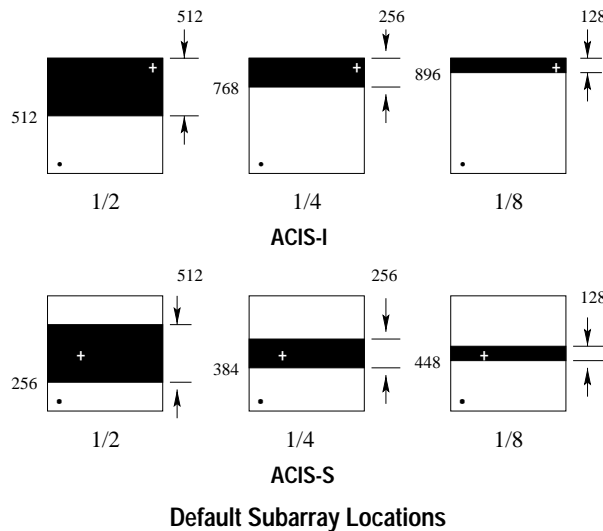


Figure 6.20: Examples of various subarrays. The heavy dot in the lower left indicates the origin

This has the interesting consequence that each CCD pixel is exposed, not only to the region of the sky at which the observatory was pointing during the long (frame time) integration, but also, for $40 \mu\text{sec}$ each, to every other region in the sky along the column in which the pixel in question resides. Thus, any single pixel always contains data from all of the other pixels in the column. Figure 6.21 is example where there are bright features present, so intense, that the tiny contribution of the flux due to trailing is stronger than the direct exposure - hence the trailed image is clearly visible. The user needs to be aware of this phenomenon as it has implications for the data analysis - e.g. estimates of the background. In some cases, the trailed image can be exploited to estimate the impacts of pileup (section 6.17) on the direct image.

6.12.5 Continuous Clocking Mode

The continuous clocking mode is provided to allow 3 msec timing at the expense of one dimension of spatial resolution. In this mode one obtains 1 pixel x 1024 pixel images, each with an integration time of 3 msec. Details as to the spatial distribution in the columns are lost - other than that the event originated in the sky along the line determined by the length of the column. The on-board processing electronics still grades events in the usual

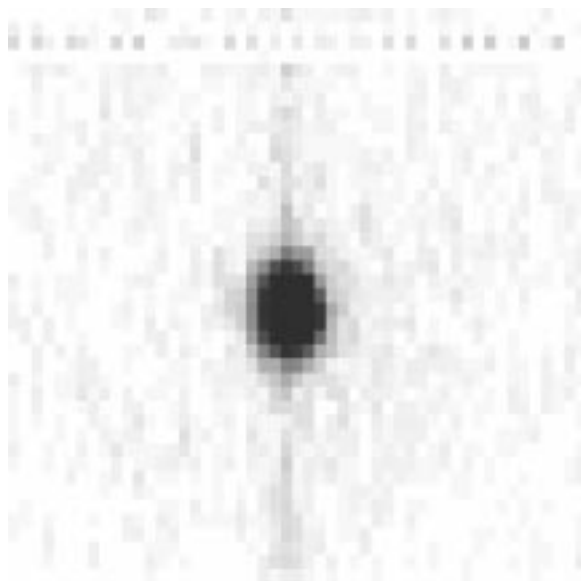


Figure 6.21: An example of a trailed ground-calibration image.

fashion, except at the border between rows 511 and 512 (assuming an origin of (0,0)), where no grades are assigned - as with the first two and the last two rows.

6.13 Bias Maps

In general the CCD bias, the amplitude of the charge in each pixel in the absence of external radiation, is determined at various times - every change of mode when ACIS is in place at the focus of the telescope. These bias maps have proven to be remarkably stable, and thus the user need not, in general, concern themselves with this issue. As discussed below, however, provisions have been made for one to obtain more detailed information by utilizing the Faint + Bias format, or by requesting additional bias data in the proposal request.

6.13.1 Telemetry Formats

There are a number of telemetry formats available. Specifying a format determines the type of information that is included in the telemetry stream. The number of bits per event depends on which mode and which format is

Table 6.7: Telemetry Saturation Limits

Mode	Format	Bits/event	Events/sec* in full buffer	Number of Events
CC	Graded	58	375.0	128,000
CC	Faint	128	170.2	58,099
TE	Graded	58	375.0	128,000
TE	Faint	128	170.2	58,099
TE	Faint + Bias	236	92.3	31,508
TE	Very Faint	320	68.8	23,273

*(includes a 10% overhead for housekeeping data)

selected. The number of bits per event, in turn, determines the event rate at which the telemetry will saturate and data will be lost until the onboard-buffer empties. The formats available depend on which mode (Timed Exposure or Continuous Clocking) is used. The modes, associated formats, and approximate event rates at which the telemetry saturates and one begins to limit the return of data, are listed in Table 6.7. The formats are described in the following paragraphs.

Faint Faint format provides the event position in detector coordinates, an arrival time, an event amplitude, and the contents of the 3 x 3 island that characterizes the event grade. The bias map is telemetered separately. Note that certain grades may be not be included in the data stream (section 6.10.1).

Graded Graded format provides event position in detector coordinates, an event amplitude, the arrival time, and the event grade. Note that certain grades may be not be included in the data stream (section 6.10.1).

Very Faint Very Faint format provides the event position in detector coordinates, the event amplitude, an arrival time, and the pixel values in a 5 x 5 island. As noted in Table 6.7, this format is only available with the Timed Exposure mode. This mode was included in the ACIS suite of modes prior to launch. Thus far, there has been very little experience with this mode. Events are still graded by the contents of the central 3 x 3 island. Note that certain grades may be not be included in the data stream (section 6.10.1).

Faint+Bias Faint+Bias format provides the event position in detector coordinates, an arrival time, an amplitude, the pixel values in the 3x3 island, and the corresponding 3x3 bias map. Note that certain grades may be not be included in the data stream (section 6.10.1).

6.14 Calibration

Calibration of ACIS includes laboratory calibrations, a system-level ground calibration of the HRMA and ACIS at the X-Ray Calibration Facility (XRCF) at MSFC, and on-orbit calibration using celestial and on-board radioactive X-ray sources.

The on-orbit calibration of ACIS is an on-going activity. The radiation-induced damage impacted the planned calibration schedule, so portions of certain analyses may not yet have been completed. All calibration data are, or will be, described in detail, at:

<http://asc.harvard.edu/cal/>

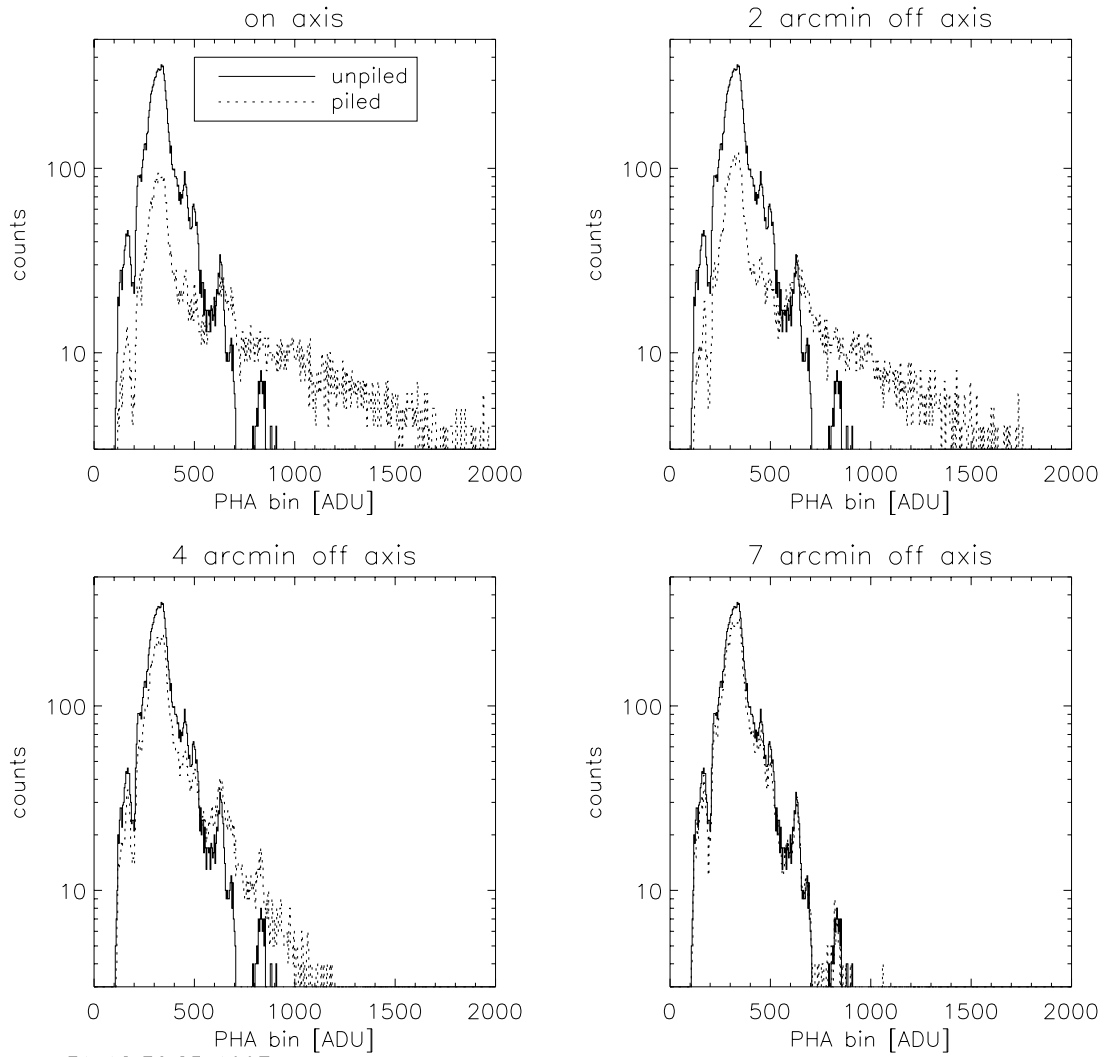
The user is urged to consult the WWW site and its pointers for the latest information.

6.15 Hot Pixels and Columns

Hot columns and pixels are defined to be those which produces a high or saturated pulse-height for a large number of consecutive frames of data. These depend on operating conditions such as temperature. One should always refer to the *CXC* web site for the most recent list. To date, S1 is the device with the largest number of such pixels and columns.

6.16 Anomalies

There are two instrument anomalies that we have encountered. The first was the changed energy resolution of the FI devices resulting from proton-induced radiation damage and was discussed in section 6.7. The second involves the ACIS Front End (digital) Processors (FEPs). There are six FEPs, and they are assigned, by command, to the active CCD. During the early phase of the mission, one of these devices (FEP0) exhibited intermittent problems which created numerous spurious events that saturated the telemetry. Subsequently, a software patch has been developed and installed



Mon Mar 31 12:36:25 1997

Figure 6.22: MARX simulations of the effect of pileup on the shape of the spectrum. The true (solid line) and the detected (dotted line) spectra are shown for four different viewing angles. The corresponding “pileup fractions” -see Section 6.17.2 are 46%, 40%, 15%, and 2% as the image is moved progressively further off-axis. (Source: J. Kastner and M. Wise, *CXC*)

which will detect when the device is misbehaving and prevents telemetry saturation from occurring. Should the situation arise again, the patch prevents data from the “upper half” (i.e. the half farthest from the framestore region) from being included in the telemetry stream. The data from the lower half continues to be processed and placed in the telemetry uninterrupted.

FEP0 is routinely assigned to the CCD which produces the least useful data for an observation. The defaults are:

FEP0 is assigned to S0 when S0 through S5 are in use,

FEP0 is assigned to S2 when I0 through I3 and S2 and S3 are in use and the aimpoint is on the I-array,

FEP0 is assigned to I2 when I2,I3, and S1 through S4 are in use and the aimpoint is on S3,

FEP0 is unassigned if only 5 CCDs are in use.

6.17 Pileup

Pileup results when two or more photons are detected as a single event. The fundamental impacts of pileup are: (1) a distortion of the energy spectrum - the apparent energy is approximately the sum of two (or more) energies; and (2) an underestimate as to the correct counting rate - two or more events are counted as one. A simple illustration of the effects of pileup is given in Figure 6.23. There are other, somewhat more subtle impacts discussed below (6.17.1).

Although numerous efforts are underway to create analysis tools that propose to remove some or all of the effects of pileup from ACIS data, there are currently no such tools endorsed by the *CXC*. Proposers are urged to either use the information in Section 6.17.2 or the MARX simulator to estimate the degree of pileup and the impact on the observation. If the resulting degree of pileup appears to be unacceptable given the objectives, then the proposer should employ some form of pileup mitigation (Section 6.17.3) as part of the observing strategy. In general, pileup should not be a problem in the observation of extended objects, the Crab Nebula being a notable exception, unless the source has bright knots or filaments.

6.17.1 Other consequences of pileup

There are other consequences of pileup in addition to the two principal features of spectral hardening and underestimating the true counting rate by

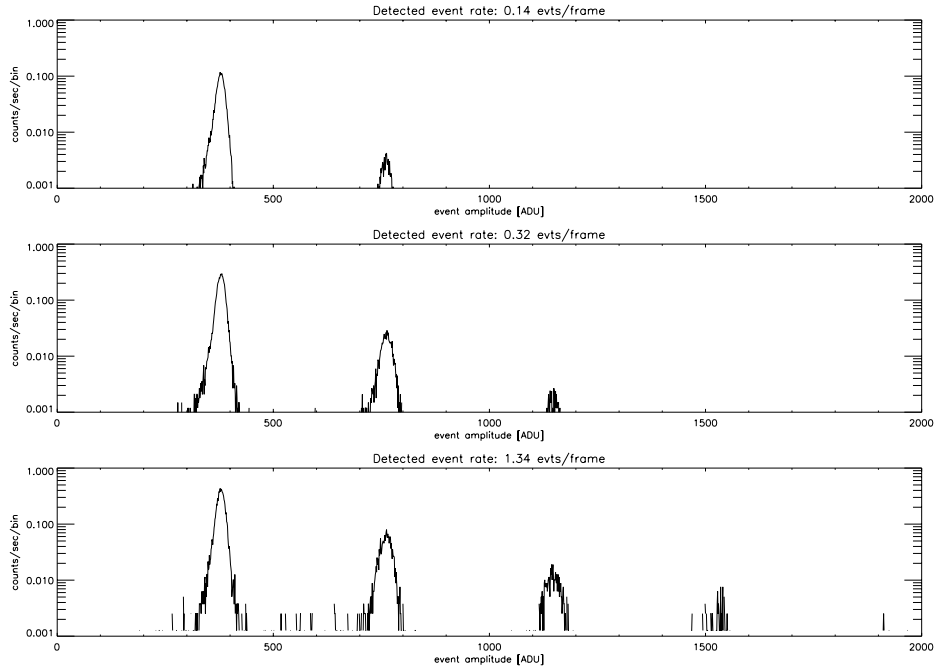


Figure 6.23: The effects of pileup at 1.49 keV ($\text{Al K}\alpha$) as a function of source intensity. Data were taken during HRMA-ACIS system level calibration at the XRCF. Single-photon events are concentrated near the pulse height corresponding to the $\text{Al K}\alpha$ line (~ 380 ADU), and events with 2 or more photons appear at integral multiples of the line energy.

Table 6.8: *ASCA* Grade Distributions for different Incident Fluxes at 1.49 keV (Al-K α , based on data taken at the XRCF during ground calibration using chip I3; *CXC* Calibration Group)

Incident Flux*	G0	G1	G2	G3	G4	G5	G6	G7
9	0.710	0.022	0.122	0.053	0.026	0.009	0.024	0.035
30	0.581	0.057	0.132	0.045	0.043	0.039	0.029	0.073
98	0.416	0.097	0.127	0.052	0.050	0.085	0.064	0.108
184	0.333	0.091	0.105	0.040	0.032	0.099	0.077	0.224

*arbitrary units

undercounting multiple events. These additional effects are grade migration and pulse saturation, both of which can cause to distortion of the apparent *PSF*.

Grade migration Possibly the most troubling effect of pileup is that the nominal grade distribution that one expects for X-ray events changes. The change of grade introduced by pileup has become to be referred to as “grade migration”. Table 6.8 shows an example of grade migration due to pileup as the incident flux is increased. In this simple test, which involved only monoenergetic photons, the largest effect is the depletion of G0 events. In general, as the incident flux rate increases, the fraction of the total number of events occupying a particular event grade changes as photon-induced charge clouds merge and the resulting detected events “migrate” to other grades which are not at all necessarily included in the standard (G02346) set. If one then applies the standard calibration to such data, the true flux will be under-estimated.

Pulse Saturation One consequence of severe instances of pileup is the creation of a region with no events! In this case the pileup is severe enough that the total amplitude of the event is larger than the onboard threshold (~ 15 keV) and is rejected. Holes in the image can also be created by grade migration of events into grades (e.g. 255) that are filtered on-board.

***PSF* distortion** Obviously the effects of pileup are severest when the flux is highly concentrated on the detector. Thus, the core of the *PSF* suffers

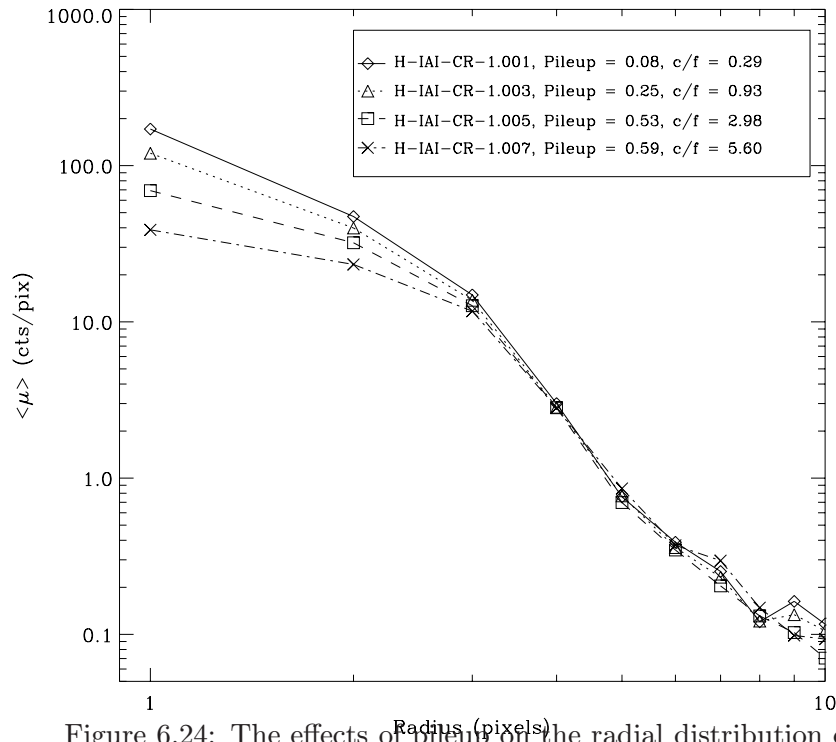


Figure 6.24: The effects of pileup on the radial distribution of the *PSF* are illustrated. These data were taken during ground calibration at the XRCF. The specific “OBSIDs”, the counting rate per CCD frame (“c/f”), and the “pileup fraction” as defined in Section 6.17.2 are given in the inset.

more from pileup induced effects than the wings. Figure 6.24 illustrates this point.

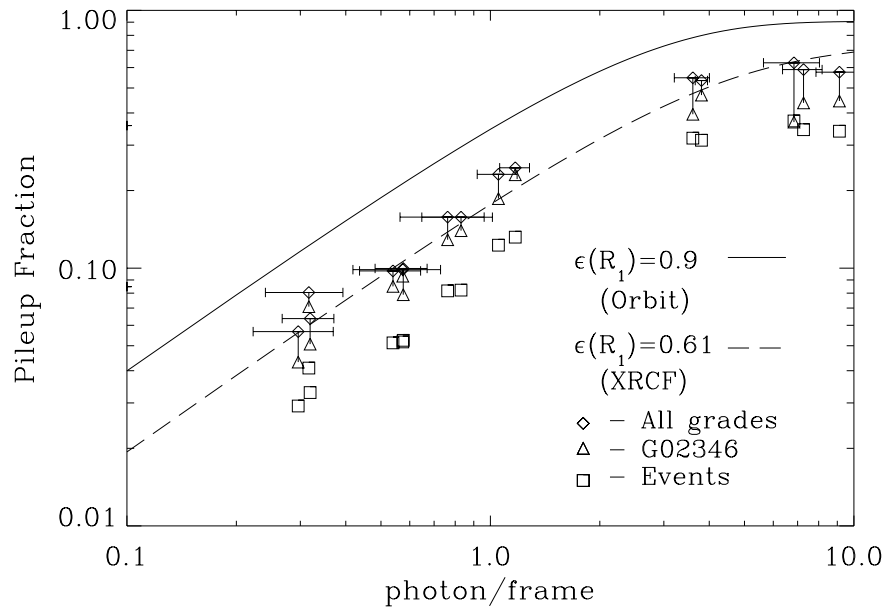
6.17.2 Pileup Estimation

It is clearly important in preparing a *Chandra* observing proposal to determine if the observation will be impacted by pileup, and if so, decide what to do about it (or convince the peer review why the specific objective can be accomplished without doing anything). There are two approaches to estimating the impact of pileup on the investigation. The most sophisticated makes use of the MARX simulator which allows one to create a simulated data set that can be analyzed and the impact of pileup on the specific objectives of the investigation - e.g. the measure of the power-law index of a synchrotron source - can be directly evaluated. A less sophisticated, but very useful, approach is described here. *The approach is only directly applicable to point sources.*

An estimate of the pileup fraction, defined as the ratio of multiple events to true events in the absence of any pileup, can be determined from Figure 6.25. The algorithm parameterizes the HRMA+ACIS *PSF* in terms of the fraction of encircled energy that falls within the central 3×3 pixel event detection cell, ϵ , and assumes that the remaining energy is uniformly distributed among the 8 surrounding 3×3 pixel detection cells. The probabilities of single- and multiple-photon events are calculated separately for the central and surrounding detection cells and subsequently averaged (with appropriate weighting) to obtain the pileup fraction as a function of the true count rate - the *solid* line in Figure 6.25. The model was tested against data taken on the ground under controlled conditions - also shown in Figure 6.25.

As a general guideline, if the estimated pileup fraction is $> 10\%$ the proposed observation is very likely to be impacted. The first panel (upper left) in Figure 6.22 qualitatively illustrated the effect on a simulated astrophysical x-ray spectrum. *However, the degree of pileup that is acceptable for a particular objective will depend on the particular scientific goals of the measurement, and there is no clear-cut tolerance level.* If one's scientific objective demands precise flux calibration, then the pileup fraction pileup should probably be kept well below the 10% number discussed above.

The PIMMS tool provides the pileup fraction using the algorithm described here, both for direct observation with ACIS and also for the zeroth-image when a grating is inserted.



BRM-Wed Aug 5 16:23:58 1998

Figure 6.25: The pileup fraction as a function of the the counting rate in the absence of pileup in units of photons/frame. The solid line is for on-orbit, the dashed line and the data points are for, and from, ground-based data respectively. The difference between the ground and flight functions are a consequence of the improved *PSF* on-orbit, where gravitational effects are negligible - see Chapter 4.

6.17.3 Reducing Pileup

We summarize here various methods which can be used to reduce pileup.

Shorten exposure time: By cutting back on CCD exposure time, the probability of pileup decreases. The user is advised to select the best combination of a subarray and framerate in order to avoid losing data as discussed in Section 6.12.3.

Use the Alternating Exposure option: This option simply alternates between exposures that are subject to pileup and those that are not. The capability was originally developed for use with certain grating observations to allow one to spend some time obtaining useful data from a zeroth order image, which would otherwise be piled up.

Use CC mode If two-dimensional imaging is not required, consider using CC mode (Section 6.12.5).

Insert a transmission grating: Inserting either the HETG (Chapter 8) or the LETG (Chapter 9) will significantly decrease the counting rate as the efficiency is lower. The counting rate in the zero order image may then be low enough to avoid pileup.

Offset point: Performing the observation with the source off-axis spreads out the flux and thus decreases the probability of pileup at the price of a degraded image. Figure 6.22 illustrated the impact.

Defocus: The option is only listed for completeness, the option is *not* recommended or encouraged.

6.18 Observing with ACIS- the input parameters

This section describes the various inputs that either must be, or can be, specified in order to perform observations with ACIS. The sub-sections are organized to match the RPS form. We have added some discussion as to some of the implications of the possible choices. As emphasized at the beginning of the Chapter, ACIS is moderately complex and the specific characteristics of the CCDs and their configuration in the instrument lead to a number of alternatives for accomplishing a specific objective - *detailed trade-offs are the responsibility of the observer*. Thus, e.g. it might seem obvious that observations of a faint point source may be best accomplished by selecting the ACIS-S array with the aim point on S3, the BI device that

can be placed at the best focus of the telescope, and the CCD with the best average energy resolution. On the other hand, perhaps the science is better served by offset pointing (by a few arcminutes) the target onto S2, very near to the framestore, where the FI energy resolution is better than that of S3. On the other hand, if the object is very faint, so that the number total number of photons expected is just a handful – not enough to perform any significant spectroscopy – the advantage of S2 nor S3 may not be so obvious considering the smaller field of view, and perhaps the ACIS-I array, which would optimize the angular resolution over a larger field, may be more attractive.

A short summary of this section can be found in Chapter 12 (Proposal Preparation) under “ACIS Parameters”.

6.18.1 Required Parameters

There are certain ACIS input parameters that must be specified: the number and identity of the CCDs to be used, the Exposure Mode, and the Event Telemetry Format. If pileup and telemetry saturation are not considered to be a problem for the observation, then these are the only parameters that need to be specified.

• Number and Choice of CCD

Up to six CCDs can be operated at once. Specifying ACIS-S turns on S0-S5 and sets the aimpoint. Specifying ACIS-I turns on I0-I3, S2 and S3, and sets the aimpoint. For any other combination, the identity of the CCDs and the desired aimpoint will have to be specified.

• Exposure Mode

There are only two choices: Timed Exposure (Section 6.12.1) or Continuous Clocking (Section 6.12.5).

Timed Exposure Mode The timed exposure mode with the default nominal (and optimal) frame time of 3.2s is the typical mode for ACIS observations. Note that the option of selecting frame times shorter than nominal reduces observing efficiency, and hence the number of photons collected for a given observation time.

Continuous Clocking Mode The Continuous Clocking mode is useful when timing data are so critical and/or pileup is such a problem that the sacrifice of one dimension of spatial data is warranted. The use of continuous clocking may also lead one to consider specifying a particular satellite roll orientation (see Chapter 3) in order to avoid having two different sources produce events in the same CCD column.

6.18.2 Optional Parameters

Alternating Exposures This option applies *only* to Timed Exposures. The parameters specifying an Alternating Exposure are:

- the number of secondary exposures per primary exposure (1-15)
- the primary exposure frame time
- the secondary exposure frame time (default the optimum frame time)

Frame times and efficiencies in TE mode are discussed in Sections 6.12.2 and 6.12.3.

Energy Filtering

It is possible to remove events from the telemetry stream, and thus avoid telemetry saturation, by specifying an energy acceptance filter within which detected events will be telemetered. The default discards events above 3750 ADU (nominally 15 keV).

Spatial Windows

A more sophisticated approach to removing data from the telemetry stream, and thus avoiding telemetry saturation, is by the use of a Spatial Window. This option offers a good deal of flexibility. One may define up to 6 Spatial Windows per CCD. Each window can be placed anywhere on the chip. Note there is a significant difference between a Spatial Window and a Subarray (Section 6.12.3): Subarrays affect the transmission of CCD data to the on-board ACIS processors; Spatial Windows select events detected by the processors and only impact the telemetry rate. The user may also specify the window energy threshold and energy range.

Spatial windows can be inclusive or exclusive - in which case the sample rate is irrelevant. A Spatial Window could be used to eliminate a bright, off-axis source that would otherwise overwhelm the telemetry stream. The

order in which the spatial windows are specified is important if they overlap (see Chapter 12.)

Request Bias

The user can request additional bias data, however, see the discussion of bias in Section 6.13. *The time to take the additional bias data must be included in the proposed time requested.* The time cost is 1.5 ks per request.

6.18.3 Non-ACIS Parameters Relevant to an Observation with ACIS

There are a small number of additional parameters that need to be considered in specifying an observation with ACIS: (1) the off-axis pointing (if required), which reduces the flux, and spreads out the image; (2) the roll angle (Chapter 4; (3) time constraints (if any); and (4) time monitoring intervals (if any). Detailed definitions of these parameters are given in the instructions for filling in the entries in the RPS in Chapter 12.

6.19 Examples: Choosing the Instrument Parameters

In this section, we consider a handful of examples of configuring ACIS to achieve a particular objective. These examples are meant to be illustrative, but should **not** be considered definitive!. The examples are only representative of the kinds of considerations involved in utilizing ACIS.

6.19.1 Detection of a Faint Point Source

If the principal goal of the observation is to detect a faint object, then the primary consideration for using ACIS will almost surely be determined by secondary objectives such as observing or detecting other objects in the field of view. In this case, the target itself is too weak to have to worry about pileup effects, and, if the observation is concentrating on detection (as opposed to spectroscopy) then very few counts are needed or expected, and so the quality of spectral resolution of the chip at the best focus is irrelevant. In this case other, possibly interesting, targets in the field will determine how to configure the ACIS instrument. For example, if the field contains only very faint ROSAT sources, one would probably select the aimpoint so that the target is focused onto the ACIS-I. With this choice,

the observation also becomes a mini-survey over the rest of the field with the highest sensitivity for detecting sources. Also S3 is moderately far off-axis (see Figure 6.5). You may not wish to risk any loss of data due to the infrequent and transient increases in the background which have a more severe impact on BI CCDs than FI CCDs when such episodes occur. Thus your 6-CCD selection might be ACIS-I together with S2 and S4. Since pileup won't be a problem, you select the timed exposure mode with the optimum frame time in order to avoid introducing any inefficiency. You select the faint format as it provides you with all the information your investigation requires and is the one with which other observers and the *CXC* have the most experience.

On the other hand, if there is a very bright source in the field, not too far (say within 3 arcmin) of your target, considerations change. Suppose you find that the interloper is so bright as to totally saturate telemetry, rendering your observation less efficient. There are several options you could invoke to deal with the situation. One choice might be to specify a roll angle and assure yourself as to the location of the source on the ACIS detector and then use a spatial window to exclude the data. Or, specify the roll angle in such a way so that the interloper's image is not in the field of view.

One might be tempted to specify the roll so that the bright source is on another chip, and then include the data in a spatial window with sufficiently sparse sampling so that the telemetry isn't saturated, but you still get some data. Of course now you have to consider the possibility that these data may be impacted by the effects of pileup. If you can arrange things so that pileup effects on the detected flux from the bright source can be dealt with, you might consider trying to use the ACIS-S aimpoint, with the brighter source's image falling onto S2 at a point near the framestore region - in order to take advantage of the superior energy resolution. Of course if this source is highly absorbed, then it may be more advantageous to arrange the observation with both targets on S3 as the BI energy response extends to lower energies.

As is evident by the discussion above, there are a number of things to consider in planning an observation with ACIS.

6.19.2 Pulse Phased Spectroscopy on a Bright Point Source in a Crowded Field

One of the unique features of ACIS is the capability of performing spectroscopy on sources in crowded fields. Consider the objective of performing pulse-phased spectroscopy of a bright point source in a crowded field. Sup-

pose the pulse period is less than 0.2 s, the shortest nominal frame time. In this case, the continuous clocking mode is called for as this mode provides the necessary time resolution. Since the field is crowded, a roll angle specification will be necessary to avoid source confusion in the one dimension in which there is no spatial resolution. Format choices, and other options, may be dominated by considerations of the telemetry rate. In general, there are very few individual sources that are bright enough to saturate telemetry, but it is the flux from all the objects in the field, together with the background, that is the determining factor.

Chapter 7

High Resolution Camera (HRC)

7.1 Introduction and Instrument Layout

The High Resolution Camera (HRC) is a microchannel plate (MCP) instrument comprised of two detectors, one optimized for imaging (HRC-I), and one (HRC-S) serves as a readout for the Low Energy Transmission Grating (LETG) discussed in Chapter 9. The HRC-I provides the largest field-of-view ($\sim 30' \times 30'$) of any detector aboard *Chandra*, and its response extends to energies below the sensitivity of the ACIS (Chapter 6), albeit without comparable spectral resolution. The time resolution of the HRC detectors (16 μ sec) is the best on the observatory.

A schematic of the HRC layout is shown in Figure 7.1, and a summary of the characteristics is given in Table 7.1. A cross-section of the HRC-S layout, the relationship to the optical axis and to the LETG Rowland circle is shown in Figure 7.2.

The HRC is a direct descendant of the Einstein (Giacconi *et al.* 1979) and ROSAT High Resolution Imagers (HRIs) (David *et al.* 1996). The ROSAT HRI had the same coating (CsI) as the HRC.

The Instrument Principal Investigator is Dr. Stephen S. Murray of the Smithsonian Astrophysical Observatory.

7.2 Basic Principles

Figure 7.3 illustrates the features of the HRC MCPs. X-rays enter through an UV/Ion shield, necessary in order to reduce/avoid signals from UV light,

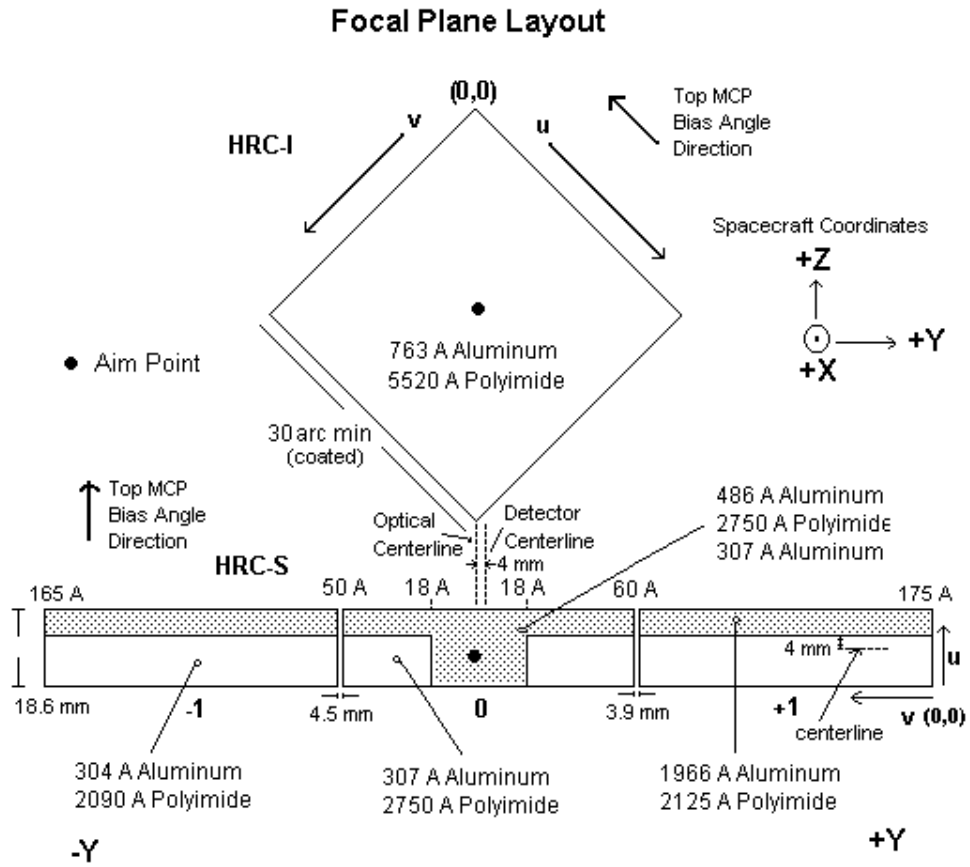


Figure 7.1: A schematic of the HRC focal plane geometry as viewed along the optical axis from the telescope towards the focal plane.

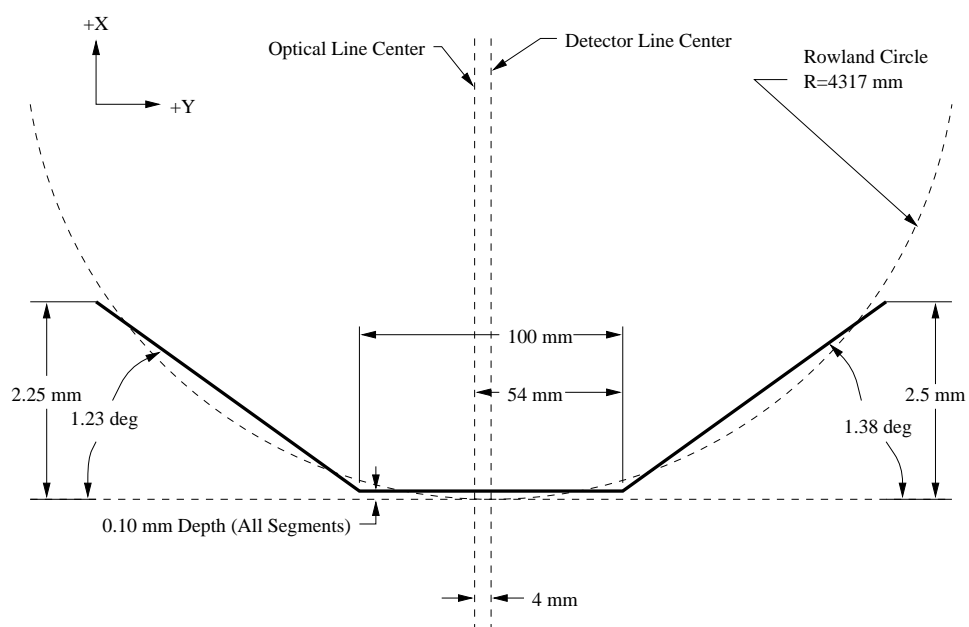


Figure 7.2: A schematic cross-section of the HRC-S MCP (not to scale). The HRC-S is shifted 0.1 mm forward of the tangent plane, so the Rowland circle intersects each segment at two points.

Table 7.1: HRC Parameters

Focal Plane Arrays		
HRC-I:	CsI-coated MCPpair	90 × 90 mm coated (93 × 93 mm open)
HRC-S:	CsI-coated MCPpairs	3-100 × 20 mm
Field of view	HRC-I:	~ 30 × 30 arcmin
	HRC-S:	6 × 99 arcmin
MCP Bias angle:		6°
UV/Ion Shields:	HRC-I:	5520 Å Polyimide, 763 Å Al
	HRC-S:	
	Inner segment	2750 Å Polyimide, 307 Å Al
	Inner segment “T”	2750 Å Polyimide, 793 Å Al
	Outer segment	2090 Å Polyimide, 304 Å Al
	Outer segment (LESF)	2125 Å Polyimide, 1966 Å Al
Spatial resolution	FWHM	~ 20μm, ~ 0.4 arcsec
	HRC-I: pore size	10μm
	HRC-S: pore size	12.5μm
	HRC-I: pore spacing	12.5μm
	HRC-S: pore spacing	15μm
	pixel size (electronic readout)	6.429μm [0.13175 arcsec pixel ⁻¹]
Energy range:		0.08 – 10.0 keV
Spectral resolution	$\Delta E/E$	~ 1 @1keV
MCP Quantum efficiency		30% @ 1.0 keV 10% @ 8.0 keV
On-Axis Effective Area:	HRC-I, @ 0.1 keV	5 cm ²
	HRC-I, @ 1 keV	227 cm ²
Time resolution		16 μsec
Limiting Sensitivity	point source, 5 count detection in 3 × 10 ⁵ s (power law spectrum: α = 1.4, N _H = 3 × 10 ²⁰ cm ⁻²)	7 × 10 ⁻¹⁶ erg cm ⁻² s ⁻¹
On-orbit quiescent background (prior to ground processing)	HRC-I	9 × 10 ⁻⁶ cts s ⁻¹ arcsec ⁻²
	HRC-S	1.8 × 10 ⁻⁴ cts s ⁻¹ (res. elm.) ⁻¹ (0.07 Å × 0.1 mm)
Intrinsic dead time		50 μs
Constraints:	telemetry limit	184 cts s ⁻¹
	maximum counts/observation/aimpoint	450000 cts
	linearity limit (on-axis point source)	
	HRC-I	~ 5 cts s ⁻¹ (2 cts s ⁻¹ pore ⁻¹)
	HRC-S	~ 25 cts s ⁻¹ (10 cts s ⁻¹ pore ⁻¹)

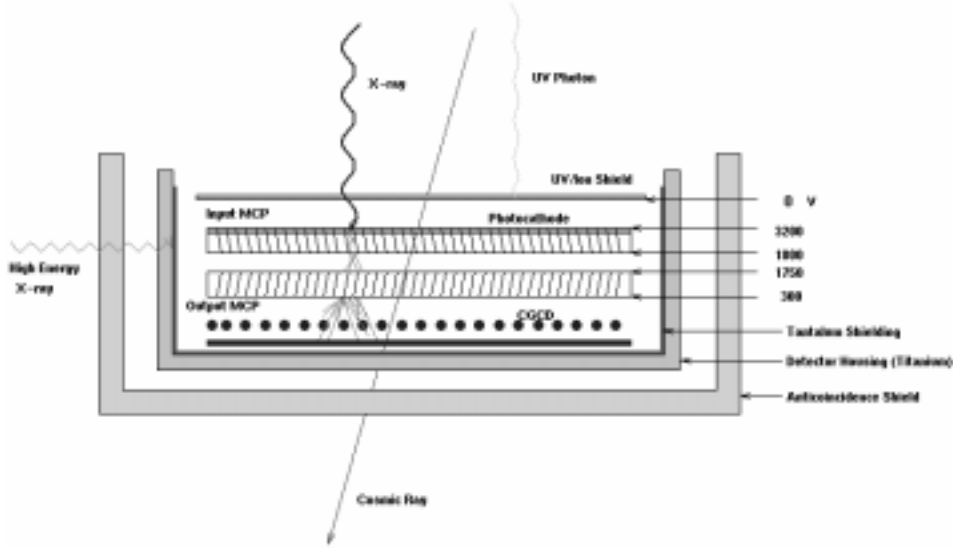


Figure 7.3: A schematic of the HRC Micro-channel-Plate detector.

ions, and low energy electrons. Most of these X-rays are then absorbed in the CsI-coated walls of the first (input) of two consecutive MCPs. The axes of the millions of tubes that comprise the input and output MCPs are not parallel to the optical axis but are canted (“biased”) at an angle of 6° , but in opposite directions as shown. This bias is introduced to improve the probability of an interaction. The CsI coating serves to enhance the photoemission over that from a bare MCP. The resulting photoelectrons are then accelerated by an applied electric field. The next interaction with the walls releases several secondary electrons and so on until a cascade of electrons is produced.

One purpose of the second (output) MCP is to provide additional gain. In addition, reversing the direction of the second MCPs bias angle with respect to the first removes a clear path for positive ions, and hence reduces the possibility of (positive) ion feedback - wherein an accelerated ion moving in the opposite direction as that of the electrons ends up causing the release of electrons and starts the process all over again.

The electron cloud — typically about 2×10^7 electrons per photon — that emerges from the output MCP is accelerated towards a position-sensitive charge detector. The HRC employs two types of charge detectors: HRC-I uses a crossed grid charge detector; the HRC-S uses a hybrid where one

axis is comprised of wires, while the other has gold lines deposited on a ceramic substrate. Adjacent wires (or lines) are resistively connected and every eighth wire is attached to a charge-sensitive amplifier, referred to as a “tap”, as illustrated in Figure 7.4.

The X-ray position is determined by calculating the centroid of the charge cloud exiting the rear MCP via the “three tap algorithm”. In short, the three tap algorithm determines the charge cloud centroid using a combination of digital and analog electronics and off-line processing. Fast discriminators and logic circuits first determine a “coarse” position, which is based on the amplifier with maximum detected charge. Analog switches then select the three amplifiers centered on that coarse position and steer them to analog to digital converters. The coarse position and 3 digitized values are then telemetered to the ground and used off-line to calculate the event position. This process is performed for each axis. The reconstructed X-ray position can then be written as the sum of a coarse position and a charge centroid term centered on the coarse position:

$$pos = cp_i + \left(\frac{Q_{cp_{i+1}} - Q_{cp_{i-1}}}{Q_{cp_{i-1}} + Q_{cp_i} + Q_{cp_{i+1}}} \right) \times \Delta \quad (7.1)$$

where cp is the coarse position, $Q_{cp_{i+1}}$ is the charge measured on the cp_{i+1} tap, and Δ is the distance between taps. Since the charge cloud extends beyond the two outer taps, each of the outer amplifiers underestimates the amount of charge needed to calculate the true centroid. For an event perfectly centered on the middle tap, the amount of charge missed by the two outer taps cancel in the equation. If however, the event position is not over the center of a tap, the fractional amount of missing charge is different and produces a small systematic error in the reconstructed position. The small systematic positional error combined with the coarse position logic produce “gaps” in the HRC images. These gaps are perfectly aligned with the detector axes and correspond to positions exactly half-way between amplifier taps. Since the gaps are systematic, they can and are removed in data processing.

For more details concerning the HRC see Murray & Chappell (1989) and Zombeck *et al.* (1995) and references therein.

7.2.1 Aimpoints

The aimpoints are the positions on the instrument where the flux from an on-axis point source is placed. There are two nominal aimpoints as indicated in Figure 7.1 - one at the approximate center of the HRC-I, and

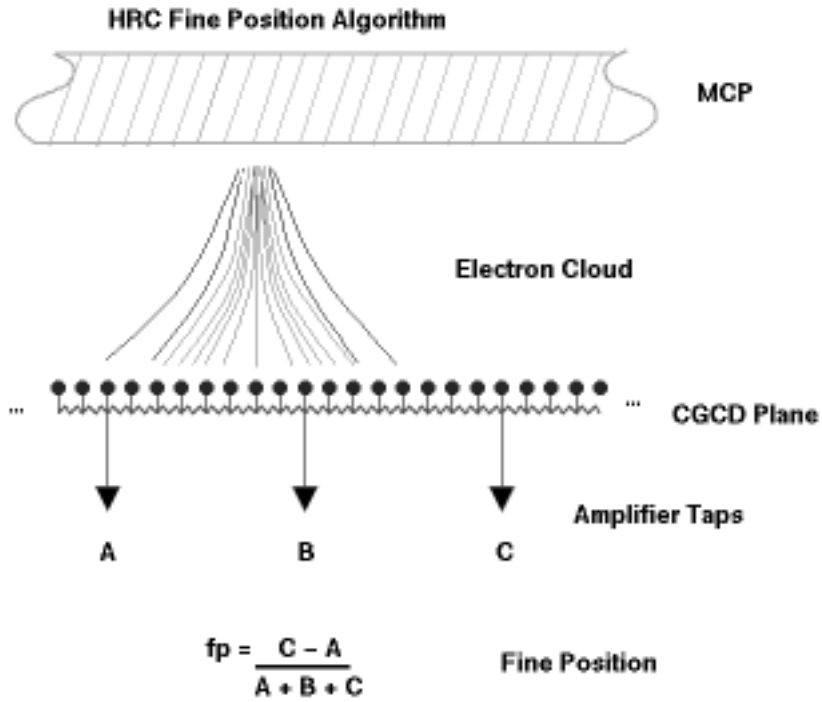


Figure 7.4: Schematic representation of event position determination for one axis of the crossed grid charge detector (CGCD). The electron cloud is divided between several amplifiers. The position of the event relative to the central coarse position is calculated from the difference between the signals on either side of the coarse position divided by the sum of the three signals.

the other slightly off-center on HRC-S. The HRC-S aimpoint Z-offset places the LETG-dispersed image along the centerline of the two white rectangles in the diagram. The HRC-S aimpoint Y-offset is slightly off-center, so that the boundaries between the three HRC-S segments correspond to different wavelengths of the grating-dispersed spectrum (See Chapter 9 for details).

7.3 Dither

The spacecraft is dithered during all observations in a Lissajous figure. For observations with the HRC, the dither amplitude is 40 arcsec peak-to-peak. Dither serves the purpose of smoothing pixel-to-pixel variations in the response. The dither also provides some exposure in the gaps between the HRC-S elements. The effects of dither are removed during high-level ground processing of the data.

7.4 Spatial Resolution & Encircled Energy

Imaging with the HRC is best performed with the HRC-I because of the much lower background (section 7.8) and larger field of view. The intrinsic PSF of the HRC is well modeled by a gaussian with a FWHM of $\sim 20\mu\text{m}$ (~ 0.4 arcsec). The HRC pixels, determined by the electronic readout and *not* the pore size, are $6.429\mu\text{m}$ (0.13175 arcsec). The HRC response is thus well matched to the intrinsic HRMA resolution (Chapter 4).

Approximately 90% of the encircled energy lies within a 14 pixel diameter region (1.8 arcsec) from the center pixel for the observation of AR Lac shown in Figure 7.5. The measured PSF is as good or better than the simulations because a very conservative pre-flight estimate of the aspect solution was used in the simulations.

The imaging resolution of the HRC-I/HRMA combination degrades off-axis for two reasons: the HRMA PSF increases with increasing off-axis angle and the deviation increases between the flat HRC-I detection surface and the curved HRMA focal surface. The off-axis imaging behavior of the HRC-I/HRMA is shown in Figure 7.6. The nominal best-focus of the HRC-I is chosen to provide the best image quality in the center of the field-of-view.

7.5 Energy Resolution

The pulse-height amplitude of each event is telemetered. However, the energy dispersive resolution is poor. Figure 7.7 shows the HRC-I pulse height

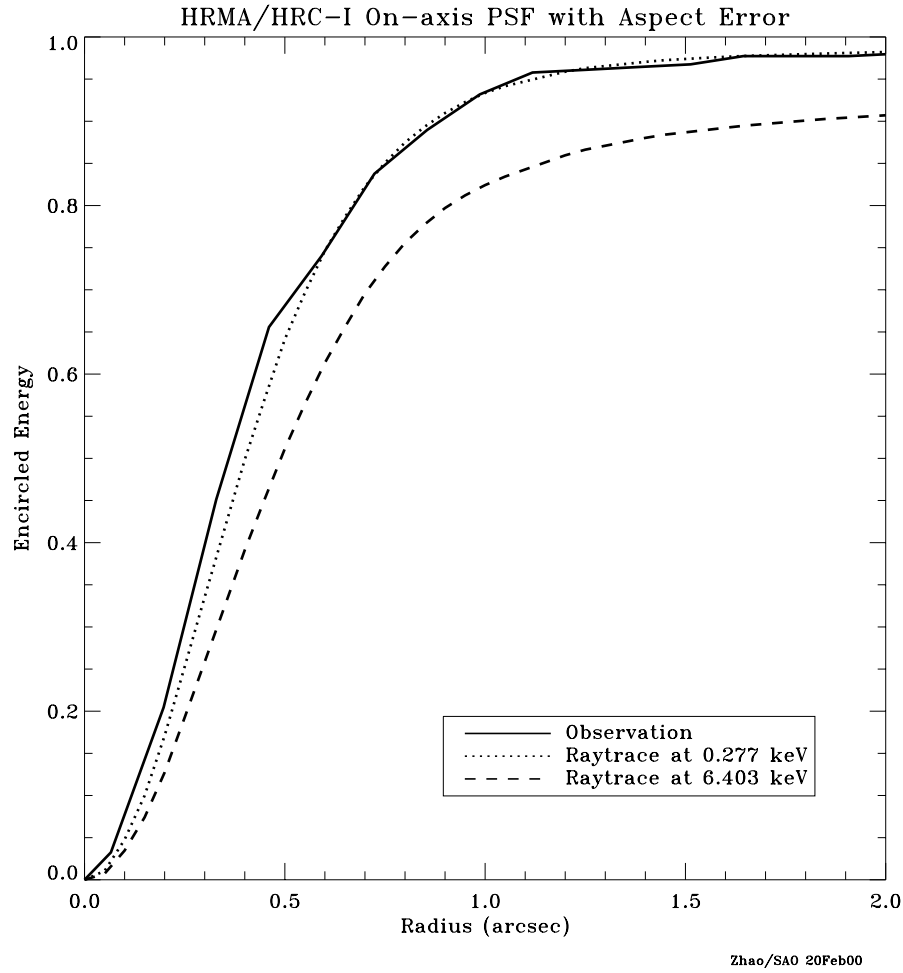


Figure 7.5: The predicted and observed fractional encircled energy as a function of radius for an on-axis point source observed with the HRMA/HRC-I. The calculations (at two energies, 0.277 keV and 6.40 keV) include a very conservative estimate of the aspect solution ($\text{FWHM} = 20\mu\text{m}$ ($0.41''$)). Flight data from an observation of AR Lac are also shown.

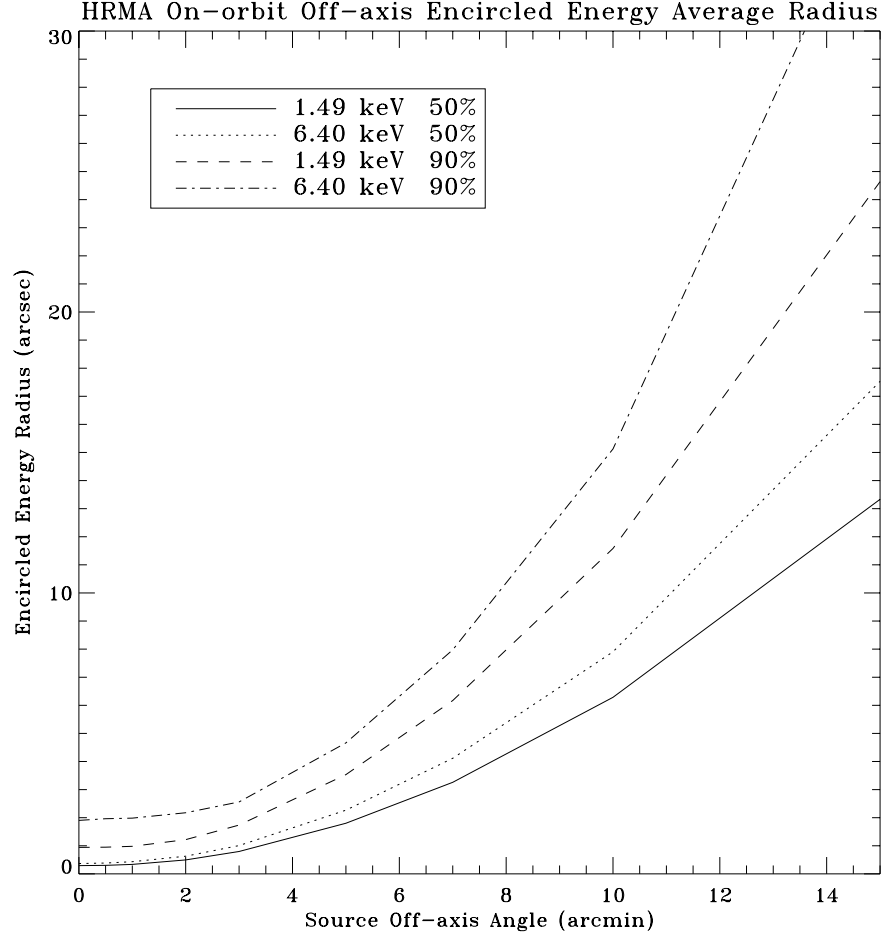


Figure 7.6: Encircled energy as a function of source off-axis angle for 50% and 90% encircled energy for 1.49 and 6.40 keV for the combined HRMA/HRC-I. A conservative contribution from the aspect solution is included ($\text{FWHM} = 20\mu\text{m}$ ($0.41''$)). A plot for the combined HRMA/HRC-S would be almost identical since the PSFs of the two instruments are virtually identical and independent of off-axis angle.

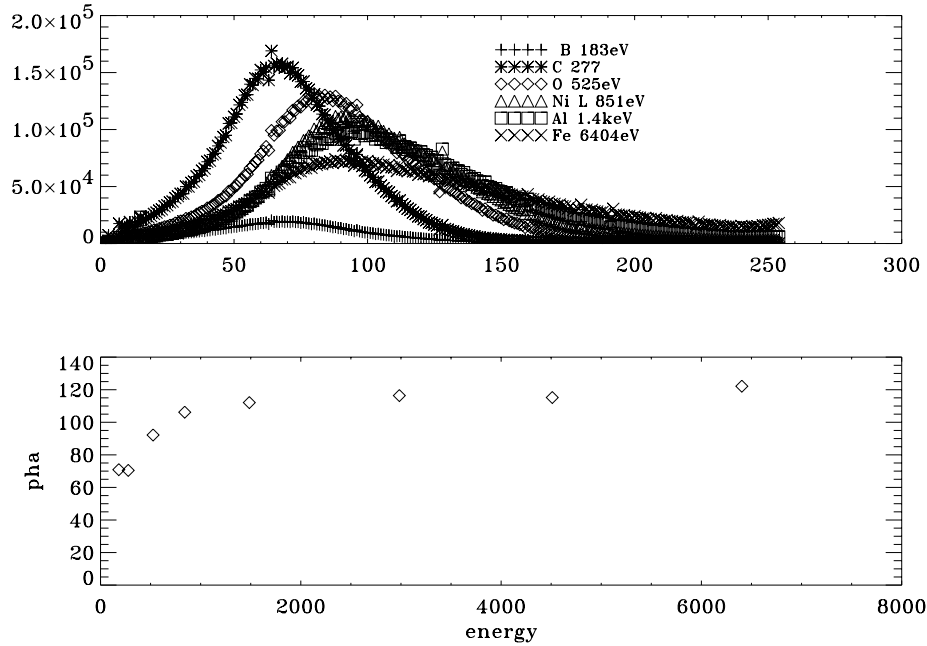


Figure 7.7: The pulse height versus energy for the HRC-I detector and the centroid of the pulse height distribution versus energy. This data set was obtained at SAO during flat field, normal-incidence-illumination tests. The voltage settings have been changed in-flight and thus the applicability of these data is questionable and they are presented here for purposes of illustration only.

distributions for six energies obtained during sub-assembly calibration. The pulse-height distributions for the HRC-S detector are somewhat narrower. There is significant spatial variation in the gain across both instruments.

7.6 UV/Ion Shields

The placement, composition, and thickness of the various UV/ion shields (filters) are shown in Figure 7.1. The transmission of the HRC-I UV/ion-shield is shown in Figure 7.8. The transmission of the various HRC-S UV/Ion shields are shown in Figure 7.9.

The shields are useful in suppressing out-of-band (outside the x-ray band) radiation from the ultraviolet through the visible. The detector re-

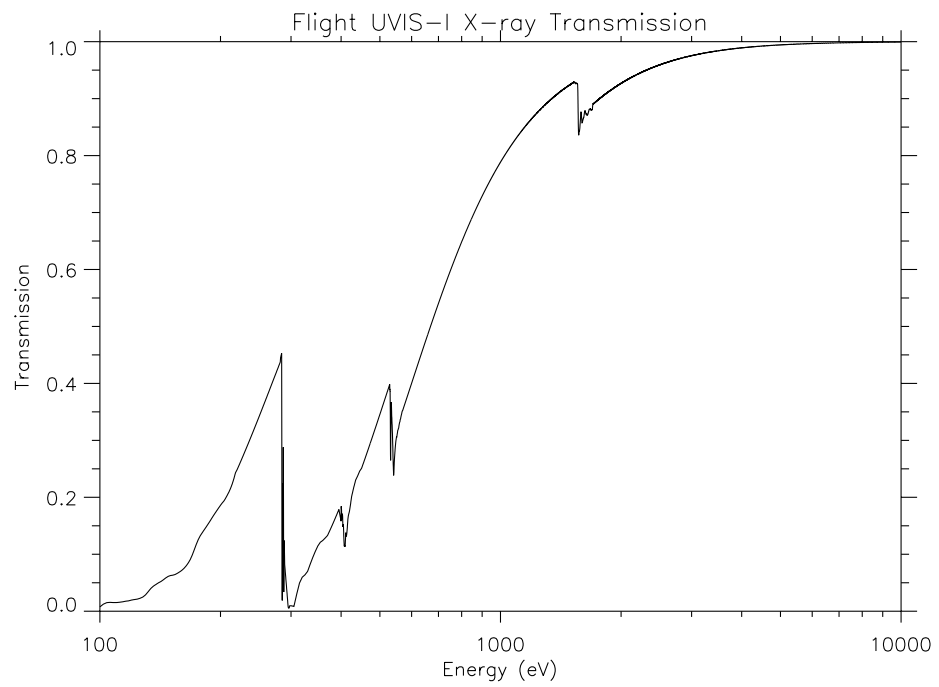


Figure 7.8: The transmission of the HRC-I UV/Ion shield as a function of energy.

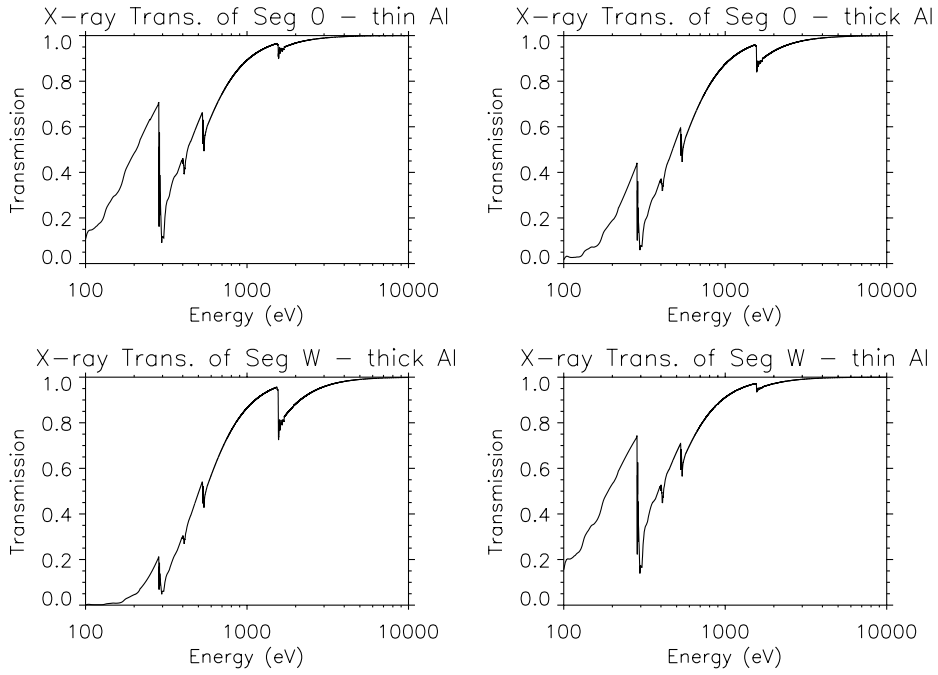


Figure 7.9: The transmissions of the HRC-S UV/Ion shields for (upper left) the thin Al inner segment (seg 0); (upper right) the thick Al inner segment (seg 0, “T”); (lower left) the thick Al outer segments (“wings” or seg +1,-1); (lower right) the thin Al outer segments (“wings” or seg +1,-1). See Figure 7.1 for a sketch of the shield geometry.

sponse to out-of-band light for an object in its field-of-view is a possible source of unwanted signal. Suppressing out-of-band radiation is particularly important for observing sources which have bright XUV and UV fluxes. The HRC has strongly reduced sensitivity in this spectral region, as shown in Figure 7.10. As part of the in-flight calibration program the bright A star Vega (A 0V, U=0.02, B=0.03, V=0.03) was observed with both the HRC-I and HRC-S. The predicted count rate for HRC-I is 7×10^{-4} cts s^{-1} . The observed upper limit is 1×10^{-3} cts s^{-1} . The image of Vega was also placed on three regions of the HRC-S - the inner segment "T", the thin aluminum inner segment, and on one of the thin aluminum outer segments. The predicted count rates are 1, 400, and 2000 cts s^{-1} , respectively. The corresponding observed rates are 0.2, 240, and 475 cts s^{-1} . Sirius was observed with the HRC-S/LETGS in order to obtain a soft X-ray spectrum of Sirius B (white dwarf) and Sirius A (A1V, V=-1.46, B-V=0.01) was seen in 0 order at about the expected count rate. Based upon these sets of observations, the UV/Ion shields are performing as designed. Other stars will be observed as part of future calibration activities.

Scattered UV, far-UV (FUV), and extreme-UV (XUV) light from the Sun or bright Earth may cause a background strongly dependent on viewing geometry. The spacecraft was designed to limit the contribution from stray scattered radiation to 0.01 cts $cm^{-2} s^{-1}$ on the HRC. The imaged components of scattered radiation are dependent on the solar cycle, but are at most ~ 0.01 cts $cm^{-2} s^{-1}$ for most lines of sight.

7.7 Quantum Efficiency and Effective Area

The quantum efficiency of the HRC detector is the product of the appropriate UV/Ion shield transmission and the quantum efficiency of the CsI coated MCP. The filter transmissions at x-ray energies are shown in Figures 7.8 and 7.9. The models of the quantum efficiency of the coated MCPs are shown in Figure 7.11. Pre-flight flat field measurements show a 10% variation in the QE across the HRC-I. The HRC-S also exhibits QE variations of the same magnitude, where the complex structure of the HRC-S UVIS contributes to the spatial variations.

The combined HRMA/HRC-I and -S effective areas - the product of the HRMA effective area, the quantum efficiency of the HRC and the transmission of the appropriate UV/Ion shield - are shown, integrated over the point spread function, in Figure 7.12. Analysis of data from in-flight calibrations is ongoing. Preliminary indications suggest that the pre-flight estimates shown

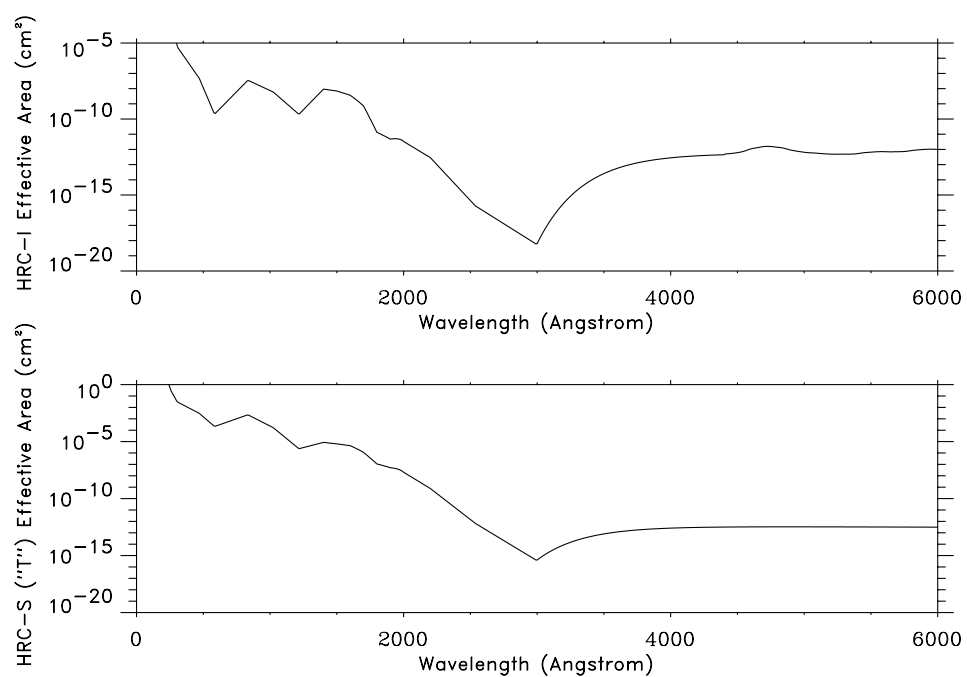


Figure 7.10: The HRC-I (top) and the center section of the HRC-S (bottom) UV/Ion shield effective area as a function of wavelength.

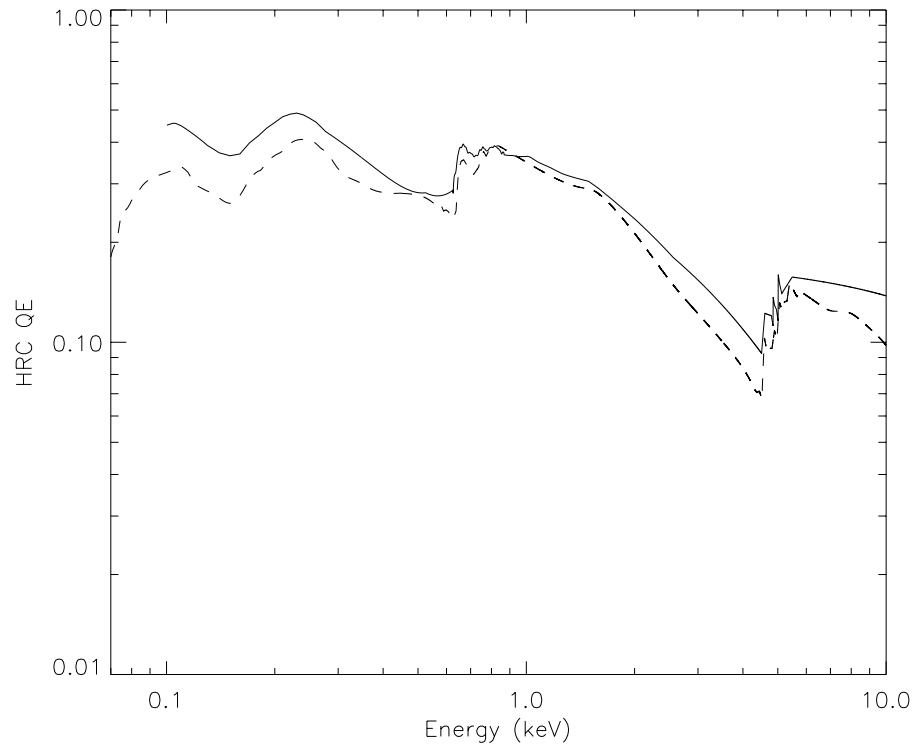


Figure 7.11: The HRC-I (solid) and HRC-S (dashed) CsI-coated MCP efficiencies as a function of energy. These data are corrected for the converging HRMA beam.

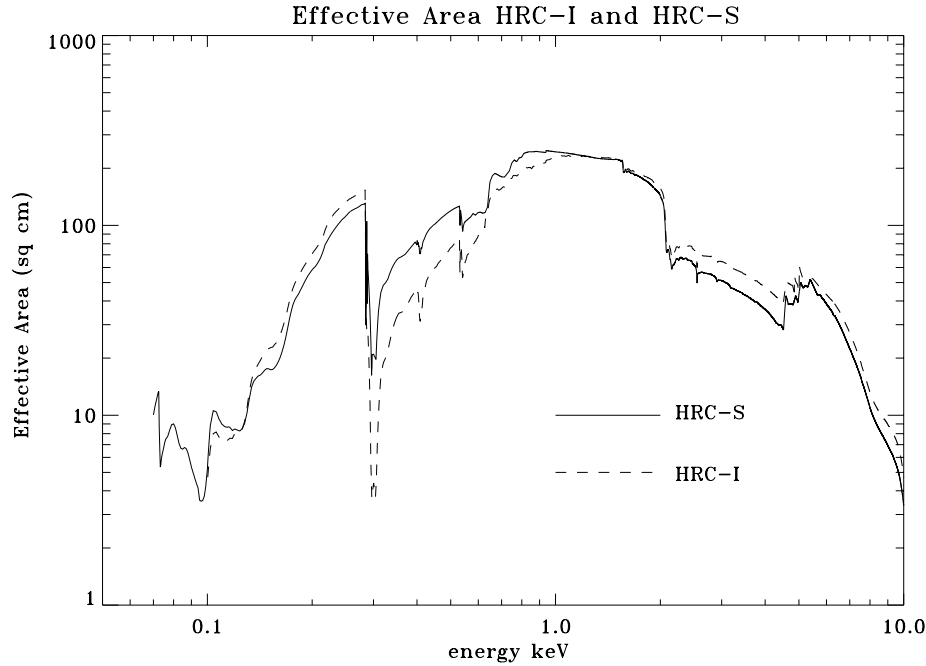


Figure 7.12: The predicted HRMA/HRC-I (solid) and the center section of the HRMA/HRC-S (dashed) effective area as a function of energy, integrated over the full PSF. Absorption edges are due to the iridium on the mirror, the CsI MCP coating, and the polyimide/Al UV/Ion shield.

in Figure 7.12 are valid for $E > 0.277$ keV. In-flight calibrations indicate that the long wavelength QE of the HRC-S may be considerably lower than the pre-flight models currently in use.

7.8 On-Orbit Background

7.8.1 HRC-I

The HRC-I counting rate on orbit is about 250 cts s^{-1} total. These are mostly cosmic ray events which are detected in the anti-coincidence shield (AC). The observed cosmic ray event rate is about twice what was assumed pre-launch and corresponds to $\sim 2 \text{ cts cm}^{-2} \text{ s}^{-1}$. Because this rate of 250 cts s^{-1} saturates the telemetry limit for HRC of $184 \text{ events sec}^{-1}$, the on-board veto function has been activated. This reduces the valid event

rate to about 50 c/s over the field yielding a background rate of 10^{-5} cts s^{-1} arcsec $^{-2}$. The background is generally flat, or at least smoothly varying over the field with no more than a 20% difference between the center (higher) and edges (lower) of the detector. Note, the total event rate remains unchanged, but events where the AC veto is active are no longer processed as valid events and do not enter the telemetry data stream. Before launch the expected rate, after vetoing the effects of cosmic rays, was 10-20 cts s^{-1} composed of mainly the internal rate of the MCPs (10-15 cts s^{-1}), and a small contribution from cosmic rays due to AC inefficiency. Thus there is perhaps an additional background in the HRC-I that is not understood. However, for point source detection and exposure times of 100 ks or less the background is virtually negligible. For studies of extended objects of low surface brightness, however, even this relatively low rate can become significant depending on the specific details of the feature.

Techniques are under investigation to further reduce the non-x-ray background in the HRC-I. These techniques using various screening schemes in ground processing. These efforts have recently reached a point where it is clear that an effective ground screening processes is capable of reducing the total valid event background by about 40% from the unscreened level. The corresponding reduction in x-ray events is much less than 10% (perhaps only $\sim 1\%$). The screening is also successful in removing a “ghost” image effect (see section 7.10). As a result of these studies, the screening algorithm has been given over to the Data Systems Group for implementation in the on-ground data-processing pipelines. The HRC Team continues to work on optimizing the parameter values of the event screening technique. It appears that the screening also “flattens” the background across the detector. At present, however, more experience with the data screening is required before definitive conclusions are reached.

7.8.2 HRC-S

The anti-coincidence shield of the HRC-S is not working because of a timing error in the electronics. The error is not correctable. As a result the event rate is very high and exceeds the total telemetry rate limit. To cope with this problem the HRC Team has defined a “spectroscopy region” which is about 1/2 of the full width and extends along the full length of the HRC-S detector. The spectroscopy region is ~ 10 mm x 300 mm in size. The region is imposed by using the edge blanking feature of the electronics. With this change, the quiescent background rate is about 85 cts s^{-1} .

As with the HRC-I, this background can be further reduced in ground data processing by using pulse height filtering that preferentially selects X-rays over the cosmic ray events. A reduction in background of a factor of about three for dispersed spectra is possible. Thus there are two relevant background rates for the HRC-S: a telemetry rate of 85 cts s⁻¹ and a post-processing rate for calculating signal to noise. The latter is discussed in detail in Chapter 9 (see especially Figure 9.26).

7.8.3 Temporally Variable Background

Both the HRC-I and HRC-S experience occasional fluctuations in the background due to charged particles. These times of enhanced background are typically short (a few minutes to a few tens of minutes) and are anywhere from a factor of 2 to a factor of 10 over the quiescent rates. The increased background appears to be uniformly distributed over the detector and introduces no apparent image artifacts. On the average it seems that no more than about 20% of the observing time is affected by these events, and they are easily recognized in the secondary science rate data and so can be filtered out if desired. An example of this behavior is shown in Figure 7.13.

7.9 Source Sensitivity

Examples of the minimum flux detectable (5 count source) by the HRC-I in a 1 arcsec radius circle on-axis and for a 20" diameter extended source are shown as a function of observing time and spectral form in Figure 7.14.

7.10 Instrument Anomalies

There is a very faint “ghost” image displaced 10 arcsec on one side of every source in the field of view in the HRC-I. An event processing algorithm is currently under development by the IPI team to reduce or eliminate this “ghost” image. The intensity of the “ghost” is < 3% of the source signal without filtering and < 0.1% with filtering. The same feature is present in the HRC-S, but at a much reduced intensity.

7.11 Calibration

Calibration of the HRC included laboratory calibrations, a system-level ground calibration with the HRMA and HRC at the X-ray Calibration Fa-

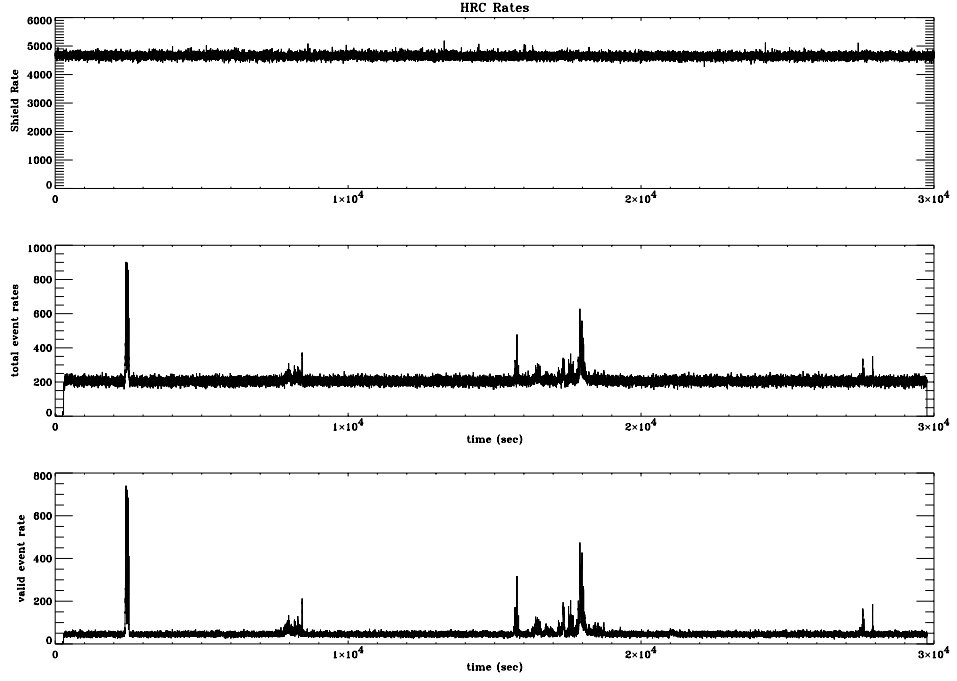


Figure 7.13: An example of the background variability during a ~ 30 ks HRC-I observation of the SNR G21.5-09 taken on 1999-10-25. The total event rate and the valid event rate show correlated bursts up to $\approx 800 \text{ cts s}^{-1}$, the data in the bursts are uniformly distributed over the detector. The anti-coincidence shield exhibits no correlated enhancements; the shield rate is approximately constant at $\sim 4500 \text{ cts s}^{-1}$. The total rate and the valid rate differ by $\approx 200 \text{ cts s}^{-1}$ due primarily to cosmic ray events that are vetoed and don't appear as valid events in the telemetry.

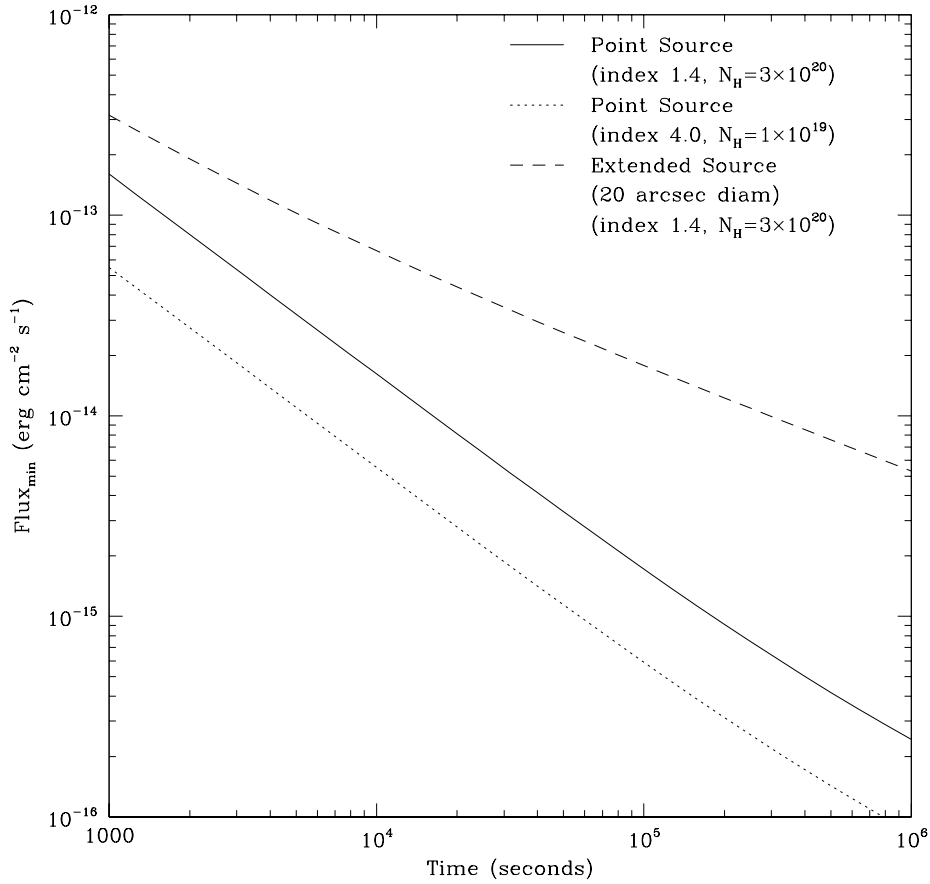


Figure 7.14: Predicted HRC minimum detectable flux (5 counts, 0.08-10.0 keV) on axis in a $1''$ radius circle plotted against exposure time. Three curves are shown, two for a point source with a power law plus cold absorption: photon index 1.4, $N_{\text{H}} = 3 \times 10^{20} \text{cm}^{-2}$ (solid line); photon index 4.0, $N_{\text{H}} = 1 \times 10^{19} \text{cm}^{-2}$ (dotted line). The dashed line is for a 20 arcsec diameter diffuse extended source (3σ) with the first spectral form. The background is assumed to be $9 \times 10^{-6} \text{cts arcsec}^{-2} \text{s}^{-1}$.

cility (XRCF) at MSFC, and on-orbit calibration using celestial and on-board radioactive X-ray sources. The on-orbit calibration of the HRC is an on-going activity. Furthermore, the radiation-induced damage to ACIS extended the planned calibration schedule for the HRC, so portions of the HRC calibration analysis have not yet been completed. All calibration data are, or will be, described in detail on our website:

<http://asc.harvard.edu>

under the link “Calibration” (or directly: <http://asc.harvard.edu/cal>).

The user is urged to consult the WWW site and its pointers for the latest information.

7.12 Operational considerations and constraints

In addition to the general Chandra observatory level constraints (Chapter 3), there are a handful of HRC-specific considerations and constraints that must be taken into account in planning an observation.

7.12.1 Total Count limits

Both the gain and the quantum efficiency are adversely affected by the total amount of charge extracted from the MCP at the point of extraction. To minimize such effects, the high voltage on the detector is lowered during passage through the radiation belts and at times of very high particle radiation. To limit the impact from x-ray sources themselves, a 450,000 count limit distributed over the dither pattern from an on-axis source at a given aimpoint has been imposed. *Users anticipating to exceed this value should so note in the comments section of the RPS form when submitting their proposal.* In this case, the CXC will establish new aimpoints as necessary. Offsets in the pointing may be imposed, if necessary, in order to limit the accumulated dose to a given region of the MCP.

7.12.2 Count rate limits

There are two counting rate limits:

Telemetry Limit

The maximum telemetered counting-rate is 184 cts s^{-1} . This is a limitation on the total count rate received over the full field-of-view rather than for

one individual source within the field. It is possible to exceed this limit and to subsequently correct the total count rate by using the secondary science rates, which keeps track of the actual detected rate, to determine the deadtime correction. The resulting deadtime fraction increases rapidly with valid event rates above 184 cts s^{-1} . For example, at 200 cts s^{-1} the deadtime fraction is 8%, at 250 cts s^{-1} 26%, and at 300 cts s^{-1} 39%. In the following we list some methods of dealing with situations where the telemetry limit is exceeded.

1. *Bright target:*

- Insert either the LETG or the HETG as appropriate and perform the investigation viewing the zeroth-order image. This solution may be so dramatic as to substantially increase the required observing time.
- Offset point. To be effective, this solution may result in substantially reduced spatial resolution.

2. *Bright nearby source*

- Depending on the proximity, an appropriate choice of roll angle and/or aim point can position the problematical source(or sources) off the detector. Note that in order to limit the use of mechanical systems, a request for an off-nominal aimpoint is discouraged if an equally scientifically useful alternative is feasible.
- Request a rectangular window for the on-board data so that events produced by the nearby bright source (or sources) do not contribute to the telemetry limit.
- Select a roll angle which allows use of the HRC shutters to block the light from a bright source near the edge of the field of view. Observers should contact the *CXC* to investigate this possibility and enter their requirements in the Comment field of the RPS form. This request should only be made if all other proposed solutions - included accomplishing the objective with a different instrument - fail.

There are of course, other combinations and situations that can lead to telemetry saturation - numerous faint sources on the field, a too-bright extended source, etc.

Linearity limit

The HRC-I was found to be linear for incident photon rates up to ~ 2 cts s⁻¹ pore⁻¹, which translates to ~ 5 cts s⁻¹ for an on-axis point source (see Kenter *et al.* 1997, Figure 7). The HRC-S was found to be linear for rates five times greater. (We note that in the case of the HRC-I there is no evidence that linearity does not extend beyond the stated limit, only that no data were taken for higher incident fluxes.)

It is important to be aware that *avoiding telemetry saturation does not guarantee that linearity limits are not exceeded*. There are only three approaches to assure oneself that the the linearity limit is not exceeded:

- Offset point to smear the image out.
- Insert a transmission grating to reduce the flux and offset point (if also necessary).
- Defocus – only mentioned for completeness – the option is not recommended or encouraged.

7.13 Output data

Housekeeping Data:

Information about the health and configuration of the HRC instrument, known as housekeeping data, is telemetered to the ground every 2.05 seconds when the HRC is at the focus of the telescope.

Secondary Science Rate Data:

The HRC has three rate scalars on-board that measure the number of events per second that trigger the MCPs (Total Event Rate), the number of triggers per second that are “good” events (Valid Event Rate), and the number of events per second that occur in the anticoincidence shield (Shield Event Rate).

Primary Science Data:

The information concerning an X-ray event, is stored in the format outlined in Table 7.2. A brief explanation of these items is given below.

- Coarse positions U and V are the numbers of the U and V amplifiers that have the largest signal amplitudes.

- The Scale Factor gives the value of the multiplier (1x, 2x , or 4x) used to boost the amplitude of low amplitude events; this allows the 12-bit fine position ADC's to represent a 14-bit range.
- V1, V2, V3, U1, U2, U3 ADC values are the amplitudes of the signals from the three U and three V amplifiers that are centered on the U and V coarse positions. They are used for the fine position calculation.
- The pulse height is the value of the sum of all the detector's U and V amplifiers.
- The veto status records the detection of events of various kinds, as listed below. The HRC may be operated with some (or all) of the veto functions enabled with the corresponding event rejection occurring on-board. This results in reduced telemetry rates for a specific observation. The veto elements are:
 1. edge/center-blank events (x-ray events are indicated to be either outside or inside a specified rectangle)
 2. wide events (the width of the charge cloud is larger than the pre-selected width for a valid event)
 3. shield events (an event has been detected in the anti-coincidence shield that is in coincidence with a detector event)
 4. upper-level discriminator (the event amplitude exceeds the upper level discriminator)
 5. 1 bit spare
- The Detector ID identifies whether the event is from the HRC-I or HRC-S (note however that only one of the detectors can be sending event data at a given time).
- Sub Frame ID is the 3 least significant bits of the science frame in which the event occurred. It is used with the Event Time Tag to establish the actual time that the event occurred.
- Event Time Tag is the number of 15.625 microsecond clock ticks from the start of the science frame at which the event occurred.

Table 7.2: HRC Event Data Format

No. bits	Use
8	V coarse position
6	U coarse position
2	scale factor
12	$V1$
12	$V2$
12	$V3$
12	$U1$
12	$U2$
12	$U3$
8	pulse height
10	veto status
3	sub-frame address
1	detector ID
18	event time tag
128	Total number of bits.

7.14 Observing with HRC - the input parameters

For many observations, other than specifying the instrument, the exposure time, and the target coordinates there are no other parameters that one needs to provide. There are, however, a number of optional parameters that one might wish to consider invoking if the proposed observation seems to run into any of the HRC constraints discussed in section 7.12. The observer is encourage to make use of the various tools provided when planning an observation as discussed in Chapter 12 and not to forget to include the background when estimating sensitivity.

7.15 REFERENCES

The following is a list of publications, documents, and memos containing information about the the High Resolution Camera (HRC). The most current information can be found on the HRC Project WWW page:

<http://hea-www.harvard.edu/HRC/HomePage.html>.

General:

David, L.P., Harnden, F.R. Jr., Kearns, K.E, and Zombeck, M.V. “The ROSAT High Resolution Imager (HRI) Calibration Report”, revised (1999).

http://hea-www.harvard.edu/rosat/rsdc_www/hr

Fraser, G., “X-ray Detectors in Astronomy” , 1989, Cambridge University Press.

Giacconi, R., et al., 1979, Ap. J., 230, 540.

Murray, S.S., Chappell, J.H., Elvis, M.S., Forman, W.R., Grindlay, J.E., Harnden, F.R., Jones, C.F., Maccacaro, T., Tananbaum, H.D., Viana, G.S., Pounds, K.A., Fraser, G.W., and Henry, J.P., “The AXAF High Resolution Camera (HRC) and its use for observations of Distant Clusters of galaxies” Astro. Lett. Comm., 26, 113-125, 1987.

Murray, S.S., et al., “In-flight Performance of the Chandra High Resolution Camera”, SPIE, 4012, 2000.

Zombeck, M.V., Chappell, J. H , Kenter, A, Moore, R., W., Murray, S. S., Fraser, G.W., Serio, S., “The High Resolution Camera (HRC) on the Advanced X-ray Astrophysics Facility (AXAF)”, Proc. SPIE, 2518, 96, 1995.

http://hea-www.harvard.edu/hrc_art/hrc_spie/hrcspie0.html

Position modeling and de-gap corrections

Murray, S.S., Chappell, J.H., 1989, SPIE 1159, 460-475. “Position Modeling for the AXAF High resolution Camera (HRC)”

Kenter, A., “Degap as a Transformation of Probability Distribution Problem”, 3/1/99.

<http://hea-www.harvard.edu/HRC/calib/degap.ps>

Count rate limitations and linearity

Juda, M and Dobrzycki, A, “HRC Deadtime and Telemetry Saturation”, 6/18/99.

http://hea-www.harvard.edu/~juda/memos/tlm_sat.html

Kenter, A.T., Chappell, J.H. Kobayashi, K., Kraft, R.P., Meehan, G.R., Murray, S.S., Zombeck, M.V., Fraser, G.W., Pearson, J.F., Lees, J.E., Brunton, A.N. and Pearce, S.E. Barbera, M., Collura, A., Serio, S., “Performance and Calibration of the AXAF High Resolution Camera I ” SPIE 3114, 1997.

HRC Calibration

<http://asc.harvard.edu/cal> (CXC calibration site)

<http://hea-www.harvard.edu/HRC/calib/calib.html> (HRC Instrument Team calibration)

Meehan, G, ”Calibration of the HRC-I UV/Ion Shield”, 10/13/99.

http://hea-www.harvard.edu/HRC/calib/hrci_cal_report.ps

Meehan, G.,”Calibration of the HRC-S UV/Ion Shields”, 10/13/99.

http://hea-www.harvard.edu/HRC/calib/hrscs_cal_report.ps

Kenter, A.T., Chappell, J., Kobayashi, K., Kraft, R.P., Meehan, G.R., Murray, S.S., Zombeck, M.V., “Performance and Calibration of the AXAF High Resolution Camera: I. Imaging Readout”, SPIE, 3114, 26, 1997.

http://hea-www.harvard.edu/HRC/calib/spie97_kenter.ps

Kenter, A., et al., “In-flight Performance and Calibration of the Chandra High Resolution Camera Spectroscopic Readout (HRC-I)” SPIE, 4012, 2000.

<http://hea-www.harvard.edu/HRC/calib/hrci.spie2000.ps>

Kraft, R.P., Chappell, J., Kenter, A.T., Kobayashi, K., Meehan, G.R., Murray, S.S., Zombeck, M.V., “Performance and Calibration of the AXAF High Resolution Camera: II. the Spectroscopic Detector”, SPIE, 3114, 53, 1997.

http://hea-www.harvard.edu/HRC/calib/spie97_kraft.ps

Kraft, R., et al., “In-flight Performance and Calibration of the Chandra High Resolution Camera Spectroscopic Readout (HRC-S)” SPIE, 4012, 2000.

<http://hea-www.harvard.edu/HRC/calib/hrcs.spie2000.ps>

Meehan, G.R., Murray, S.S., Zombeck, M.V., Kraft, R.P., Kobayashi, K., Chappell, J.H., and Kenter, A.T., “Calibration of the UV/Ion Shields for the AXAF High Resolution Camera”, SPIE, 3114, 74, 1997.

http://hea-www.harvard.edu/HRC/calib/spie97_meehan.ps

Murray, S. S.; Chappell, J.H.; Kenter, A. T.; Kobayashi, K.; Kraft, R. P.; Meehan, G. R.; Zombeck, M. V.; Fraser, G. W.; Pearson, J. F.; Lees, J. E.; Brunton, A. N.; Pearce, S. E.; Barbera, M.; Collura, A.; Serio, S., “AXAF High-Resolution Camera (HRC): calibration and recalibration at XRCF and beyond”, SPIE, 3114, 11, 1997.

Detector coordinate systems

McDowell, J., “Coordinate Systems for Analysis of On-orbit Chandra Data, Paper I: Imaging”,

<http://hea-www.harvard.edu/~jcm/asc/docs/ps/ncoords.ps>

Count life

Kenter, A.T., K.A. Flanagan, G. Meehan, S.S. Murray, M.V. Zombeck, G.W. Fraser, J.F. Pearson, J.E. Lees, A.N. Brunton, and S.E. Pearce, “Microchannel plate testing and evaluation for the AXAF high resolution camera (HRC)”, Proc. SPIE, 2518, 356, 1995.

Out-of-band response

Zombeck, M.V., HRC-I out of band response.

http://hea-www.harvard.edu/HRC/calib/hrci_cal.html/uv_vis

Zombeck, M.V., HRC-S out of band response.

http://hea-www.harvard.edu/HRC/calib/hrcs_cal.html/uv_vis

Zombeck, M.V., et al., Vega calibration observations.

<http://hea-www.harvard.edu/HRC/calib/vega/vega.html>

Chapter 8

HETG: *Chandra* High Energy Transmission Grating

8.1 Instrument Overview

HETG is the High-Energy Transmission Grating. In operation with the High Resolution Mirror Assembly (HRMA) and a focal plane imager, the complete instrument is referred to as the HETGS — the High-Energy Transmission Grating Spectrometer. There are two sets of gratings, each with different period. One set, the MEG, intercepts rays from the outer HRMA shells and is optimized for medium energies. The second set, the HEG, intercepts rays from the two inner shells and is optimized for high energies. Both gratings are mounted on a single support structure and therefore used concurrently. The two sets of gratings are mounted with their rulings at different angles so that the dispersed images from the HEG and MEG will form a shallow X centered at the undispersed (zeroth order) position; one leg of the X is from the HEG, and the other from the MEG. The HETG is designed for use with the spectroscopic array of the *Chandra* CCD Advanced Imaging Spectrometer (ACIS-S) although other detectors may be used for particular applications. The HETG provides for high resolution spectroscopy (with $E/\Delta E$ up to 1000) between 0.4 keV and 10.0 keV. A summary of characteristics is given in Table 8.1.

The Instrument Principal Investigator for the HETG is Dr. Claude Canizares of the MIT Center for Space Research.

Table 8.1: HETG(S) Parameters

HETGS Range:	0.4 – 10.0 keV, 31 – 1.2 Å
HEG Range:	0.8 – 10.0 keV, 15 – 1.2 Å
MEG Range:	0.4 – 5.0 keV, 31 – 2.5 Å
Effective Area (see plots): (MEG+HEG first orders, with ACIS-S)	7 cm ² @ 0.5 keV 59 cm ² @ 1.0 keV 200 cm ² @ 1.5 keV 28 cm ² @ 6.5 keV
Resolving Power ($E/\Delta E$, $\lambda/\Delta\lambda$)	
HEG:	1070 – 65 (1000 @ 1 keV, 12.4 Å)
MEG:	970 – 80 (660 @ 0.826 keV, 15 Å)
Resolution:	
ΔE :	0.4 – 77 eV FWHM
$\Delta\lambda$, HEG:	0.012 Å FWHM
$\Delta\lambda$, MEG:	0.023 Å FWHM
Absolute Wavelength Accuracy:	
HEG	± 0.01 Å, 3-sigma
MEG	± 0.02 Å, 3-sigma
HEG angle on ACIS-S:	$-5.235^\circ \pm 0.01$
MEG angle on ACIS-S:	$4.725^\circ \pm 0.01$
HETGSRowland Spacing	8632.65 mm (for flight analysis)
Wavelength Scale:	
HEG	0.0055625373 Å / ACIS pixel
MEG	0.011124491 Å / ACIS pixel
HETG Rowland Diameter:	8633.69 mm
Diffraction Efficiency: (single-side, first order)	2.5% @ 0.5 keV (MEG) 19% @ 1.5 keV (MEG & HEG) 9% @ 6.5 keV (HEG)
HETG Zeroth-order Efficiency:	4.5% @ 0.5 keV 8% @ 1.5 keV 60% @ 6.5 keV
Grating Facet Average Parameters	
HEG and MEG bar material:	Gold
HEG / MEG period:	2000.81 Å, / 4001.41 Å
HEG / MEG Bar thickness:	5100 Å, / 3600 Å
HEG / MEG Bar width:	1200 Å, / 2080 Å
HEG / MEG support:	9800 Å, / 5500 Å polyimide

8.1.1 Example of HETGS Observation

An example of an HETGS observation is presented in Figure 8.1 using data from the Capella observation, Obsid 1318. The top panel shows an image of detected events on the ACIS-S detector with the image color indicating the ACIS-determined X-ray energy. In this detector coordinate image (TDETX, TDETY), the features are broad due to the nominal dither motion which serves to average over detector non-uniformities. The ACIS-S chips are numbered S0 to S5 from left to right, with the aim point in S3 where the bright zeroth-order image is visible and includes a vertical frame-transfer streak (a trailed image). The HRMA optical axis passes through S3 approximately 6 mm from the S2-S3 chip gap. For further ACIS information see the ACIS Flight Focal Plane figure 6.1 and related text in the ACIS section.

HETG-diffracted photons are visible forming a shallow “X” pattern; the full opening angle between the HEG and MEG spectra is of order 10° , specific values are given in Table 8.1. The back illuminated (BI) chips are S1 and S3. The S1 location was chosen to enhance the first order MEG spectrum since back illumination provides higher efficiency below 1 keV. The location of the zeroth-order for any particular observation, however, may be changed by offset pointing in order to select the energies which will be affected by the gaps between the chips. Details on gaps are presented in section 8.2.1.

The middle panel shows an image after the data have been aspect corrected and data filters applied to include only valid zeroth and first-order events. The lower set of panels shows an expanded view of the MEG minus-first-order spectrum with emission lines clearly visible. Wavelengths are assigned based on the diffraction angle of the events, that is, how far the events are from the zeroth-order image. Using the grating equation, below, absolute wavelengths can be assigned based on the dispersion angle. A spectrum of the source is then created by binning the events into energy or wavelength bins; the spectrum from another Capella observation is shown in Figure 8.2.

Note: Because the dispersion distance on the detector is nearly proportional to wavelength, wavelength bins are “natural” from an instrument perspective. Wavelength is also commonly used in the high-resolution spectroscopy community. However, photon energy has been used in general in X-ray astrophysics in the HETGS bandpass. Hence, in working with the HETGS, a high-resolution high-energy spectrometer, both energy and wavelength appear depending on the context. No effort has been made in this

document to exclude either photon measure; the relation

$$E \times \lambda = hc = 12.3985 \text{ keV}\text{\AA}$$

provides a straight forward conversion.

Each of the “arms” of the HETGS diffracted X pattern yields a first-order spectrum identified by type (HEG or MEG) and sign of the order (plus or minus.) Using *ARF*’s (ancillary response files) and *RMF*’s (response matrix files) these spectra can be analyzed in an *XSPEC*-like framework. Additionally, the *CXC* software package “Interactive Spectral Interpretation System” (ISIS, <http://space.mit.edu/ASC/ISIS/>) can be used to identify spectral lines, e.g., as seen in Figure 8.2, based on high-resolution line lists.

8.1.2 Scientific Objectives and Grating Heritage

The HETGS allows one to probe the physical parameters of emitting regions of all classes of X-ray emitters, including stars, X-ray binaries, supernova remnants, galaxies, clusters of galaxies, quasars, and interstellar and intergalactic material. Plasma diagnostic techniques applied to emission lines, absorption lines and absorption edges will convey source properties such as temperatures, ionization states, densities, velocities, elemental abundances, and thereby structure, dynamics, and evolution of various classes of sources. The energy band amenable to observation is extremely rich in lines from both coronal and photo-ionized plasmas, containing the L-shell lines from ionization stages of Fe XVII to Fe XXIV and the K-shell lines of hydrogenic and helium-like ions of oxygen through nickel. The 6 keV Fe K lines are well within the observable band. The highest resolutions available will also allow detailed study of motions through Doppler line shifts in supernova remnants, X-ray binaries, turbulent intra-cluster or intra-galactic gas, or early-type galaxies in clusters.

Although gratings have flown on Einstein and EXOSAT, the HETGS shares only the basic operating principles with these. Advanced grating technology has enabled achievement of greater efficiency and increased dispersion. The Rowland geometry of the grating plate and spectroscopic arrays maintains the telescope focal properties in the dispersion direction by minimizing dispersed image aberrations and hence contributes to improved spectral resolution.

8.1.3 HETGS Operating principles

The HETG is mounted, and can be inserted, just aft of the HRMA as shown in the schematic of the HRMA-HETG-detector system, Figure 8.3. The

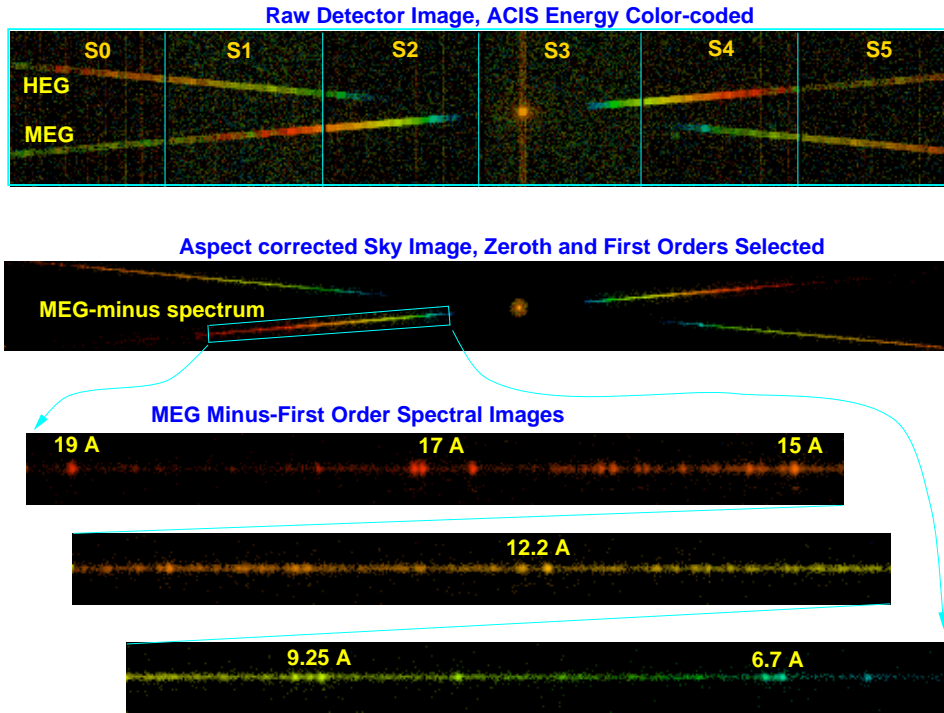


Figure 8.1: HETGS Observation of Capella, Obsid 1318. The top panel shows an image of detected events on the ACIS-S detector with the image color indicating the ACIS-determined X-ray energy. The bright zeroth-order image is visible on CCD S3 and includes a trailed image (the vertical frame-transfer streak). Diffracted photons are visible forming a shallow “X” pattern; the HEG and MEG spectra are indicated. The images are broad due to aspect motion. The middle panel shows an image after the data have been aspect corrected and selections applied to include only valid zeroth and first-order events. Finally, the lower panel shows an expanded view of the MEG minus-first-order spectrum with emission lines clearly visible.

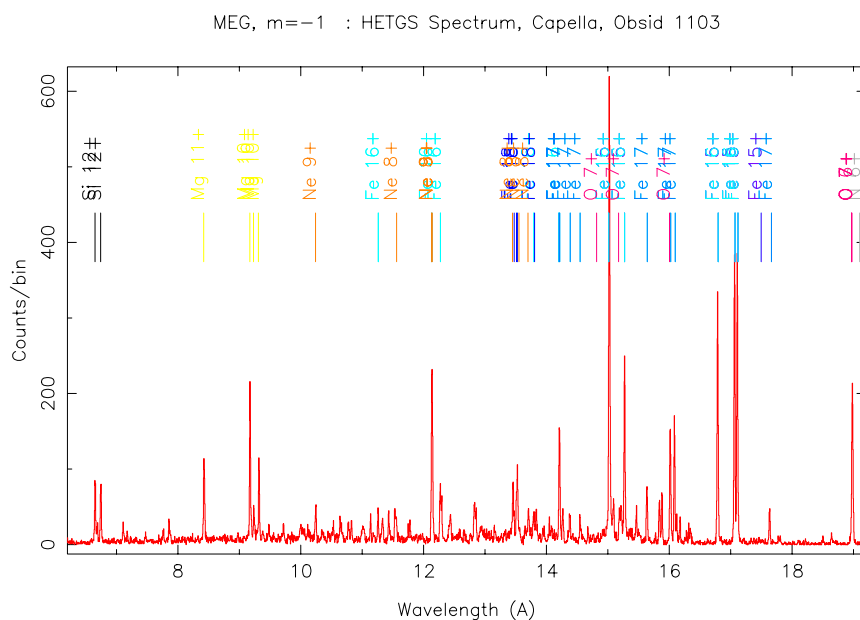


Figure 8.2: HETGS Capella spectrum, MEG $m = -1$, Obsid 1103. The first-order events identified in the MEG minus-side “arm” of the HETG X pattern are assigned wavelengths by *CXC* pipeline software according to the grating equation and known instrument parameters. These values are then binned to produce a pulse height analysis spectrum (`pha2.fits` file) which is plotted here. The ISIS software package from *CXC* has also been used to plot expected emission lines based on a simple source model.

HETG provides spectral separation through diffraction. X-rays from the HRMA strike the transmission gratings and are diffracted (in one dimension) by an angle β given according to the grating equation,

$$\sin \beta = m\lambda/p,$$

where m is the integer order number, λ is the photon wavelength in angstroms, $\lambda = hc/E = 12.3985/E$, E is the energy in keV, p is the spatial period of the grating lines, and β is the dispersion angle. A “normal” undispersed image is formed by the zeroth-order events, $m = 0$, and dispersed images are formed by the higher orders, primarily the first-order, $m = 1$.

The HETGS-Faceted Rowland design is shown in Figure 8.4. To understand the construction, a short introduction to the terminology is necessary. The “Rowland circle” is a circle whose diameter is simply the distance from the grating that would lie on the optical axis to the point in the focal plane, where the zeroth order image is placed. The “Rowland torus” is formed by rotating the circle about the optical axis. Individual grating facets are mounted such that their centers lie on the torus. In the figure, the axis of the torus is perpendicular to the page for the side view and lies in the plane of the top view. Ideally, the detector is shaped to follow the counterpart Rowland torus in the image plane. The result is that the telescope focal properties in the dispersion direction are maintained for a large range of diffraction angle, β , thereby minimizing any grating-added optical aberrations.

An important parameter of the HETGS is the Rowland Spacing, the distance from the outer intersection of the HETG axis and Rowland Circle to the HRMA focus. This parameter was introduced since the HETG was built to a particular Rowland circle whose diameter was not the precise value for the as-assembled observatory. The slight difference between the Rowland diameter and spacing introduces negligible effects on the HETGS performance. The Rowland spacing is, however, what determines the value of β in the grating equation. The values of the various Rowland parameters are listed in Table 8.1.

Order overlap and source confusion can be discriminated by the intrinsic energy resolution of the CCD detector (ACIS-S is the preferred detector for HETG spectroscopy since it has intrinsic energy resolution and so can separate orders; HRC can also be used for high time resolution). The form of a spectral image on the ACIS-S array is shown in Figure 8.1. The spectroscopic array spans about 8 arc minutes \times 48 arc minutes of the sky, though image quality and resolving power degrade rapidly for sources more than

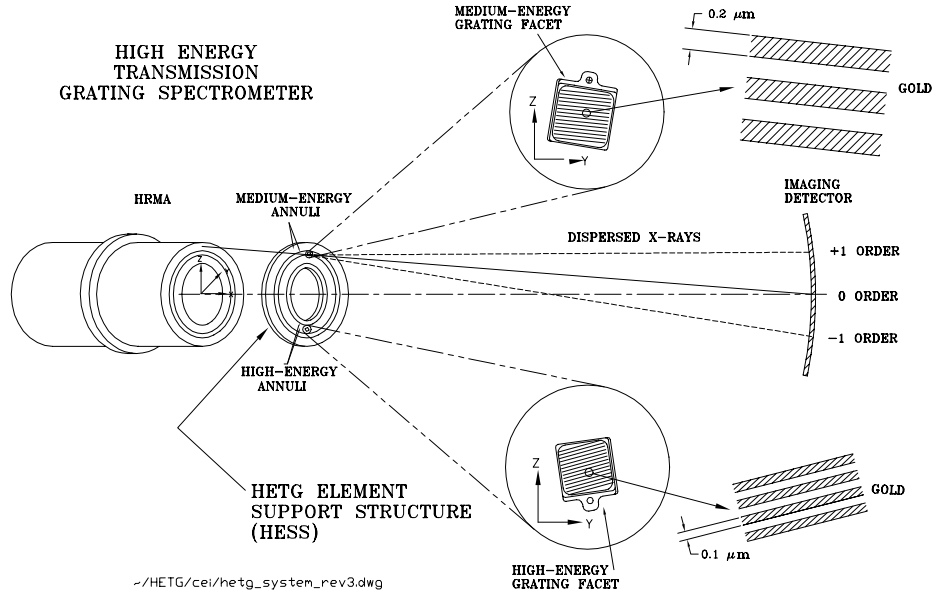


Figure 8.3: A schematic layout of the High Energy Transmission Grating Spectrometer. (Dimensions shown are approximate.)

about 4 arcmin off-axis. For an on-axis source, the detector edge in the dispersion direction causes a low energy cutoff of the spectrum at about 0.4 keV for the MEG and 0.8 keV for the HEG. Order selection and chip gaps are described more fully in section (8.2.1).

A “grating” coordinate system has been defined in the AXAF-I to SI Interface Control Document (ICD). Various *Chandra* coordinate systems have been summarized in the ASC document, “ASC Coordinates, Rev. 4.1” (J. McDowell, 27 Feb 1997).

8.1.4 HETG Physical Configuration

The HETG support structure (HESS) is a circular aluminum plate (110 cm diameter by 6.35 cm thick) which can be swung into operation behind the HRMA. Mounted on the HESS are 336 grating facets, each about 25 mm square. The position and orientation of the HESS mounting surfaces have been designed and machined to place each grating center on a Rowland torus of diameter 8633.69 mm. A detailed drawing of the HETG (HESS plus facets) is shown in Figure 8.5.

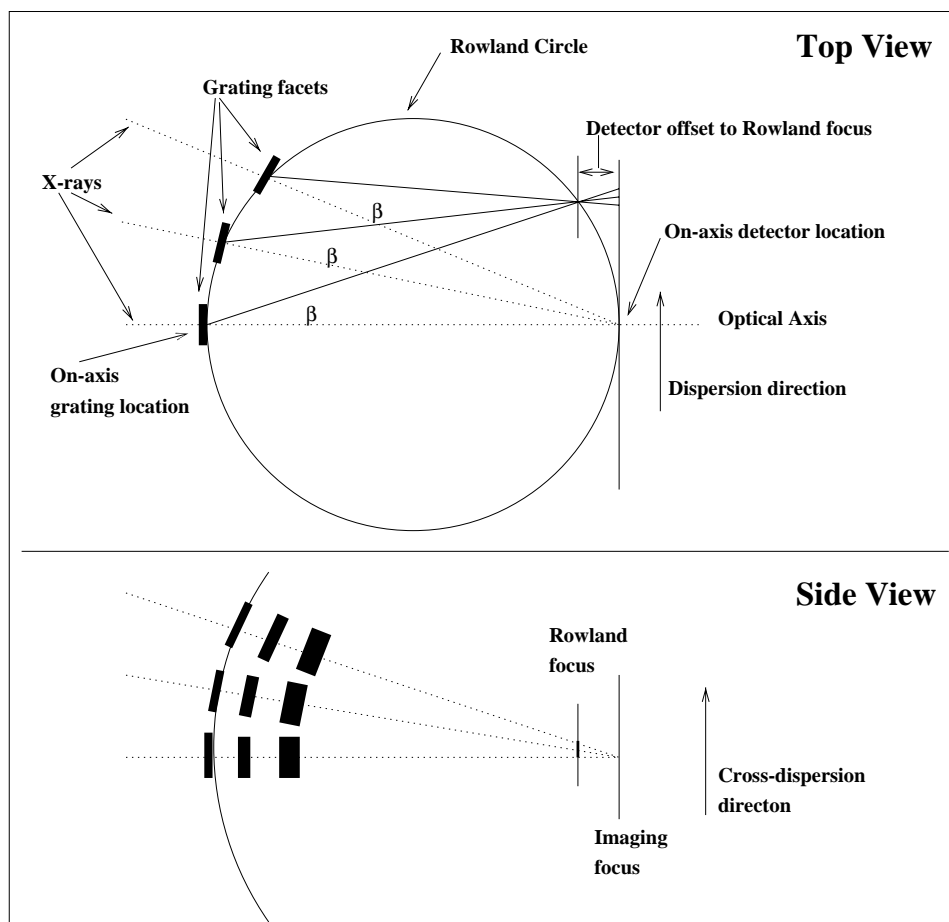


Figure 8.4: The Rowland geometry is shown schematically. In the “Top” view, we are looking across the dispersion direction. The diffraction angle is β , which through the geometric properties of the circle, causes rays diffracted from gratings on the Rowland circle to converge at another point on the Rowland circle. The dotted lines represent zeroth-order rays and the solid lines the grating first-order diffracted rays. The bottom panel (“Side” view) looks along the dispersion direction at rays from a set of gratings arranged perpendicularly to those in the “Top” view and schematically shows the astigmatic nature of the spectrally focused image: since the converging rays have not yet reached the imaging focus, they are extended across the dispersion (by less than 100 microns).

The gratings cover the annular regions through which the X-rays pass. The 192 grating facets on the outer two annuli (Medium Energy Grating, MEG) have a period of 4001.41 \AA . Tiling the inner two annuli are 144 High Energy Gratings (HEG), which have a period of 2000.81 \AA (see Table 8.1). The two sets of gratings are mounted with their rulings at different angles so that the dispersed images from the HEG and MEG will form a shallow X centered at the undispersed (zeroth order) position; one leg of the X is from the HEG, and the other from the MEG.

The HETG grating facets are composed of electro-plated Gold bars supported on a polyimide substrate, as shown schematically in Figure 8.6. The grating bar design parameters, height and width, are nominally chosen to reduce zeroth-order and maximize first-order intensities. Choosing to have the bar width one-half of the grating period suppresses even orders and provides maximum 1st order efficiency for a rectangular profile; this is closely achieved for the MEG gratings. For the HEG gratings, the bar is wider and results in a higher 2nd order efficiency and reduced 3rd order. The bar height choice “tunes” the efficiency peak in energy by allowing X-rays to constructively interfere in first order in the region where the gold is partially transparent primarily, above 1.2 keV.

8.2 Instrument Characteristics

As a spectrometer, the HETGS can be described at the simplest level by a throughput measured by the *Effective Area* (how many events are diffracted into the “X”) and a *Line Response Function* (the distribution of dispersed photons from a monochromatic input.) In addition an HETGS observations will include *Background* events which must be accounted for in analyses and the *Absolute Wavelength* accuracy is of key interest. Summaries of the status of these characteristics (as opposed to calibration methods and details) are presented in the following sections.

8.2.1 HETGS Effective Area

The HETGS effective area depends on the HETG efficiency coupled with the HRMA effective area and the ACIS quantum efficiency. Additional effects can arise from the process of selecting events, the effect of chip gaps, and the use of “ACIS ENERGY” to do order sorting. In this chapter we use the term ACIS ENERGY to describe the energy deduced from the ACIS pulse height. Current calibration values and assessments of these effects are described.

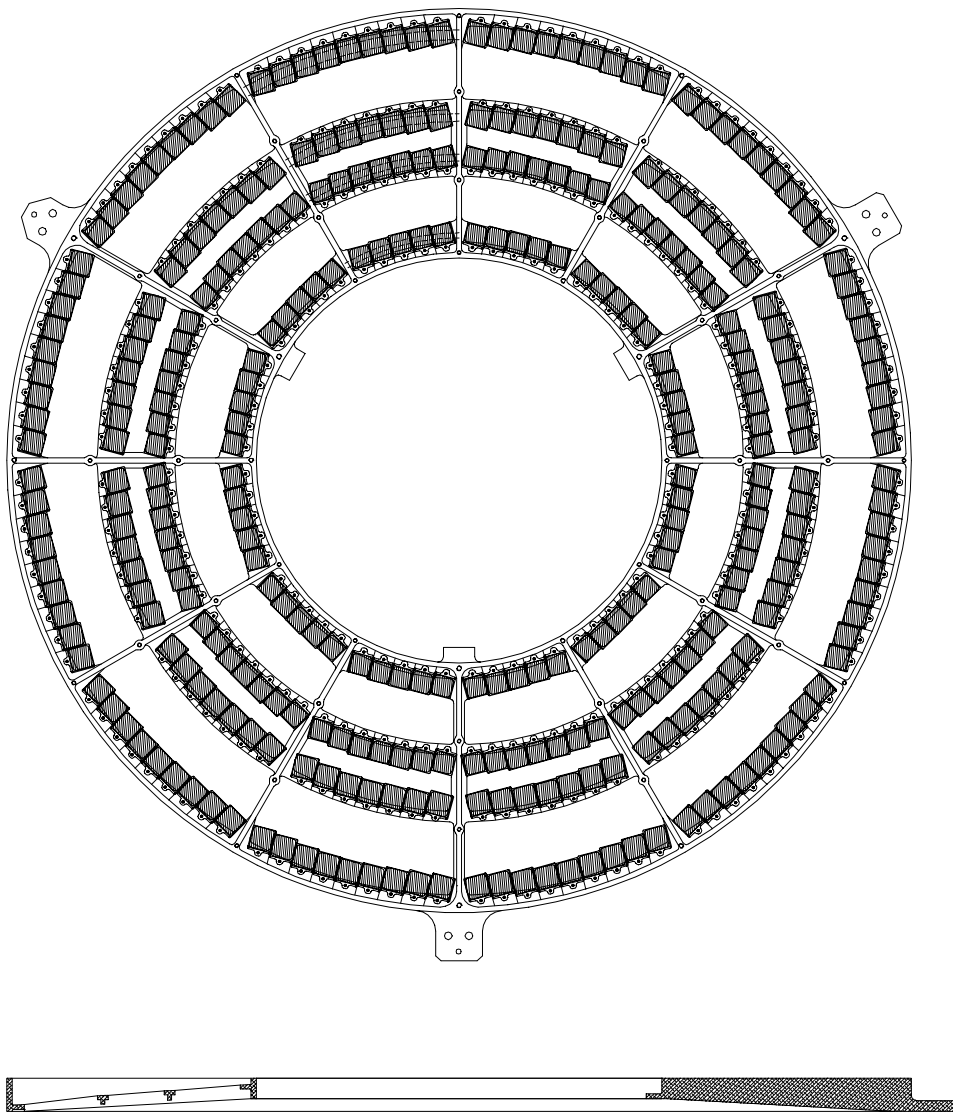


Figure 8.5: A front and side view of the HETG support structure (HESS). The grating facets are mounted to intercept the X-rays as they exit the HRMA; the front view is from the HRMA side, i.e., what an approaching X-ray would see. In the side view, the left cross-section shows that the four support rings are in different planes due to the Rowland curvature. The right cross-section is through a radial rib at one of the three mounting “ears”.

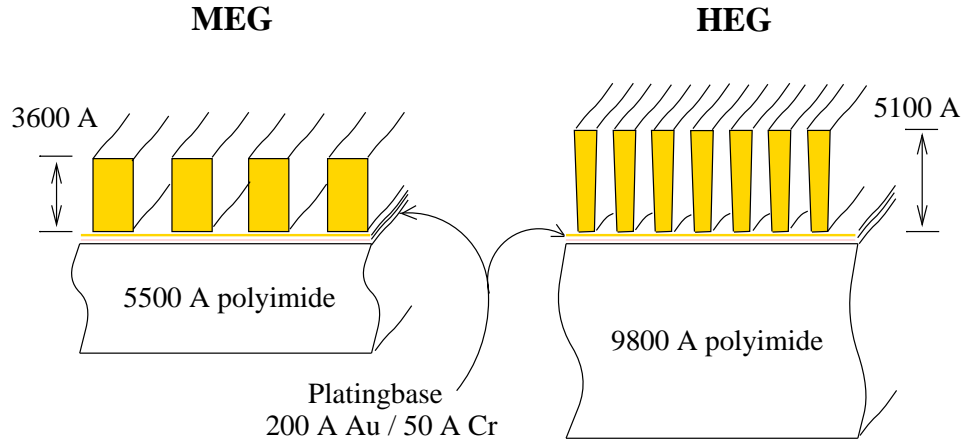


Figure 8.6: Cross-sections of the MEG and HEG membranes. The soap-bubble-thin membranes of the HETG consist of gold bars attached to a polyimide support layer. The MEG grating bars are close to rectangular, typically with a height of 3600 Å and a bar-to-period fraction of 52 %. The HEG bars have a crudely trapezoidal shape, typically 5100 Å high with an effective bar-to-period fraction around 60 % .

Nominal HETGS *ARF*'s

Combining the HETG diffraction efficiencies with the HRMA effective area and the ACIS-S detection efficiency produces the system effective area as a function of energy, described by an “ancillary response file” or *ARF*. Plots of HETGS *ARF*'s are shown in Figures 8.7 and 8.9 which are plotted with log vertical axes; the same plots with linear vertical scale are shown in Figures 8.8 and 8.10. The values are plotted from *ARF* files created by the *CXC* tool *mkgarf*. Specifically, these effective areas are based on the following HETG efficiencies (version “N0003”, 7/14/99), XRCF-corrected HRMA on-axis effective areas (version “N0004”, 5/10/99) and ACIS-S QE models (version “N0002”, 8/98.) Since first-order photons from both the HEG and MEG gratings provide information, a useful comparison plot is the total HETGS effective area, the combined plus and minus first-order areas of both the HEG and MEG, shown in Figure 8.11.

Note the dips caused by the gaps between chips in these figures. The observatory is dithered in order to spread the signal across a large number of pixels. For HETGS observations sinusoidal motions with 8 arc second amplitude in spacecraft *Y* and *Z* axes are used with periods of 1000.0 and ≈ 707.0 seconds, respectively. When the combination of the chip gaps and

dither are accounted for a “pitch fork” dip occurs at each gap region in the *ARFs*. Although this motion is removed in on-ground processing through the *ARF* values, observers are advised to avoid placing known spectral features of interest near the gaps, more gap details are in the next section.

Note that these effective area values assume integration over the full PSF of the HRMA; in practice this can be achieved by including an aperture of diameter 10 arcsec (≈ 20 pixels). Equivalently for HETGS analysis, all events that are within ± 10 pixels of the dispersion axis are included, ensuring that over 95% of the full effective area is achieved while reducing extraneous background events. Further discussion of the spatial distribution of events can be found for the HRMA PSF in Chapter 4 and for the HETGS in section 8.2.2 below.

The goal for HETGS effective area calibration is 10 % absolute and 3 % relative (e.g., for a line ratio).

The HETG-ACIS areas at a few energies are given in Table 8.1.

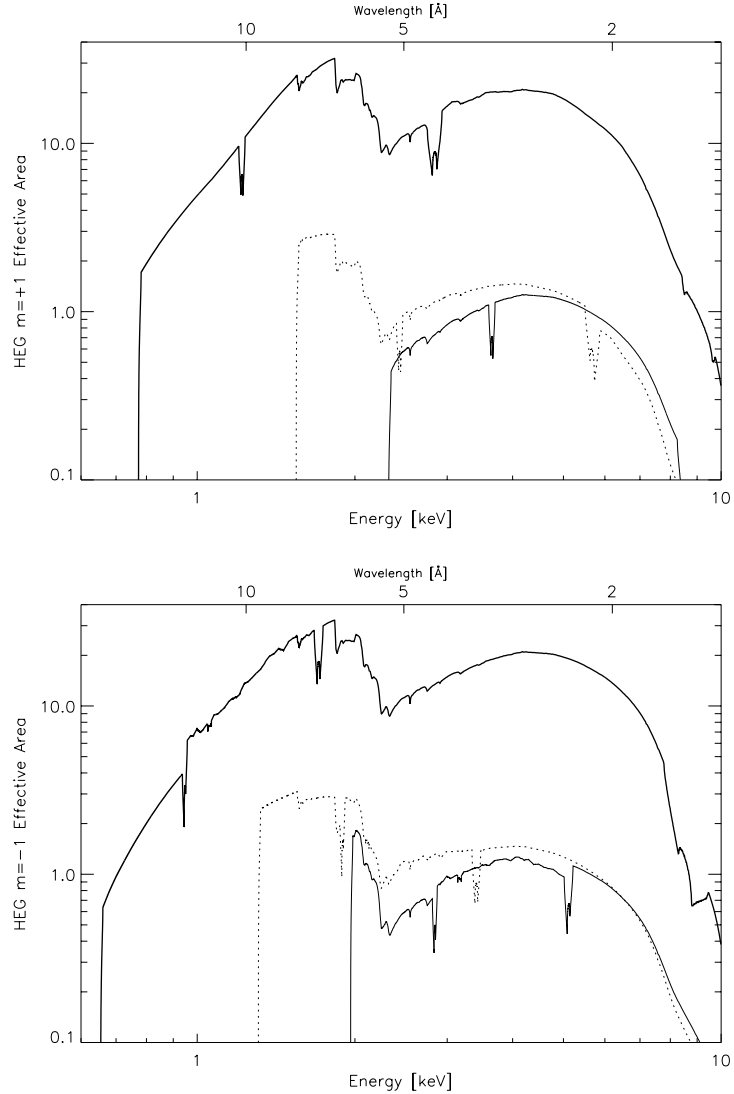


Figure 8.7: The HETGS HEG predicted effective area, integrated over the PSF, is shown with energy and wavelength scales. The $m = +1, +2, +3$ orders (falling on ACIS chips S5, S4, S3; left to right) are displayed in the top panel and the $m = -1, -2, -3$ orders (falling on ACIS chips S0, S1, S2; left to right) are in the bottom panel. The thick solid lines are first order; the thin solid line is third order; and the dotted line is second order. These effective areas are from an *ARF* file created by the *mkgarf* tool which includes the effects of the ACIS-S hybrid front and back illuminated chip array QEs and a nominal dither pattern. The pitch-fork looking dips are dithered chip gap effects. Data files used are described in the text.

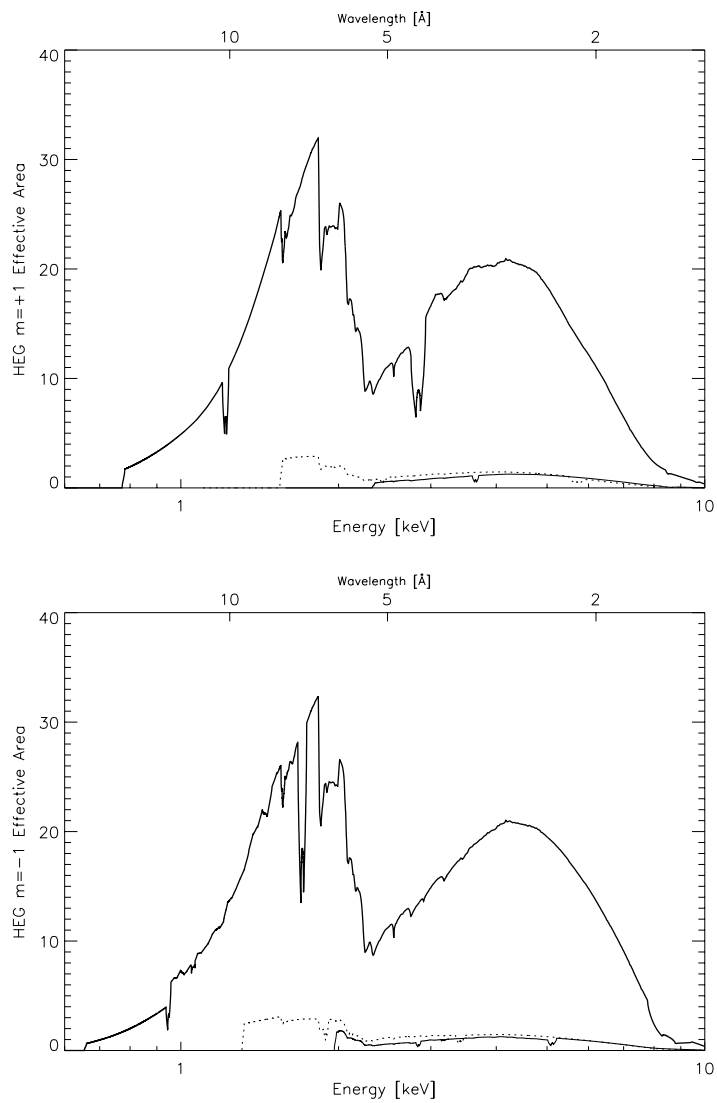


Figure 8.8: The HETGS HEG predicted effective area: same as previous figure, except the vertical scale is now linear.

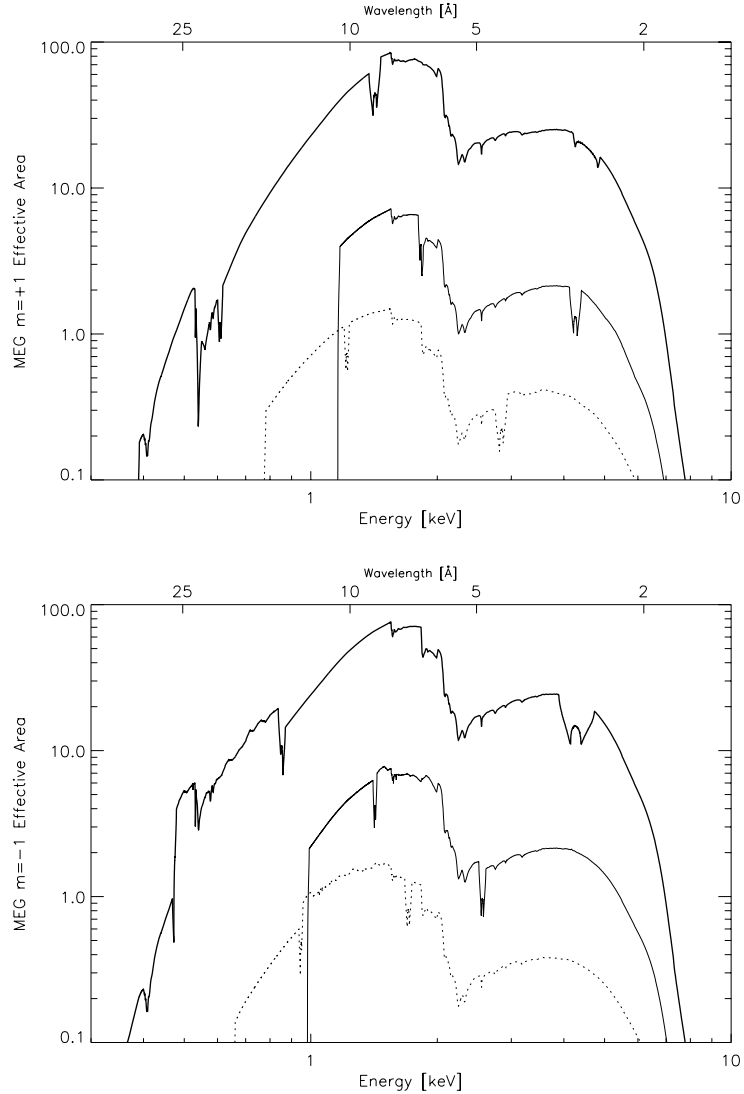


Figure 8.9: The HETGS MEG predicted effective area, integrated over the PSF, is shown with energy and wavelength scales. The $m = +1, +2, +3$ orders (falling on ACIS chips S5, S4, S3; left to right) are displayed in the top panel and the $m = -1, -2, -3$ orders (falling on ACIS chips S0, S1, S2; left to right) are in the bottom panel. The thick solid lines are first order; the thin solid line is third order; and the dotted line is second order. These effective areas are from an *ARF* file created by the *mkgarf* tool which includes the effects of the ACIS-S hybrid front and back illuminated chip array QEs and a nominal dither pattern. The pitch-fork looking dips are dithered chip gap effects. Data files used are described in the text.

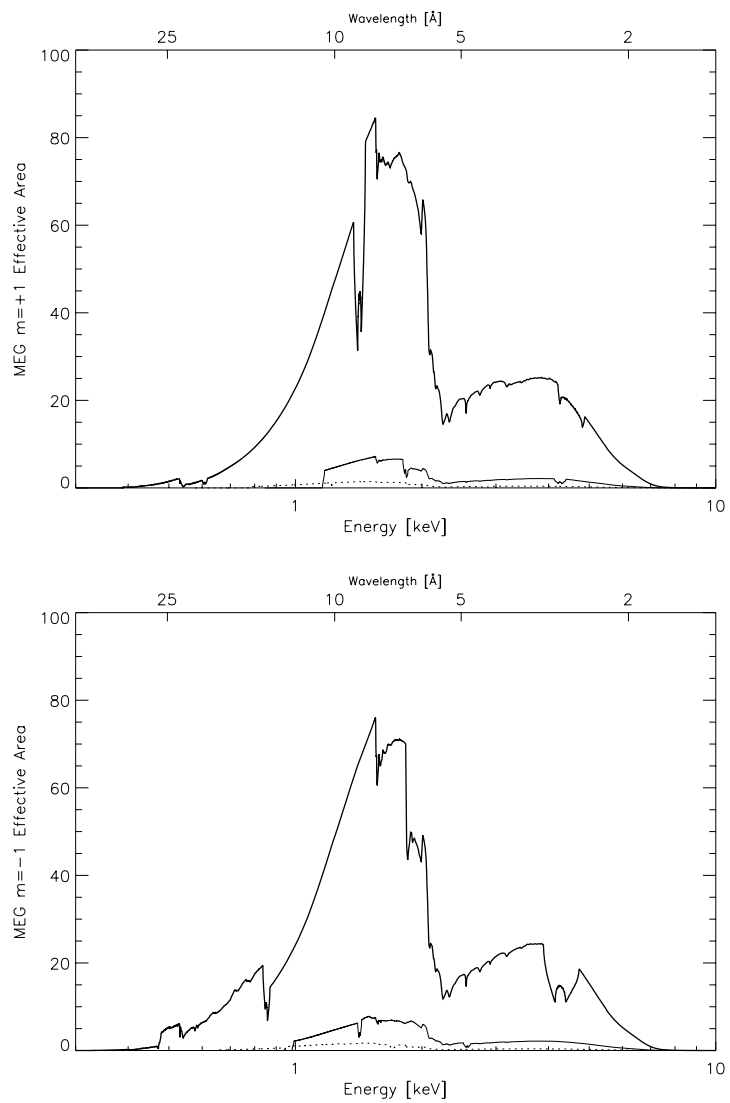


Figure 8.10: The HETGS MEG predicted effective area: same as previous figure, except the vertical scale is now linear.

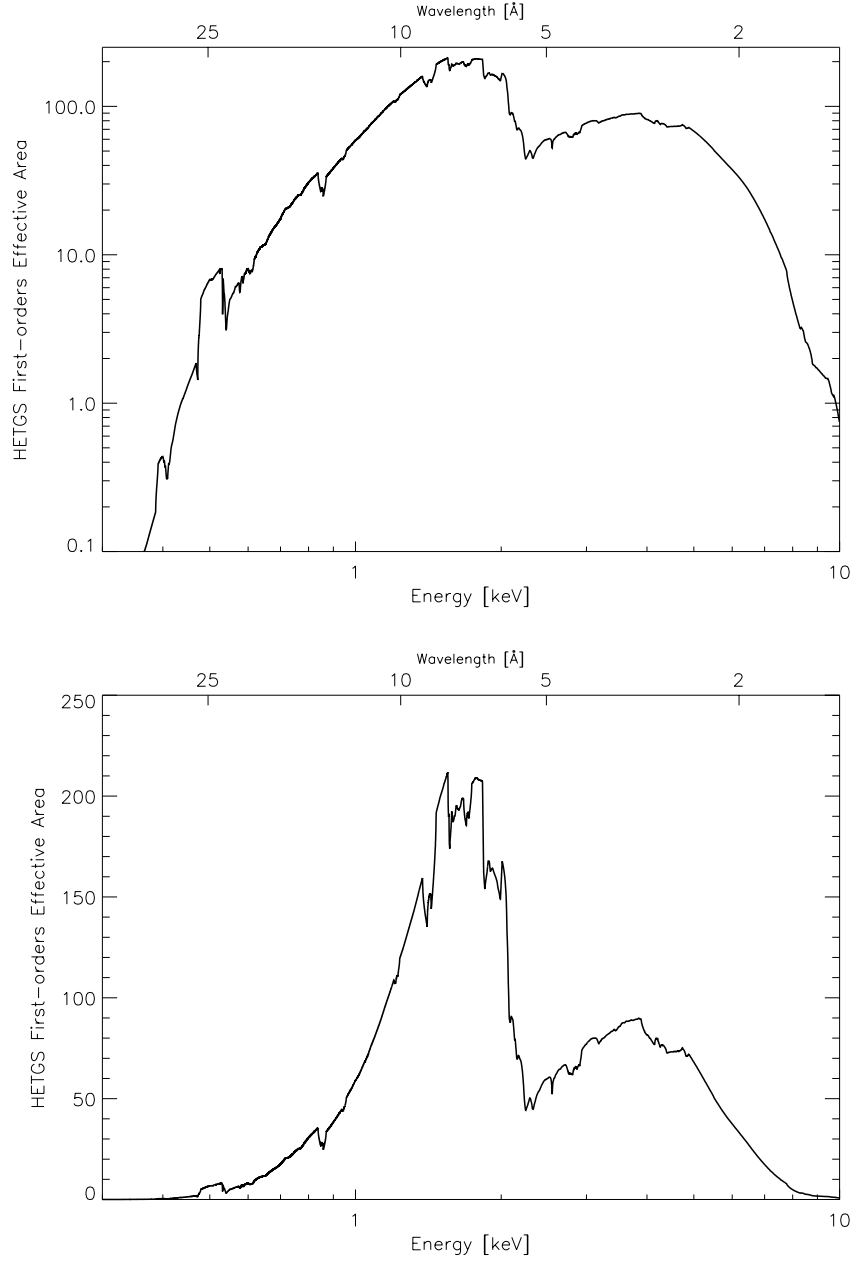


Figure 8.11: The model first-order predicted effective area, integrated over the PSF, of the HRMA-HETG-ACIS-S combination, as a function of energy. The data are the same as those plotted in Figures 8.7 and 8.9. The plotted values are the sums of the photons at a particular energy from both orders (+/-) of both MEG and HEG spectra. Both a log-log and a log-linear version are shown.

HETG Efficiency

The HETG contribution to the effective area comes in through the efficiencies of the HETG gratings; the values of these are shown in Figure 8.12. These “N0003” version efficiencies are the best values to date (HETG IPI released 7/14/99) and are based on laboratory measurements of each facet, reference grating corrections, and improved polyimide transmission models. The newest Gold optical constants have *not* been incorporated but this is expected to have an effect less than 2% in the 2 to 2.5 keV range.

ACIS-S Order Sorting Effects

One of the advantages of using the ACIS-S as the HETG readout detector is the ability of ACIS to determine the energy of detected X-rays. This crude (by HETGS standards) energy measure can be used to determine the diffraction order of the photon, i.e., perform “order sorting”, as shown in Figure 8.13. Ideally this order sorting would have high efficiency, that is, all first-order events would be correctly identified. This can be achieved in practice by accurately calibrating the ACIS ENERGY values and by accepting events in a large ENERGY range. Slight modification to the effective area may be made based on the details of the order sorting.

A closeup of the MEG banana plot, Figure 8.14, shows that ACIS pileup can mimic higher-order photons. This pileup generally only occurs significantly for bright regions of the first-order spectrum.

ACIS-S Chip Gap Effects

The nominal ACIS-S aim point is on chip S3, 2.0' direction from the gap between chips S2 and S3. Energies of gap edges in both dispersed spectra for the nominal aim point and for 3 offsets in both (+/-) Y directions are given in Table 8.2. *Note well that when ACIS-S is placed in the focal plane, the standard procedure includes a -0.33 arcmin offset to avoid placing the image of a point source on the boundary between the nodes in S3.* Thus, for example, with zero order at the nominal aimpoint, the gap between chips S3 and S4 spans the energy range 1.519-1.477 keV in the MEG spectrum (lower energies on S4).

These values are based on an effective gap size of 0.502 mm, corresponding to 10" on the sky. It is “effective” in the sense that the gap includes columns 1 and 1024 of the devices from which no events are reported. This value for gap size is approximate and accurate to about 2 pixels. The actual gap sizes vary slightly; the precise values of the ACIS-S chip geometry

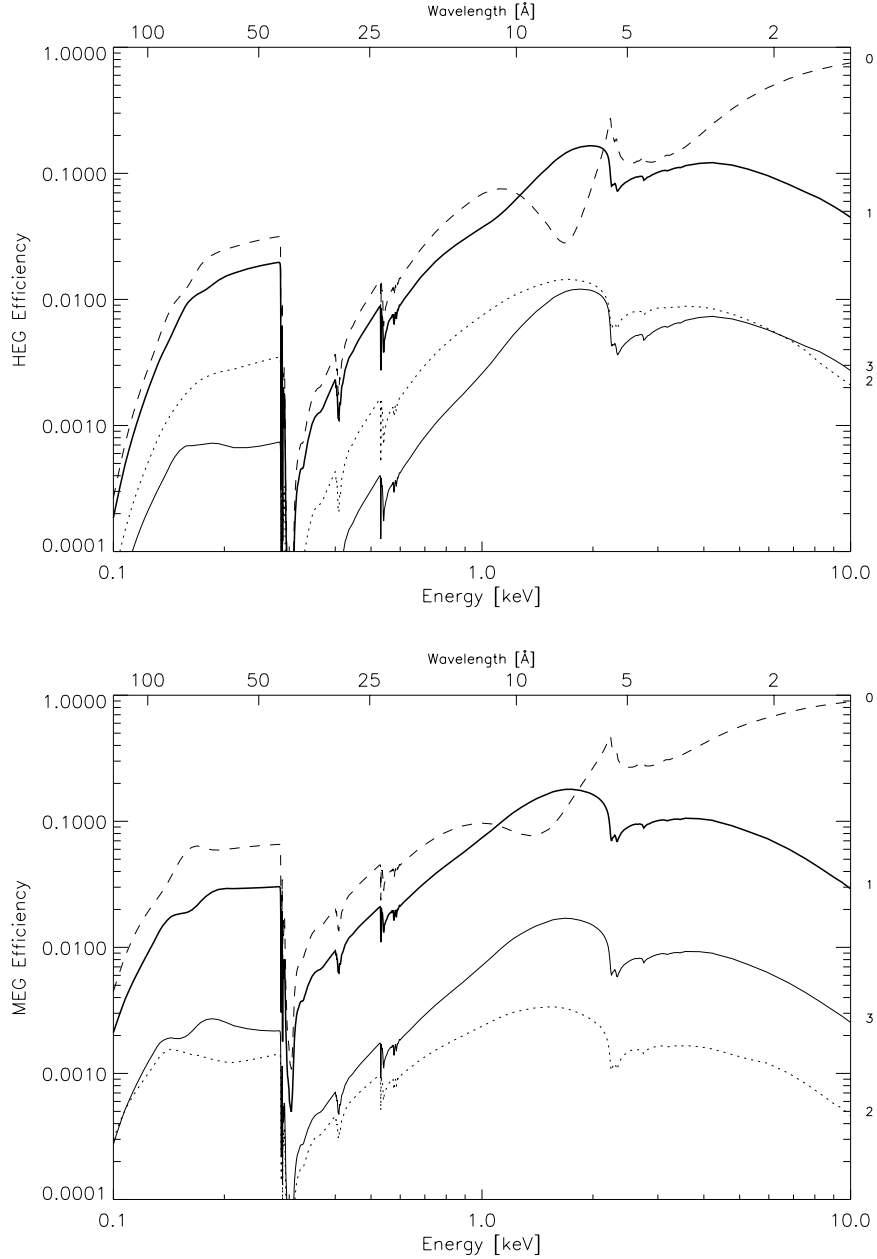


Figure 8.12: HEG (upper panel) and MEG (lower panel) efficiencies as a function of energy. The values plotted are the mirror-weighted efficiency into a single plus, minus, or zero order (labelled on the right edge). The dashed line is zeroth order; the thick solid line is first order. Note that the relative strengths of the third orders (thin solid lines) are comparable, whereas the second order strengths (dotted lines) are significantly different between the HEG and MEG. The efficiencies are taken from models determined by subassembly data and confirmed by XRCF testing and are version “N0003” from the HETG IPI.

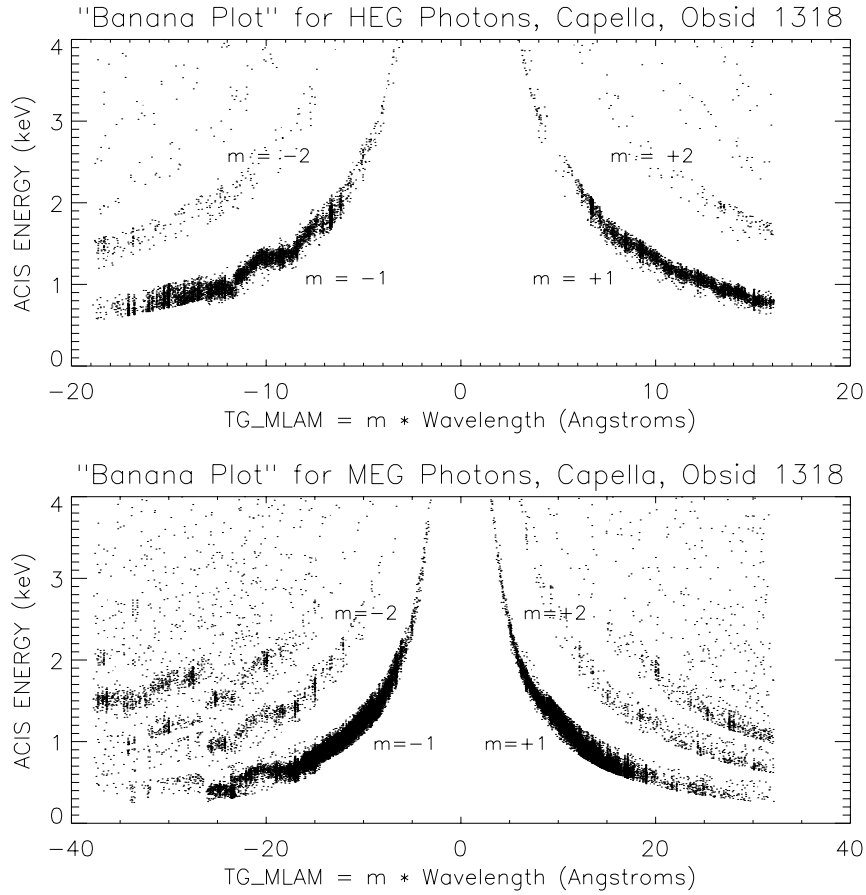


Figure 8.13: HEG (upper panel) and MEG (lower panel) “Banana Plots”. A useful look at the HETGS data is obtained by plotting the ACIS-measured event ENERGY as a function of $m\lambda = \text{TG_MLAM}$ (or versus dispersion distance.) These “banana plots” are shown here for HEG and MEG parts of the Obsid 1318 Capella observation. The various diffraction orders show up as hyperbolae in these plots. Events can be assigned to a diffraction order based on their location in this space. By accurately calibrating the ACIS ENERGY and by taking an appropriate acceptance region, events can be order sorted with high confidence and efficiency. A “zig-zag” in the $m = -1$ events pattern is visible around -10 \AA in the HEG plot and is due to uncorrected serial charge transfer inefficiency in the BI device S1 which produces a slow variation of gain across a node.

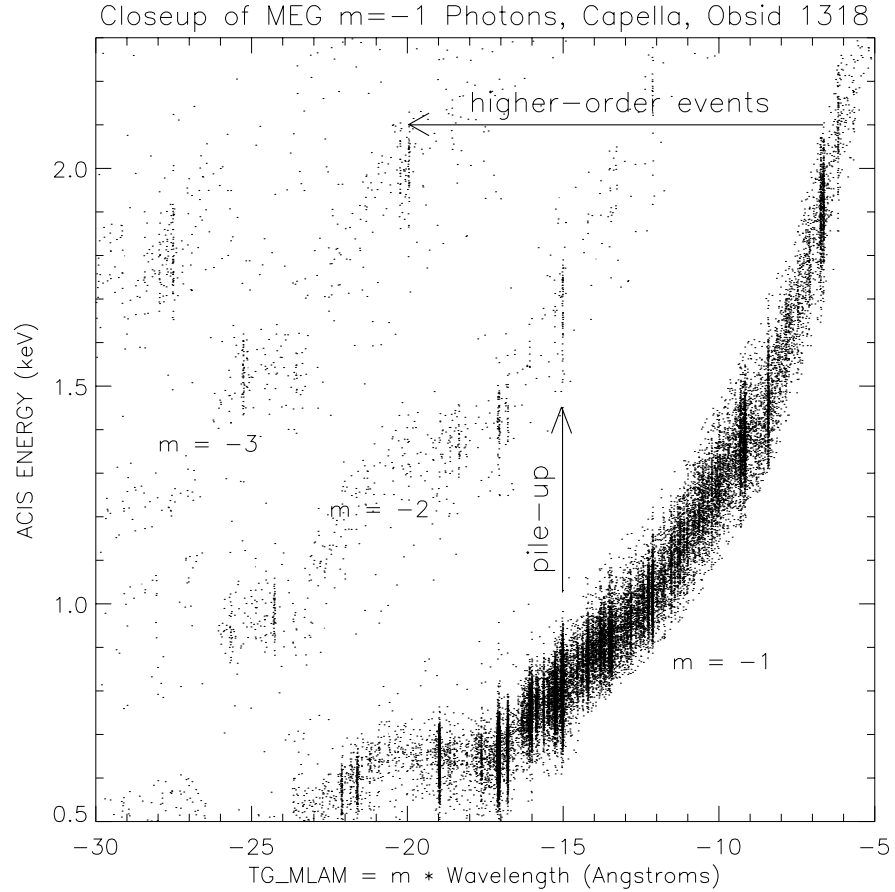


Figure 8.14: HETGS pile-up and higher-order events. Taking a close look at the MEG “banana plot” demonstrates how the ACIS ENERGY can be used to identify higher-order events and pileup in an HETGS spectrum. The 3rd order of the $\approx 6.7 \text{ \AA}$ lines are clearly visible; the lines are only weakly present in 2nd order because the MEG 2nd order is suppressed. In comparison, the 15 \AA line (and others) are so bright in 1st order that a fraction of the events ($\approx 6 \%$ here) pile-up and produce events with twice the ACIS ENERGY.

are given in the CXCDs file `pix_corner_lsi.par` and incorporated in *MARX* version 2.50.

All HETGS observations are nominally dithered with an amplitude of ± 8 arc seconds. There will thus be reduced coverage in the spectral regions within one gap-width on either side of the gaps.

Finally, the observer is advised to *try to avoid placing known features of interest within three gap widths of the tabulated gap edges*. Note that the nominal acquisition accuracy (Chapter 5) should be taken into account.

8.2.2 HETGS Line Response Function

A high-resolution spectrum is created by the projection of events along the dispersion axis and binning the events into energy or wavelength bins as shown in Figure 8.2. The HETGS line response function (LRF) at a given wavelength is the underlying distribution which would result if the source were monochromatic at that wavelength. Examples from flight data are shown in Figures 8.16 and 8.17. To a good first approximation the core of the LRF can be modeled as a Gaussian, parameterized by a *Resolution*, ΔE or $\Delta\lambda$, given as the full-width at half-maximum of the Gaussian, 2.35σ . The *Resolving Power*, $E/\Delta E = \lambda/\Delta\lambda$, is a useful dimensionless measure of the spectrometer performance. Plots of the HETGS resolving power are presented in Figure 8.18.

Of course the HETGS LRF is not simply a Gaussian and, as for other spectrometers, the response can be encoded at a higher level of fidelity through the use of response matrix files, *RMF*'s. As the discussions below detail, the LRF (*RMF*) of the HETGS depends on all system components as well as the source spatial properties. Thus, LRF creation is carried out using a system model, e.g., the *MARX* ray-trace software; a typical set of *RMF*'s can be created assuming a point source and nominal telescope properties.

The line response function can be decoupled approximately into three contributing components: the telescope zeroth-order image, the HETG effects in the dispersion direction, and HETG effects in the cross-dispersion direction. These are described in the sections below. With the exception of "HEG scatter", all effects described here are included in the *MARX* version 2.50 ray-trace software.

LRF: Telescope PSF and Zeroth-order

The HETG itself does not focus the X-rays emerging from the HRMA. Rather, *the Rowland design attempts to maintain the focal properties of the*

Table 8.2: Table of HETGS Gap Locations

Y Offset		Grating	HETGS Gaps (keV)						
arc min.	mm		S0	S0-S1	S1-S2	S2-S3	S3-S4	S4-S5	S5
+1.00	+2.93	MEG		0.497	0.931	7.423	1.243	0.574	0.373
			0.341	0.502	0.948	8.629	1.215	0.568	
		HEG		0.993	1.861	14.834	2.485	1.146	0.745
			0.681	1.002	1.894	17.244	2.428	1.134	
+0.66	+1.93	MEG		0.488	0.900	5.812	1.304	0.586	0.378
			0.337	0.492	0.916	6.527	1.273	0.580	
		HEG		0.975	1.799	11.615	2.606	1.171	0.756
			0.673	0.984	1.830	13.043	2.543	1.159	
+0.33	+0.97	MEG		0.479	0.872	4.801	1.369	0.599	0.383
			0.333	0.484	0.886	5.279	1.334	0.592	
		HEG		0.958	1.742	9.595	2.735	1.197	0.766
			0.665	0.967	1.771	10.548	2.666	1.184	
0.00	0.00	MEG		0.471	0.845	4.090	1.440	0.612	0.389
			0.329	0.475	0.859	4.431	1.402	0.605	
		HEG		0.942	1.689	8.173	2.878	1.223	0.777
			0.657	0.950	1.716	8.855	2.802	1.209	
-0.33	-0.97	MEG		0.463	0.820	3.562	1.519	0.626	0.394
			0.325	0.467	0.833	3.818	1.477	0.619	
		HEG		0.926	1.638	7.118	3.036	1.251	0.788
			0.649	0.934	1.664	7.630	2.952	1.237	
-0.66	-1.93	MEG		0.456	0.796	3.155	1.608	0.641	0.400
			0.321	0.460	0.808	3.354	1.561	0.633	
		HEG		0.910	1.591	6.305	3.213	1.280	0.799
			0.642	0.918	1.615	6.703	3.118	1.265	
-1.00	-2.93	MEG		0.448	0.773	2.822	1.710	0.656	0.406
			0.317	0.452	0.785	2.981	1.657	0.648	
		HEG		0.895	1.545	5.640	3.418	1.312	0.812
			0.634	0.903	1.568	5.957	3.311	1.296	

HRMA in the dispersion direction even as the focus is deflected by the diffraction angle β . The 1-D projection of the telescope PSF onto the dispersion axis is thus at the heart of the HETGS LRF and can be thought of as the “zeroth-order LRF”. Testing at XRCF showed no measurable effect on the telescope PSF due to the HETG insertion; this was taken advantage of in the famous Crab image, Obsid 168, where the jet and swirling structure are seen in the zeroth-order HETGS image. Thus, the zeroth-order image in an HETGS observation can be used to determine the telescope contribution to the LRF.

Image quality depends on many factors, and so, while a nominal LRF can be modeled, the detailed LRF will be observation dependent at some level. Factors in the telescope PSF performance include: source size and spectrum, HRMA properties, focus setting, detector effects (e.g., pixel quantization), aspect solution and reconstruction effects, and data analysis operations (e.g., pixel randomization.) While all of these effects can be modeled, the “proof of the pudding” is in the as-observed zeroth-order image.

As an example we show the results of the observation of Capella (Obsid 1318 Figure 8.1) in Figure 8.15. Both the zeroth-order event distribution and its 1-D projection indicate that the zeroth-order is heavily piled up with an unpiled event rate of order 10 events per frame time (per few square pixels). The wings of the PSF are visible but the core shape and intensity have been severely distorted. However, because the ACIS-S CCDs have their columns perpendicular to the (average) dispersion axis, the “frame-transfer streak” events or “trailed image” (see section 6.12.4 in Chapter 6) can be used to create an accurate, nonpiled-up zeroth-order LRF as shown.,

Thus, by appropriately examining the zeroth-order image and its LRF, one can assure oneself that if HETG dispersed lines are broad, then the broadening is likely due to the astrophysical source.

LRF: Dispersion Direction

As mentioned, the profile in the dispersion direction defines the instrument spectral resolution, ΔE or $\Delta\lambda$. The resolution function has two main terms with different dependences on energy: the image blur from the mirror described above and that caused by grating period variations which come in through the dispersion relation and are described here.

From the grating equation, $m\Delta\lambda = p\Delta\beta\cos\beta + \Delta p\sin\beta \approx y\Delta p/R_s + p\Delta y/R_s$, where y is the dispersion distance and R_s is the (fixed) Rowland spacing. Then the two terms of interest are on the right side of $\lambda/\Delta\lambda = (\Delta p/p + \Delta y/y)^{-1}$. The grating fabrication process produced tightly

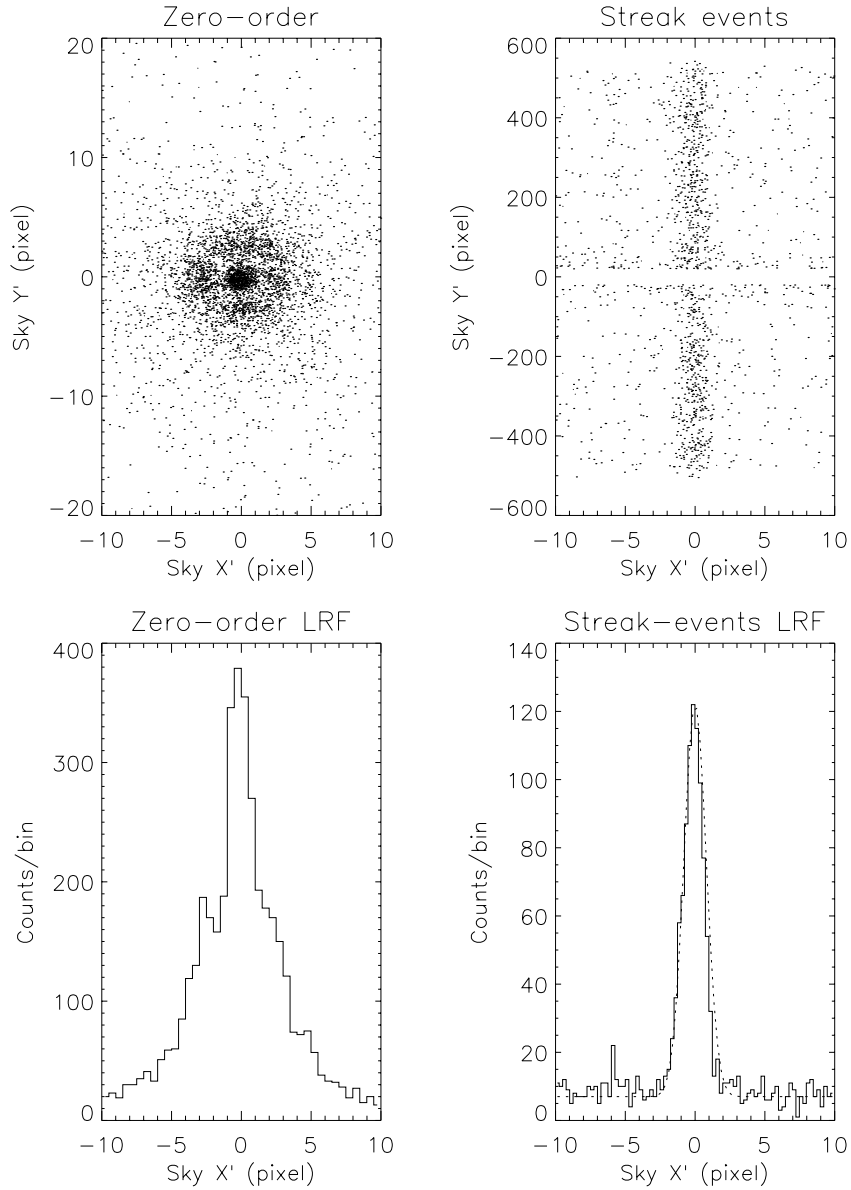


Figure 8.15: HETGS Zero-order and Frame-transfer Streak (trailed image) for ObsID 1318 of Capella. The sky coordinates, X, Y , have been rotated so that the frame-transfer streak is along the Y' axis, hence Y' is parallel to the CHIPY axis and X' is approximately along the average HEG-MEG dispersion axis. The left-side panels show the detected zero-order events and their 1-D projection; pileup is evident by the enhanced wings relative to the suppressed PSF core. The right-side panels show the frame-transfer streak events and their 1-D projection; the dotted line is a Gaussian with FWHM of 1.33 ACIS pixels.

distributed grating periods ($\Delta p/p < 2.5 \times 10^{-4}$) so that the first term is important in the spectral resolution only at very high dispersion (low energy). The mirror point response function has a nearly constant size Δy and dominates the resolution over most of the HETGS band, as shown in Figure 8.18 for both the MEGs and the HEGs. At very low energies there is a contribution from variation in the grating periods. This variation is specified for the HEG and MEG gratings separately in the *MARX* parameter file.

Tests at XRCF discovered that there is a low-level of incoherent dispersion (or “scattering”) in the HEG spectra. This scattering effect distributes a small amount of the flux along the dispersion direction. The total power involved is only 1.0% of the total in first order but the light is irregularly distributed between the coherently dispersed orders. Assuming that the power distribution scales with the first order dispersion distance, there is no more than 0.02% of the first order flux in any bin of width 0.01λ . There has been no scattering detected in the MEG spectra to a level of order 100 times fainter than in the HEG. See the HETG Ground Calibration Report listed at the end of this chapter for further details.

LRF: Cross-Dispersion Direction

The profile in the cross-dispersion direction is dominated by three effects: mirror blur, grating roll variations, and astigmatism, a by-product of the Rowland design which optimizes spectral resolution. The cross-dispersion profile that results from astigmatism is slightly edge brightened, but quasi-uniform, with a length at the Rowland focus of $2R_f y^2/R_s^2$, where R_f is the radius of the ring of facets on the HETGS structure and dominates the size of the cross dispersion profile at large dispersion.

The spread of facet roll angles (defining the dispersion direction for each facet), $\Delta\phi$, contributes a cross-dispersion term of order $y\Delta\phi$. Sub-assembly measurements predicted $\Delta\phi = 0.42$ arc minutes rms. However, analysis of XRCF measurements lead to a somewhat larger and more complex roll angle distribution for the gratings. In addition, six misaligned MEG facets were discovered during LRF calibration tests at XRCF. The inferred roll angles were misaligned from the average dispersion direction by 5-23 arc min. On average, each facet contributes only 1/192 of the flux at any given energy, so the cross dispersion profile has small deviations in the form of peaks displaced from the main distribution.

In order to include explicitly the MEG misaligned gratings *MARX* uses “sector” files which allow the specification of grating alignment and period parameters for certain regions (sectors) of each of the four shells. Using these

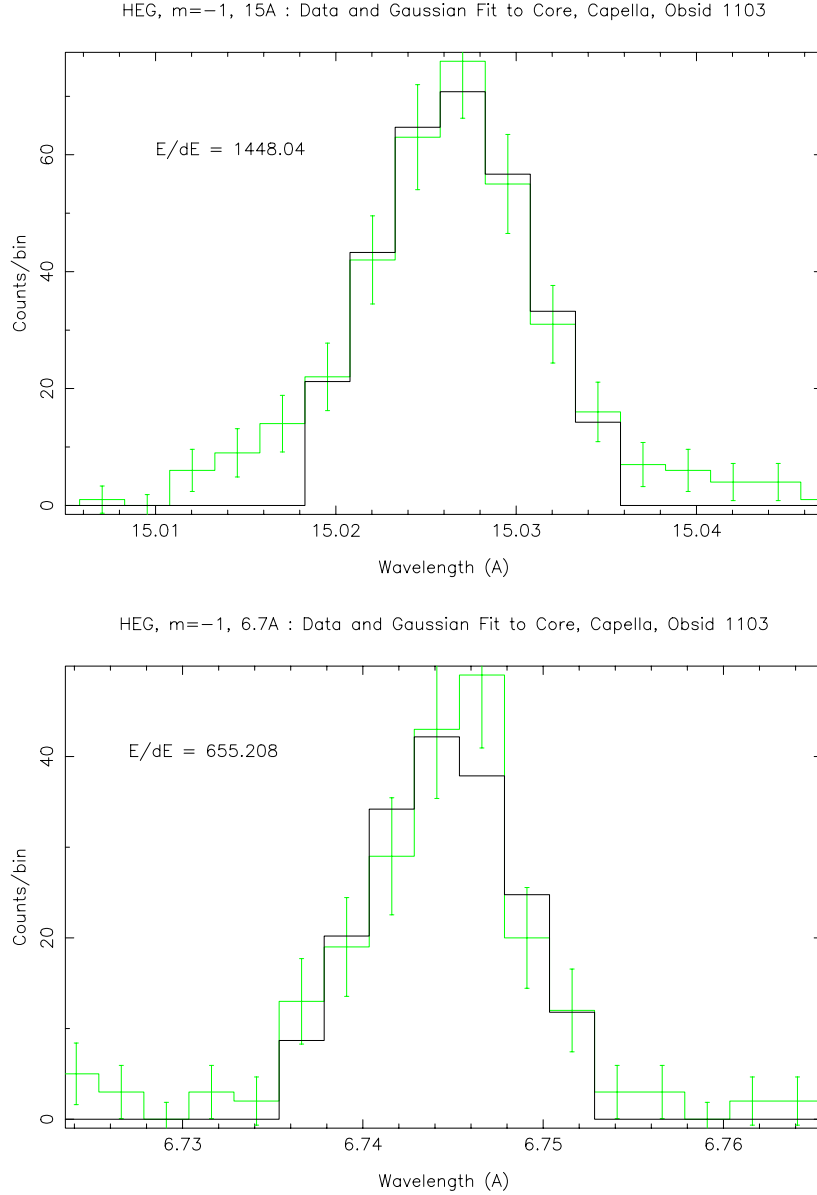


Figure 8.16: Representative Line Response Functions at two wavelengths for the HEG; 15 Å top, 6.7 Å bottom. The cores of bright lines in the HEG counterpart to the MEG Capella spectrum shown in Figure 8.2 have been fit by a Gaussian LRF using the *CXC* ISIS software; for comparison the continuous LRF is shown integrated over the data bins. $E/\Delta E$ values shown are equal to $\lambda/\Delta\lambda$ with $\Delta\lambda = 2.35\sigma$.

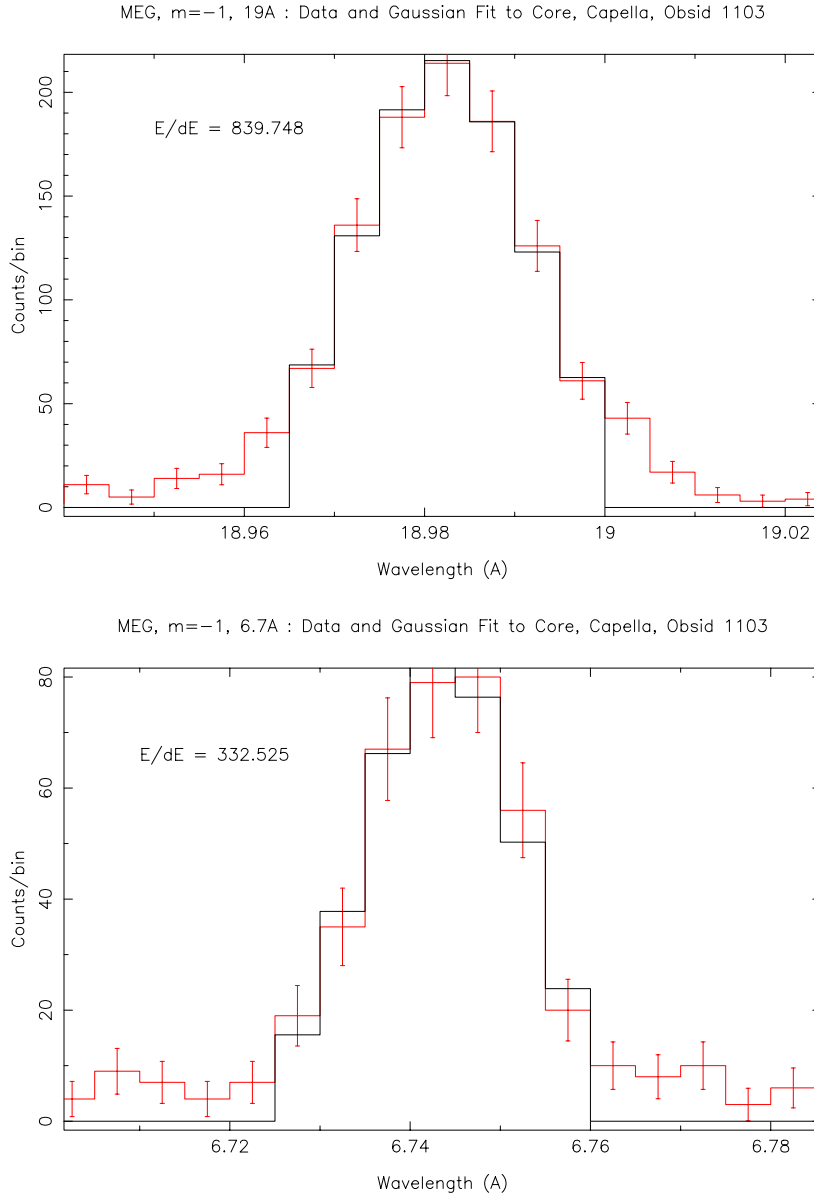


Figure 8.17: Representative Line Response Functions at two wavelengths for the MEG; 19 Å top, 6.7 Å bottom. The cores of bright lines in the MEG $m = -1$ Capella spectrum shown in Figure 8.2 have been fit by a Gaussian LRF using the *CXC* ISIS software; for comparison the continuous LRF is shown integrated over the data bins. $E/\Delta E$ values shown are equal to $\lambda/\Delta\lambda$ with $\Delta\lambda = 2.35\sigma$.

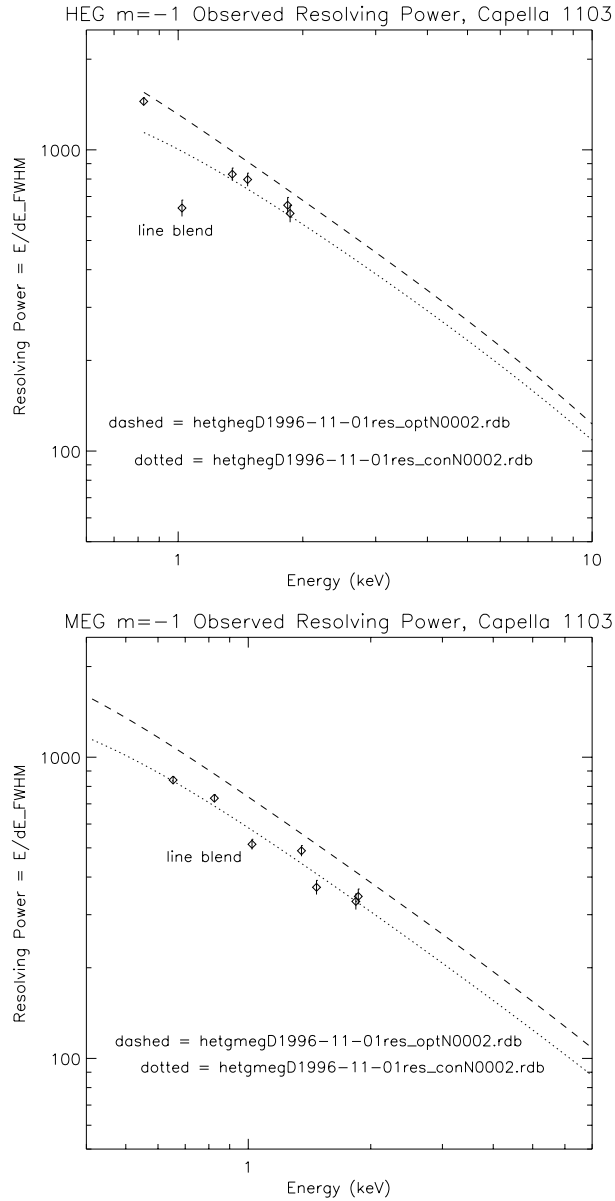


Figure 8.18: HEG and MEG Resolving Power ($E/\Delta E$ or $\lambda/\Delta\lambda$) as a function of energy for the nominal HETGS configuration. The resolving power at high energies is dominated by the telescope PSF; at low energies grating effects enter but do not dominate. The “optimistic” dashed curve is calculated from pre-flight models and parameter values. The “conservative” dotted curve is the same except for using plausibly degraded values of aspect, focus, and grating period uniformity. The cutoff at low-energy is determined by the length of the ACIS-S array. Measurements from the HEG and MEG $m = -1$ spectra, e.g., Figure 8.2, are typical of flight performance and are shown here by the diamond symbols. The values plotted are the as-measured values and therefore include any natural line width in the lines; for example, the “line” around 12.2 \AA is well below the expected value and is in fact a blend of Fe and Ne lines.

files, the agreement seen with the XRCF measurements and preliminary flight measurements is very good. For the MEG the misaligned gratings are explicitly included and the rest of the gratings' $\Delta\phi$ term is modeled as the sum of two Gaussian distributions centered at +1 and -1 arc minute w.r.t. the nominal axis, each with an rms value of 1.5 arc minutes. For the HEG a more pronounced bi-gaussian distribution is observed and modeled: the Gaussians are offset by -1.35 and +1.65 arc minutes, each with a 1 arc minute rms, and in a relative ratio of 55:45.

In each case, these effects contribute a cross-dispersion blur less than 2 ACIS pixels rms everywhere along the HEG and MEG dispersion axes and are accurately included in *MARX* version 2.50.

Extended and off-axis targets

Since dispersion along the Y axis is equivalent to wavelength or energy for the HETGS, any extent of the zeroth order image in the dispersion direction will degrade the resolution from that which could be achieved from a point source. The zeroth-order image size can increase in several ways: the telescope is out of focus, the source is off-axis, or there is a natural extent to the source.

The observation of extended sources with the HETGS adds complexity. Chiefly, the position of an event in the focal plane is no longer a unique function of the position in the source and energy. Figure 8.19 illustrates one possible consequence for extended sources - a degradation of the apparent spectral resolution.

Likewise, as the source off-axis angle increases, the image gets larger. Within 2' of the focal point, the PSF is close to that shown in Chapter 4, Figure 4.5. At 1 keV over 50% of the energy will fall in a circle of radius 0.5". The increase in image size with larger off-axis angle is shown in Figure 4.8. At 5' off-axis 50% of the energy falls within a radius of 1.5". At 10', the radius is 6". The effects of off-axis angle on the spectral resolution are shown in Figure 8.20.

The discussion and plots above assume a spectrally homogeneous source. The more general and complex case of a source with spatial-spectral variations is discussed in the Extended Source and Spatial Spectral Effects section below.

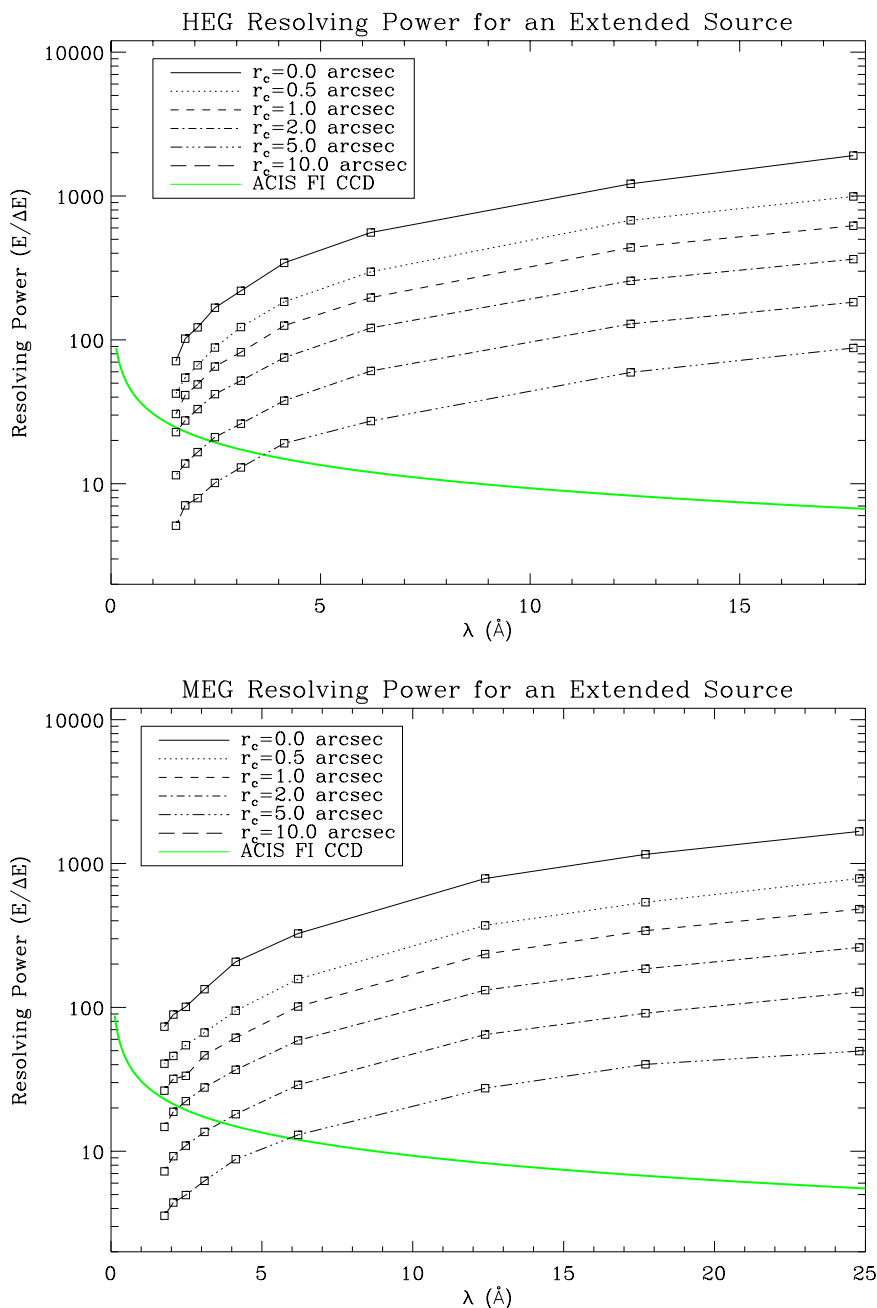


Figure 8.19: The effects of source size on the apparent HETGS spectral resolution. This *MARX* simulation uses a cluster (of galaxies) Beta model for the surface brightness profile. The Beta model is parameterized by a core radius (r_c) which represents the extension of the source. The effect on the apparent resolving power ($E/\Delta E$) is shown as a function of photon energy for source sizes of $0''$, $0.5''$, $1''$, $2''$, $5''$, and $10''$. The spectral resolution of an ACIS FI CCD near the framestore region is shown for comparison.

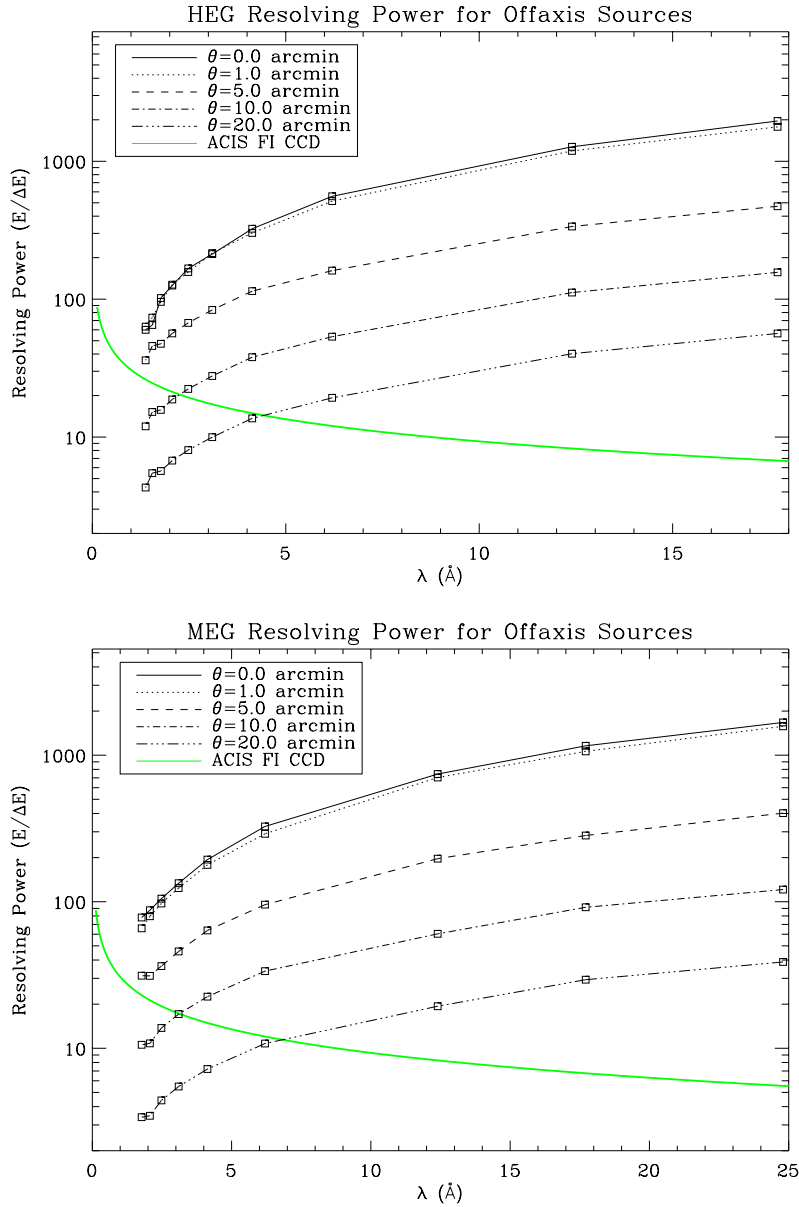


Figure 8.20: The effects of off-axis pointing on the HETG grating spectral resolution. Using *MARX*, we have simulated an observation of a point source at increasing off-axis positions. The effect on the resolving power ($E/\Delta E$) is shown as a function of photon energy for off-axis angles of $0'$, $1'$, $5'$, $10'$, and $20'$. The spectral resolution of an ACIS Front Illuminated (FI) CCD at a point near the framestore region is shown for comparison.

8.2.3 Background

Since the HETG is always used in conjunction with a focal-plane detector, spectra from the HETGS will have that detector's intrinsic, environmental, and cosmic background. In addition to this "normal" background, scattering from the gratings will produce extraneous photons in locations unexpected on the basis of the simple grating equation. One such effect is the scattering along the dispersion direction described in the Line Response Function section.

The ACIS background is described in chapter 6 and discussed in some detail in section 6.10 CCD.

8.2.4 Absolute Wavelength

The HETGS-measured wavelength depends, as the grating equation implies, on knowing the diffraction angle, the diffraction order, and the grating average period. The angle depends on knowing the HETGS geometry, specifically the Rowland Spacing and the ACIS-S pixel size and configuration.

Preliminary comparisons between measured and expected emission line wavelengths indicates an agreement to the accuracies listed in Table 8.1.

8.3 Calibration

8.3.1 Pre-launch Calibration

Prelaunch calibration of the HETG and HETGS is extensively treated in the HETG Ground Calibration Report and the web pages where the reader is directed for more details - see listings at the end of this Chapter.

Laboratory measurements of X-ray efficiency and period uniformity have been made on each grating facet (Dewey et al. 1994; Markert et al. 1995; Flanagan et al. 1995). Synchrotron data has been collected on "reference" gratings. A laser-reflection diffractometer has measured period variations within and between gratings to order of $dp/p = 1 \times 10^{-4}$, and the temperature dependence of the period. Measurements have been made of the alignment of each grating to the support plate, and hence of the angle between the HEG and MEG spectra. The support vignetting factor and point-spread-function have also been measured.

The complete HRMA/HETG optics were tested at the X-ray Calibration Facility (XRCF) at the Marshall Space Flight Center in conjunction with various non-flight detectors and the flight science instruments (SIs). Tests

were performed to measure the system spectral resolution and the cross-dispersion profile at several energies and orders and for a few off-axis angles to verify models of the HETG performance. As mentioned earlier in the LRF sections, two unexpected effects were observed: a small fraction of MEG facets are misaligned and the HEG shows some incoherently diffracted light between the orders. The average periods of the gratings were measured to a part in 10,000 or better, and the linear dispersion relation was verified to the measurement accuracy ($< 10 \mu$). Furthermore, many other tests were performed to verify the grating efficiencies and the overall system effective area.

Analysis of the ground calibrations is nearing completion and so far there are no additional surprises. XRCF measurements of the absolute effective area for the full HETGS system agree with predictions to better than 10-20%. Continuum source data sets were used to search for unexpected spectral features and none have been noted so far, confirming the detailed structure of the HETGS *ARF*'s.

8.3.2 In Flight Calibration

A list of public, calibration observations made with the HETGS to date (12/5/99) is presented in Table 8.3. Several types of in flight calibration observations are included. HETG first light and focus tests were carried out with Capella. These observations were also used to measure the orientations of the grating dispersion directions on ACIS-S. The Crab observations serve as a baseline effective area data set and calibrate the continuous clocking readout mode (CC).

Two stars with active coronae, Capella and HR1099, have been observed with long exposures; for instrument calibration these observations have served to confirm the resolving power of the HETGS, calibrate the ACIS-S chip gaps, and verify the dispersion relation in flight. Many different emission lines have been observed, statistics on the brightest allow their centroids to be measured to within 10^{-3} \AA in first order.

Continuum sources, Mkn 421 and the X-ray binary Cyg X-2 have been observed to verify that there are no unusual spectral features and that contamination is small; in the January 2000 time frame quasar 3C 273 will be observed as well. Other targets were observed to help verify that the overall effective area is correct: e.g. the Crab nebula was observed using the ACIS-S in a continuous clocking mode. Several of these sources, such as Cyg X-2 and the stars with active coronae, are being used to confirm the cross-dispersion and emission line profiles.

Table 8.3: HETGS Calibration Observations

Obsid(s)	Date(s)	Target	Comments
459	Jan-2000	3C 273	Effective Area
457	11/5/99	Mkn 421	Effective Area
1103, 1318	9/24,25/99	Capella	Emission Line Project
1102	9/23-24/99	Cyg X-2	Effective Area
62538, 1252	9/14,17/99	HR 1099	Emission Line Project
170, 168	8/29/99	Crab Nebula	Effective Area and CC mode
1101, 1237	8/29/99	Capella	Focus set: “+0.2 mm”
1100, 1236	8/28/99	Capella	Focus set: “-0.2 mm”
1099, 1235	8/28/99	Capella	Focus set: “0.0 mm”
1098	8/28/99	Capella	HETGS First-light

At periodic intervals re-observation of some of these targets is planned. For example in March 2000, the Crab and Capella will be re-observed in order to confirm that the effective area and dispersion relations are stable.

8.4 HETG Operations

8.4.1 Operational Constraints

There are no consumables and no telemetry to or from the HETG. There are no known limits to the lifetime of the gratings. The gratings are either in the beam, or not, with less than 10 minutes transition time.

The HETG has two modes: stowed and in-use. The HETG can be commanded to “in-use” or “stowed” mode at any time post-launch. Note, however, that the HETG and the LETG (Low Energy Transmission Grating) can mechanically interfere if they are both “in-use” (or in motion) at the same time, a condition prevented by ground and flight procedures, commands, and software.

There are two “failsafe” mechanisms, one for each grating. These provide for removal of the grating from its in-use position, but once so used, it would be impossible to reverse the action. Thus the decision to command a failsafe will not be taken lightly.

8.4.2 Output Data

There are no data from the HETG itself. The data are generated by the focal-plane imager in its format (e.g. Figure 8.1).

8.4.3 Performance Monitoring, Health and Safety

The HETG as an assembly has sensors or electronics. The mechanisms to insert and retract the HETG were provided by TRW. If necessary, it may be possible to check individual grating facets with an extreme out-of-focus image.

In the event that performance monitoring of the spacecraft indicates significant changes in performance, appropriate recalibration of the HETG will be done.

8.4.4 Thermal response time

There is a negligible thermal time constant for the HETG to equilibrate from near-wall storage to “in-use” temperature environments. The temperature dependence of the resolution and energy scales have been minimized through use of low-expansion material (“Invar”) and single-point-mounted facet-frames. Thus, the support structure may expand or contract, but the facets will not.

8.4.5 Observation frequency/duty cycle

There are no instrument limits on exposure time.

8.4.6 Radiation Considerations

The main radiation concern for the HETG is effects to the polyimide support material. When this material was considered in another context, as windows for proportional counters, test were carried out and no increase in (low) leak rate was seen at a dosage of 9 kRad. For the HETG, the main concern is loss of mechanical integrity. Such effects are reported in the literature to occur at levels of 1000 MRads.

The estimated proton dose to the HETG polyimide is of order 1 kRad per orbit when the HETG is inserted, and much lower values when HETG is in its stowed position. Current practice is to have the HETG retracted during radiation passages; however, even if it were left inserted the total exposure would be ≈ 1 MRad over 10 years, well below the 1000 MRad level.

A secondary concern would be changes to the Gold grating bars (which, when in place, face the HRMA) due to sputtering by particles, particularly for the high-aspect ratio HEG gratings. Monitoring of diffraction order

ratios would be sensitive to these changes, if significant. To-date, there is no evidence of such an effect.

8.5 Observation Planning

The following sections provide assorted information and topics relevant to planning an HETGS observation.

8.5.1 Focal Plane Detector Considerations

The HETG was designed for use with the ACIS-S detector and this will be the standard detector for most observations. However, the other 3 detectors can be used to satisfy particular requirements. Full details are contained in the ACIS and HRC chapters. Some considerations are:

- ACIS or HRC: ACIS provides energy resolution which is useful for order separation, background suppression, and discrimination between sources if more than one is in the field. The HRC is likely only to be useful if high time resolution is necessary and the ACIS CC mode is not useful for the observation in question. Note that the high background in HRC-S makes the HRC-I the more attractive detector – see Chapter 7.
- Operating mode of ACIS-S: The ACIS-S array can operate in many modes, giving control over e.g., the read-area, pixel-binning, and read-frequency.
- Location on the detector of the target: pointing offsets may be specified and used to include or exclude nearby sources, to keep an expected spectral feature clear of the gaps between chips, to put a desired low-energy feature on the higher efficiency BI chip S1, etc.
- HRMA point-spread-function: Offsets from the optical axis greater than one or two arc minutes will degrade the image - see Chapter 4 and also which in turn broadens the LRF as discussed in section 8.2.2.
- Change the aimpoint: The SIM allows motion of the detectors in the spacecraft Z direction, i.e., the cross-dispersion direction. This offset ability can be used to keep the dispersed X closer to the ACIS readouts and reduce somewhat the effects of the degraded energy resolution of the FI chips. For a point source, nominal recommended offsets are

−3 mm (−1193 motor steps) and −4 mm (−1591 motor steps) for ACIS TE and CC modes respectively. NB: this sort of offset may not be desirable for extended targets or when there are several sources in the field.

- Orientation of multiple (or extended) sources: One may need to request a particular spacecraft roll-angle to avoid overlapping spectra or reject other sources. Depending on the target’s celestial position and on the desired roll angle, a roll angle constraint will impose restrictions on the dates of target availability. See the discussion in Chapter3.

8.5.2 Complications from multiple sources

Multiple sources in the field of view can also lead to effects which impact the observation.

Faint background sources

The position of a faint second source might be such that the zeroth-order image falls directly on the dispersion pattern from the prime target. In this case, the zeroth-order image of the second source appears as a line in the dispersed image of the prime target. The ACIS energy spectrum can be used to minimize the contribution to the measured dispersed spectrum of the target. Also, the lack of a feature in the other side of the dispersion pattern will indicate that the “line” is spurious.

Two point sources of comparable intensity

The dispersed MEG and HEG spectra of two sources will cross if the objects are fairly close. When the two targets are less than about 3′ apart, both will be nearly in focus, so the spectra appear like two flattened “X”s. Normally, the ACIS-S pulse heights of the events will be significantly different in the regions of overlap, so that one may distinguish the events from two sources in data analysis. There are specific roll angles, however, where the identification of the source is ambiguous; a rare occurrence, but one the user should be aware of.

An example is shown in figure 8.21, where the MEG spectrum of the brighter object (source 1) overlaps the HEG spectrum of the fainter target (source 2). The first order energies at the overlap positions are a factor of 3 apart, so that $E_2 = 3 \times E_1$. An ambiguity arises from 3rd order photons from source 1 at $3 \times E_1$, which cannot be discriminated by ACIS from photons

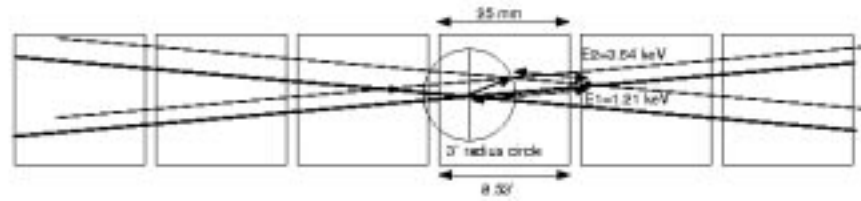


Figure 8.21: An idealized sketch of a 'collision' between two sources separated by 3 arcmin; source 1 on-axis and source 2 at PA of -67.5° . At the 'collision' point, third-order photons from source 1 will have an energy $3 \times 1.21 = 3.63$ keV and ACIS can not distinguish these from the first-order source-2 photons, at 3.64 keV. NB: the actual dimensions on the figure are approximate.

of about the same energy but from source 2. For a given angular distance between sources, it is possible to specify the observatory roll angle so that collisions like the one shown in the top of Figure 8.22 are avoided.

A strong source lying outside the field

The proposer should also take into consideration sources, other than the target, that are within the field of view of the telescope, but out of the field of view of the detector. Parts of the image of the dispersed spectrum may still fall onto the detector. If this situation presents a problem, a sensible choice of a range of allowable roll angles might ameliorate the situation.

8.5.3 Extended Sources and Spatial-Spectral Effects

The case of a simply extended, spectrally homogeneous source was described in section 8.2.2, under the heading, “Extended and off-axis targets”. Here more complex cases are briefly considered, generally these must be treated on a case-by-case basis.

For extended sources with multiple condensations, careful selection of the roll angle (see e.g. section 8.5.2) might make the data easier to analyze and interpret. It may also be possible to model the spectrum given information from the zero order image and/or a short ACIS exposure with the grating retracted. The ACIS spectrum can then be used as an initial guess in modeling the dispersed HEG and MEG spectra.

The diffracted images of extended objects which lead to position dependent spectra are complicated, but challenging. On the one hand, the complexity indicates that information is present but extracting the information is more difficult for a point or an extended source with a uniform-spectrum. In particular, the plus and minus order images may not have the same appearance. A simple example of this effect was seen in XRCF data sets using the double crystal monochromator source e.g., H-HAS-EA-8.003 which can be found at

http://hea-www.harvard.edu/acis/xrcf_archive

and is schematically presented and described in Figure 8.23. For astrophysical sources, variations in temperature, abundances, Doppler velocities, cooling flows, etc. can all create spatial-spectral variations. For these complex objects general analysis techniques are not available and forward folding of the spatial-spectral model through *MARX* is the best way to study these effects and to plan potential observations.

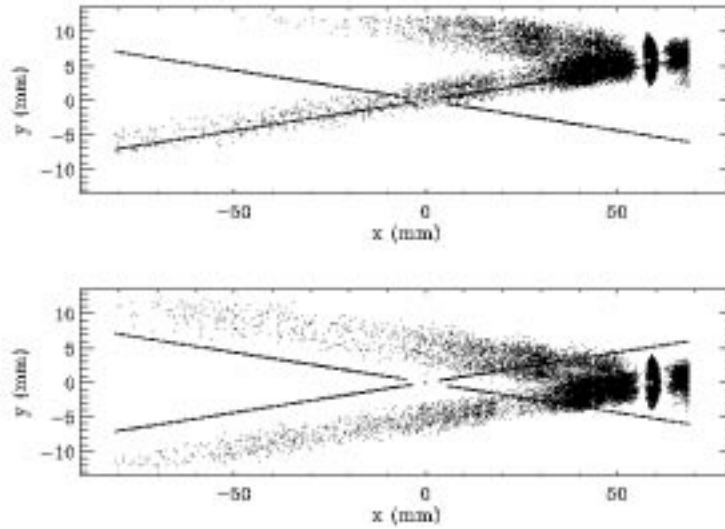


Figure 8.22: A simulation of spectral contamination caused by a second source in the field. The image of the dispersed spectrum from the second source is seen in the upper right hand corner for particular choice of roll angle. Note that the image is highly extended as the source is 20 arcmin off-axis. For this roll angle, there is significant overlap of the two images. In the lower panel we show the same situation, but for a different choice of roll angle. Here the overlap of the images is minimal and data analysis will be further aided through the use of energy discrimination provided by the ACIS-S detector. Note that the axes are labelled with “x” and “y” whereas the preferred convention is “y” and “z”.

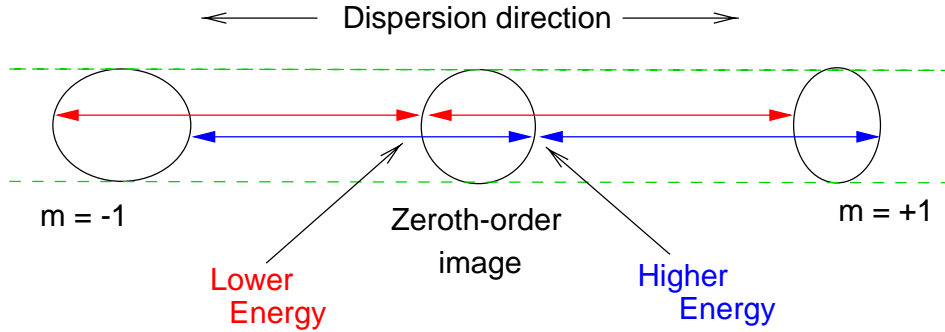


Figure 8.23: HETGS spatial-spectral effect example. In this schematic, a zeroth-order ring image emits at an energy which varies across the ring’s diameter in the dispersion direction emitting lower-energy photons on the left and higher-energy photons on the right. The resulting diffracted images in ± 1 st orders have different appearances due to the spatial-spectral interaction. In the cross-dispersion direction, however, the images have the same extent.

8.5.4 Optimizing Detection of Isolated Emission Lines: Choice of Spectrometer

If the scientific objectives require detecting emission lines against a moderately bright continuum, then the signal/noise ratio depends on the effective area of the instrument in combination with the spectrometer resolving power. Here, we compute the relative merits of each *Chandra* spectrometer in this context.

Three cases where this analysis will not apply will be when the science goals involve (1) resolving weak lines, (2) significantly extended sources, and (3) lines that are substantially broadened. In case 1, the highest resolving power at the energy of interest would be indicated while in case 3, it would probably be better to choose the spectrometer for which the spectral resolution matches or slightly resolves the emission lines. Case 2 is treated in section 8.2.2.

When a line is isolated and appears against a “background” due primarily to the source continuum, then the signal/noise ratio is given by:

$$\frac{C_L}{\sigma_C} = \frac{A_E T W n_E}{[A_E T (dE)_E n_E]^{1/2}}$$

where C_L is the number of counts in the emission line, σ_C gives the uncertainty in this number, A_E is the instrumental effective area, T is the

integration time, n_E is the photon flux in the continuum in units of photon $\text{cm}^{-2} \text{s}^{-1} \text{keV}^{-1}$, W is the equivalent width of the line in keV, and $(dE)_E$ is the spectral resolution of the spectrometer in keV. The signal-to-noise ratio per fractional equivalent width, $W_f = W/E$, is then:

$$\frac{C_L/\sigma_C}{W_f} = (Tn_E)^{1/2} \left[\frac{A_E E}{(dE)_E} \right]^{1/2}$$

This last instrument-specific term is the figure of merit for the spectrometers:

$$F_E \equiv [A_E (E/dE)_E]^{1/2}$$

Observation and source parameters are taken out to show the dependence of the signal/noise ratio on the characteristic figure of merit, F_E , of the spectrometer which is, of course, a function of energy.

The merit functions F_E were computed for several grating-detector combinations and for the ACIS-S and the ACIS-I used without a grating. In the current context, the term ‘ACIS-S’ means that parameters for the back illuminated (BI) chips were used, whereas ‘ACIS-I’ indicates the use of front illuminated (FI) chip parameters. The results are shown in figures 8.24 and 8.25. The first of these figures indicates that the LETG with the HRC-S is preferred if the emission lines of interest have wavelengths longer than 20 Å (or 0.62 keV) while the HETGS is best for emission lines shorter than about 16 Å (or 0.78 keV). In the energy range from 0.62 keV to 0.78 keV, the LETG with ACIS-S would give the best results.

The second of these figures shows that although the grating spectrometers are better for detecting isolated lines at low energies, the ACIS detectors are comparable at high energies (at least near the readout edge of the chips).

Of course, all these considerations are tempered by the additional features of each instrument setup. For example, this calculation does not take into account instrumental background effects nor the additional continuum that may result from higher energy flux detected in higher orders when the LETG is used with the HRC-S. The reduction of the line detectability then depends on the source spectrum.

Additional discussion concerning signal-to-noise estimates for grating observations may be found in Chapter 9 in section 9.5.1.

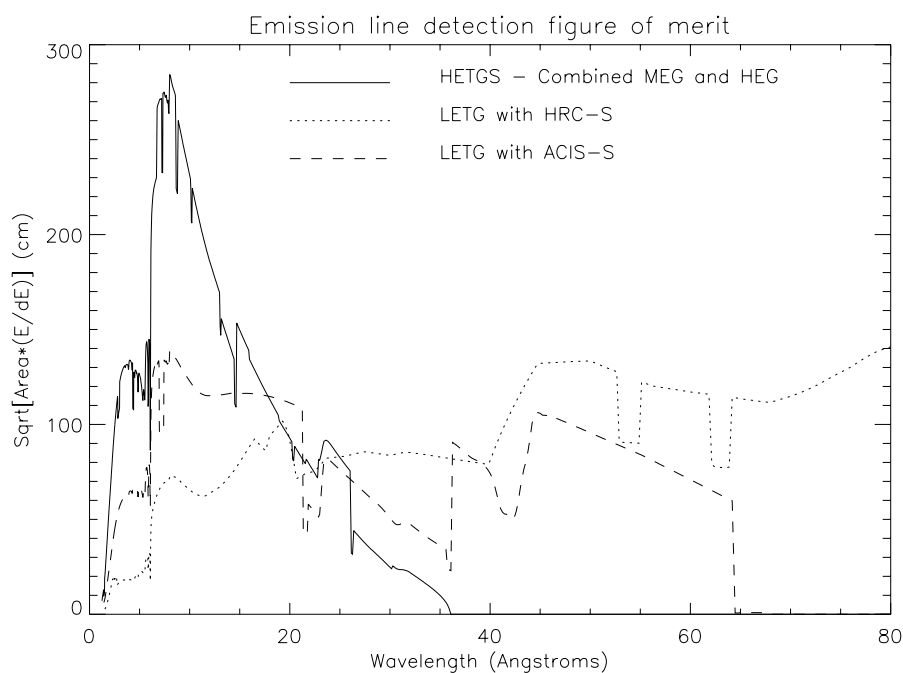


Figure 8.24: The figure of merit for detecting isolated emission lines computed according to the equations in section 8.5.4 for the HETGS, LETG with HRC-S and for the LETG with ACIS-S. The results indicate that the LETG with the HRC-S is preferred if the emission lines of interest have wavelengths longer than 20 Å (or 0.62 keV) while the HETGS is best for emission lines shorter than about 16 Å (or 0.78 keV).

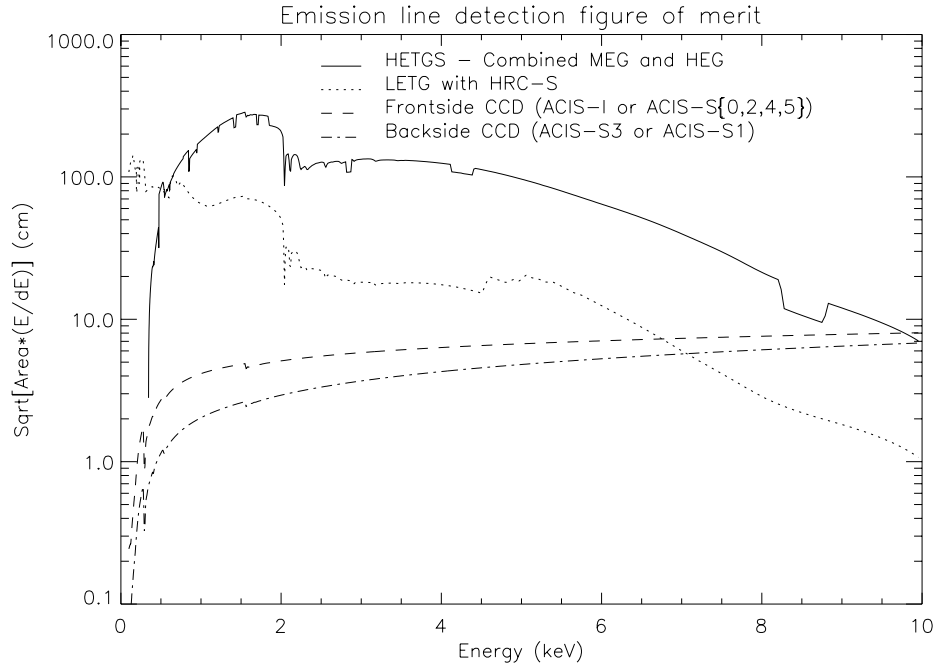


Figure 8.25: The figure of merit for detecting isolated emission lines computed according to the equations of section 8.5.4 for the HETGS, the LETG with the HRC-S, and the ACIS without either grating. For the latter case, separate curves are given for FI and BI chips. Although the grating spectrometers are better for detecting isolated lines at low energies, the ACIS detectors are comparable at high energies. NB: the ACIS FI chips have suffered degradation in spectral resolution; the plotted curve is pre-launch and now pertains only to the area of each chip near the readout edge.

8.6 Example of Planning an observation

In order to integrate the various topics presented, an example of observation planning is outlined here. There are many ways to obtain estimates of performance such as the use of ‘*XSPEC*’ with *ARF*’s and *RMF*’s and the use of *MARX*, *marx2fits*, and *CXCDS* tools. Here we present an example using *PIMMS*.

Let us assume that you want to measure the spectrum of a nearby star ($N_H = 1 \times 10^{19}$) with known X-ray luminosity, temperature, and distance. You are particularly interested in the shape of a line at 1.80 keV. You first calculate the X-ray flux and input this to *PIMMS* in order to calculate count rates for the desired source spectrum and instrument options.

8.6.1 Counting rates from *PIMMS*

The *PIMMS* software described in Chapter 11 will calculate count rates from input flux. This will be used first to calculate the rate of all photons dispersed in the first order of the HETGS. (Note, in these examples, + and - orders are summed.) In this example, the source is thermal with temperature ≈ 1 keV. Total flux in the *Chandra* band (0.2 to 10 keV) is 1×10^{-10} ergs $\text{cm}^{-2} \text{s}^{-1}$.

- Bring up the *PIMMS* window.
- Select Raymond-Smith model.
- Input model parameters, e.g.: $N_H = 1\text{e}19$, $kT = 1$
- Select unabsorbed flux as input.
- Enter flux = 1e-10.
- Enter the range 0.2 - 10 in both locations.
- Select ACIS-S/HETG/HEG1.
- Press OK.
- *PIMMS* predicts 0.54 counts s^{-1} in the first order of the HEG.
- Select ACIS-S/HETG/MEG1.
- Press OK.
- *PIMMS* predicts 2.04 counts s^{-1} in the first order of the MEG.
- Select ACIS-S/HETG/ORDER0.
- Press OK.
- *PIMMS* gives 2.50 counts s^{-1} in the zero order.

Example: The expected flux of the 1.8 keV line from the source is 0.001 photon $\text{cm}^{-2} \text{s}^{-1} = 2.9 \times 10^{-12}$ ergs $\text{cm}^{-2} \text{s}^{-1}$.

- Set *PIMMS* input and output ranges to a narrow band, 1.79-1.81 keV. Calculate rate due to this line.
- Select a continuum model, e.g. a power law with photon index = 1 and $N_H = 1e19$. (Note that the Raymond-Smith model, because it uses coarsely binned tables with approximations to the line structure, is not suitable for this narrow-band application.)
- Select ACIS-S/HETG/HEG1.
- Enter energy range and flux.
- Press OK.
- *PIMMS* predicts 0.057 counts s^{-1} in the first order of the HEG; and, similarly, 0.130 and 0.069 counts s^{-1} in the MEG first order and in the zero order.

Note that the effective area curves in Figure 8.11 and Figures 8.7 and 8.9 might, in a pinch, be used instead of *PIMMS* to give approximate rates.

Note that Figure 8.12 can be used with these numbers to predict the rates in higher orders. Thus $0.1 \times 0.13 = 0.013$ counts s^{-1} is expected in the MEG third order.

This has turned out to be a strong source. You pick the ACIS-S/HETG combination because resolving power is highest (500) with plenty of signal from the 1.8 keV line of interest. The observations will thus produce a dispersed spectrum from the HEG and MEG and a spectrum of the zeroth-order from the BI S3 chip. A modest exposure of 10^4 sec will yield 570 counts in the dispersed 1.8 keV line, and 5400 counts in the first order HEG spectrum; 20,000 counts in the MEG spectrum, and 1300 counts in the MEG-dispersed line 1.8 keV line.

8.6.2 Choice of grating and detector

PIMMS can be used to estimate fluxes for other grating/detector combinations and the spectral resolving power can be estimated from Figure 8.18. To illustrate instrument options, more examples than necessary are given in Table 8.4. We used the same spectral forms as the previous examples. NB: spectral resolution for the FI ACIS chips ('ACIS-I') refer to the area closest to the framestore (resolution = 21). At the far edge of the chip, the resolution has dropped to about 5 because of the radiation damage.

Table 8.4: *PIMMS* results for example HETGS observation

Instrument/grating	Rate (c s ⁻¹)	Resolving power @ 1.8 keV	Rate (c s ⁻¹) @ 1.8 keV
ACIS-I	17.5	<21	0.52
ACIS-S-BI	35.5	17	0.57
ACIS-S/HETG/HEG1	0.54	500	0.057
ACIS-S/HETG/MEG1	2.04	250	0.130
ACIS-S/HETG/ORDER0	2.50	17	0.069
ACIS-S/LETG/LETG1	3.61	100	0.116
ACIS-S/LETG/ORDER0	2.55	17	0.019
HRC-S/LETG/LETG1	1.58	100	0.033

8.6.3 Choice of ACIS Mode

The standard ACIS readout mode is “Timed Exposure” (TE) with graded events. Pile-up will usually not be a problem in the diffuse first order continuum. The 1.8 keV lines in the HEG-dispersed spectrum will have the appearance of a point source and the counting rate will be $.057/2 = .028$ counts s⁻¹ in each of the (+/-) orders. Using the pileup estimator (see Chapter 6 section 6.17.2) we find that approximately 2% of the events will appear at $(2 \times 1.8 =) 3.6$ keV (2 photons in one pixel during the 3 s chip integration) and can be identified via the ACIS spectrum.

You decide that 500 counts are needed in the 1.8 keV line at the highest resolution which will require binning events on a 1'' scale. Only the core of the PSF will contribute. Figure 4.6 indicates that at 2 keV 55% of the events will fall in a 1'' diameter circle. You ask for a 16,000 sec observation which should give $16,000 \times 0.55 \times 0.057 = 502$ counts.

Pileup, however, will be severe in the zero order. The core of the zero order image will not provide a useful ACIS spectrum in TE mode. To obtain this spectrum you also request a 2500 s exposure with continuous clocking (CC) mode. This exposure time will yield an ACIS zeroth-order spectrum with 5700 counts.

8.6.4 ACIS-S Gaps

If the image is placed at the nominal aim point, Table 8.2 indicates a gap spanning energies 1.689-1.716 keV in the HEG spectrum. The gap is moderately close to the line at 1.8 keV so you decide to request a Y-axis offset

pointing of $-0.33'$. This will move the gap to 1.638-1.664 keV and there is no image degradation for off-axis angles this small.

8.6.5 Other Considerations

Check for the presence of other nearby sources, which might interfere with the observation. A roll angle can be chosen to avoid or minimize interference, however this translates to a restriction on the observing window as discussed in Chapter 3.

If timing is important, a light curve with 3.24 sec resolution can be obtained by adding the dispersed events. The zero order will have too much pileup to be useful. The continuous-clocking mode data can, however, be used to search for timing structure with a resolution of 2.85 ms.

8.6.6 The Observing Proposal

Proposals are submitted with the Remote Proposal Submission (RPS) software described in Chapter 12. In this example you should submit one proposal with 2 target forms, one for each set of ACIS-S parameters. You are going to ask for 2 observations with the HETG/ACIS-S: 16,000 s in TE mode, 2500 s in CC mode. Proceed as per the instructions and, in the ‘comments’ section, write that the two observations must be contiguous.

8.7 Simulations with *MARX*

If your target is weak, it may be desirable to simulate the spectrum to demonstrate that science goals can be achieved in the observing time requested. There is a tool to do this, the “Model of AXAF Response to X-rays” (*MARX*) simulator.

MARX is a suite of programs designed to simulate the on-orbit performance of *Chandra*. It is built around a core program or engine which performs a raytrace of photon paths through all elements of the *Chandra* observatory. The user specifies a file containing the spectral energy distribution of the source to be simulated and then selects a model for the spatial distribution of the source.

Once the source has been specified, *MARX* traces the path of photons through a model of the HRMA. Models for the High Energy Transmission Grating (HETG) and Low Energy Transmission Grating (LETG) can also be included and, in the focal plane, the user has the choice of all four *Chandra* detectors.

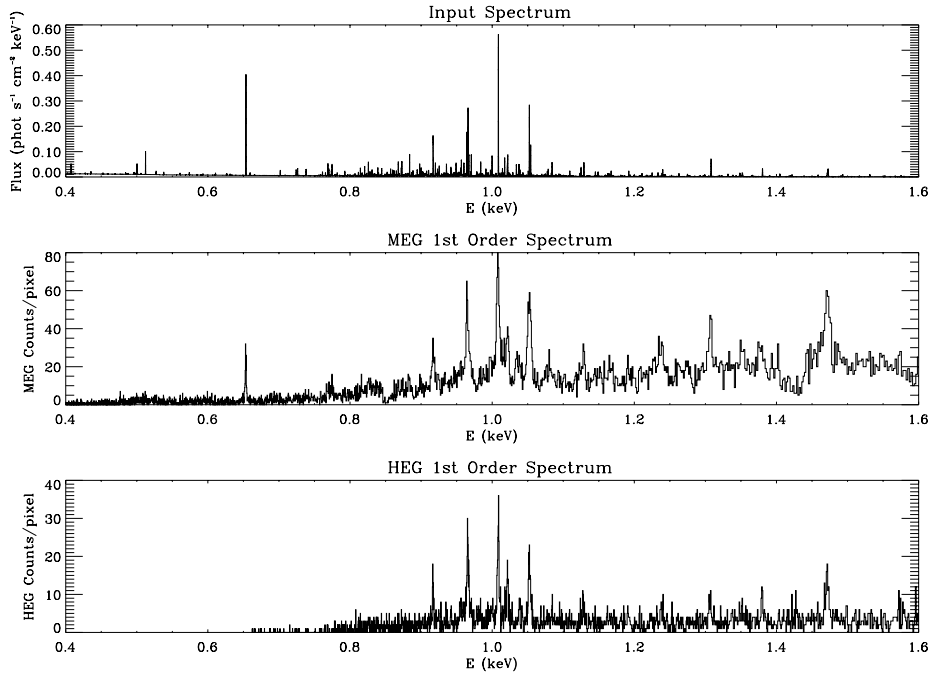


Figure 8.26: A simulation of a 60 ksec HETGS observation of the elliptical galaxy NGC1399. The galaxy's spectrum and shape were modeled as a 1.0 keV thermal plasma with a (Beta model) core radius of 1 arcsec. The upper panel shows the input spectrum while the two lower panels show the extracted MEG and HEG first order spectra, respectively.

Instructions for use of *MARX* are in Chapter 11.

To illustrate *MARX*'s capabilities, we show two examples of simulations for the HETGS in Figures 8.26 and 8.27

8.8 Document History

- Dec 92; The original version was compiled by D. Huenemoerder.
- Nov 94; updated post PDR.
- Nov 96; updated.
- May 97: updated by D. Huenemoerder and N. Evans.
- Oct 97; reorganized and updated in preparation for NRA (D. Harris).

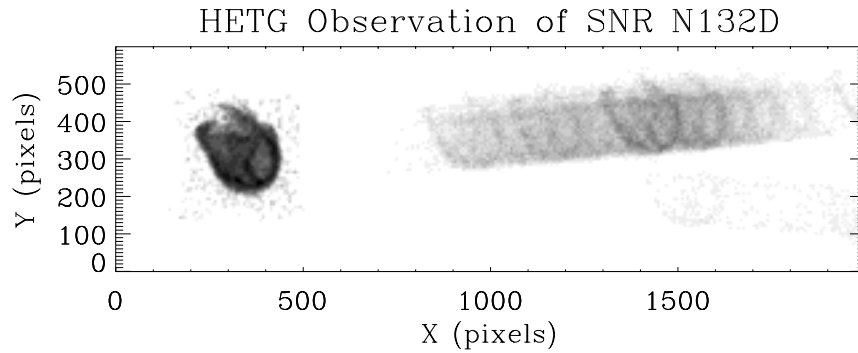


Figure 8.27: A simulation of the spectrum of N132D, a supernova remnant in the Large Magellanic Cloud with extent $\approx 2'$. The figure shows a section of the full ACIS-S image. The zeroth spectral order is very bright at the left of the image while the broad bands extending to the right represent the dispersed MEG (top) and HEG (bottom) spectra. Images of the remnant are visible in the MEG spectrum at positions (energies) of bright emission lines. The HEG spectrum is faint so that it may be difficult to see in some versions of this figure. NB: the usual convention labels the dispersion direction (the horizontal axis) as 'y' and the cross-dispersion direction as 'z'.

- Jul 99; merge Observatory Guide and Proposer's Guide (D. Harris).
- Dec 99; Re-arrange sections, update text and figures (D. Dewey).

Contributors to updates have been: C. Canizares, D. Davis, D. Dewey, N. Evans, D. Harris, D. Huenemoerder, H. Marshall, F. Seward, A. Tennant, M. Wise, and M. Weisskopf.

8.9 REFERENCES

WWW resources <http://>

space.mit.edu/HETG - HETG home page

space.mit.edu/HETG/flight.html - HETG On-Orbit page

space.mit.edu/HETG/xrcf.html - HETG (XRCF) Calibration page

space.mit.edu/HETG/report.html - HETG Ground Calibration Report access

space.mit.edu/ASC - ASC at MIT page devoted to grating analysis, spectroscopy issues, and HETG science.

asc.harvard.edu - *CXC* home page with Calibration button

wwwastro.msfc.nasa.gov/xray/xraycal/ - MSFC site with calibration reports.

Canizares, C., Schattenburg, M.L. and Smith, Henry I. 1985, *SPIE*, **597**, 253. "The High Energy Transmission Grating Spectrometer for AXAF"

Dewey, D. et al. *Grazing Incidence and Multilayer X-Ray Optical Systems, Proc. SPIE*, **3113**, (1997). "Towards the Calibration of the HETGS Effective Area"

Dewey, D., Humphries, D. N., McLean, G. Y., and Moschella, D. A. 1994, *SPIE*, **2280**, pp. 257-271, "Laboratory Calibration of X-Ray Transmission Diffraction Gratings"

- Flanagan, K. A., Dewey, D. and Bordzol, L. 1995, SPIE, **2518**, 438-456, "Calibration and Characterization of HETG Grating Elements at the MIT X-ray Grating Evaluation Facility"
- Markert, T.H., Canizares, C.R., Dewey, D., McGuire, M., Dak, C., and Schattenburg, M.L. 1994, SPIE, **2280**, 168. "The High Energy Transmission Grating for AXAF"
- Markert, T. H. et al., 1995, **SPIE**, 2518, pp. 424-437, "Modeling the Diffraction Efficiencies of the AXAF High Energy Transmission Gratings"
- Marshall, H.L. et al. *Grazing Incidence and Multilayer X-Ray Optical Systems, Proc. SPIE*, **3113**, (1997). "Towards the Calibration of the HETGS Line Response Function"
- Schattenburg, M.L. et al. 1991, Optical Engineering, **30**, 1590. "Transmission Grating Spectroscopy and the Advanced X-ray Astrophysics Facility"
- Schattenburg, M.L., Ancoin, R.J., Flemming, R.C., Plotnik, I., Porter, J., and Smith, H.I. 1994, SPIE, **2280**, 181. "Fabrication of High Energy Transmission Gratings for AXAF"

% Minor edits by Brad Wargelin Wed Mar 02 2000

Chapter 9

LETG: Low Energy Transmission Grating

9.1 Instrument Description

The Low Energy Transmission Grating (LETG) was developed under the direction of Dr. A.C. Brinkman in the Laboratory for Space Research (SRON) in Utrecht, The Netherlands, in collaboration with the Max-Planck-Institut für Extraterrestrische Physik (MPE) in Garching, Germany. The grating was manufactured in collaboration with Heidenhaim GmbH.

The Low Energy Transmission Grating Spectrometer (LETGS) is comprised of the LETG, a focal plane imaging detector and the High Resolution Mirror Assembly discussed in Chapter 4. The *Chandra* High Resolution Camera spectroscopic array (HRC-S) is the primary detector designed for use with the LETG. The spectroscopic array of the *Chandra* CCD Imaging Spectrometer (ACIS-S) can also be used, though with decreased quantum efficiency below 0.6 keV and a smaller detectable wavelength range. The High Energy Transmission Grating (HETG) used in combination with ACIS-S offers superior energy resolution and quantum efficiency above 0.78 keV. The HRC is discussed in Chapter 7, the ACIS in Chapter 6, and the HETG in Chapter 8.

The LETGS provides high resolution spectroscopy ($E/\Delta E > 1000$) between 80 and 170 Å (0.07 – 0.15 keV) and lower resolving power at shorter wavelengths. The nominal LETGS wavelength range accessible with the HRC-S, is 1.7 – 170 Å (0.07 – 7.29 keV); ACIS-S coverage is 1.4 – 63 Å (0.20 – 8.86 keV).

A summary of LETGS characteristics is given in Table 9.1.

Table 9.1: LETGS Parameters

Wavelength range	1.7–170 Å (HRC-S)
Energy range	1.4–63 Å (ACIS-S) 70–7290 eV (HRC-S) 200–8860 eV (ACIS-S)
Resolution ($\Delta\lambda$, FWHM)	0.05 Å
Resolving Power ($E/\Delta E$)	≥ 1000 (50–160 Å) $\approx 20 \times \lambda$ (3–50 Å)
Dispersion	1.148 Å/mm
Plate scale	48.80 $\mu\text{m}/\text{arcsecond}$
Effective area (with HRC-S)	1–2 cm^2 (125–170 Å) 3–7 cm^2 (60–120 Å) 7–12 cm^2 (44–60 Å) 4–8 cm^2 (19–40 Å) 10–25 cm^2 (6–18 Å) 3–5 cm^2 (2–5 Å)
Background (quiescent)	0.12 counts/pixel/100-ksec (HRC-S, on-orbit) ~ 0.04 counts/pixel/100-ksec (HRC-S, after filtering) $\ll 0.01$ counts/pixel/100-ksec (ACIS-S, on-orbit)
Detector angular size	3.37' \times 101' (HRC-S) 8.3' \times 50.6' (ACIS-S)
Pixel size	6.43 \times 6.43 μm (HRC-S) 24.0 \times 24.0 μm (ACIS-S)
Temporal resolution	16 μsec (HRC-S) 2.85 msec–3.24 sec (ACIS-S, depending on mode)
Rowland diameter	8632.31 \pm 0.50 mm
Grating material	gold
Facet frame material	stainless steel
Module material	aluminum
LETG grating parameters	
Period	0.99125 \pm 0.000087 μm
Thickness	0.474 \pm 0.0305 μm
Width	0.516 \pm 0.0188 μm
Bar Side Slope	83.8 \pm 2.27 degrees
Fine-support structure	
Period	25.4 μm
Thickness	2.5 μm
Obscuration	< 10%
Dispersion	29.4 Å/mm
Material	gold
Coarse-support structure	
Triangular height	2000 μm
Width	68 μm
Thickness	< 30 μm
Obscuration	< 10%
Dispersion	2320 Å/mm
Material	gold

9.1.1 Scientific Objectives

The LETGS provides the highest spectral resolving power (> 1000) on *Chandra* at low ($0.08 - 0.2$ keV) energies. High-resolution X-ray spectra of optically thin plasmas with temperatures between 10^5 and 10^7 K, such as stellar coronae, reveal a wealth of emission lines which provide diagnostics of temperature, density, velocity, ionization state, and elemental abundances and allow precise studies of structure, energy balance, and heating rates. Absorption features provides similar information in cases where bright compact X-ray sources are embedded in cooler, extended gas clouds.

The high resolution ($\Delta\lambda \approx 0.05$ Å) of LETGS spectra at longer wavelengths ($\gtrsim 100$ Å) also permit for the first time detailed studies of spectral line *profiles* in the X-ray region. These studies may provide non-thermal velocities of stellar coronae, flow velocities along active-region loops, orbital velocities in X-ray binaries, and upflow velocities in stellar flares.

The LETGS also allows time resolved spectroscopy, 1-D spatially resolved spectra, and spectra of multiple point sources within its 4 arcmin field of best focus.

Since the ultimate spectral resolution can only be achieved for point sources, the prime candidates for study in our Galaxy mainly comprise stellar coronae, white dwarf atmospheres, X-ray binaries, and cataclysmic variables. Extragalactic sources include relatively bright active galactic nuclei (AGN) and cooling flows in clusters of galaxies.

9.1.2 Heritage

Flat transmission gratings were flown aboard Einstein and EXOSAT. The LETG grating elements are produced using a technique similar to that used for production of the EXOSAT gratings. However, the LETG shares only basic operating principles with earlier instruments. Advanced grating technology has enabled the achievement of greater efficiency and increased dispersion. The Rowland geometry (see Figure 8.4 in Chapter 8) of the grating plate and spectroscopic arrays reduces dispersed image aberrations and hence contributes to improved spectral resolution.

9.1.3 Operating principles

When inserted behind the HRMA, the LETG diffracts X-rays into a dispersed spectrum according to the grating diffraction relation, $m\lambda = p \sin \theta$, where m is the integer order number, λ the photon wavelength, p the spatial period of the grating lines, and θ the dispersion angle. Parameters are

summarized in Table 9.1. The grating facets are mounted on an aluminum support plate which has been machined so that the centers of individual grating facets lie on a Rowland torus. The grating facets are aligned to produce a single dispersed image. Spectral resolution is determined, among other factors, by grating line density, line density variations, HRMA point-spread function, pointing stability, alignment accuracy, pixel size of the readout detector, and detector geometry. Spectra retain the timing and energy resolution of the readout detector.

9.1.4 Physical configuration

When the LETG is used, the Grating Element Support Structure (GESS), an aluminum frame approximately 110 cm in diameter and 6 cm thick, is inserted ~ 300 mm behind the rear of the HRMA and 1.4 m behind the HRMA mid-plane. It holds approximately 180 trapezoidal grating modules, which measure about 13×50 mm. A design drawing of the full GESS is shown in Figure 9.1; a closer view, showing some mounted modules, is seen in Figure 9.2. Each grating module has three circular facet rings, each of which holds a grating facet. Figure 9.3 shows empty grating modules mounted on the GESS.

Within each grating facet the grating bars are supported by perpendicular “fine support” bars and triangular “coarse support” bars. The parameters of these structures are given in Table 9.1. A schematic of the grating structure is shown in Figure 9.4. Both the fine and coarse grating supports form long-period transmission gratings themselves. The fine support produces a dispersion pattern perpendicular to the grating dispersion direction, seen in Figure 9.20 in section 9.3.7. The coarse support produces a six-pointed star pattern, shown in the 0-th order image of Sirius in Figure 9.24.

In contrast to the HETG gratings, which have a substrate, the LETG gratings are free-standing wires held by a support mesh. Since the gratings are produced from the same master mask, there is negligible variation in the period between facets. Uniformity in the grating-wire cross-sections is being carefully analyzed, however. The thickness of the gold of the grating bars on top of the support mesh determines the “phasing,” or efficiency of redistribution of photons into each spectral order in wavelengths where the gold is partially transparent. The thickness is designed to optimize the first-order response at energies of interest.

To reduce aberrations, the GESS is shaped to follow the Rowland torus. The primary readout detector (HRC-S) is made of three tilted array seg-

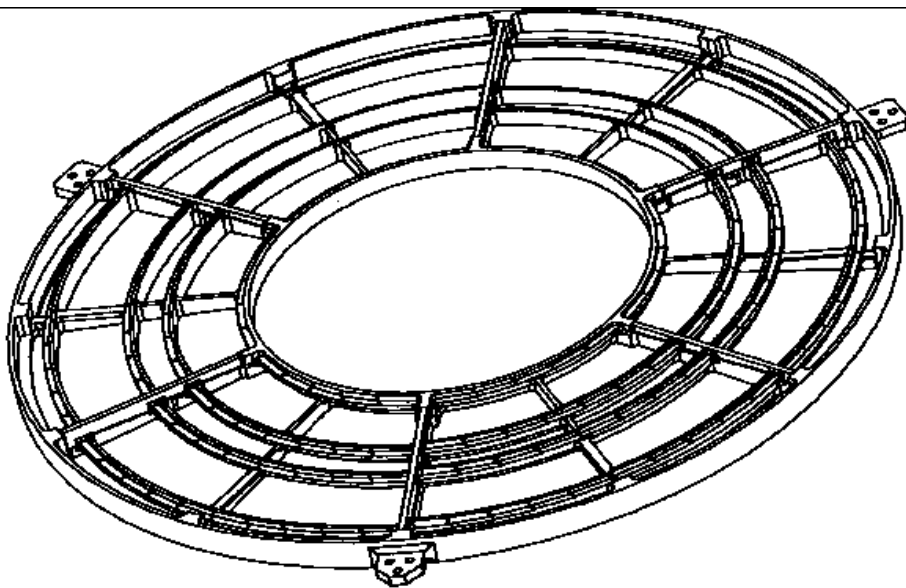


Figure 9.1: LETG Grating Element Support Structure, a machined aluminum plate approximately 110 cm in diameter which holds grating modules on a Rowland torus behind the *Chandra* mirrors.

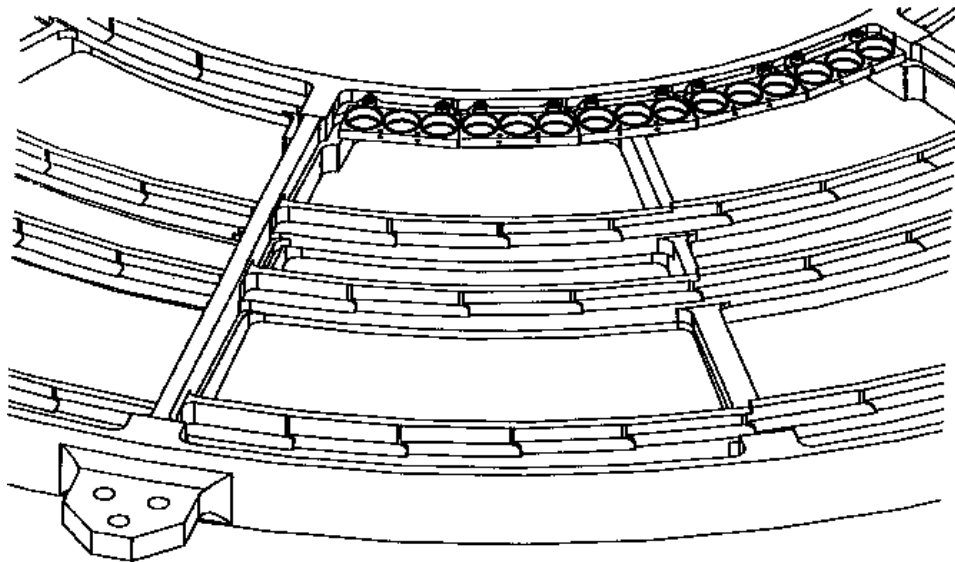


Figure 9.2: Detail of the LETG Grating Element Support Structure showing grating modules mounted on the inner annulus.

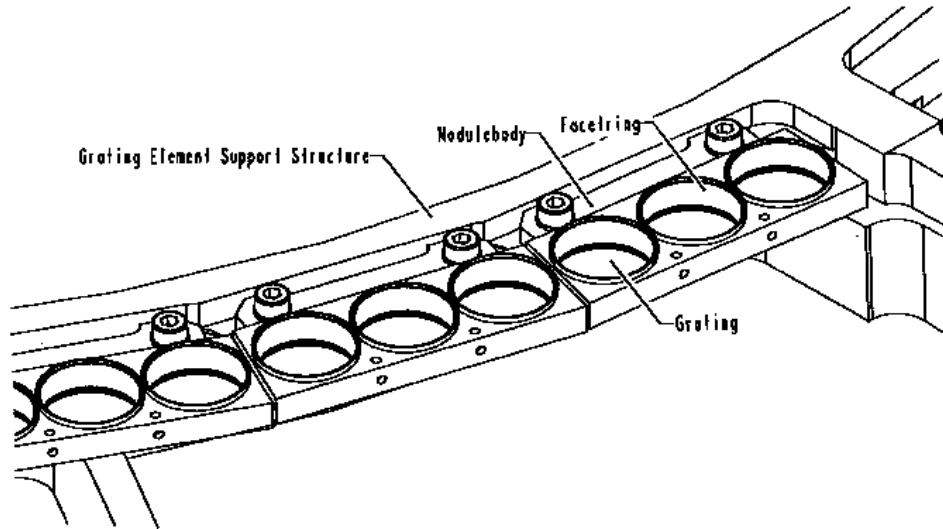


Figure 9.3: A closeup view of the LETG GESS showing two complete grating modules. Each module has three holes which hold the arrays of grating facets.

ments which also follow the Rowland circle in the image plane (see Figure 7.2 in Chapter 7, and Figure 9.5). The secondary readout detector, ACIS-S, has 6 CCDs which are similarly tilted (Chapter 6). Application of this toroidal setting improves resolution by a factor of ~ 40 at the longest wavelengths. The readout detector position along the optical bench is adjusted so that the “average” focus is best. Since the detector array elements are flat, the distance from the Rowland circle changes with position, and hence the spectral resolution changes with wavelength. The relation between the HRC-S geometry and the Rowland circle is shown in Figure 9.5. The basics of the Rowland geometry are shown in Figure 8.4.

The arrangement of the HRC-S array is shown schematically in Figure 7.1. The HRC-S subtends about 7 by 101 arcmin, though image-quality degrades substantially more than about 4 arcmin off axis. The HRC-S edges in the dispersion direction correspond to dispersed wavelengths of about 165 and 175 Å for on-axis sources.

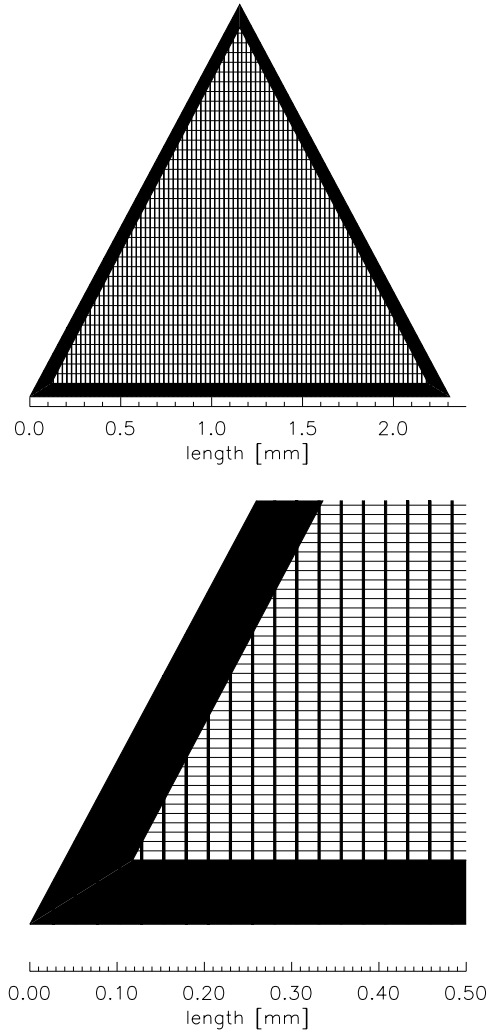


Figure 9.4: LETG facet structure schematic showing the basic shape of the individual grating elements and the relative sizes of the support structures. The upper view shows the entire facet, which is comprised of the triangular coarse support, the vertical fine supporting bars, and the (horizontal) grating bars. The grating bars themselves are not shown to scale. In the upper view every 50th bar is drawn, in the lower view every 10th bar is drawn.

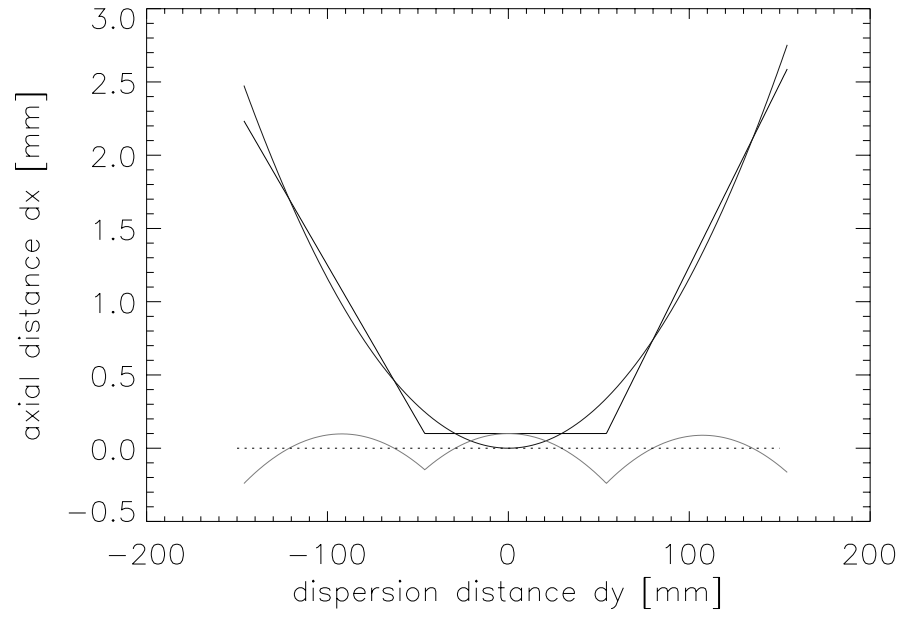


Figure 9.5: The HRC-S array elements are shown along with the Rowland circle. The scalloped line beneath them is the difference between the array position and the Rowland circle.

9.2 Calibration

9.2.1 Pre-launch Calibration

Prior to assembly, individual grating elements were tested using a visual light spectrograph at the Max-Planck-Institut. Laboratory calibration of grating period and resolution was performed for individual grating elements at optical wavelengths, and extrapolated to the X-ray range. Grating efficiencies at X-ray wavelengths were modeled using near-infrared spectrophotometry, and verified by X-ray measurements of a sample of facets. Grating facet and module alignment was also tested. LETGS efficiency, resolution, and line response function were tested at the X-ray Calibration Facility at MSFC in Huntsville, AL for both ACIS-S and HRC-S combinations. Absolute energy scale and off-axis response were also measured. Efficiency and the Line Spread Function (LSF) of the LETG and HRMA/LETG subsystem were also characterized using a detector system designed for HRMA calibration, the HRMA X-ray Detection System (HXDS). Details may be found at the first WWW reference at the end of this Chapter.

9.2.2 In Flight Calibration

In flight calibration was planned and is being executed by the *CXC* LETG team. LETG first light and focus observations were of the active late type binary Capella whose coronal spectrum is rich in narrow spectral lines (see section 9.3.7). LETGS effective area and HRC-S relative QE studies have been performed using observations of Capella and the quasar continuum source 3C273 at shorter wavelengths ($< 44 \text{ \AA}$; $> 0.28 \text{ keV}$) and using observations of the hot DA white dwarfs HZ43 and Sirius B observations at longer wavelengths ($> 44 \text{ \AA}$; $< 0.28 \text{ keV}$). Observations of Capella and the late type star Procyon (F5 IV) are also being used in calibration of the dispersion relation, resolving power, line response function, and HRC-S/LETG relative azimuthal orientation. The bright A0 V star Vega was observed with the HRC-S to test detector optical and UV susceptibility (see 7.6). Observations of the supernova remnant G21.5-0.9 were used for HRC-S effective area studies. Periodic calibration observations will be taken to monitor LETGS operation. Currently planned (February, 2000) observations are listed in Table 9.2.

Table 9.2: Planned LETGS Calibration Observations

Target	Date (months from Nov. 2000)	Purpose
G21.5-09	+3, +9	HRC-S gain, EA, QE
Vega	0, +6	UV susceptibility
HZ43	0, +6	HRC-S/LETG QE, EA
PKS2155-304	+3	LETGS EA, ACIS-S/HRC-S cross calibration
Capella	+9	LRF, dispersion relation
AR Lac	0, +6	HRC-S spatial characteristics

9.3 LETGS Performance

9.3.1 Usage

Overview

The primary use of the LETG is expected to be for on-axis observations of point sources, which produce a zero-order image and a dispersed spectrum. Typical LETGS observations range from a few to several 100 ksec; substantially longer observations may require a “Large Project” (section 10.1.6) proposal. No real-time observations are allowed, and to reduce the (small) risk that the grating mechanism might fail, the frequency of use is minimized by concatenating grating observations into consecutive time blocks whenever possible.

Since use of the LETG decreases the 0th-order intensity by roughly an order of magnitude, excessive counting rates should not generally be a concern with respect to exceeding detector count rate limits or telemetry saturation. However, some bright sources (e.g. Sco X-1) if observed for long exposure times could cause significant charge depletion in the HRC MCPs – see Chapter 7, especially section 7.12. Indeed, some observers may find it useful to insert the LETG for imaging observations simply to reduce the detected photon counting rate. Even moderate rates may cause pileup problems when using ACIS-S (see Section 6.17).

Detectors

In standard operation, the LETGS uses the HRC-S as its detector, covering a wavelength range of approximately -165 to +175 Å in first order for on-axis sources. This wavelength range can be shifted somewhat by offset pointing, but image quality degrades substantially beyond about 4'. The HRC-S does not have sufficient energy resolution to allow sorting of overlapping spectral

orders. In some cases it might be useful to use the HRC-S Low Energy Suppression Filter (LESF), as discussed in Section 9.4, in order to obtain a predominantly higher-order ($m > 1$) spectrum.

The ACIS-S detector can be used instead of the HRC-S, but effective wavelength coverage is reduced because of its smaller size in the dispersion direction and lower QE at low energies. ACIS also has lower temporal resolution, which may be important when observing periodic or rapidly varying sources. In some cases, however, those disadvantages may be outweighed by the lower background rate and intrinsic energy resolution of ACIS, which can be used to separate diffraction orders. The degraded energy resolution of the ACIS FI CCDs (section 6.7) does not pose a problem for LETG point-source observations, since the source position can be placed close to the ACIS readout, thus minimizing any effects.

In some specialized cases, the HRC-I may also be used with the LETG. A detailed discussion of the various merits of LETGS detector choices from a point of view of proposal planning is given in Section 9.4.

Off-Axis and Multiple Sources

Because the LETGS is essentially an objective-grating system, it is possible to do multi-object spectroscopy, although as noted above, the point-spread function degrades rapidly off axis. To include or reject secondary sources, or to avoid overlapping diffraction from multiple sources, observers may specify the orientation (roll angle) of the grating dispersion direction on the sky (see Chapter 3). Observations of extended sources are also possible, but at the expense of resolving power and with the loss of the simple relation between position and energy. In angular extent, the standard HRC-S spectroscopy readout region is $3.37' \times 101'$, and ACIS-S covers $8.3' \times 50.6'$. Only half of the available HRC-S width is used because of background/telemetry rate constraints. In special cases, a different detector “window” may be selected, as described in Section 9.4.

9.3.2 Wavelength Coverage and Dispersion Relation

The active extent of the HRC-S in the dispersion direction is 296 mm, almost exactly twice that for the ACIS-S. The nominal 0th-order aimpoint is offset from the detector center by 4 mm so that gaps between the three HRC-S segments (six ACIS-S segments) will occur at different wavelengths in negative and positive orders. With a dispersion of 1.148 \AA/mm for the LETG, the

standard wavelength range of the LETGS with HRC-S is therefore -165 Å and +175 Å (-79 and +93 Å with ACIS-S).

Off-Axis Pointing

Wavelength coverage can be adjusted (with an increase in wavelength range on one side and a decrease on the other) by changing the central offset (the observatory ‘y’ coordinate - see the discussion in chapter 3), although spectral resolution degrades rather quickly beyond about 4'. From the information in Table 9.1, one can derive the relationship between angular offset (in the dispersion direction) and wavelength as 3.36 Å per arc minute, so an offset of 10' would stretch the positive order coverage to approximately 208 Å (60 eV). In addition to standard on-axis observations, flight LETG calibration data have been collected at 5' off-axis (for resolution testing) and 10' off-axis (for effective area calibration).

Detector Gaps

As noted above, there are gaps between detector segments which create corresponding gaps in wavelength coverage. The location of these gaps (without dither) are listed in Table 9.3. Dithering the spacecraft will partially smooth these gaps, but observers may wish to adjust the source pointing if a favorite line falls in a gap. Standard HRC dither amplitude (full width, in both directions) is 40'' (1.95 mm), which covers 2.3 Å, and standard ACIS dither is 16'' (0.78 mm), or 0.9 Å. Also listed in Table 9.3 is the location of the UV/Ion Shield (UVIS) inner “T” filter edge (see the HRC chapter - 7). Note that the boundaries between the regions of thick and thin aluminum coatings on the UVIS in the LESF – the upper part of the “T” in Figure 7.1 – lie in the gaps between detector segments.

Also note that all these detector features are position-specific, as opposed to fixed in wavelength; the corresponding wavelengths when using a given offset pointing (in the dispersion direction) are easily derived from the 3.36 Å/arc minute relationship mentioned above. Energy-dependent features (from absorption edges in the HRMA, LETG, or detector) do *not* depend on source position to any significant degree, and are discussed in section 9.3.5, and listed in Table 9.4.

Dispersion Calibration

As of this writing (February 2000), overall wavelength calibration is accurate to a level of a few parts in 10000. Residual deviations, currently believed

Table 9.3: LETG Position-Dependent Features. Listed values are for nominal on-axis pointing without dither. Standard dithering will smear out feature edges over a range of 2.3 Å for HRC-S and 0.9 Å for ACIS-S. For offset pointing along the dispersion axis, the associated wavelengths (in Å) are shifted by approximately 3.36 times the offset (in arcmin).

Detector	Feature	Energy (keV)	Wavelength (Å)
HRC-S	UVIS Inner T	0.690	18.0
HRC-S	seg-1 end	0.075	165.5
HRC-S	seg-1/seg0 gap	0.238 - 0.217	52.0 - 57.0
HRC-S	seg0/seg+1 gap	0.205 - 0.191	60.5 - 65.0
HRC-S	seg+1 end	0.071	174.5
ACIS-S	S0 end	0.133	93.1
ACIS-S	S0/S1 gap	0.191 - 0.193	65.0 - 64.4
ACIS-S	S1/S2 gap	0.342 - 0.348	36.2 - 35.6
ACIS-S	S2/S3 gap	1.657 - 1.795	7.5 - 6.9
ACIS-S	S3/S4 gap	0.583 - 0.568	21.2 - 21.8
ACIS-S	S4/S5 gap	0.248 - 0.245	50.0 - 50.6
ACIS-S	S5 end	0.158	78.7

to arise from small-scale position non-uniformities in the HRC-S, are of the order of 1 pixel (6 μm , or 0.007 Å). It should be possible, however, to derive dispersion corrections at the sub-pixel level.

9.3.3 Resolving Power

Since the dispersion relation (Å per mm) is fixed by the grating line density and Rowland circle diameter, the LETGS resolving power is determined by its resolution, or line response function (LRF). The dominant factor is the HRMA point-spread function (PSF), which is $\sim 25 \mu\text{m}$ FWHM, depending on energy. The next most important factor is the detector PSF, which is $\sim 20 \mu\text{m}$ FWHM for the HRC-S, with 6.43- μm -wide pixels in the dispersion direction; ACIS pixels are 24 μm wide. Finally, uncertainties in correcting photon event positions for the observatory aspect, which occurs during ground data processing, does add an additional small blurring term. In most cases, the contribution of aspect errors to the PSF/LRF is of order a few μm .

When all these effects are combined, the LETGS line response function is generally $\sim 40 \mu\text{m}$ FWHM, so that a good figure of merit for LETGS res-

olution is 0.05 Å. Because the three segments of the HRC-S can not perfectly follow the Rowland circle (see Figure 9.5), however, resolution varies slightly along the detector, and is lowest near the ends of each detector segment. Resolution degradation is almost negligible when using the ACIS-S, since its six segments more closely follow the Rowland circle, although the coarser ACIS pixel size (24 μm vs. $\sim 40\text{-}\mu\text{m}$ -FWHM LRF) means that line profiles are barely sampled adequately. A plot of LETGS resolving power for an on-axis point source, based on results from an observation of Capella, is shown in Figure 9.6.

Plots of fits to the LETG+HRC-S LRF at zeroth order and at Fe XVII and XVIII lines at ~ 17 and 94 Å are given in Figure 9.7 and Figure 9.8. The fitted function is a beta model of the form:

$$I(\lambda) = [1 + \left(\frac{\lambda}{\lambda_c}\right)^2]^{-\beta}$$

which is a fairly good approximation of the LETG/HRC-S LRF. Figure 9.9 illustrates the χ^2 of fits to the zeroth order profile vs. β , and shows a best fit profile with an index of ~ 2.5 . (The Lorentzian profile has $\beta = 2.0$.)

Extended Sources

If a source is extended, there is no longer a unique mapping between the position of an event in the focal plane and wavelength, which results in the apparent degradation of spectral resolving power. For very large sources, the grating resolution may be no better than the intrinsic ACIS energy resolution.

The effect of increased source size on the apparent LETG spectral resolving power has been simulated using the MARX program, and results are shown in Figure 9.10. Currently, MARX tends to slightly overestimate resolving power, so the curves should be viewed as indicating trends rather than absolute values. Another illustration of the effect of source extent may be seen in Figure 9.28 (Section 9.4), which shows model spectra over a small wavelength range.

In each case, extended sources were modeled using a Beta model for the surface brightness profile. Beta models are often used to describe the distribution of emission in galaxies and clusters of galaxies, and have the form:

$$I(r) = [1 + \left(\frac{r}{r_c}\right)^2]^{-\beta}$$

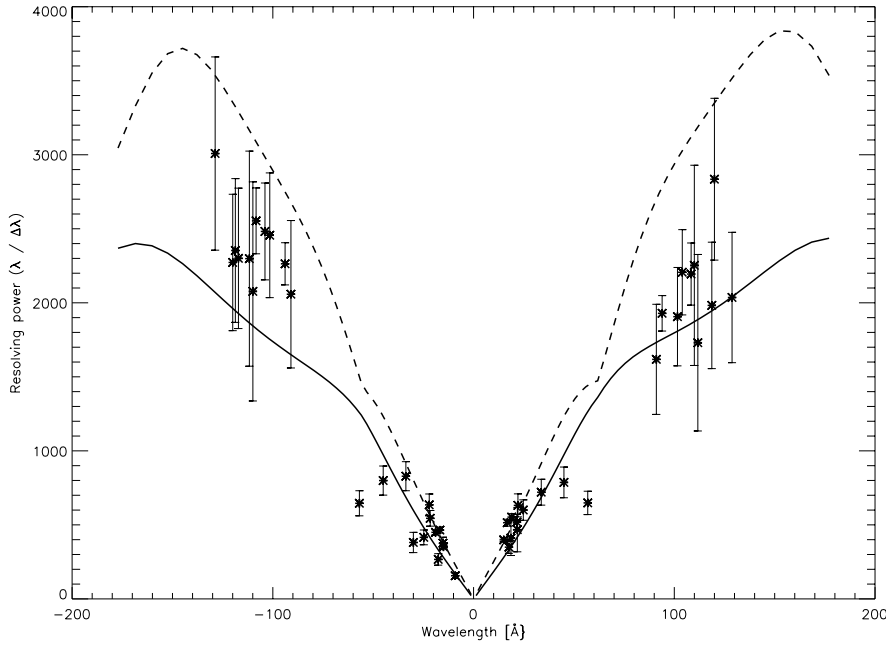


Figure 9.6: LETG spectral resolving power, as derived from a preliminary analysis of observations of Capella with the HRC-S. Measured line widths were corrected for orbital, rotational, and thermal motion. The dashed line is an optimistic error budget prediction calculated from pre-flight models and instrument parameters. The conservative solid curve is based on plausible in-flight values of aspect, focus, and grating period uniformity. The deviations from approximate linearity near ± 60 Å and at the longest wavelengths arise from deviations of the HRC surface from the Rowland circle (see Figure 9.5). Discrepant points near ± 50 Å may be from blended lines.

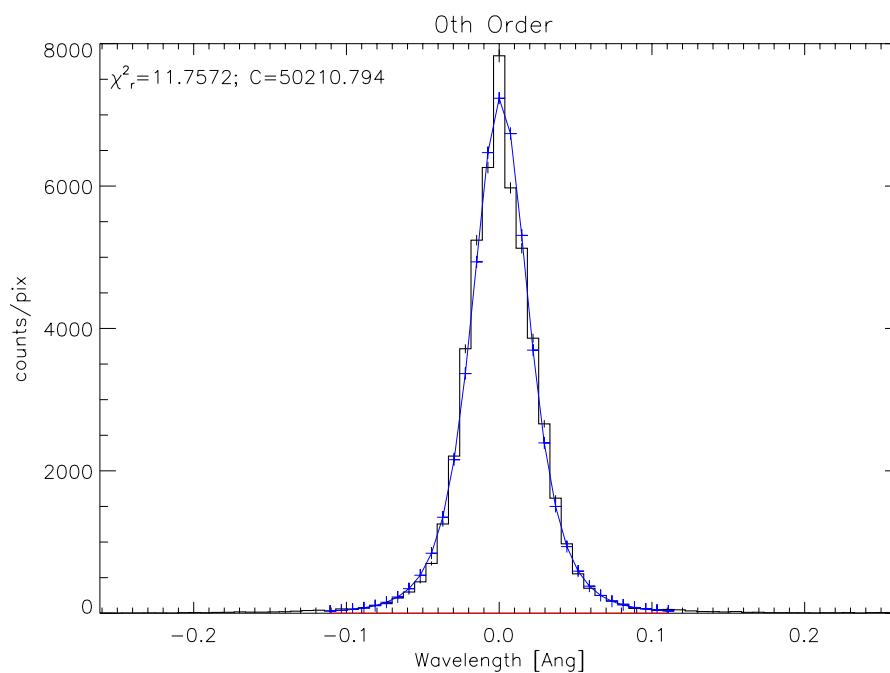


Figure 9.7: Observed LETG zeroth-order LRF from in-flight calibration observations of the active late-type binary Capella. The model profile, the continuous curve, is a beta model (see text) corresponding to the best fit value of $\beta = 2.5$. The reduced χ^2 of 11.8 certainly indicates a statistically poor fit to these very high S/N data, but the beta model is an excellent approximation to the LRF for weaker dispersed lines.

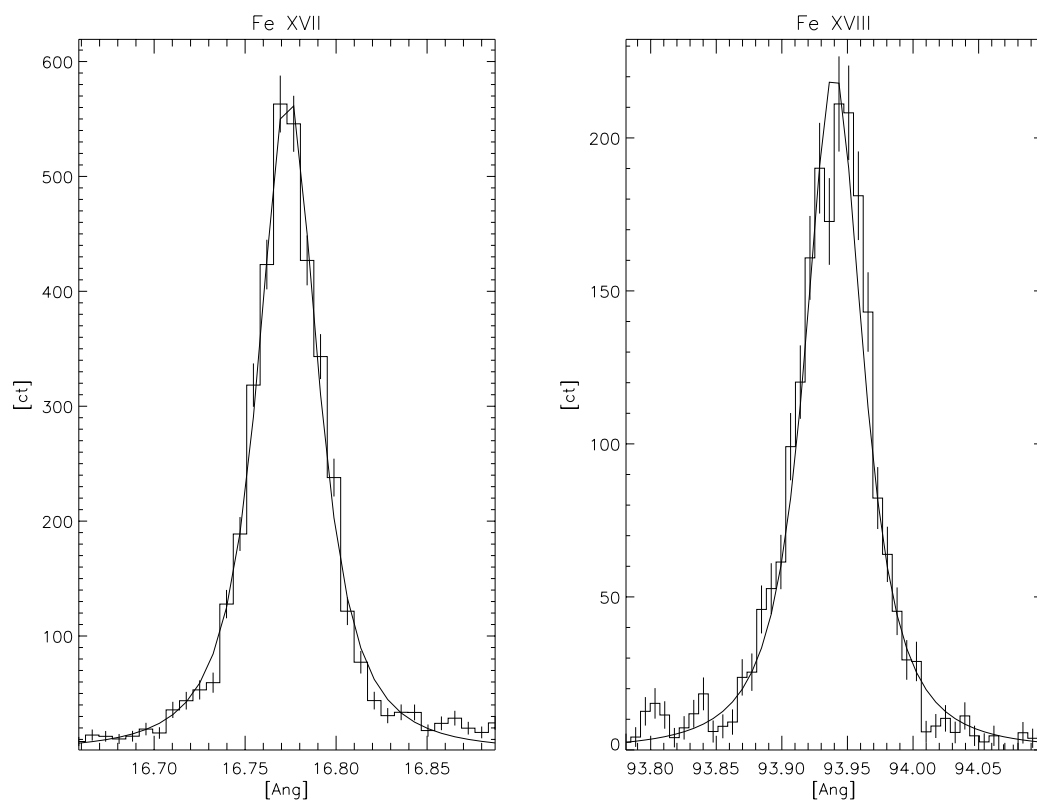


Figure 9.8: LETGS line response function as illustrated by two bright Fe lines (Fe XVII at ~ 17 Å and Fe XVIII at ~ 94 Å) using in-flight calibration observations of Capella. The solid curves are best fit beta models ($\beta = 2.5$).

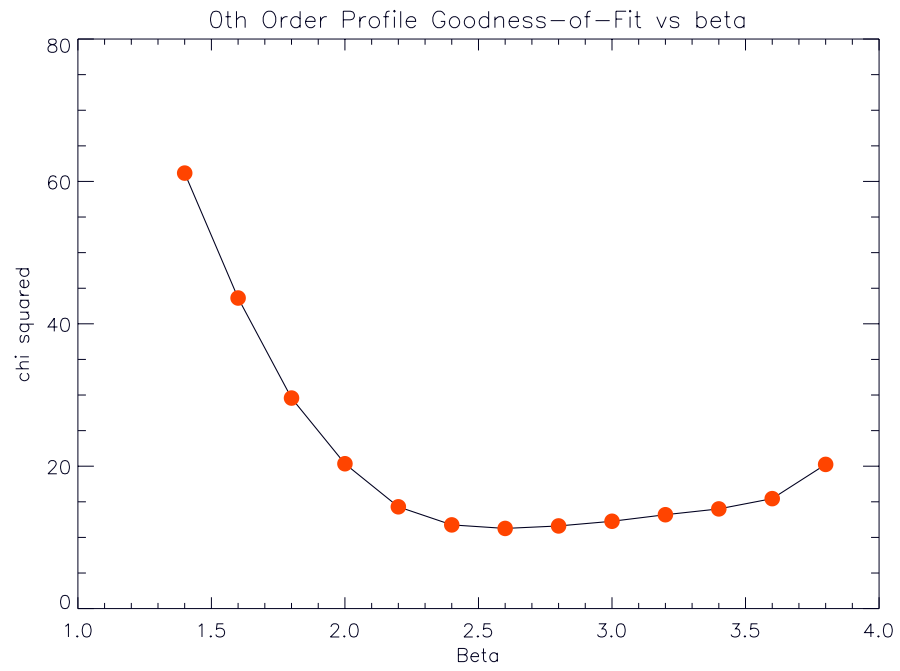


Figure 9.9: LETGS zeroth order profile goodness of fit vs. β , showing a best fit profile with an index of ~ 2.5 (see text).

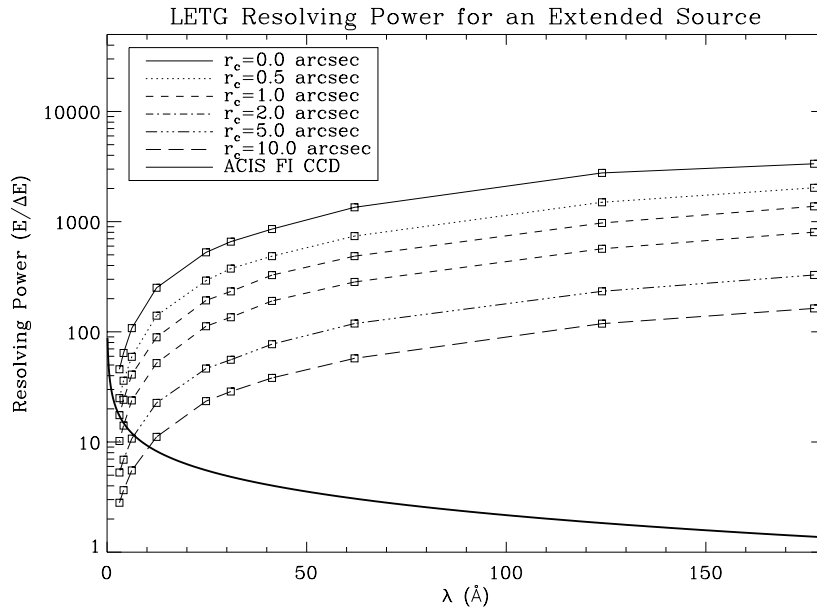


Figure 9.10: LETG spectral resolving power for extended sources. The predicted LETG resolving power ($E/\Delta E$) is shown versus wavelength for several source sizes. The MARX simulator has been used, and the source is represented by a β model as discussed in the text. (Note that MARX tends to somewhat overestimate resolving power.) For comparison, the spectral resolution for ACIS front illuminated CCD chips is shown (thick solid line). Note that the ACIS/FI curve was generated pre-launch, so it now refers only to that area of the FI chips adjacent to the readout edge.

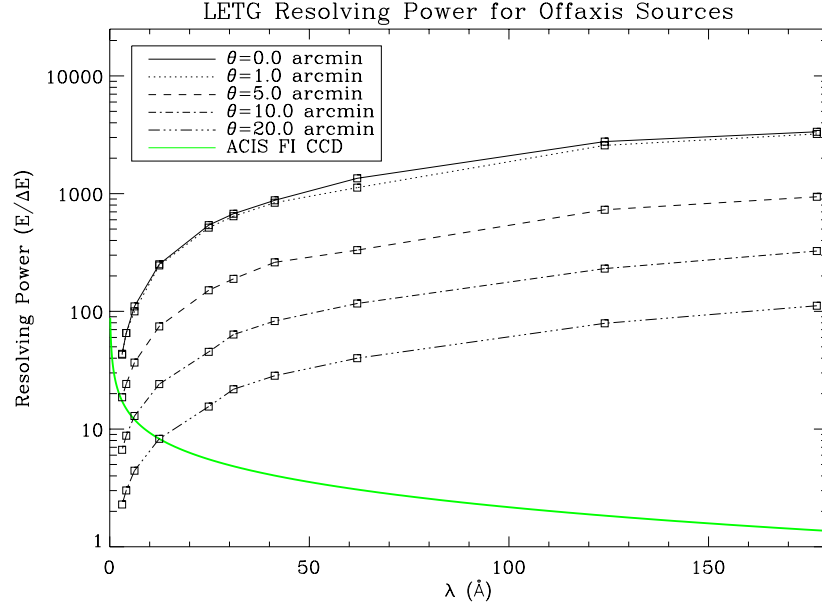


Figure 9.11: LETG spectral resolving power for off-axis sources. The predicted LETG resolving power ($E/\Delta E$) is shown versus wavelength for various off-axis distances. The MARX simulator has been used, which somewhat overestimates the on-axis resolving power. For comparison, the spectral resolution for ACIS front-illuminated CCD chips is shown. The ACIS/FI curve was generated pre-launch, so it now refers only to that area of the FI chips nearer to the framestore region.

where $I(r)$ is the surface brightness, and r is the radius, and r_c characterizes the source extent. β was set to a typical value of 0.75 for the simulations. r_c is very close to the radius of a uniform disk fit to a source and was varied in the simulation.

Off-Axis Sources

Similarly, for sources off axis, the increased point-spread function decreases the spectral resolving power. The effect on off-axis sources has been simulated with MARX and is shown in Figure 9.11.

As with extended sources, an ACIS image may, in extreme cases, provide energy resolution comparable to or better than the LETG for a source far off axis.

Calibration Status

Accurate resolution calibration is often needed for line-profile diagnostics, such as for determinations of thermal or orbital broadening. Such calibration based on in flight data is currently in progress (see *CXC* LETG Observer Information web page listed at the end of the chapter).

9.3.4 Grating Efficiency

Fine and Coarse Support Structure Diffraction

As explained in Section 9.1, the LETG has fine and coarse support structures which are periodic in nature, and have their own diffraction characteristics. The fine support structure disperses photons perpendicularly to the main spectrum, with about 1/26 the dispersion of the main grating. The coarse support is a triangular grid, and creates a very small hexagonal diffraction pattern which is generally only discernible in 0th order or for very bright lines. Examples of this secondary diffraction are visible in Figures 9.20, 9.21, and 9.24, all in Section 9.3.7.

Each support structure diffracts roughly 10% of the x-ray power. But the coarse-support diffraction pattern is so small that essentially all its photons are collected along with the primary spectrum during spectral-region extraction in data analysis. A significant fraction of the fine-support diffraction pattern, however, may lie outside the spectral extraction region, resulting in a loss of several percent of the total x-ray intensity (see, e.g. Figure 9.20).

Total Efficiencies

The zeroth, first, and selected higher-order grating efficiencies, based on a rhomboidal grating bar analytical model and verified by ground calibration, are shown in Figure 9.12. Plotted values are for the total diffraction efficiency (including photons diffracted by the coarse and fine support structures), excluding obscuration by the Grating Element Support Structure (GESS – see Section 9.1.4. Even orders are generally weaker than odd orders up through roughly 6th order.

The wiggles near 80 Å, and the stronger features near 6 Å, arise from partial transparency of the gold grating material to X-ray photons. Note that there are no absorption-edge features from C, N, or O in the LETG efficiency as there are in the HETG, because the LETG does not use a polyimide support film.

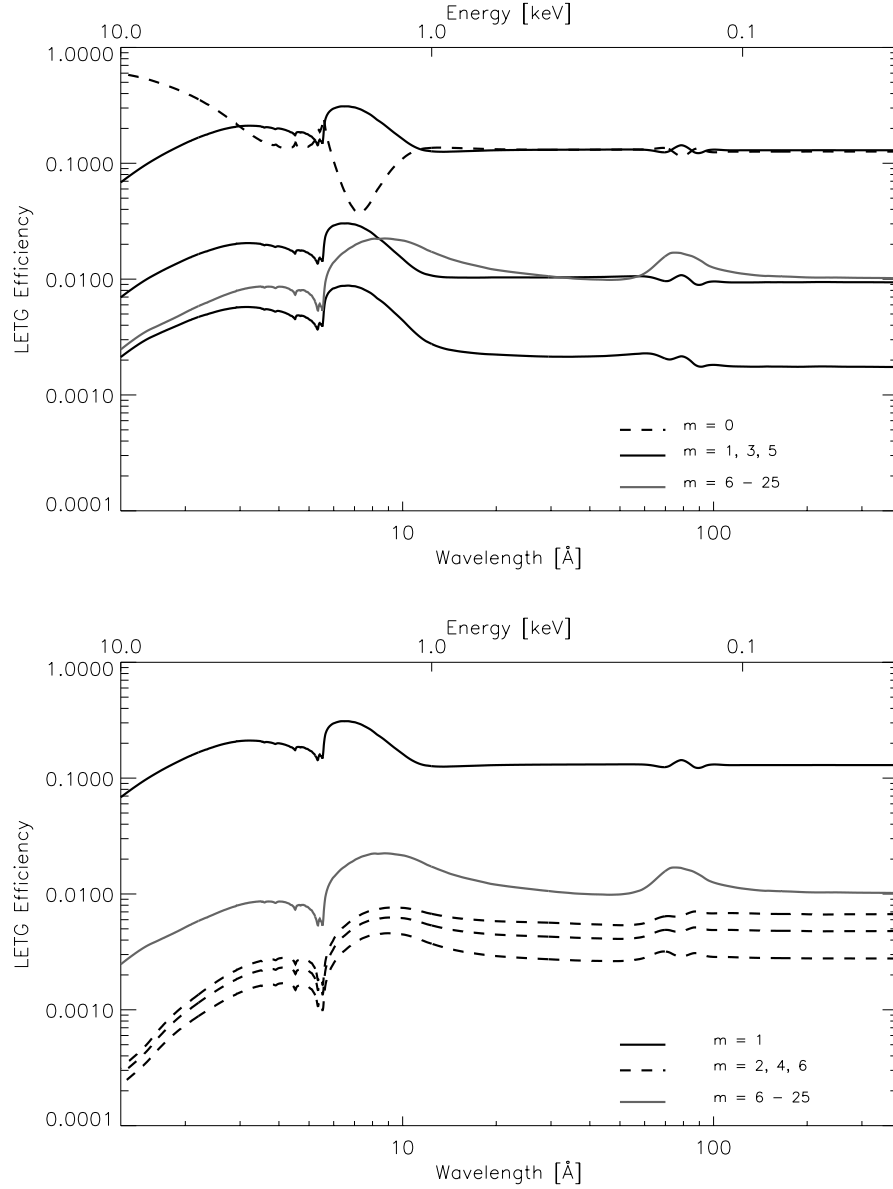


Figure 9.12: LETG grating efficiency. Summed positive and negative order efficiency is plotted versus wavelength. The top panel shows the zeroth and odd orders ($m < 6$); the bottom panel shows 1st and even orders ($m \leq 6$). The summed efficiency of orders 6 through 25 is also included in both panels. Plotted values include all support structure diffraction but exclude support structure obscuration. Features near 6 and 80 Å are due to the partial transparency of the gold grating material at these wavelengths.

9.3.5 Effective Area

The LETGS effective area for any diffraction order is equal to the product of the HRMA effective area, the net LETG efficiency for that order (including GESS obscuration), and the overall detector efficiency (which may vary slightly depending on exactly where the diffracted spectrum falls on the detector).

Of these three contributors, the HRMA (see Chapter 4) is the best calibrated within the LETGS energy band. Secondly ranked is the LETG efficiency, based on both calibration data and theory. The major contributor to the effective area uncertainty lies in the efficiency of the HRC-S, especially at longer wavelengths ($> 44 \text{ \AA}$; $< 0.28 \text{ keV}$). Ground calibration of the HRMA plus HRC-S in this range proved problematic. Flight calibration (see Section 9.2.2), particularly of the net first order effective area, has provided the best and most extensive data. Higher order effective areas are straightforward to derive from grating efficiencies relative to first order. However, the uncertainty in the diffraction efficiency increases significantly with order number and is also large in even orders.

Instrument Spectral Features

In addition to fixed-position detector features (primarily detector segment gaps—see Section 9.3.2) there are instrumental spectral features which occur at fixed energies because of absorption edges in the materials comprising the HRMA, LETG, and HRC-S or ACIS-S. The edges are tabulated in Table 9.4 and can be seen in the effective area curves (such as Figure 9.15) as decreases or increases in effective area depending on whether the material is part of the mirror, the filter, or the detector. Every effort has been made to adequately calibrate *Chandra* over its entire energy range, but it should be understood that effective areas near absorption edges are extremely difficult to quantify with complete accuracy and uncertainties in these regions are inevitably higher.

Spectral Extraction Region Efficiency

In practice, it is impossible to “put back” photons which undergo secondary diffraction in a real observation. Instead, one defines an extraction region for the observed spectrum and adjusts the derived spectral intensities to account for the fraction of total events that are contained within the extraction region.

Table 9.4: Absorption Edges

Instrument	Element	Edge	Energy (keV)	Wavelength (Å)
HRC	Cs	L	5.714	2.170
HRC	Cs	L	5.359	2.313
HRC	I	L	5.188	2.390
HRC	Cs	L	5.012	2.474
HRC	I	L	4.852	2.555
HRC	I	L	4.557	2.721
LETG	Au	M	3.425	3.620
LETG	Au	M	3.148	3.938
HRMA	Ir	M	2.909	4.262
LETG	Au	M	2.743	4.520
HRMA	Ir	M	2.550	4.862
LETG	Au	M	2.291	5.412
LETG	Au	M	2.206	5.620
HRMA	Ir	M	2.156	5.750
HRMA	Ir	M	2.089	5.935
ACIS	Si	K	1.839	6.742
HRC ,ACIS	Al	K	1.559	7.953
HRC	Cs	M	1.211	10.238
HRC	I	M	1.072	11.565
HRC	Cs	M	1.071	11.576
HRC	Cs	M	1.003	12.361
HRC	I	M	0.931	13.317
HRC	I	M	0.875	14.169
HRC	Cs	M	0.7405	16.743
HRC	Cs	M	0.7266	17.063
HRC	I	M	0.6308	19.654
HRC	I	M	0.6193	20.019
HRC,ACIS	O	K	0.5431	22.828
HRMA	Ir	N	0.496	24.996
HRC	N	K	0.4099	30.246
HRC,ACIS	C	K	0.2842	43.624
HRC	Al	L	0.0729	170

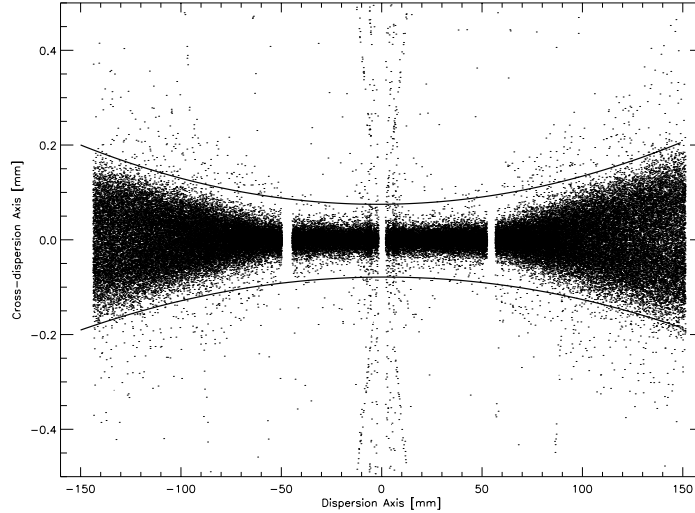


Figure 9.13: A MARX simulation of a flat spectrum designed to illustrate the broadening of the LETG+HRC-S profile in the cross-dispersion direction, and to illustrate an optimized parabolic extraction window designed to decrease background.

A non-rectangular LETGS extraction region is shown in Figure 9.13. Its width varies with wavelength and has been optimized to match the astigmatic cross-dispersion that is a feature of Rowland-circle geometry, with the goal of including as much of the diffracted spectrum as possible while minimizing the included background. Extraction efficiency varies from $\sim 90\%$ near zero order to 96% at the longest wavelengths. All effective areas provided in this chapter and on the LETGS Observer Information web site correspond to this new extraction region shown in the figure. NB: this extraction region or some variant such as a 'bowtie' region will be adopted by the standard data processing at some future date.

Zeroth and First-Order Effective Areas

Although the HRC-S is the default detector for the LETG, other detector configurations are possible. Figures 9.14 (0th order) and 9.15 show effective areas for the LETG when using the HRC-S, HRC-S with LESF, or ACIS-S as the readout detector. Based upon these and other plots, the various tradeoffs of each detector are thoroughly discussed in Section 9.4.

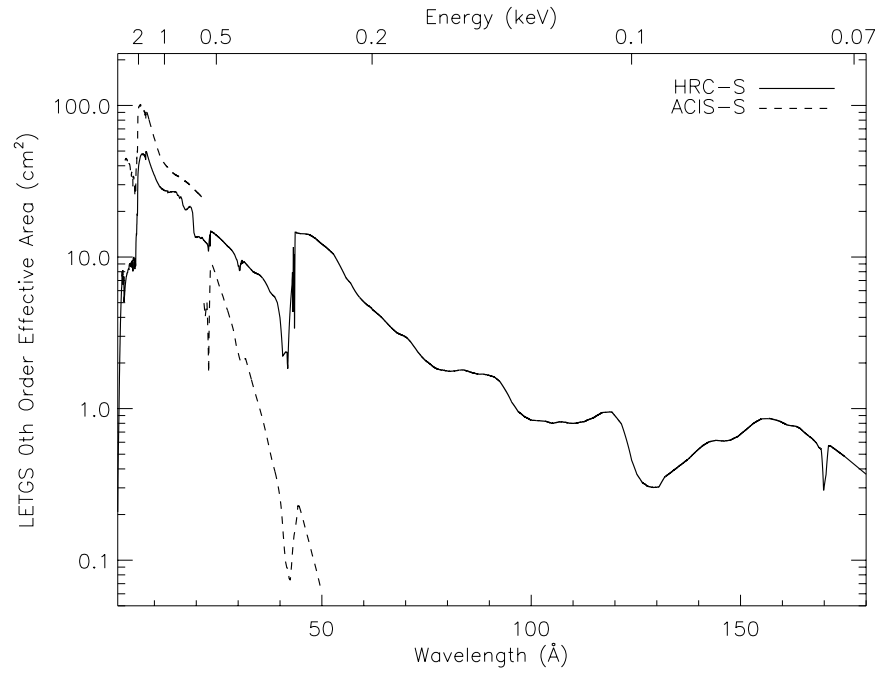


Figure 9.14: LETGS 0th-order effective area for an on-axis point source for the LETG with HRC-S and ACIS-S detectors. The 0th-order effective area for the HRC-S/LESF combination is the same as for the HRC-S.

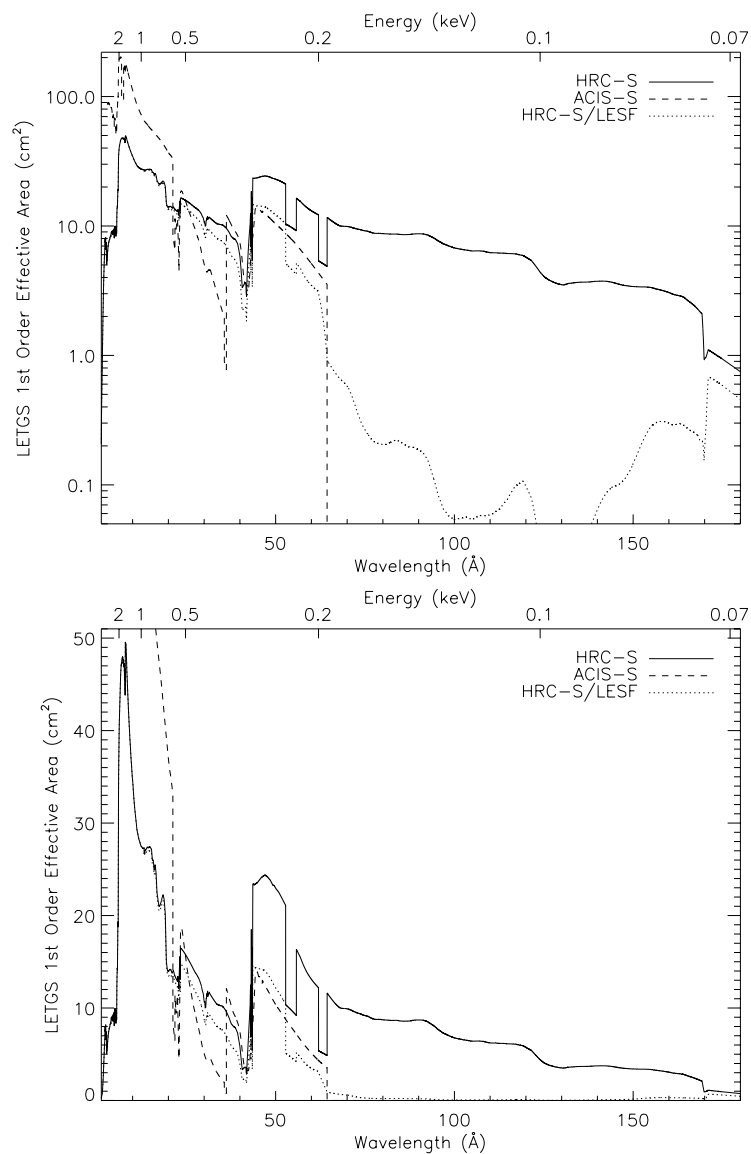


Figure 9.15: LETGS 1st-order effective area for an on-axis point source, with HRC-S, HRC-S LESF and ACIS-S detector configurations. Note that the vertical scale of the linear plot has been truncated.

Off-Axis and Extended Sources

Differences in the LETGS effective area for off-axis and significantly extended sources compared to the on-axis point source case is primarily determined by the HRMA vignetting function (see Chapter 4).

High-Order Diffraction Effective Areas

Although LETG (and HETG) has been designed to reduce complications from higher-order diffraction by suppressing even orders, many grating spectra will have overlapping diffraction orders. When ACIS-S is used as the detector, order separation is relatively easy because of the intrinsic energy resolution of the ACIS CCDs. The situation is more complicated, however, with HRC-S, which has very little energy resolution. Detector options and various data analysis techniques are described in Section 9.4. Section 9.3.6 (Background) describes how HRC-S pulse-height filtering might also help mitigate to some extent the effects of higher order flux.

The relative contribution of higher-order photons with different detector configurations can be estimated by inspection of Figures 9.16, 9.17, and 9.18. As an example, say an observer plans to use the LETG/HRC-S configuration and wants to determine the intensity of a line at 45 Å, but knows that line may be blended with the 3rd order of a 15-Å line which has 10 times the emitted intensity of the 45-Å line. Looking at Figure 9.16, she or he reads the 1st- and 3rd-order curves at $m\lambda = 45$ Å and sees that the 3rd-order value is about one-tenth the 1st-order value. Multiplying by 10 (the ratio of the emitted intensities of the 15- and 45-Å lines), she or he computes that ~50% of the feature at $m\lambda = 45$ Å will come from the 15-Å line. As discussed in Section 9.3.6 the 3rd-order contamination can be reduced somewhat by pulse height filtering, but the estimate above is a useful upper limit.

9.3.6 Background

The LETG is always used in conjunction with a focal-plane detector, so the LETG spectra will share that detector's intrinsic, environmental, and cosmic background. The components of the background of the HRC are discussed in Chapter 7, section 7.8. The raw quiescent rate is ~ 200 counts/sec over the full detector, which is above the 184 counts/sec telemetry limit. Imposition of the spectroscopy window reduces the rate to 85 counts/sec, as discussed below.

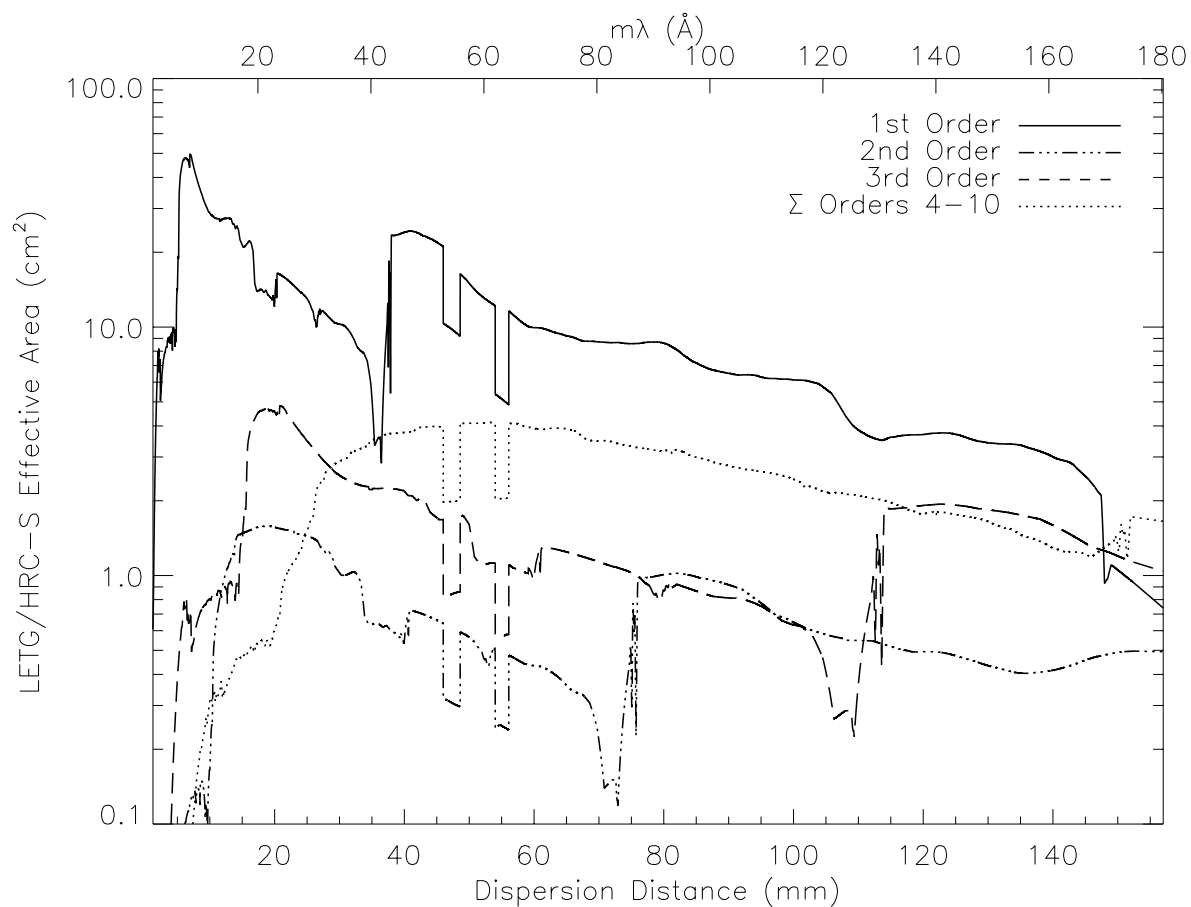


Figure 9.16: The combined HRMA/LETG/HRC-S effective area, illustrating the relative strengths of 1st and higher orders. In the label for the top axis, m is the order number. See text for an example of how to determine relative strength of overlapping lines from different orders.

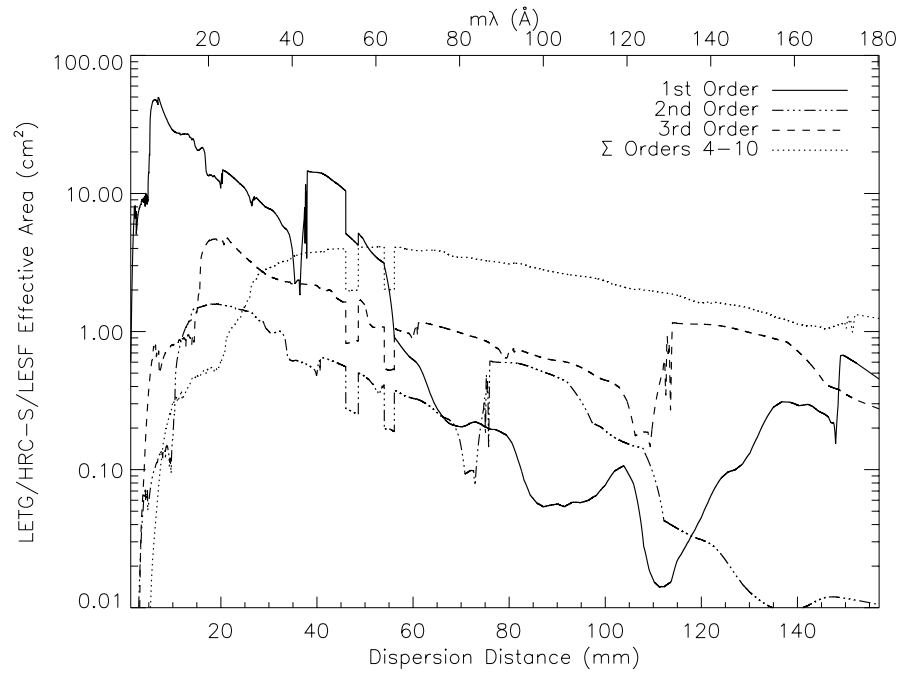


Figure 9.17: The combined HRMA/LETG/HRC-S/LESF effective areas for first and higher orders.

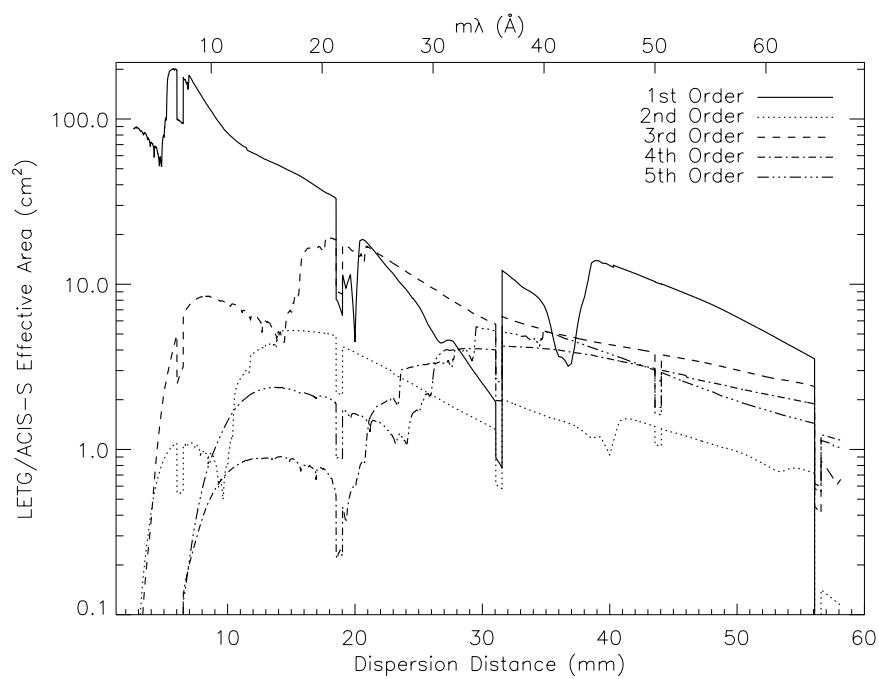


Figure 9.18: The combined HRMA/LETG/ACIS-S effective areas for first and higher orders.

Telemetry Limit and Deadtime

To avoid constant telemetry saturation, the HRC-S is currently operated in a “windowed down” configuration, in which only data from 6 of the 12 coarse taps in the center of the detector in the cross-dispersion direction are telemetered (see section 7.8.2 in Chapter 7). The edge-blanking creates an active detector area slightly less than 10 mm, or 3.4 arcmin, in the cross-dispersion direction. This window easily accommodates the (dithered) dispersed spectra of point sources, but one must consider the size of extended sources. In this configuration, the total quiescent count rate for the HRC-S is about 85 count/s.

HRC-S Background Reduction via On-Ground Data Filtering

The quiescent background rate in the HRC-S is currently about 7×10^{-5} counts/s/arcsec², or 0.12 counts per pixel in 100,000 seconds. The area of a dispersed line in the LETGS spectrum is ~ 7 pixels in the dispersion direction (FWHM) by ~ 20 to 65 pixels in the cross-dispersion direction corresponding to roughly 17 to 55 background counts beneath the line in a 100,000 s exposure.

About 25% of this background occurs in PHA channel 255. Excluding this channel in ground data processing reduces the rate to 0.09 counts per pixel per 100 ksec without impacting the x-ray detection efficiency. Indeed, the HRC-S pulse height distribution is narrow enough – with a sigma/mean of ~ 0.22 – that a large fraction of pulse-height space can be excluded from the data to further reduce the background.

Pulse-height filtering will be part of the standard data processing for LETG/HRC-S data. Observers will also be able to tailor the filtering level to their particular needs if more than the standard (minimal) filtering is required.

The pha filtering tool is still under development as of Feb. 2000 but preliminary tests indicate that roughly 60% of the background can be removed with a 2% loss of x rays, $\sim 2/3$ background removed with $\sim 5\%$ x-ray loss, and $\sim 3/4$ background removed with $\sim 15\%$ x-ray loss. This is illustrated in Figure 9.19, where the successively lower curves correspond to the more stringent filtering. The fourth of these curves which removes $\sim 2/3$ of the background with $\sim 5\%$ x-ray loss is a reasonably conservative filter that can be used as a baseline for estimating realistic “effective” background levels for LETG+HRC-S observations.

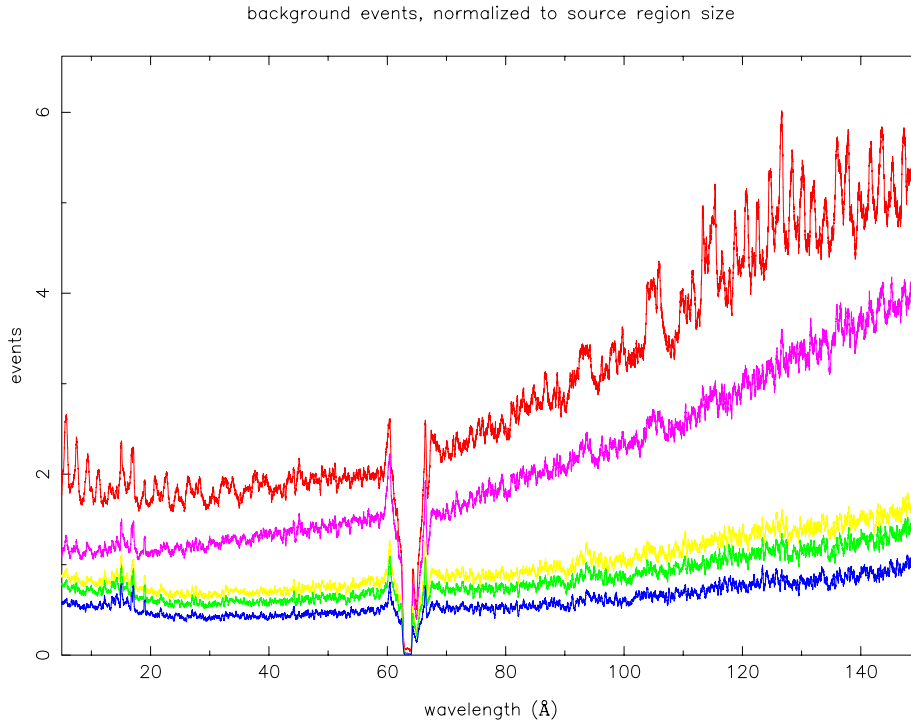


Figure 9.19: The LETG+HRC-S background from an observation of Capella. Spectra were extracted from rectangular regions above and below the dispersed x-ray spectrum, and then combined and normalized to the width of the parabolic x-ray spectral extraction window (see Figure 9.13). The curves from the top down correspond to: background spectrum with no filtering; minimal filtering (pha=255 events removed) with 0% X-ray event loss; filtering with 2% X-ray loss; 5% X-ray loss; and 15% X-ray loss. The units of the y axis are total events/dispersion-pixel (summed in the cross dispersion direction), where one pixel is $6.43 \mu\text{m}$ wide (0.0074 \AA). The exposure time was 85 ks.

Relevance for Higher Orders Since the mean of the pulse-height distribution scales in proportion to the log of photon energy, pha filtering can also be useful in separating higher order flux. A factor of two difference in energy corresponds to a shift in the mean of $\sim 12\%$, which is about one-half sigma. Therefore, the mean pulse height of fourth order will lie about one sigma away from the first order mean. With moderate filtering, orders higher than roughly 8th will be almost completely eliminated with a loss of less than 5% of first-order photons. Further work in this direction is still in progress.

Relevance for Observation Planning As a consequence of the on-ground data filtering, *there are two relevant backgrounds for the LETG/HRC-S*: one (~ 85 ct/s) for telemetry saturation; the other ($\sim 15\text{--}55$ counts in a FWHM spectral bin per 100,000 s integration) for estimating signal-to-noise (see also the discussion in section 9.5.1 and Figure 9.26 for the spectral dependence).

ACIS-S Background

As with the HRC-S detector, background rates in ACIS are somewhat higher than expected, but still much lower than in the HRC. The effective background rate when using ACIS-S with a grating is therefore very low. The reader is directed to Chapter 6 for further discussion.

9.3.7 Sample Data

Figure 9.20 is a detector image of a 85 ksec LETGS observation of Capella (obsid 1248). The central 30 mm of the dispersion axis and the full extent of the telemetered cross-dispersion window (9.9 mm) is shown. The image is in angular grating coordinates (TG_D, TG_R), which have been converted to \AA . The lines radiating from zeroth order above and below the primary dispersion axis are due to fine support structure diffraction. Star-shaped coarse support structure diffraction is seen around zeroth order. Figure 9.21 is a close-up of the bright Fe XVII, Fe XVIII, and O VIII lines between $\sim 15\text{--}17\text{ \AA}$, in which many orders of fine support diffracted flux can be seen.

Figure 9.22 is a HRC-S detector image of a second Capella observation (obsid 1420, 30 ksec), showing positive order dispersion. The increasing cross-dispersion extent of lines at longer wavelengths is due to astigmatism in the HRMA/LETG system (see also Figure 9.13). The positive order HRC-S plate gap is seen at $\sim 63\text{ \AA}$. An extracted Capella spectrum (obsid

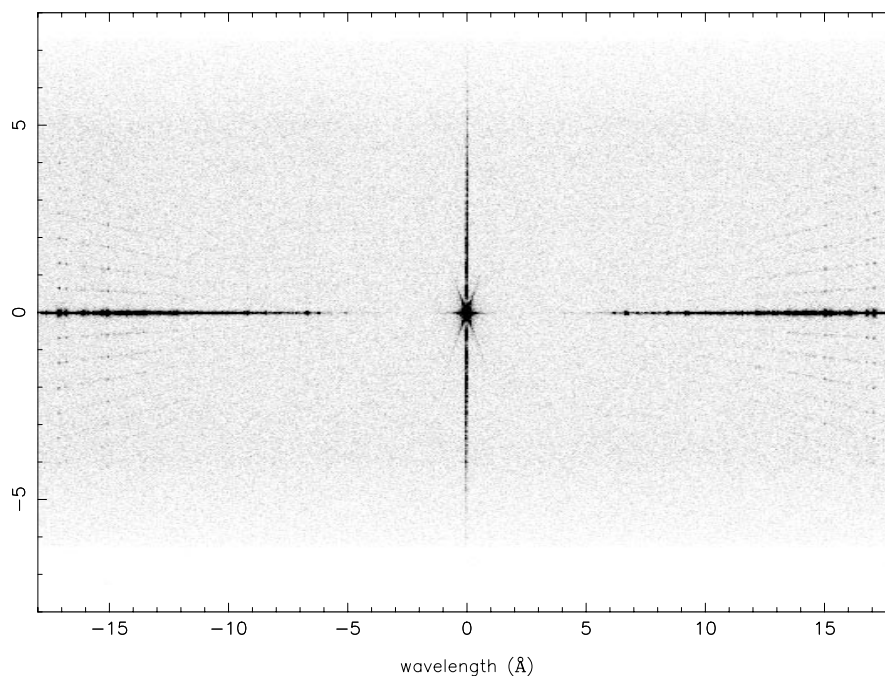


Figure 9.20: HRC-S detector image of LETGS observation of Capella. In order to illustrate the stretching of the cross-dispersion axis, both axes are in \AA with 1.148 \AA/mm ; only the central 30 mm of the central plate is shown. The full extent of the telemetered six tap cross-dispersion window is seen and measures 9.9 mm. The areas of reduced background at top and bottom are due to dither effects. Star-shaped coarse support structure diffraction is seen around zeroth order, and “cat’s whiskers” fine support structure diffraction is seen above and below the primary dispersion axis, as well as in the vertical line through 0th order.

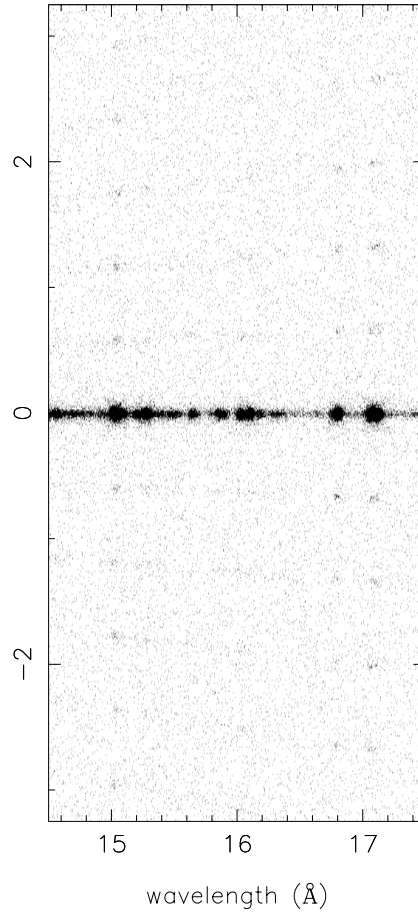


Figure 9.21: Detail of Figure 9.20, showing LETG/HRC-S image of bright lines in Capella. Both axes are in \AA with 1.148 \AA/mm . The Fe XVII lines at ~ 15 and 17 \AA are the brightest in the LETG Capella spectrum. Faint features above and below the primary spectrum are due to fine support structure diffraction.

62435, 32 ksec), is shown in figure 9.23. Positive and negative order flux has been summed.

Figure 9.24 is a zeroth-order image of co-added Sirius AB observations (obsids 1421, 1452, 1459) with a total exposure time of 23 ksec. The star-shaped pattern is due to coarse support structure diffraction. Sirius A and B are separated by $\sim 4''$. The flux from Sirius A is due to the small but finite UV response of the detector.

9.4 Observation Planning

The purpose of this section is to provide further information directly related to planning LETGS observations and that is not explicitly presented in sections 9.1 and 9.3, and to reiterate the most relevant issues of instrument performance that should be considered when preparing an observing proposal.

9.4.1 HRC-S, ACIS-S and HRC-I Detector Choices

The best choice of detector will depend on the exact application; some considerations are listed below. For further details concerning the HRC and ACIS detectors, refer to chapters 7 and 6, respectively.

HRC-S

- The HRC-S provides wavelength coverage from 1.2-175 Å (10-0.7 keV).
- The HRC provides the highest time resolution at $16\mu s$.
- The HRC-S can provide slightly better spatial (and thus spectral) resolution than ACIS for the LETG.
- HRC-S has essentially no intrinsic energy resolution and so overlapping spectral orders cannot be separated.
- The HRC-S QE is smaller than that of ACIS-S in the 1.2-20 Å (10-0.6 keV) range.
- The HRC-S background count rate is about 85 count s^{-1} in its windowed-down spectroscopic configuration during times of quiescence. However this can rise to exceed the HRC telemetry saturation limit of 184 count s^{-1} during background “flares”. This saturation causes deadtime that can be corrected for to an accuracy of 5-10%

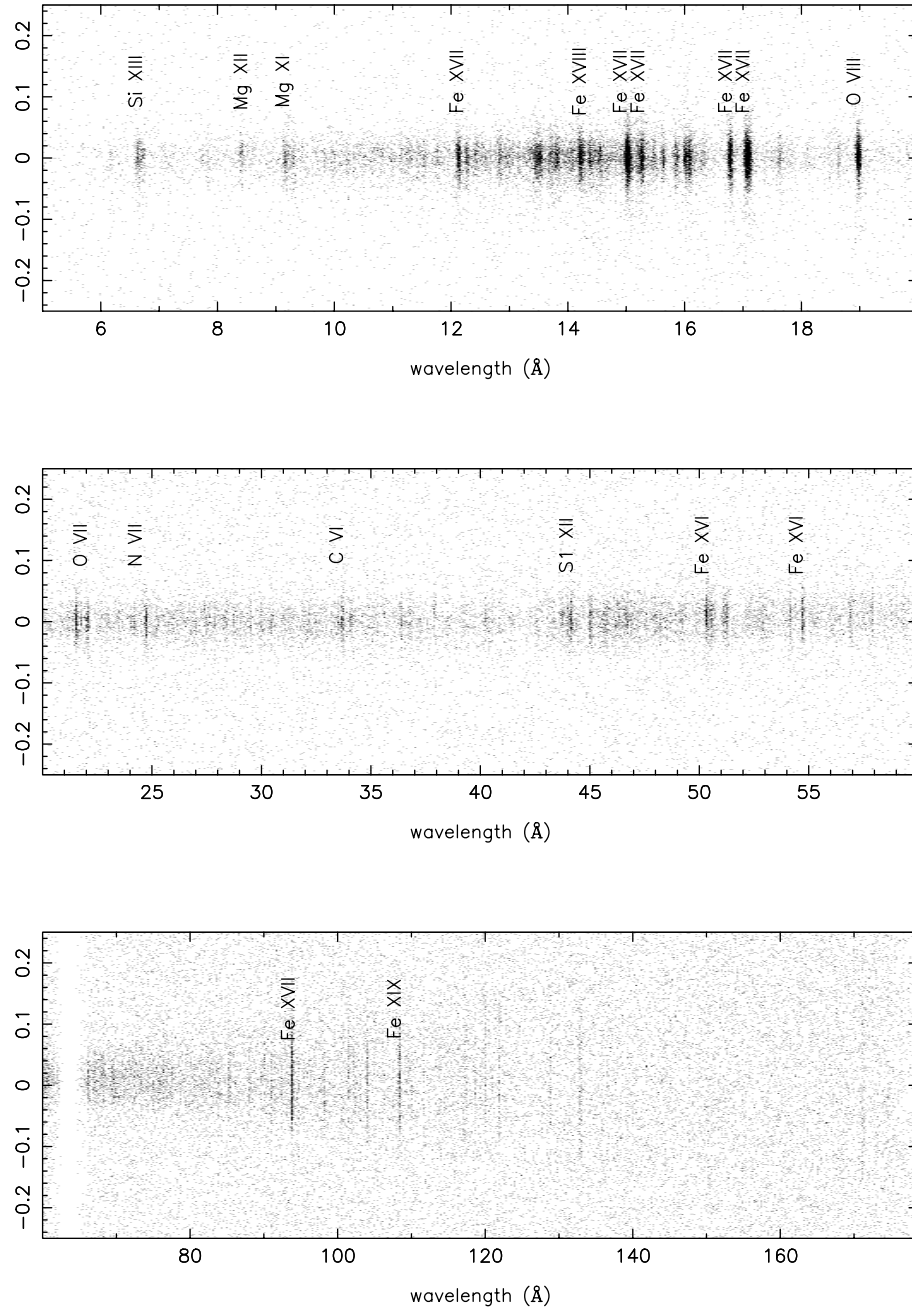


Figure 9.22: HRC-S detector image of Capella observation, showing positive order dispersion. Both axes are in \AA with 1.148 \AA/mm . The increasing cross-dispersion extent of lines at longer wavelengths is due to astigmatism in the HRMA/LETG system. The positive-order HRC-S plate gap is at $\sim 63 \text{ \AA}$.

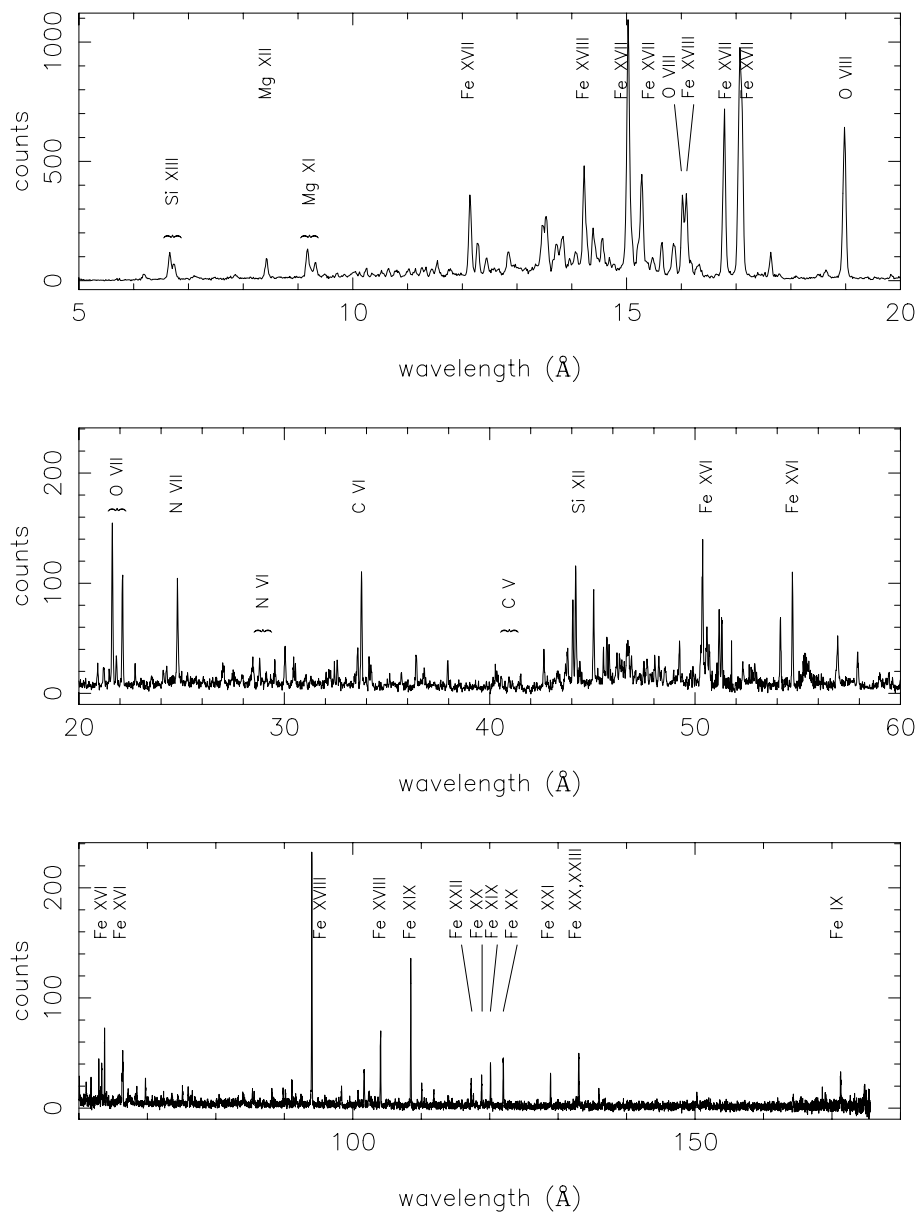


Figure 9.23: Extracted LETGS spectrum of Capella with some line identifications (from Brinkman et al. 2000, ApJL, 530, in press). Many of the lines visible between 40 and 60 Å are third order dispersion of the strong features seen in panel 1.

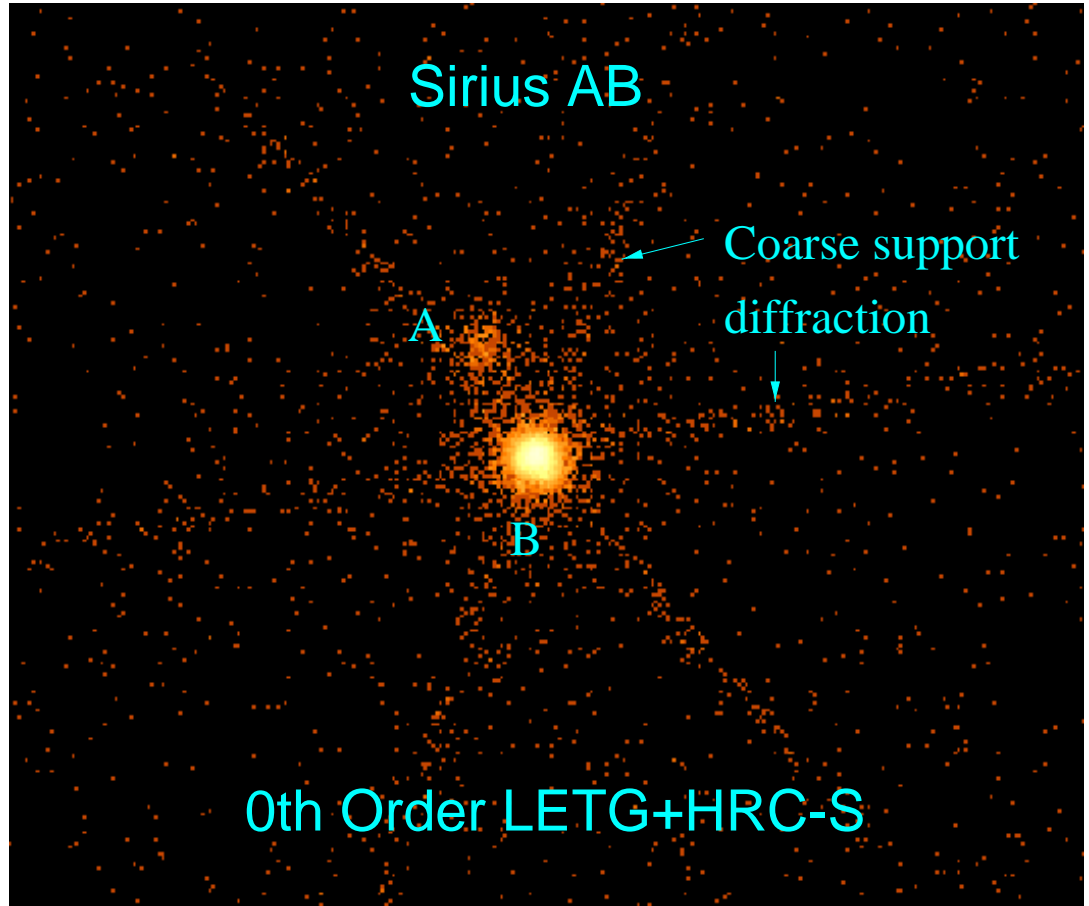


Figure 9.24: LETG/HRC-S zeroth order image of Sirius A and B. The two stars are separated by $\sim 4''$. Flux from Sirius A is due to the small but finite UV response of the detector. The star-shaped structure is due to coarse support diffraction.

at present. Background flares can also be filtered out using CIAO or other software tools. These flares can typically affect at most about 10-20% of an observation.

- The LESF filter region in principle can be used to obtain a higher-order spectrum relatively uncontaminated by first order for wavelengths above 75 Å ($E < 0.17$ keV; see Figure 9.15). This could be useful either for observing features in a high order for high spectral resolution that cannot be easily observed with the HETG/ACIS-S combination, or for providing a direct observation of higher order contamination in conjunction with an LETG+HRC-S observation in its nominal configuration. NB: as of 2000Mar, this configuration had not yet been used in flight.

Summary HRC-S is probably the best detector choice for spectroscopic observations in which one or more of the following observational goals apply:

- signal longward of 50 Å is of significant interest;
- the highest time resolution is required;
- the highest spatial or spectral resolution *Chandra* can provide is required.

HRC-I

- The HRC-I provides wavelength coverage from 1.2-73 Å (10-0.17 keV).
- The raw HRC-I quiescent background event rate per unit area is lower than that of the HRC-S by about a factor of 8. After moderate filtering in both detectors, the ratio is about a factor of 4. HRC-I might therefore be a consideration if the source count rate is expected to be sufficiently high that HRC-S would be running close to saturation (note though the limitations on instrument count rates in the Chapter 7 in section 7.12).
- The HRC-I has similar imaging and timing capabilities as HRC-S, though the UVIS is comprised of different thicknesses of polyimide and Al and consequently has different transmission characteristics. Most notably, the HRC-I has a lower sensitivity to longer wavelengths than HRC-S.
- The HRC-I QE for wavelengths > 44 Å is not well known.

- The HRC-I offers a broad detector in the cross-dispersion direction and this might be a consideration for observation of sources with extended components exceeding ~ 2 arcmin or so. Note, however, that the *Chandra* spectrographs are slitless, and the apparent spectral resolution is degraded according to source extension—see Figure 9.10).
- The HRC-I detector has certain count rate constraints discussed in Chapter 7 section 7.12. It may be that the 0th order image is too bright, or would extract significant amounts of charge. The HRC constraints need to be accounted for, and could require moving the 0th order off the nominal HRC-I aimpoint; this would result in a slightly reduced wavelength coverage by ~ 6 Å.
- The flat detector HRC-I departs from the Rowland geometry, hence degrading spectral resolution. A small focus offset can be used to optimize the focus of the dispersed spectrum.

Summary HRC-I is possibly the best detector choice for sources in which signal longward of 73 Å (0.17 keV) is not of primary interest and accurate effective area knowledge for > 44 Å (< 0.28 keV) is not a strong concern, and in addition one or more of the following observational goals apply:

- HRC-S would be the detector of choice but the source is expected to have a count rate of more than an average of ~ 80 count s^{-1} and accurate photometry is required;
- very accurate light curves with the minimum of high background event filtering are required;
- a larger detector area in the cross-dispersion direction than is provided by the HRC-S is required.

ACIS-S

- ACIS-S provides an effective LETG 1st order wavelength limit of about 55 Å (0.23 keV) because longward of this the ACIS-S QE is essentially zero (see Figure 9.15).
- The intrinsic energy resolution of ACIS-S allows for discrimination between different and otherwise overlapping spectral orders. For dispersion distances of > 48 mm, the LETG+ACIS-S response is entirely due to higher order throughput (Figure 9.15) and ACIS-S can therefore be useful for observing these higher spectral orders.

- Spectral resolution and line profile information are less well sampled due to the large pixel size.
- ACIS-S allows several modes of operation (see Chapter 6) including continuous clocking (CC) if high time resolution is desired, or to avoid pileup.
- The full frame 3.2s exposure of ACIS-S in TE mode means that photon pileup can be a serious consideration, especially in 0th order. Pileup has also been found to cause a greater impact on dispersed spectra than expected. At a count rate of about 0.05 photon/pixel/frame, up to a 50% loss of events due to pileup has been seen in the first order spectra obtained with the HETG/ACIS-S combination. Some of these events can be recovered by examining the higher order spectra but some events will have “migrated” out of the standard grade set, so the standard calibration curves no longer apply. Pileup can affect both the shape of the PSF and the apparent spectral energy distribution of your source. See the ACIS chapter 6 for details concerning pileup, its effects, and how best to avoid it.
- ACIS-S time resolution is lower than that of HRC and depends on the control mode adopted. In timed exposure (TE) mode the full frame exposure is 3.24s. This is reduced when using a subarray due to the shorter read-out time for the smaller detector region (again see Chapter 6 for details). The highest time resolution possible with ACIS-S (2.85 ms) is obtained in CC mode, but imaging information in the cross-dispersion direction is lost.
- The reduced energy resolution the FI chips suffer from early on-orbit radiation damage increases with distance from the CCD readout. The LETG dispersion axis is parallel to the ACIS-S readout and the spectrum of a point source can be placed close to the readout such that the energy resolution is no longer a significant problem; a default SIM z offset of -8 mm is routinely applied to LETG+ACIS-S *point source* observations. If observations with extended sources are under consideration, or if for other reasons a SIM offset is undesirable, the resolution in the FI CCDs of the ACIS-S array might be a point to consider. From an LETG perspective, the effects of concern are a lowering of the CCD energy resolution that is needed for order sorting, and grade migration that can make for difficult calibration of detector quantum efficiency—see Chapter 6 for a detailed discussion.

- The ACIS-S energy resolution enables removal of the vast majority of background events in LETG spectra; the effective ACIS-S background is consequently lower than that of HRC-S or HRC-I.

Summary ACIS-S is possibly the best detector choice for sources for which signal longward of 50 Å (0.25 keV) is not of any interest and one or more of the following observational goals apply:

- Particular spectral features of interest occur where the LETG+ACIS-S effective area is higher than that of LETG+HRC-S;
- High time resolution beyond the 3.2 s exposure of TE mode (less if a sub-array is used), or the 2.85 ms of CC mode (if applicable), is not important;
- A low resolution 0th order spectrum from the S3 BI chip is of high scientific value, in addition to the dispersed LETG spectrum;
- Order separation is important;
- Pileup can either be avoided or mitigated or is not likely to be a problem.

9.4.2 Other Focal Plane Detector Considerations

Instrument Features and Gaps

Attention should be paid to the locations of instrument edge features and detector gaps to make sure that spectral features required to achieve science goals are not compromised by these. These features and gaps are listed for both HRMA+LETG+HRC-S and HRMA+LETG+ACIS-S combinations in Tables 9.4 and 9.3. Note that intrinsic instrumental features, such as edges, are not affected by dithering and offset pointing (see below), but chip gaps in ACIS-S and HRC-S plate gaps, as well as the boundaries between “thick” and “thin” regions of Al that make the “T” shape of the HRC-S UVIS, are.

@@

Dither

The standard LETG+HRC-S dither amplitude is 20 arcsec (40 arcsec peak-to-peak; 2 mm in the focal plane) and that of LETG+ACIS-S is 8 arcsec (16 arcsec peak-to-peak; 0.8 mm), in both axes. Spectral features in dispersed LETG spectra will experience the same dither pattern, and allowance for the size of the dither must be made when considering if spectral features of interest will encounter detector gaps.

In special cases, different dither amplitudes can be specified by the observer, though it must be kept in mind that detector safety constraints, such as accumulated dose/pore in the HRC (see 7.12), must not be violated.

SIM z Offsets

The SIM permits movement of the focal plane detectors in the spacecraft z direction (perpendicular to the LETG dispersion axis). This can be used to better position a source on ACIS-S or HRC detectors, for example to accommodate multiple sources, or to place a source over the HRC-S LESF filter region. The nominal aim point for the LESF requires a SIM z offset of +7 mm.

In the case of LETG+ACIS-S, a standard SIM z offset of -8 mm is applied to point source observations, *unless otherwise requested by the observer*, in order to place the source closer to the ACIS readout. In the case of extended sources, this offset might not be desirable as it could place part of the source off the detector. The effects of spacecraft dither should always be considered when choosing a SIM z offset.

Offset Pointing

Pointing off-axis in the observatory y axis can be used to change the wavelengths at which detector gaps occur, or to change the wavelength corresponding to the ends of the detectors. Examples of offset pointings are shown in Chapter 3. When designing such offsets, the approximate focal plane and dispersion relation scales of 20 arcsec/mm and 1.148 Å/mm are sufficiently accurate. As an example, by invoking a +2 arcmin offset pointing (see Chapter 3 for the convention), the long wavelength cut-off of the HRC-S can be extended in the + order from approximately 175 Å (0.0708 keV) for on-axis pointing to nearly 182 Å (0.0682 keV). This of course is obtained at the expense of a commensurate shortening of coverage in the – order.

Offset pointing leads to degradation of the PSF, and consequently the spectral resolution—see Figure 9.11. For offsets of order 2 arcmin or less this degradation is noticeable but fairly small. For offsets of > 4 arcmin, spatial and spectral resolution will be considerably degraded.

HRC-S Windowing

As described in section 9.3, the HRC-S has a default spectroscopic “window” defined that limits the detector area from which events are telemetered to the ground. The window is a rectangle based on coarse position tap boundaries;

the default rectangle is comprised of the central 6 taps in the cross-dispersion direction (corresponding to ~ 9.9 mm) and the whole detector length in the dispersion direction. However, this window can be specially defined to suit the observational goals. E.g., if there is an expected long wavelength cut-off in the source flux, perhaps due to an intervening ISM neutral H column density of $\geq 10^{19}$ cm², the rectangle could be reduced in size in the dispersion direction. Of course one would no longer be able to detect or use in analysis the higher orders that are dispersed to $m\lambda$ for order m and wavelength λ .

When considering defining a special HRC-S window, it is reasonable to assume that the detector background is spatially uniform for the purposes of computing the total source + background count rate. The telemetry capacity of 184 count s⁻¹ should be kept in mind to avoid telemetry saturation by using a window that is too big.

ACIS-S Modes

An LETG+ACIS-S observation needs to make a careful consideration of which control mode to adopt. The ACIS detector is very flexible but can also be complicated when deciding the best set-up. Prospective observers considering using ACIS-S for the focal plane detector are urged to read the ACIS Chapter (6) carefully.

9.4.3 General Considerations

Complications from Other Sources

Field sources coincident with the target source dispersed spectrum should be avoided. This avoidance is most simply accomplished by imposing a roll angle constraint. Note that it is also desirable to retain a pristine region either side of the dispersed spectrum to enable an accurate estimation of the background within the spectral extraction window.

In some circumstances, photons dispersed by the LETG of bright sources outside of the direct field of view of the HRC or ACIS detectors might also give rise to significant signal on the detector.

Particular attention should be paid to optically-bright and UV-bright sources, even if these are some distance off-axis. The ACIS-S and HRC-S filters are much more transparent to optical and UV light than are those of HRC-I and ACIS-I (the HRC-S central “T” segment is closer in performance to that of HRC-I, but has completely different thicknesses of polyimide and Al layers). As an example, an observation of the bright A0 V star Vega

($V = 0.03$) in one of the outer HRC-S UVIS segments gave a count rate of about 475 count s⁻¹.

The energy resolution of the ACIS-S detector enables filtering out of all photons except those in a fairly narrow wavelength or energy range corresponding to the wavelength or energy of photons in a spectrum dispersed by the LETG. This means that contamination of the dispersed spectrum by, for example, the 0th order or dispersed spectrum of other sources *might* not be a significant problem.

However, a much better solution to problems of source contamination is, if it is possible within other observation constraints, to choose a roll angle (Chapter 3) that avoids the source contamination issue.

Roll Angle Considerations

Roll angle constraints can be specified to avoid contamination by off-axis sources, as described above, or to help separate the dispersed spectra of multiple sources in the cross-dispersion direction. The maximum separation between dispersed LETG spectra of two sources is obviously one that places the sources in a line perpendicular to the dispersion axis.

It is important to remember that roll angle constraints will also impose restrictions on the dates of target availability as discussed in Chapter 3. Exact restrictions depend on celestial position. Their impact can be examined using the observation visualizer tool discussed in Chapter 12.

High Order Throughput

It is expected that the majority of observations with the LETG will make use of the HRC-S as the readout detector because of its wavelength coverage and high quantum efficiency at long wavelengths. Since the HRC-S has very little energy resolution, the overlapping of spectral orders could be a significant issue and prospective observers should assess the degree to which their observation might be affected. The following list summarizes some of considerations:

Scientific Utility: Higher spectral orders provide higher spectral resolution than the first order spectrum by the approximate factor of the order number m . For observations in which features are expected to be seen in higher orders, this capability could be scientifically useful.

LESF: At the time of writing, the LESF, the thicker filters on the HRC-S, remains untested in flight, but could be useful for obtaining a spectrum containing mostly higher order flux.

Source Spectrum: For some sources higher orders will contain very little flux and will not be an issue. Typical examples are hot white dwarfs or relatively cool stellar coronae $T \sim 10^6$ K. Sources whose spectra are fairly weak in the region where the effective area of the LETG+HRC-S is highest ($\sim 8\text{-}20$ Å; 1.5-0.6 keV) compared to the spectrum at longer wavelengths are also going to be less affected by higher order throughput.

Estimates: Figure 9.16 can be used to estimate high order contamination. PIMMS (see section 9.5) can be used for gross estimates of higher order count rates; the PIMMS higher order calculation uses an effective area curve for orders $m > 1$ combined.

Instrumental Capabilities: Order separation is straightforward with ACIS-S. With HRC-S orders cannot be separated. It is possible in the future that filtering methods based on the HRC-S event pulse height information might enable some reduction of higher order events. Such techniques are limited by the width of the X-ray event pulse height distributions (section 9.3.6) and will be of little use for removing 3rd order events, but could be of increasing use for successively higher order removal.

Deconvolution and Forward Modeling: By folding a spectral model through an LETG -HRC-S instrument response that includes all significant higher orders (generally ≤ 10), the whole spectrum can be modeled at once. This approach will be available in CIAO software using response matrices that include the relevant higher orders. The SRON X-ray modeling code SPEX also uses this approach. An alternative approach is “bootstrap” modeling, where the analysis begins by only considering the shortest wavelengths. The approach assumes that contamination from the higher orders is minimal at the highest energies. The high energy data are used to deduce the higher order contribution at somewhat lower energies which is subtracted, and the process is repeated, working down in energy. The bootstrap approach is independent of an assumed source-model, but it may suffer from the amplification of noise in the case of weak sources and has mathematical problems in distributing photons into successively higher resolution orders.

The latter renders the method better for continuum sources than for those dominated by spectral lines.

ISM Absorption

The long wavelength cutoff of the LETGS in tandem with the HRC-S detector of ~ 170 Å (which can be extended with offset pointing as described above), extends well into the extreme ultraviolet (EUV). In this wavelength regime, even very nearby sources with relatively low ISM absorbing columns can be appreciably attenuated by H and He bound-free photoionizing transitions. Therefore observers should be aware that the effective long wavelength cutoff for anything but the most nearby sources (~ 100 parsec or less) will probably be determined by ISM absorption. It is also important to remember that neutral and once-ionized He can dominate the ISM absorption cross-section in the 44-200 Å (0.28-0.062 keV) range, and consideration of the neutral H absorption alone is generally not sufficient. Shortward of the C edge near 44 Å (0.28 keV), metals become the dominant absorbers. For illustration, the ISM transmittance for a “typical” mixture of neutral and ionized H and He H:He:He⁺ of 1:0.1:0.01 is illustrated in Figure 9.25 for the 5-200 Å range and for different values of the neutral hydrogen column.

The tools for estimating the line-of-sight neutral H column density can be found on the Center for EUV Astrophysics WWW page

http://www.cea.berkeley.edu/~science/html/Resources_tools.html

Also, the *CXC* web page has a tool COLDEN that provides the total galactic neutral hydrogen column for a given line-of-sight. This is described in Chapter 12.

9.5 Technical Feasibility

The technical feasibility section of an observing proposal for LETG observations should demonstrate the following:

1. That LETG, together with the proposed detector choice, is the optimum instrument combination to achieve the proposed scientific goals.
2. That LETGS has adequate spectral resolution to achieve the proposed goals.

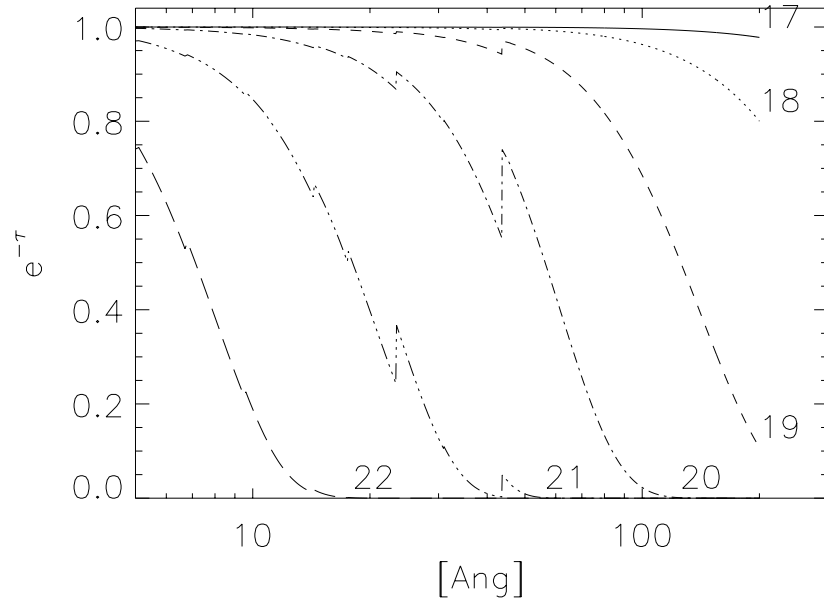


Figure 9.25: The ISM transmittance within the LETGS bandpass for different values of neutral hydrogen column density 10^{17} - 10^{22} cm^{-2} .

3. That the requested exposure time provides sufficient S/N in the features that are to be used to achieve the proposed scientific goals. The effects of instrument background must be taken into consideration, as must the effects of ISM absorption (unless it is easily shown to be negligible). In the case of HRC-S, if spectral orders other than that of the main features of interest are expected to yield significant signal in the region of these features, then this must also be taken into account in the S/N computation or simulation (see below).
4. That the proposed observation does not violate any viewing, instrument, or other observatory constraints.
5. That sources other than those of interest do not contaminate the field of view to an extent that compromises the proposed observation.

If the scientific goals demand spectral resolution that is at the LETGS performance limit, simulations using the MARX simulator discussed in Chapter 12 are recommended.

Item 3 (and possibly item 1) requires quantitative calculation. For LETG observations there are a variety of acceptable ways to determine and to demonstrate what exposure time is required to achieve a given observational goal. These include:

- Using tables of instrument effective areas and spectral resolution performance, in combination with spectral model fluxes for the object under consideration.
- MARX modeling and prediction of observations using a user-supplied spectral model.
- CIAO SHERPA or XSPEC modeling and prediction of observed spectra based on appropriate instrument response matrices. Such response matrices are available on the LETG *CXC* web site referenced at the end of this chapter.

Another tool, PIMMS, can be used for *rough planning purposes* and to predict 0th order pileup fractions in LETG+ACIS-S observations; see below and Chapter 12.

In all cases, proposers should be aware of possible limitations in the physical models and methods they are using. For example, older XSPEC versions might not include ISM absorption edges or spectral models at the high resolutions appropriate for *Chandra* grating observations. Available optically

thin, collision-dominated plasma radiative loss models are also relatively untested in detail at the line-by-line level, especially in the relatively unexplored spectral region 25-75 Å (0.5-0.17 keV). Some limitations in MARX modeling of LETG+HRC-S spectra are detailed below. MARX is described in more detail in Chapter 12.

9.5.1 Simple Calculation of Exposure Times and Signal-to-Noise Ratio for Line and Continuum Sources

There is a discussion in chapter 8 (HETG), section 8.5.4 concerning the detection of an isolated emission line or absorption line. The discussion is based on a figure of merit which shows the dependence of signal-to-noise ratio on the combined effective area and resolution. The figure of merit graphs (Figures 8.25 and 8.24) include the LETG+HRC-S combination. The discussion in Chapter 8 is based on line equivalent width, which is appropriate for broadened lines and continuum features but which is more difficult to apply to simple modeled estimates of expected line fluxes. Additional formulae which are simple to apply are presented below. The units use Å rather than keV, Å being a much more natural unit of choice for dispersed spectra, and especially for the LETG range.

Emission Line Sources The source signal S in a bin is the difference between the total counts and the background counts B . The estimated standard deviation of the source counts S in a spectral bin is given by Poisson statistics as:

$$\sigma_S = \sqrt{S + B} \quad (9.1)$$

Here we have made the important assumption that there is effectively no additional uncertainty in the estimation of the background B . Such an assumption may only be valid if, for example, the detector region used to estimate the background within the spectrum extraction window is much larger than the window itself.

Spectrometer count rates for emission features are given by

$$s_l = A_{eff}(\lambda)\mathcal{F}_l(\lambda) \quad (9.2)$$

where s_l is the source count rate in the resolution element centered at λ , in counts/s, A_{eff} is the effective area in cm², and \mathcal{F}_l is the source flux at the telescope aperture, in photons/cm²/s. For A_{eff} , it is reasonable to use the total area obtained from the sum of + and - orders as illustrated in

Figure 9.15. Raw source counts are estimated by multiplying this instrument count rate by an integration time.

Using equations 9.1 and 9.2, the signal-to-noise ratio for an integration time t is then

$$\frac{S}{\sigma_S} = \frac{s_l \sqrt{t}}{\sqrt{s_l + b}} \quad (9.3)$$

where b is the background count rate *within the spectrum extraction window* (i.e. “underneath” the spectrum) in the same resolution element centered at λ , in counts/s. Equation 9.3 provides the expected relation that is valid in the limit where the background count rate b is small compared with the source count rate s_l , the signal-to-noise ratio scales with the square of the exposure time.

The exposure time required to achieve a given signal-to-noise ratio is then provided by inversion of equation 9.3,

$$t = \left(\frac{S}{\sigma_S} \right)^2 \frac{s_l + b}{s_l^2}. \quad (9.4)$$

In order to make the exposure time estimate one needs to determine the background count rate, b . Since the spectrograph does not have infinite resolution, the flux from an otherwise narrow spectral line is spread over a typical line width, w_l . For LETG+HRC-S spectra, a good estimate for w_l is 0.07 Å. This is somewhat larger than the FWHM value of 0.05 Å listed in Table 9.1, but is more appropriate for calculations of signal-to-noise because it includes more of the line flux. For lines that are additionally broadened, simply use a value of w_l that covers the region under the feature of interest. The background rate b is then given by the quantity $b = w_l b'$, where b' is the background rate in units of count/Å. Background spectra for LETG+HRC-S from which one can readily estimate b are illustrated in Figure 9.26. Two scales are shown, one corresponding to b' and one corresponding to b where a width $w_l = 0.07$ Å was assumed. Note the y -axis units are per 10 ks. These curves correspond to both + and - orders added together and so are appropriate for use with the *LETG+HRC-S total 1st order* effective area curves. These spectra are also available in ASCII format from the LETG Observer Information web page listed at the end of this chapter.

Using the signal count rate s_l , provided by the product of source flux (at the telescope aperture) and effective area as stated in equation 9.2, we then obtain the two equations for the signal-to-noise ratio S/σ_S resulting from an exposure time t ,

$$\frac{S}{\sigma_S} = \frac{\mathcal{F}_l A_{eff} t}{\sqrt{\mathcal{F}_l A_{eff} t + b' w_l t}} \quad (9.5)$$

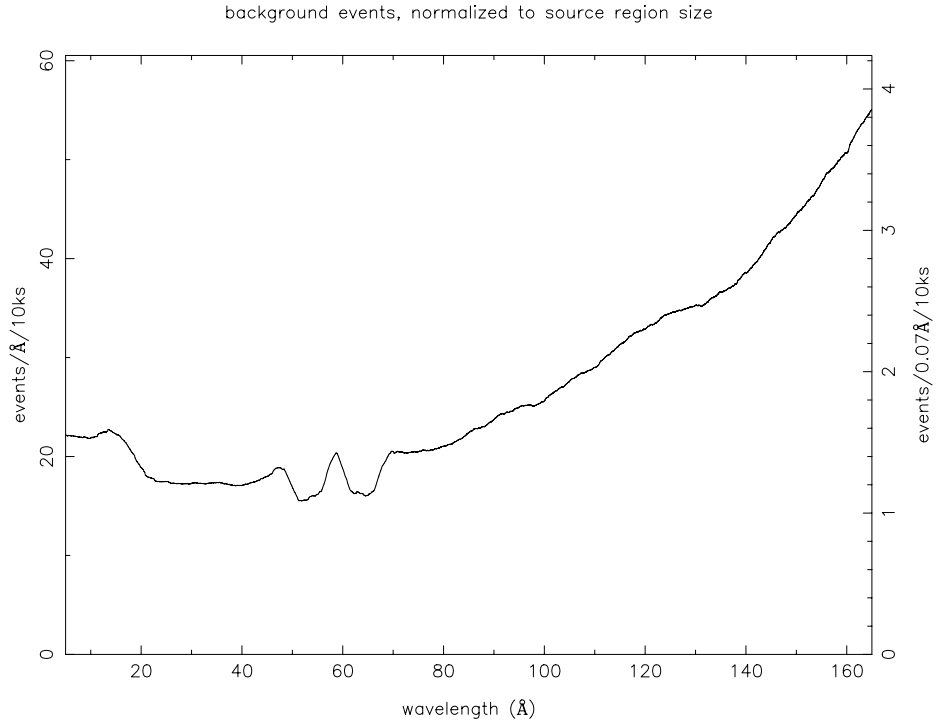


Figure 9.26: The LETG+HRC-S background count rate in the spectral extraction window as a function of wavelength for use in observation planning. Both + and - orders have been combined. These curves correspond to the “moderate” (5% x-ray loss) PH filter described in the text. The left y axis is in units of counts/Å/10 ks, while that on the right is in units of counts/0.07 Å/10 ks; the latter corresponds to a typical line width over which most of the observed flux is distributed in the case of an intrinsically narrow spectral line compared to the instrument LRF.

and for the exposure time t required for a signal-to-noise ratio S/σ_S

$$t = \left(\frac{S}{\sigma_S} \right) \frac{\mathcal{F}_l A_{eff} + b' w_l}{(\mathcal{F}_l A_{eff})^2}. \quad (9.6)$$

These simple equations, which include the effects of instrumental background, can also be easily applied to observations of lines on top of continua, as well as to situations in which features of interest lie on top of higher (or lower) spectral orders (HRC). In these cases, the continuum or higher order flux acts as an additional background term—the count rate/Å due to these additional terms is simply added to b' .

Continuum Sources Model fluxes for continuum sources can be expressed as flux densities in units of photons/cm²/s/Å. To compute instrument count rates s_c from a continuum source spectrum, the A_{eff} function and spectrum must be partitioned with some bin size w , large enough to give adequate count rates. The product of the source spectrum with the A_{eff} function is then summed over some wavelength region of interest. Equation 9.2 becomes the sum:

$$s_c(\lambda) = \sum_{j=1}^N \mathcal{F}_c(\lambda_j) A_{eff}(\lambda_j) w \quad (9.7)$$

where \mathcal{F}_c is the model source flux in photons/cm²/s/Å, $A_{eff}(\lambda_j)$ is the effective area of the j th bin in cm². The region of interest spans bins 1 through N , and w is the bin width in Å. In using this formula for planning purposes, proposers must choose a spectral bin width that will demonstrate the viability of the program proposed. For fairly narrow spectral ranges in which A_{eff} is nearly constant, the sum over 1- N reduces to

$$s_c(\lambda) = \mathcal{F}_c(\lambda_j) A_{eff}(\lambda_j) N w \quad (9.8)$$

In this case one can of course simply chose a new bin size $w' = N w$.

The difference between the continuum and the emission line case above lies in the units of \mathcal{F}_c , which is a flux density. The equations corresponding to the line source equations 9.5 and 9.6 are, for the signal-to-noise resulting from an exposure time t

$$\frac{S}{\sigma_S} = \frac{\mathcal{F}_c A_{eff} w t}{\sqrt{\mathcal{F}_c A_{eff} w t + b' w t}} \quad (9.9)$$

and for the exposure time t required for a signal-to-noise ratio S/σ_S

$$t = \left(\frac{S}{\sigma_S} \right) \frac{\mathcal{F}_c A_{eff} w + b' w}{(\mathcal{F}_c A_{eff} w)^2}. \quad (9.10)$$

Note also in the above equations that the background b' is in units of counts/Å/s.

PIMMS for Rough Planning Purposes

PIMMS is described in Chapter 12 and some examples are also presented. PIMMS is best suited to performing rough estimates of total or 0th order count rates, or estimating the fraction of 0th order events that would be piled up. Some degree of caution should accompany PIMMS calculations of detailed quantities such as count rates within narrow spectral bands using the Raymond-Smith model. For example, line positions and intensities in this model were only designed to represent total radiative loss and do not stand up to high resolution scrutiny. Calculations using powerlaw and featureless continua are not prone to such difficulties, but are susceptible to other PIMMS limitations. One particular limitation concerns the background model for HRC-S, which in PIMMS is currently (February 2000) assumed to be a single average number per spectral resolution element of 32 counts/100 ks. This approximation overestimates the background at higher energies, and underestimates the background at lower energies - see Figure 9.26.

MARX Simulations

The best tool available for the most accurate observation simulations is the MARX ray trace simulator. MARX is described further in Chapter 11; there is also a detailed user guide available. MARX allows one to simulate observations using any of the available *Chandra* instrument combinations. At the time of writing (Feb 2000), MARX has the following limitations for LETG+HRC-S observations:

- As described in section 9.2.1, due to necessary changes in the HRC instruments following the ground calibration at the NASA Marshall Space Flight Center XRCF, the LETG+HRC-S effective area calibration performed is no longer applicable. Laboratory calibration measurements were subsequently performed, but for wavelengths longward of 44 Å (0.28 keV) the instrument was essentially uncalibrated. In-flight calibration observations have been performed using observations

of hot white dwarf stars (section 9.2.2), but analysis is still ongoing. Current data suggest that the existing MARX HRC-S and HRC-I QE model overestimates the QE by about 10-15 % for wavelengths $> 44 \text{ \AA}$.

- The HRC-S QE is known to be spatially non-uniform at the 10-15% level. The non-uniformity is characterized by a fairly steady gradient in QE from one side of each MCP to the other in the dispersion direction. The QE is more uniform in the cross-dispersion direction. This gradient in QE is not currently (February 2000) included in the MARX HRC-S model.
- Instrument, sky and particle background is *not* directly included in MARX and need to be input by the user. Ignoring background will affect HRC-S observation predictions the most. See section 9.3.6) and Figure 9.26. One way of simulating this for a point source is to obtain the empirical background spectra from the LETG Observer Information web page listed at the end of this chapter.

LETGS Example Simulations Two different kinds of spectra which might be used to discuss feasibility are illustrated here. The first simulation is of a long observation of an AGN represented by a power-law spectrum with a warm absorber. Figure 9.27 shows the LETGS spectrum created by MARX. A large fraction of the LETG energy range is displayed.

As the second example, a simulation of a smaller energy range is shown. Figure 9.28 demonstrates the effect of source extent on resolution. A simulation of this kind could be used to discuss the resolution of line pairs and spectral features, the S/N in an emission line or continuum region, or the effect of weak lines. The top panel shows the input spectrum from a collisional-equilibrium plasma with an electron temperature 0.25 keV and solar abundances. It has been put through the MARX program to simulate sources of different sizes in panels b-d. In all panels, the count rate normalization is arbitrary. Panel b shows the simulated LETG+ HRC-S spectrum of a point source. Panels c and d are simulated LETG observations of a uniform surface brightness disk with radii $4''$ and $8''$ respectively. The effects on an off-axis spectrum would be very similar. A preliminary estimate of the effects of resolution at other energies or other source sizes can be estimated from comparisons of Figure 9.28, and Figure 9.10 and Figure 9.11.

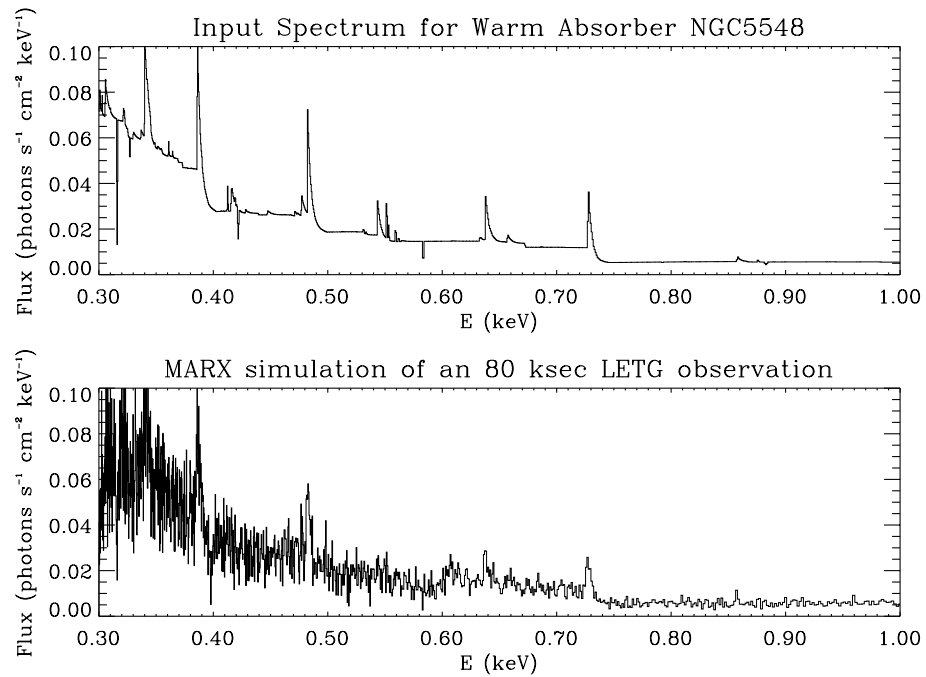


Figure 9.27: This figure shows the extracted first order spectrum for an 80 ksec observation of the AGN NGC5548. The input spectrum consists of a power-law plus a “warm” absorber (shown in the top panel). The simulated spectrum (bottom panel) has been corrected for the instrument response to give the flux from the source.

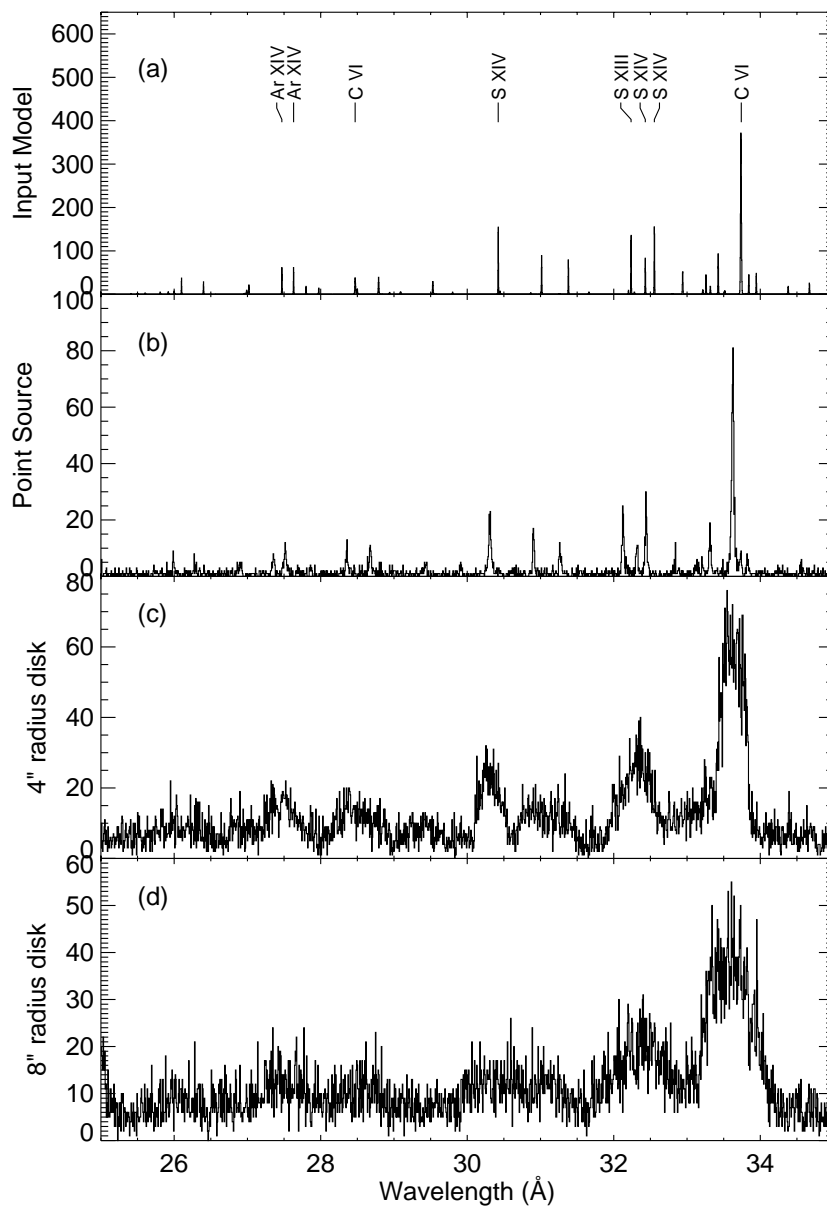


Figure 9.28: MARX simulation of spectra showing the effect of source extent. The panels show (a) computed input spectrum, (b) a MARX output of LETG spectrum of a point source, (c) the same as (b) except that the source is a disc of uniform brightness with radius of $4''$, and (d) the same but with radius of $8''$. See text for discussion.

9.6 References

Further LETGS information and calibration data can be found on the LETG Observer Information page¹ off the *CXC* website.² Newsletter articles summarizing calibration can be found in Issue 4 subassembly calibration³, Issue 5 XRCF calibration⁴, and Issue 6 calibration reports.⁵

Document history

- 00 Feb - revised and re-written by J.J. Drake, B. Wargelin and O. Johnson – some editing and cross-referencing by M. Weisskopf.
- 99 Dec - removal of LESF and HESF; D. Harris
- 99 Jun - updated by N. R. Evans
- 97 Aug - updated by N. Evans, J. Drake, J. Juda, D. Huenemoerder, M. Juda, M. Weisskopf, A. Tennant, P. Predehl, D. Swartz
- 97 May - updated by N. R. Evans, B. Wilkes, and J. Juda
- 94 Nov - updated using PDR material.
- 93 Jan - updated during visit to Utrecht; comments from A. Brinkman, R. Mewe, T. Gunsing, J. Heise, J. van Rooijen.
- 92 Nov - first draft

¹<http://asc.harvard.edu/cal/Links/Letg/User>

²<http://asc.harvard.edu/cal/Links/links.html>

³http://asc.harvard.edu/udocs/news_04/issue4aplatex.html

⁴http://asc.harvard.edu/udocs/news_05/issue5latex.html

⁵http://asc.harvard.edu/udocs/news_06/index.html

Part II

Policy, Planning, and Proposal Preparation

Chapter 10

Observing Policy

10.1 *Chandra* observing policy

10.1.1 Introduction and scope

This document establishes the observing policy for *Chandra*. This policy reviews and confirms the distribution of observing time amongst the Guaranteed Time Observers (GTOs) and General Observers (GOs), establishes guidelines for the resolution of conflicts between and within these groups, and sets guidelines for the distribution of observing time.

10.1.2 Applicable documents

Chandra Level-I Requirements and Policy

10.1.3 Distribution of data

Proprietary data

All data awarded either to GTOs or to GOs will be proprietary for one year (unless the observer specifies a shorter proprietary period), beginning when the data are made available to the observer. For fragmented "Long Duration" observations (see section 10.1.6), the one-year period for each target begins when 80% of the data have been made available to the observer.

Data from unanticipated Targets Of Opportunity (TOO) and other use of Director's Discretionary Time (see section 10.1.7) may be proprietary for limited periods – no more than three months – before they are placed into the public archive.

Calibration data scheduled and obtained by the *Chandra* X-ray Observatory Center (*CXC*) will not be proprietary and will be placed directly into the public archive. Data obtained during slews from one target to another and from pointings made for operational reasons will also be placed directly into the public archive.

Distribution of Observing Time

Distribution between GO and GTO Scientific observations commence approximately 2 months after launch. Any x-ray data obtained during these first 2 months are considered calibration data and shall be placed directly into the public archive. Subsequent to this commissioning period, and exclusive of calibration time, the distribution of observing time between GTO and GO is as follows:

Months after launch	GO	GTO
3 - 4		100%
5 - 22	70%	30%
23 - end of mission	85%	15%

Distribution amongst GTO's As specified in the *Chandra* Level-I Policy and Requirements Document, the GTOs comprise the following: Four Instrument Principal Investigators (IPIs) for the *Chandra* Imaging Spectrometer (ACIS), for the High-Resolution Camera (HRC), for the Low-Energy Transmission Grating (LETG), and for the High-Energy Transmission Grating (HETG); the Telescope Scientist (TS); and six Interdisciplinary Scientists (IDSs). Their observing time is based on a distribution of 4.6 "shares" as follows:

Six IDSs	0.1 shares each	0.6 shares total
TS and LETG IPI	0.5 shares each	1.0 shares total
HETG, ACIS, and HRC IPIs	1.0 shares each	3.0 shares total

GTO time utilization All GTOs except the IDSs are required to use their observing time in the proportions listed above, according to the time phasing given. However, each IDS may use his/her entire observing allocation (based on the assumption that the mission ends after month 62) during months 3-22. Should any of the IDSs invoke this option, the remainder of

the GTO time-phased total observing time will be adjusted accordingly, in order to satisfy the above GO/GTO distribution.

10.1.4 Target selection and phasing

Target selection will be phased with *NASA* Research Announcements (NRAs). The cycle of target selection will begin with the GTOs specifying their targets for the first cycle of observation (nominally months 3-13). These will be made public with the issuance of the first NRA for General Observers. Targets resulting from peer review of the responses to the NRA will be added to those proscribed by the GTOs. This cycle of events will be repeated in this order for the second NRA, which nominally covers the period from months 14-25 inclusive. GTOs may not reserve targets for the second cycle prior to GO target selection from the first NRA.

For the third and subsequent NRAs, both GTOs and GOs must submit proposals for observing time. In principle, GTOs are guaranteed to receive the observing time in accordance with section 10.1.3, but will no longer be able to reserve targets in advance of the NRA. If GTO proposals consistently require invoking guaranteed time in order to meet the allocation specified in section 10.1.3, *NASA* will consider reducing guaranteed time.

10.1.5 Conflict resolution

GTO-GTO conflicts Any GTO-GTO conflict in preparing observing plans for NRAs 1 and 2 shall be resolved by *Chandra* Project Science. Subsequent conflicts (NRAs 3 and beyond) will be settled as part of the peer-review process, with selection based on scientific merit (section 10.1.8).

GO-GTO conflicts GO-GTO conflict is avoided through the provisions of section 10.1.4.

10.1.6 Large Projects

Large Projects are those that require more than 300 ks observing time, whether long-duration observations of single targets or shorter duration observations of many targets. Large Projects are encouraged: At least 20% of the observing time awarded during NRAs 2 and beyond will be allocated for Large Projects, subject to reasonable standards of scientific merit, as determined through peer review.

This section of the policy will be carefully reviewed prior to NRA 4, in order to determine whether the large-project quota should be adjusted. Large

projects shall be proposed to be completed within the time span covered by an NRA and cannot reserve targets beyond this. Finally, those projects which are large owing to the observation of numerous objects (e.g., of a given class) should propose alternate targets (via a priority-ordered, slightly over-subscribed list), in the event of a conflict with an individual target of high scientific merit from another proposal during the same proposal cycle. The peer review shall either approve the individual observation from the other proposal and suggest (or select) alternate target(s) for the Large Project, or simply inform the Large Project proposers that one of their targets will be available in the public archive a year after the observation.

10.1.7 Targets of Opportunity (TOOs)

There are two categories of Targets of Opportunity: Those that are proposed and selected through peer review; and those that simply occur and have been brought to the attention of the Director of the *CXC*, who may reschedule *Chandra* to obtain the appropriate observations, in the best interest of the scientific community.

Pre-proposed TOOs

A proposed TOO may be reserved for a single proposal cycle. The proposer may attempt to renew the opportunity in subsequent cycles.

For Cycle 2, a maximum of 3 TOOs can be reserved by GTOs provided the data are made public immediately.

Unanticipated TOOs

Data obtained from an unreserved TOO is considered Directors Discretionary Time. These data may be kept proprietary for a period not to exceed three months.

10.1.8 GO time allocation

All GO time allocation will be subject to peer review.

All GTO target allocation beginning with the third proposal cycle will be subject to peer review, consistent with the provisions of section 10.1.4.

10.1.9 Director's Discretionary Time

5% of the observing time is reserved for Director's Discretionary Time (DDT). This allocation includes unanticipated TOOs.

10.2 Procedures concerning TOO's and DDT

The deep orbit of *Chandra* will permit relatively easy access to any TOO. The planned response time to TOO's is ~ 24 hours but operational experience may change this. The total number of TOO's performed are also limited by operational and man-power constraints.

Requests to either initiate a pre-approved TOO or to propose a new one are made to the *CXC* Director and it will be his/her decision to interrupt the timeline and conduct the observation. The investigator is required to submit an abbreviated version of the RPS form. The form, a Request for Observation (RfO), can be found at the *CXC* home page (<http://asc.harvard.edu>) and submitted via the WWW.

10.2.1 Pre-proposed TOO's

TOO's generated by an NRA-approved proposal are similar in spirit to the *IUE* or *XTE* in that time is allocated to the proposal, but the time is unscheduled. To initiate the scheduling process, the investigator is required to specify in the RfO how the trigger condition has been met.

TOO's disrupt the timeline and it is possible that the TOO conflicts with a time-critical observation and/or with another TOO. In such situations, the *CXC* Director will determine priorities. Any disrupted preplanned observation will, however, be ultimately accomplished if at all feasible.

10.2.2 Unanticipated TOO's

A request for an unanticipated TOO observation is made directly to the *CXC* Director. Submission of an RfO is required. The procedure is as follows:

- The proposer must determine whether the target falls within the portion of the sky visible to *Chandra*. The *ObsVis* tool described in Chapter 12 can generate such information.
- The proposer must establish whether the target can be detected by *Chandra*. The tools described in Chapter 12 can be used for this purpose.
- The proposer must address the following questions:
 - Why is the science from the observation important, and why not simply propose during the next *Chandra* NRA?

- Is there an impending, previously approved, *Chandra* observation, that can accomplish the objectives?
- How urgent is the TOO? Must the observation be done immediately?
- If relevant, what is the likelihood of additional transient behavior (i.e. does the phenomenon recur?) If reoccurrence is likely, what is the consequence if the target is not observed until the next occurrence?
- If data already exist in the archive, why is another observation with *Chandra* necessary?
- What is the proposed/suggested detector configuration?

If the proposed observation is accepted, a new timeline will be created as soon as possible. Some negotiation between the observer and the *CXC* may be necessary to achieve the optimum blend of response time and minimum impact on the rest of the schedule.

10.2.3 Directors Discretionary Time

Requests for DDT must follow the same procedure as required for an unanticipated TOO. The procedure is described in section 10.2.2.

- The proposer may apply for a short period of time (≤ 3 months) during which the data is considered proprietary.
- A limited amount of funds are available to support DDT observations.

10.3 Criteria for Completeness and Data Quality

10.3.1 Completeness

Completeness refers to time on target or exposure time. Observations are scheduled based on the approved exposure time. Very occasionally, circumstances such as telemetry dropouts, scheduling efficiency, etc. may prevent us from achieving this exposure time. The observation is considered complete if the achieved exposure is $\geq 80\%$ of the approved exposure time.

Observations ≤ 3 ks, will not be repeated, due to the associated high overhead and inefficiency. In this case, performing a single, best-efforts attempt to observe for the approved amount of time constitutes a completed observation.

10.3.2 Data quality due to high background

Data can be lost (or overwhelmed) because of occasional episodes of very high background. If the principle target was a point source and the background is ≥ 10 times nominal for $\geq 50\%$ of the observation, the target may be observed again for a period of time equal to the amount of time lost due to the high-background. If the target is extended, and the background increase is ≥ 5 times nominal for $\geq 50\%$ of the observation, then another observation may be scheduled to replace the amount of time lost due to the high-background. We realize that application of these limits are somewhat arbitrary. The intent is to only schedule additional observations if the scientific objectives were not achieved due to the high background. If “cosmic weather” causes only some deterioration in data quality, the observation is considered complete.

Although the *CXC* monitors space weather, there is no real time contact with the Observatory. Ultimately, it is the observer’s responsibility to determine if the data require another observation according to the criteria above. An application for an additional amount of time on target should be made to the *CXC* Director. Providing a plot of the background counting rate vs. time and a short table with the integrated time at different background levels is required.

10.3.3 Data quality - telemetry saturation due to x-ray sources

Telemetry saturation produced by the target and/or other sources in the field of view are the responsibility of the observer. The unique case of a previously unknown transient appearing in the field of view will be handled case-by-case.

Chapter 11

Tools for Assessing Feasibility

11.1 Purpose and Scope

At the minimum, proposers are required to estimate a detector count rate for the desired observation. The estimated rates will be reviewed during the technical assessment and during the peer review.

This chapter is meant to acquaint the GO with the methods by which the feasibility of an observation can be assessed. Information is given on count rate calculations and simulations of spectra. Additional simulations are presented in the detector-specific chapters.

11.2 Assessing Feasibility: the Methods

The feasibility of using one of the *Chandra* detectors to observe a specific target can be assessed using any of the following methods.

- *PIMMS* (Portable Interactive Multi-Mission Simulator);
- *XSPEC* ;
- *MARX* (Model of AXAF's Response to X-rays);

All these tools can help provide a reasonable estimate of exposure time when appropriately used. It is important that the user understands the relative strengths and weaknesses of each tool.

PIMMS is useful if the source spectrum is simple and you have some estimate of source flux, either a count rate estimated from a previous mission

or a flux (absorbed or unabsorbed) in some energy band. *PIMMS* cannot deal with complicated spectral or spatial structure. *PIMMS* estimates the amount of ACIS pile-up (assuming an on-axis point source) and the impact of that pile-up on the count rate.

For more complicated spectra, investigate the use of *XSPEC* to provide a simulation. *XSPEC* provides a method to estimate spectral shape (for example, temperature) and uncertainty. Note that the Raymond-Smith model in both *PIMMS* and *XSPEC* is not necessarily applicable to high-resolution spectroscopy (other models in *XSPEC* are better) as lines are grouped together. *XSPEC* does not model ACIS pileup and cannot directly simulate grating spectra of extended sources.

Finally, for a source with a complicated spatial structure or a highly piled-up ACIS spectrum, consider using the *MARX* software. Use *MARX* to perform a Monte-Carlo simulation of the observation, including an approximation to mirror and instrument characteristics. *MARX* output is a simulated data set. *MARX* output can be analyzed with *CIAO* and other data analysis packages (e.g. *XANADU*)

11.3 Estimating a Count Rate

The two tools to be described are only for estimating count rates. The accuracy of the *estimates* is dependent upon the model assumed and the tool used.

11.3.1 *PIMMS*

Functional Description

PIMMS, the *Portable, Interactive Multi-Mission Simulator*, was developed at NASA-GSFC by Dr. K. Mukai¹. It allows the user to convert between source fluxes and count rates for different missions. *PIMMS* also uses simple models (blackbody, bremsstrahlung, power, Raymond-Smith) in calculating count rates or fluxes.

Accessing *PIMMS*

PIMMS is available from the *CXC* science web page (asc.harvard.edu; see Figure 11.1 or can be downloaded and run as a stand-alone process on the GO's local machine (instructions are in Chapter 12).

¹We thank Koji for making some changes to the code for *Chandra* .

Figure 11.1: An image of the WWW version of *PIMMS*.

Technical Description

The general approach to estimating a count rate using *PIMMS* is as follows (the order is not important).

- Set the input source parameters: flux vs. count rate, input energy band, satellite/detector, etc.
- Define a model and set the model parameters.
- Run *PIMMS* (using the ‘go’ command).

As a general warning, the Raymond-Smith model in *PIMMS* is computed at a limited number of temperatures. The corresponding accuracy of the estimated count rate may not be high.

Worked Example

A sample *PIMMS* session follows using the stand-alone version for a randomly-chosen *Chandra* detector. In the sections that follow, the text that will appear on the monitor screen during a session appears in typewriter font.

The initial header for *PIMMS* is:

```
hypatia-44: prop_pimms
ASCDS_PROP_PMS_DATA (for instrument effective area data) =
    /data/udoc2/PropTools/CXCDS_ROOT_SOLARIS/config/pimms/data
ASCDS_PROP_PMS_MODEL (for spectral models) =
    /data/udoc2/PropTools/CXCDS_ROOT_SOLARIS/config/pimms/models
*** PIMMS version 2.7 ***
    1999 July 9 release
    (this version does not simulate images)
    Reading mission directory, please wait
* Current model is BREMSSTRAHLUNG, kT= 10.0000 keV; NH = 1.000E+21
  <--- Use 'MODEL' command to change
* By default, input rate is taken to be
  Flux ( 2.000- 10.000 keV) in ergs/cm/cm/s
  <--- Use 'FROM' command to change the default
* Simulation product will be
  Count rate in ASCA SIS
  <--- Use 'INSTRUMENT' command to switch to another instrument
PIMMS >
```

We are interested in estimating a count rate for the front-illuminated ACIS chips on *Chandra*, so the command is:

```
PIMMS > inst chandra-ao2 acis-i
```

The model choice is the power law with a photon spectral index of 1.68 absorbed by a hydrogen column of $7 \times 10^{22} \text{ cm}^{-2}$. As *PIMMS* does not have a rich suite of models, we will only consider the continuum contribution. The next command tells *PIMMS* to calculate the count rate based upon the 2-10 keV flux of NGC 4151 (with units of $\text{ergs cm}^{-2} \text{ s}^{-1}$, indicated by the key word “ergs”).

```
PIMMS > from flux ergs 2-10
PIMMS > mo pl 1.68 7e22
```

```

PIMMS > go 1.8e-10
* For power law model with photon index = 1.6800; NH = 7.000E+22
  and a flux ( 2.000- 10.000keV) of 1.800E-10 ergs/cm/cm/s
  (Model normalization = 6.577E-02)
* PIMMS predicts 5.635E+00 cps with CHANDRA-A02 ACIS-I
% Pileup estimate for ACIS:
  Pile-up is too high (37.1 %) at the fastest single-chip frame time (0.2 s)
  Consider using the Continuous Clocking mode

```

Proposers should be aware that that pulse pileup is a problem for ACIS; in the example above the count rate is high and the pileup percentage is 37%. The proposer should also note that the pileup estimator in *PIMMS* **assumes** the entire ACIS bandpass is used when estimating pileup. If the proposer has used less than the full bandpass, then the pileup will be *underestimated*. Material describing the mitigation of pileup is contained in the ACIS chapter.

11.4 Simulating Spectra

While the two tools that follow can be used to estimate count rates, their primary power is the ability to generate a “fake” spectrum that can be analyzed as if it were a real observation. Again, text in **typewriter font** will appear on the screen.

The basic steps to simulate a spectrum are:

- define the model;
- read in the response matrix and effective area files;
- generate a fake spectrum;
- calculate the resulting flux or count rate;
- adjust the model normalization so that the fake model will generate the correct flux (and generate a new fake spectrum);
- assess whether the resulting spectrum has sufficient counts to address the scientific goals;
- adjust the exposure time (and regenerate a new fake spectrum);
- fit the faked spectrum (if desired).

11.5 *XSPEC*

11.5.1 Functional Description

XSPEC is the spectral analysis portion of the Xanadu X-ray data analysis package. The material that follows will present a brief synopsis of the use of the commands to generate a fake spectrum. Readers are urged to consult the *XSPEC* manual for additional details.

As a reminder, the Raymond-Smith model in *XSPEC* is somewhat inappropriate for carrying out simulations of the *Chandra* gratings. The inherent spectral resolution of the model is not sufficient for an accurate simulation of grating data. *XSPEC* can be used for grating simulation *provided* the model has sufficient spectral resolution. The Mewe-Kaastra-Liedahl model in *XSPEC* (“mekal”) has sufficient resolution, *provided* the run-time option that forces the code to calculate (rather than using a precalculated look-up table) is used.

For the gratings, another useful tool is *MARX* (described in the next section). For extended sources, only *MARX* has a capability to simulate a spectrum.

11.5.2 Accessing *XSPEC*

XSPEC comes in two versions. The stand-alone program is large and sophisticated. It has extensive on-line help, is a command-driven code, and allows the user to fit spectral data or to create a faked spectrum that can be analyzed with *XSPEC* itself.

The spectral simulation portion of *XSPEC* can also be run over the WWW. *WEBSPEC* can be accessed from

`http://heasarc.gsfc.nasa.gov/webspec/webspec.html`

It is also available as a link from the *CXC* proposer page (`asc.harvard.edu/soft`.) The WWW *XSPEC* interface was developed at the HEASARC; they have kindly given the interface code to the *CXC* for use by *Chandra* so that two WWW sites will be available.

WEBSPEC comes in two versions, a “base” version:

`http://heasarc.gsfc.nasa.gov/webspec/webspec.html`

and a more advanced version:

`http://heasarc.gsfc.nasa.gov/webspec/webspec_advanced.html`

for more experienced users. Both are supported by detailed help. In the following section, we describe how to simulate a spectrum using *XSPEC*.

11.5.3 Stand-alone example

The text that follows presents a generic simulation of a fake spectrum, arbitrarily chosen for ACIS-I, using the stand-alone version of *XSPEC*. (Note that this choice limits the simulation to the Front-Illuminated (FI) chips. A mix of FI and BI (Back-Illuminated) chips would require two simulations, one for each type of chip, to assess the feasibility more accurately.) The steps to simulate a spectrum have been listed in section 11.4 above.

The example that follows will *not* be a complete introduction to *XSPEC*, so the user is urged to work through this example as well as others to learn the full power of the *XSPEC* environment.

11.5.4 The Setup

The example that will be presented is for the AGN NGC 4151. This target was chosen because it has been observed with *ASCA* and *BBXRT*, so the simulated *Chandra* ACIS spectrum can be compared with observed spectra. We expect all three spectra to appear nearly identical because (i) the effective areas of the three detectors are not significantly different (by factors of 5 or more); and (ii) the spectral resolutions of the three detectors are nearly identical ($E/\Delta E \sim 50$ at 1 keV).

The parameters of the NGC 4151 model have been taken from the literature². The adopted model is a power law with spectral index 1.68 and 1 keV normalization of 0.056 ph/s/cm²/keV, absorbed by (a) a fully covering absorber with column density of $7.0 \times 10^{22} \text{ cm}^{-2}$ and (b) a partial covering absorber with $N_H = 3.0 \times 10^{22} \text{ cm}^{-2}$ and covering fraction of 0.9. The model also contains a gaussian to represent a Fe-K emission line. The measured flux in the 2-10 keV band is $1.37 \times 10^{-10} \text{ ergs s}^{-1} \text{ cm}^{-2}$. We will ignore the redshift-dependent nature of these quantities; the proper model should use redshift-dependent components (i.e., *zwabs*, *zpower*, etc.).

Defining A Model

Models are constructed from basic components. A list of the components that are available may be obtained by typing

```
XSPEC> model ?
```

²Weaver et al. 1992, ApJ, 402, L11

Information about the `model` command may be obtained by typing

```
XSPEC> help model
```

Basic help can be obtained by working through the walk-through example presented at the front of the *XSPEC* manual.

The *XSPEC* model is:

```
XSPEC> mo phabs * pcfabs (power)
```

We will add the gaussian components later.

Generating a Fake Data File The use of the `model` command will generate a reply from the *XSPEC* code that will request values for the model parameters.

```
XSPEC> mo phabs * pcfabs (power)
```

```

Input parameter value, delta, min, bot, top, and max values for ...
Mod parameter 1 of component 1 phabs nH 10^22
1.000 1.0000E-03 0. 0. 1.0000E+05 1.0000E+06
7.0                                     (change the default to 7.0)
Mod parameter 2 of component 2 pcfabs nH 10^22
1.000 1.0000E-03 0. 0. 1.0000E+05 1.0000E+06
3.0                                     (change the default to 3.0)
Mod parameter 3 of component 2 pcfabs CvrFract
0.5000 1.0000E-02 0. 5.0000E-02 0.9500 1.000
0.9                                     (change the default to 0.9)
Mod parameter 4 of component 3 powerlaw PhoIndex
1.000 1.0000E-02 -3.000 -2.000 9.000 10.00
1.68                                    (change the default to 1.68)
Mod parameter 5 of component 3 powerlaw norm
1.000 1.0000E-03 0. 0. 1.0000E+05 1.0000E+06
-----
mo = phabs[1] * pcfabs[2] (powerlaw[3])
Model Fit Model Component Parameter      Value
par  par comp
1    1    1  phabs      nH 10^22      7.00000    +/- 0.
2    2    2  pcfabs     nH 10^22      3.00000    +/- 0.
3    3    2  pcfabs     CvrFract      0.90000    +/- 0.
4    4    3  powerlaw   PhoIndex      1.68000    +/- 0.
5    5    3  powerlaw   norm          1.00000    +/- 0.
-----
5 variable fit parameters
```

Now, the fake spectrum must be generated. The command to do so is `fakeit none`. The ‘none’ indicates that no response matrix has yet been specified, so *XSPEC* should prompt the user for a name. The `show` command allows the user to check on the model and file names specified. **Note that the files `w215c2r_norm.rm` and `w215c2r_norm.ar` are dummies.** They are the response matrix (*RMF*) and ancillary response (*ARF*) files that were created for AO1, and are inaccurate. Well before the AO2 proposal deadline, appropriate *RMF* and *ARF* files will be made available through the web. Instructions for retrieving them will be found on the Proposer page (<http://asc.harvard.edu/soft/>).

In the example below, the requested exposure time is 10 ksec. The defaults may be adopted for all of the other parameters (e.g., “use counting statistics”, “A”, “Bkg”, etc.). The reader should note that no background file has yet been specified. Furthermore, the model normalization has not been set. *Count rates at this point are pure fiction.*

```
XSPEC > fakeit none
  For fake data, file # 1 needs response file: w215c2r_norm.rm
    ... and ancillary response file: w215c2r_norm.ar
Use counting statistics in creating fake data? (y)
Input optional fake file prefix (max 12 chars):
Override default values for file # 1
Fake data filename (): test.fak
T, A, Bkg, cornorm ( 1.0000 , 1.0000 , 1.0000 , 0. ): 10000.0
Net count rate (cts/cm^2/s) for file 1 71.90 +/- 8.4836E-02
Chi-Squared = 1329. using 2048 PHA bins.
Reduced chi-squared = 0.6505
XSPEC> show
15:32:33 26-Oct-94
Fit statistic in use is Chi-Squared
Minimization technique is Lev-Marq
Convergence criterion = 1.0000000000000D-02
Querying enabled
Prefit-renorming enabled
Solar abundan
ce table is angr
Log file : xspec.log

Information for file 1
belonging to plot group 1, data group 1
```

```

telescope = AXAF , instrument = ACIS  channel type = PHA
Current data file: test.fak
No current background
No current correction
Response (RMF) file : w215c2r_norm.rmf
Auxiliary (ARF) file : w215c2r_norm.arf
Noticed channels      1 to 2048
Spectral bins         1 to 2048
File integration time  1.0000e+04
File observed count rate  71.90  +/-8.4836E-02 cts/cm^2/s
Model predicted rate:  71.97

```

```

-----
mo = wabs[1] * pcfabs[2] (powerlaw[3])
Model Fit Model Component  Parameter Value  error
  1    1    1    phabs      nH 10^22    7.00  +/- 0.
  2    2    2    pcfabs      nH 10^22    3.00  +/- 0.
  3    3    2    pcfabs      CvrFract    0.90  +/- 0.
  4    4    3    powerlaw    PhoIndex    1.68  +/- 0.
  5    5    3    powerlaw    norm         1.00  +/- 0.

```

```

-----
Chi-Squared = 1329. using 2048 PHA bins.
Reduced chi-squared = 0.6505

```

Note that we have not specified any background component. The point spread function (PSF) of *Chandra* is sufficiently small that a background may not be necessary, particularly for stronger sources (stronger relative to the background). The PSF places $\sim 90\%$ of the flux into a circle with a diameter of $\sim 2''$. This means that a detection cell for *Chandra* is about a factor of 4^2 *smaller* than for the *ROSAT* HRI. The contribution of the background to the overall strength of the signal in the direction of the source is correspondingly reduced. We note that the ACIS-I background, when used for imaging observations, is about 0.7 counts/s/chip in the energy range 0.5 to 7 keV (section 6.10.2). We choose not to use a background file.

For the user that requires a background, a background spectrum can be simulated using *MARX* (see next section). in the identical manner as the target spectrum. It can then be included by using

```
XSPEC> backgr <filename>.
```

At this point a new simulation will produce the source plus background faked spectrum:

```
XSPEC> fakeit.
```

Note that we did not use “none”. *XSPEC* will use background, responses, correction files, and numerical information from the currently defined data.

We now want to calculate the 2-10 keV flux:

```
XSPEC > flux 2.0 10.0
Model flux 0.2654 photons (2.4150E-09 ergs)cm**-2 s**-1 ( 2.000- 10.000)
```

Alternately, we might want to change one or more parameter values to repeat the simulation:

```
XSPEC > newpar 5 0.056
5 variable fit parameters
Chi-Squared = 6.4063E+05 using 2048 PHA bins.
Reduced chi-squared = 313.6
```

Using `fakeit` again will produce a new faked spectrum.

The Result

Figure 11.2 shows the final continuum spectrum. The count rate should match the rate generated from *PIMMS* (within the approximations made in *PIMMS*; *PIMMS*, for example, does not handle partial covering absorption); the calculated flux should also match the value from the literature. At this point, the ‘faker’ can decide whether there are sufficient photons or signal-to-noise to meet the scientific objectives.

One **HUGE** warning specific to ACIS must be made about the faked spectrum: *no* pileup has been included (i.e., the faked spectrum is what would be detected if pileup in ACIS did *not* exist). The estimated count rate, ~ 4.0 counts/sec (*XSPEC*) or ~ 5.3 counts/sec (*PIMMS*) will yield pileup at about the $>90\%$ level. pileup will harden the spectrum (see the material on pileup in the ACIS chapter (Section 6.17). The pileup should be mitigated in a manner that depends upon the science goals. The total number of counts in the continuum spectrum is expected to be $\sim 40\text{K}$ ($10\text{ ksec} * \sim 4\text{ counts/s}$). The behavior of pileup affectively acts to generate a count rate that is *lower* for the source flux relative to an ideal detector.

There are several approaches to mitigating pileup for this source: (i) use a Subarray which will reduce the pileup because the chip can be read by a

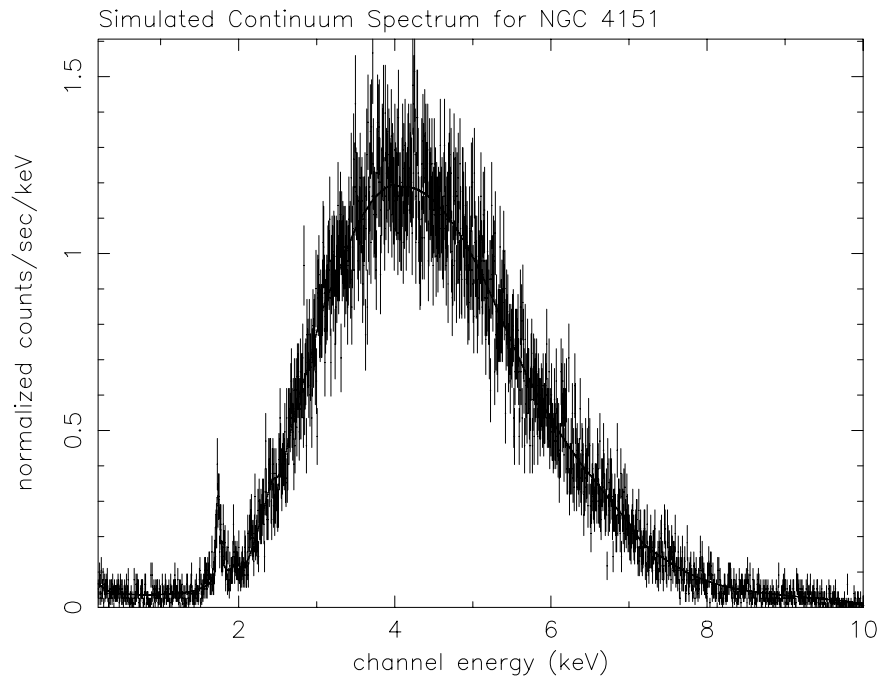


Figure 11.2: The simulated continuum spectrum for NGC 4151. No pileup has been included because *XSPEC* does not handle pileup.

maximum factor of 8 faster (1024 rows / minimum number of rows = 128). This will reduce the detected frame rate from ~ 17.5 ($= \sim 5.3 \text{ counts s}^{-1} \times 3.2 \text{ sec frame}^{-1}$) to $\sim 2.2 \text{ counts/frame}$. The estimated pileup fraction is still very high $\sim 60\%$; (ii) place the source off-axis by $7'$. The increase in the size of the PSF will decrease the maximum count rate per chip by ~ 20 (vignetting is a relatively smaller effect). A factor of 20 drop will produce a pileup fraction between ~ 5 – 10% .

Adding a Gaussian component: Simulating an Emission Line

For completeness, we continue with the example. A gaussian component may be added by typing

```
XSPEC > addcomp 3 gaussian
```

where the '3' indicates that this is the 3rd spectral component in the model. The first is **wabs**, the second is **pcfabs** (the partial covering absorption). Previously the third component was the power law itself, but that now becomes the 4th component. (Defining the new component (the gaussian) as the last component of the model would force *XSPEC* to define it as the first additive component of a second additive group.)

At this point you will be prompted for the three gaussian parameters (center, FWHM, and normalization). The values of the line center and FWHM are adopted from the literature.

Once we have the line parameters set, we use the **fakeit** command again to generate a new fake spectrum. The equivalent width of the line can be calculated by using

```
XSPEC > eqw 3
```

where the '3' is the number of the component for which the equivalent width is to be calculated (i.e., here, the gaussian is the 4th component of the total model).

Fitting the Fake Spectrum

The user may desire to fit the faked spectrum to see the magnitudes that are likely for the error bars of the fitted parameters. This can be done by treating the fake spectrum as if it were an observed spectrum. Thus,

```
XSPEC > data <fake_spectral_file_name>
```

will read in the fake spectral file as if it were an observation. The regular *XSPEC* commands (**model**, **fit**, **steppar**) for carrying out a spectral fit and assessing the significance of the fitted parameters can then be used.

Consult the *XSPEC* manual for all of the commands that can be used to fit the spectrum.

11.6 *MARX*

MARX is a suite of programs created by the *MIT/CXC* group and designed to enable the user to simulate the on-orbit performance of the *Chandra* X-ray Observatory (AXAF). *MARX* provides a detailed ray-trace simulation of how *Chandra* responds to a variety of astrophysical sources and can generate standard FITS events files and images as output. It contains detailed models for the HRMA mirror system onboard *Chandra* as well as the HETG and LETG gratings and all focal plane detectors. This section describes the capabilities of *MARX 2.5*, however the basic functionality is quite similar to the previous release. More detailed information, including the source code and documentation, is available from the *MIT MARX* Web Page.

11.6.1 What's New in Version 2.5?

The *MARX 2.5* release is a significant upgrade. Virtually all of the internal calibration data (HRMA mirror model, detector geometries, and quantum efficiencies) have been updated to reflect the results of the continuing analysis of XRCF and flight calibration data. In addition to calibration changes, a number of improvements and enhancements to *MARX*'s functionality have been made. These include:

- Simulation of Aspect motions
- CTI-induced spatial variations in ACIS gain and resolution
- Flat Field mirror model for simulating background
- Simulation of the HETG “streak”
- Updated HETG efficiency model
- Mis-aligned HETG grating facets
- Improved compatibility with *CIAO* data analysis tools
- Miscellaneous bug fixes

The majority of these changes will be transparent to previous *MARX* users. Users wishing to recreate existing *MARX* simulations will, however, need to update their parameter files.

11.6.2 Do you need *MARX*?

As always, the level of detail required in proposal planning will depend on the unique science goals of the proposer. However, we can identify a number of unique *MARX* capabilities which may help determine whether a *MARX* simulation is necessary.

- Spatially extended sources
- Multiple, overlapping point sources with unique spectra
- Observations susceptible to CTI-induced ACIS resolution variations
- Spectral and spatial effects of ACIS pileup
- HETG observations of extremely bright objects
- HETG and LETG observations of extended objects
- Higher order contamination of LETG spectra

If any of these descriptions characterize your proposal, you may find a *MARX* simulation useful. We note that *MARX* has been designed to emulate the realistic behavior of the science instruments onboard *Chandra*. Consequently, **analyzing *MARX* simulations to assess a proposal's feasibility is no more or less complicated than analyzing actual *Chandra* data.**

11.6.3 Technical Description

To run a simulation with *MARX*, the user specifies a file containing the spectral energy distribution of the source to be simulated and then selects a model for the spatial distribution of the source. Sources can be either on- or off-axis. *MARX* provides a number of built-in models for the spatial distribution of source photons including point sources, Gaussians, and Beta models (often used to model clusters of galaxies). A FITS image may also be specified to describe the spatial distribution of source photons. User-supplied source models can be linked dynamically to allow expansion of *MARX*'s capabilities.

Once the spatial and spectral properties of the source have been specified, *MARX* traces the path of photons through a model of the HRMA. This model has been tuned to match the results of the HRMA calibration. If desired, models for the High Energy Transmission Grating (HETG) and Low

Energy Transmission Grating (LETG) can be also be included to simulate *Chandra*'s high resolution spectroscopy capabilities. In the focal plane, the user has the choice of all four *Chandra* detectors (ACIS-I, ACIS-S, HRC-I, and HRC-S). The current ACIS model includes the spatially-varying effects of CTI on the spectral resolution of the CCDs (see Figure 11.3).

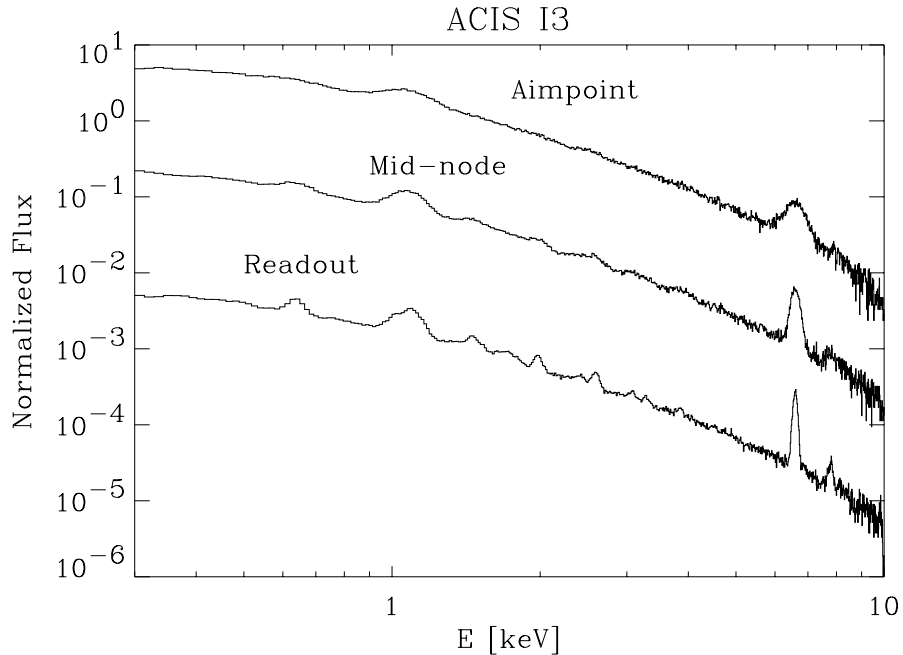


Figure 11.3: *MARX* simulation showing the effects that CTI-induced spatial variations in CCD resolution can have on an ACIS observation. The curves shown are for a 3.0 keV thermal source observed at the ACIS I3 aimpoint, the middle of the node, and near the readout. The normalizations have been shifted for display purposes. Note the decrease in spectral resolution as one moves away from the readout. For more about CTI effects, the user is referred to the ACIS section of the *Proposers' Observatory Guide*.

The *MARX* suite consists of a set of UNIX executables and has been successfully built under SunOS, Solaris, Linux, HP/Unix, and NeXT systems. Control of the program is accomplished through a parameter file utilizing a custom version of the SAO/IRAF parameter interface library. The user can either edit this parameter file directly or modify *MARX* parameters on the call line. For example, the command:

```
[1]unix% marx ExposureTime=50000 GratingType='HETG' \
      DetectorType='ACIS-S' SourceType='POINT'
```

would run a 50 ksec simulation of a point source as observed with the HETGS. A detailed discussion of the various *MARX* parameters and options is available in the *MARX* Technical Manual. The simulator is reasonably compact (requiring only 40 MBytes for the entire distribution) and fast (seconds to minutes).

Once a simulation has been created, the resulting output can be converted to a standard *CXC* Level 1 FITS events file. These Level 1 event files are completely compatible with the *CIAO* 1.1 data system. Consequently, users may transparently extract spectra using such tools as *DMEXTRACT* or images using *DMCOPY*. Similarly, HETG or LETG spectral simulations can be analyzed using the standard *CIAO* grating pipeline tools. Descriptions of the *CIAO* data analysis system are available online from the *CXC* Web site. Detailed examples of using *CIAO* to work with *MARX* output are available in the *MARX* Technical Manual.

11.6.4 Obtaining *MARX*

The *MARX 2.5* distribution is available from the *CXC* at *MIT* as a compressed TAR file. This distribution includes the source code for all executables, necessary parameter files, and assorted scripts and support routines. The distribution may be obtained on the Web from:

<http://space.mit.edu/ASC/MARX>

In addition to Web access, the latest *MARX* distribution can be obtained via FTP at:

<ftp://space.mit.edu/pub/ASC/MARX>

The directory contains a *README* file describing its contents. Other *MIT/CXC* software (such as the *ISIS* spectral analysis package) is also available in this directory. Full instructions for compiling the distribution are included in the TAR file. Note that these locations have changed since the original release.

11.6.5 Obtaining help

The *MIT/CXC* group maintains an informational web page on the *MARX* package at:

<http://space.mit.edu/ASC/MARX>

Information on the following topics is available:

- FAQs (Frequently Asked Questions)
- Online documentation
- Bug reports
- Sample *MARX* parameter files
- Example simulations
- User contributed software
- Future development plans

If you encounter a problem with *MARX* which is not addressed by the *MARX* Technical Manual, please send an email describing your problem to the *MARX* group:

marxhelp@space.mit.edu

Please be sure to include the version of *MARX* you are using as well as any diagnostic output or error messages produced. Bug reports and comments should also be sent to this email address.

Chapter 12

Proposal Planning Tools

12.1 Overview of Proposal Planning Tools

A summary of Proposal Planning Tools described in this chapter is given Table 12.1. The the Observation Catalog Browser is available as a Java WWW tool. The *CXC* target pages (<http://asc.harvard.edu/targets>) allow limited searches of the Observation Catalog, and also give X-ray and optical overlays of the target fields (where available). *ObsVis* and the other Proposal Tools are available both over the web and as downloadable command-line versions.

12.2 Obtaining and Installing Command-line Versions

Command line versions of tools are available as tar files from the *CXC* website URL <http://asc.harvard.edu>, and via anonymous FTP

Table 12.1: Summary Proposal Tools

Tool	Function	WWW?	Command Line?
<i>ObsCat</i>	Browse <i>Chandra</i> Observation Catalog	yes	no
<i>precess</i>	Coordinate Conversion	yes	yes
<i>colden</i>	Evaluate Galactic N_H	yes	yes
<i>dates</i>	Calendar conversion	yes	yes
<i>ObsVis</i>	Observation scheduling/planning	yes (limited)	yes
<i>PIMMS</i>	Countrate Evaluation (Chapter 11)	yes	yes

from asc.harvard.edu. To download tools from the web, click on *Proposer* on the *CXC* homepage and follow links to the Proposal Toolkit. To download the tools via FTP, log into asc.harvard.edu and go to the directory pub/software. The tools are available for Solaris 2.6 & 2.7, Linux Redhat 6.0 & 6.1 and Slackware 3.5. Since most users will not need command-line versions of *dates*, *colden*, *pr*, and *dates*, *ObsViscan* be separately. *ObsViscan* also be downloaded bundled with the other tools.

The first step in the installation (source-code or binaries) is to gunzip and unpack the tar file with

```
gunzip filename.tar.gz
tar xvf filename.tar
```

Details of the installation procedure are given in the README file. We give a “cookbook” example of how to complete the installation below.

12.2.1 Sun-Solaris Executables

A user running Solaris on a Sun computer can down-load executables. The code is already compiled and the data files are included in the distribution.

First of all unzip and untar the distribution:

```
unix> cd /soft/chandra/
unix> gunzip prop_obs_bin_sun.tar.gz
unix> tar xvf prop_obs_bin_sun.tar
```

In this example the tar file was downloaded into a directory /soft/chandra. The tar file will create a directory CXCD_ROOT_SOLARIS. To configure the proposal tools:

```
unix> cd CXCD_ROOT_SOLARIS
unix> ./configure
```

To complete the installation you need to create a login file in your home directory. This file must be sourced once per login. The login file is created with the following command:

```
unix> sh bin/config_cxc_nra2
```

You must be in the CXCD_ROOT_SOLARIS directory. For *csh* and *tcsh* users the file will be called *.cxc_nra2.csh*. To use the proposal tools *cd* to your home directory and type:

```
unix> source .cxc_nra2.csh
```

12.3 *ObsCat* – The Chandra Observation Catalog

12.3.1 Introduction

The Observation Catalog contains a list of approved targets which have been scheduled or observed. *ObsCat* is a Java tool to browse the Observation Catalog over the WWW. A complete listing of targets is also available both on our web page (asc.harvard.edu) under *Target Lists...* and via FTP at [asc.harvard.edu/pub/doc](ftp://asc.harvard.edu/pub/doc).

A non-Java search page is also available, see Section 12.4.

12.3.2 Running *ObsCat* over the WWW

To access *ObsCat* follow these steps:

1. Open the *CXC* website, <http://asc.harvard.edu>
2. Click the *proposer* icon at the top of the *CXC* page and the link *ObsCat*. This Java interface will take 1-2 minutes to load.
3. If you are a first-time user you will have to download a 7 Mbyte “plugin” (with Netscape 4). Instructions will appear which should enable you to install the plugin successfully.

You may search for a particular target or group of targets. Targets found are listed on a new page and detailed target information can be displayed by highlighting the target of interest and clicking the *Detail* button at the bottom of the listing. To start a new search, click the *New Search* button. DO NOT click Netscape *Back*; this will require you to *ObsCat*

Examples:

1. Search by name - one may use target name, PI name or Co-I name (or part of the name).
To list all *Chandra* imaging observations for PI “Garmire”.
 - Note the default is to include all instruments so click *HETG* and *LETG* off.
 - Type PI Name “garmire”.
 - Click *Submit* button.

ObsCat lists ≈ 110 targets. Coordinates listed are J2000.

2. Search by position - one may use coordinates in two ways.

Chandra Observation Catalog

Display Options

☒ Table
 ☐ File: **Summary**
 Order by: **RA**

Search Options

Instrument: ☒ HRC-I ☒ HRC-S ☒ ACIS-I ☒ ACIS-S Grating: ☒ HETG ☒ LETG ☒ NONE

☐ File Input:

Target Name: PI Name:

Proposal Number: Sequence Number:

Obsid: Exposure (ks):

Status: **All** Type: **All** Category: **All**

Search By Position:

Input: Coordinate System: **Equatorial J2000** Equinox: **J2000**

☒ hh mm ss.s/ +/-dd mm ss
☐ decimal degrees

Output: Coordinate System: **Equatorial J2000** Equinox: **J2000**

☒ hh mm ss.s/ +/-dd mm ss
☐ decimal degrees

RA: **18 36 55.4** DEC: **38 48 48** Radius (arcmin): **5**

Figure 12.1: The first WWW page of the *ObsCat* tool. Parameters entered will perform a cone search for *Chandra* observations within 5' of Vega.

SEQ_NU..	OBSID	INSTR	GRAT	APP_E..	REM_..	TARGET_NAME	PI_NAME	RA	DEC
280365	1415	HRC-I	NONE	2.0	-0.03	VEGA	CALIBRATION	18 36 55.40	+38 46 46.
280366	1416	HRC-S	NONE	3.0	0.00	VEGA	CALIBRATION	18 36 55.40	+38 46 46.
280367	1417	HRC-S	NONE	3.0	0.52	VEGA	CALIBRATION	18 36 55.40	+38 46 46.
280368	1418	HRC-S	NONE	3.0	0.07	VEGA	CALIBRATION	18 36 55.40	+38 46 46.
280369	1419	HRC-S	NONE	2.0	-0.28	VEGA	CALIBRATION	18 36 55.40	+38 46 46.
290000	31	HRC-I	NONE	3.0	3.00	VEGA	CALIBRATION	18 36 55.40	+38 46 46.
290001	32	HRC-S	NONE	3.0	3.00	VEGA	CALIBRATION	18 36 55.40	+38 46 46.
290002	33	HRC-S	NONE	3.0	3.00	VEGA	CALIBRATION	18 36 55.40	+38 46 46.
290003	34	HRC-S	NONE	3.0	3.00	VEGA	CALIBRATION	18 36 55.40	+38 46 46.
290004	35	HRC-S	NONE	3.0	3.00	VEGA	CALIBRATION	18 36 55.40	+38 46 46.
290005	36	ACIS-I	NONE	3.0	0.00	VEGA	CALIBRATION	18 36 55.40	+38 46 46.
290006	37	ACIS-S	NONE	1.0	1.00	VEGA	CALIBRATION	18 36 55.40	+38 46 46.

More Order By... Detail Save Clear Cancel New Search Help

Total rows = 12

Figure 12.2: Output WWW list produced by the *ObsCat* tool. One target is highlighted preparatory to clicking on the *Detail* button

A cone search enter, e.g. 18 36 55.4, 38 46 46, r=5. This will search the area inside a circle centered on this point with radius 5 arcminutes. Equinox J2000 is the default (see Figure 12.1).

Another example: To find HRC-I observations of M31 knowing the 1950 position,

- Click detector boxes so only *HRC-I* is on.
- Set input coordinate equinox to B1950.
- Click *RA* box (widget appears)
- Click *cone*, type RA “0 40 00”, DEC “41 00 00”, Radius “120”
- Click *OK* (widget disappears)
- Click *Submit* button. *ObsCat* lists ≈ 85 targets. Coordinates displayed are J2000 (default)

A limit search Example: find all observations of targets in the Large Magellanic Cloud”

- Click all instruments on.
- Set input coordinate equinox to B1950.
- Click *RA* box (widget appears).

Req# 290885	Status scheduled	Obs_ID 36	Prop# 01260001	AO 00
Target_Name VEGA				
Instrument ACIS-I	Grating NONE	Type CAL	Start_Date Nov 5 1999 10:04:17.200AM	
P.I. CALIBRATION	Observer CALIBRATION			
Category NORMAL STARS AND WD				
App_Exp_Time 2.0	SchedObs_Time 3.8			
RA 15 36 55.40	Dec +38 46 46.20	Equinox J2000	CoordSystem Equatorial	Time_Crit y/n N
Offset: Y	Z	X-SHM-motion	Z-SHM-motion	
Resizer_Scan N	SS_Object NONE	Rudge N		
Photometry y/n N	Vmag 0.14	Count_Rate 0.01	1st_Ord_Rate	
Dither y/n N				
Roll y/n N	angle	tolerance		
Window y/n N	Start Y	M	D	H
	Stop Y	M	D	H
Monitor N	Number	Min int	Max int	
Phase y/n N	epoch	period	Min	Min err
			Max	Max err
Remarks				

Figure 12.3: Detailed information concerning one of the targets in *ObsCat*. Only the top part of the page is shown. Instrument parameters may be displayed by scrolling.

- Click *range*, type min RA “4 0 0”, max RA “7 0 0”, min DEC “-70 0 0”, max DEC “-55 0 0”
- Click *OK* (widget disappears)
- Click *Submit* button. *ObsCat* lists ≈ 100 (AO1) targets. Coordinates displayed are J2000 (default)

3. Search (Filter) by Date, Exposure, Type and Observation Number.

Example: List all *Chandra* HETG/ACIS-S planned observations with exposures of 100 ks or greater.

- Click instrument boxes *off* except for HETG, ACIS-S .
- Click *Exposure* box (widget appears)
- Click *range*, type min “100”, no max necessary.
- Click *OK*.
- Click *Submit* button. *ObsCat* lists ≈ 40 (AO1) targets.

The filters are additive, and combinations of all the above can be used to generate output lists.

4. Saving the output:

With display option *Table* (top of the *ObsCat* main GUI), after *Submit* is pressed, the output is listed on the next screen. Display option *File/Summary* lists the same basic information to a file. Display option *File/Detail* lists *all* instrument information to a file.

To save the output from this JAVA interface is, at present, a challenge. A hardcopy or postscript file of the output screen can be made only if the system recognizes the JAVA applet as a legitimate user. If you are a first-time user, follow the instructions which will appear on the screen.

12.4 WWW Target Information (non-Java).

The WWW *Chandra* science page (<http://asc.harvard.edu>) contains a non-Java tool which performs similar searches for targets with particular characteristics and which will also display plots useful for detailed observation

File Edit View Go Communicator Help

Back Forward Reload Home Search Netscape Print Security Print

Bookmarks Location <http://asc.harvard.edu/targets/> What's Related

Members WebMail Connections BizJournal SmartUpdate MITplace HCO Tennis Club

Target Search Form

Use this form to find your observation(s). You can search by PI, sequence number, observation type and perform a cone search. [Range and comma separated list](#) searches can also be performed on the Sequence Number, Proposal Number, and Obs ID fields. [Click here for additional information.](#)

For more detailed searches, use the [QueryCat Browser](#).

Note: Not all TGO and Calibration observations are currently listed.

Sequence Number:	<input type="text"/>	Proposal Number:	<input type="text"/>
PI Name:	<input type="text"/>	Observer:	<input type="text"/>
Target:	<input type="text"/>	Obs ID:	<input type="text"/>
Coordinate Search RA:	<input type="text"/>	Dec:	<input type="text"/>
<input type="text"/>	<input type="text"/>	Radius:	<input type="text"/> Units: <input type="text"/>

The above option performs a cone search. Coordinates are J2000 in the following format: **## ## ## ##** or **## ## ## ##**
 Example of format for coordinate search: 09 34 59.86 -40 23 18.18 or 23 17 26.80 -40 23 18.18
 For exact searches leave Units pull down menu blank.

Science Instrument	Grating	Observation Type	Status
<input type="checkbox"/> ACS-I	<input type="checkbox"/> HETG	<input type="checkbox"/> GO	<input type="checkbox"/> Unserved
<input type="checkbox"/> ACS-S	<input type="checkbox"/> LETG	<input type="checkbox"/> GTO	<input type="checkbox"/> Scheduled
<input type="checkbox"/> HRC-I	<input type="checkbox"/> NONE	<input type="checkbox"/> CAL	<input type="checkbox"/> Partially Observed
<input type="checkbox"/> HRC-S		<input type="checkbox"/> TOO	<input type="checkbox"/> Observed
			<input type="checkbox"/> Archived

[Sort by:](#)

100%

Figure 12.4: WWW page for a target search (non-Java).

planning.

To use, click on *Detailed target info* (see Figure 12.4) which brings up a form similar to that displayed by *ObsCat*. Targets may be listed for a given PI, science category, instrument, or status; or, a cone search may be done to list targets close to any particular location. The result of the search is displayed on a new screen and, for detail, the user can then click on the sequence number of any of the targets listed. A new page will then appear with basic information for that target and with four buttons. Click on *target parameters* for a listing of instrument settings. Click on *DSS* for an overlay of the instrument FOV on a picture from the Digital Sky Survey (Figure 12.9). Click on *ROSAT* for an overlay on a ROSAT X-ray image (if one exists for this location). Click on *Roll/Visibility* for a plot of nominal roll and target visibility as a function of date (Figure 12.8).

This tool performs the basic *ObsCat* functions without the Java interface. It uses an information base which is updated daily. This tool does not calculate overlays as does *ObsVis* but displays overlays generated by the mission planning process after an observation date has been assigned or assumed for each target.

12.5 *precess* - Astronomical Coordinate Conversion

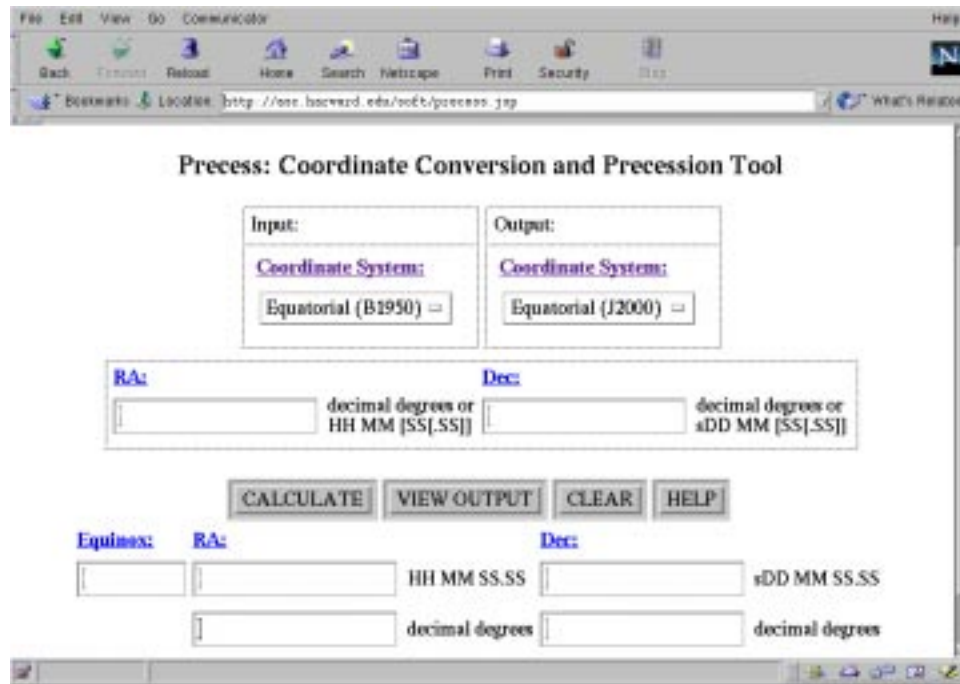
12.5.1 Introduction

precess is an interactive astronomical coordinate conversion program. It allows not only precession of equatorial coordinates but conversion between equatorial, ecliptic, galactic and supergalactic coordinates. *precess* can be run over the WWW using a browser such as Netscape, or can be downloaded and run locally using the command-line interface (see Section 12.2).

12.5.2 Running *precess* over the World Wide Web

The CXC has written an interface to *precess*, to be run over the WWW using a browser such as Netscape. To access *precess*, follow these steps:

1. Open the CXC website, URL <http://asc.harvard.edu>
2. Click on the “proposer” button at the top of the page. Follow the links to “Precess.”

Figure 12.5: *precess* Interface

3. The *precess* interface is shown in Figure 12.5

A **Help** button is available halfway down the menu.

The screen is divided into five sections:

1. Input - the input coordinate system selected from a pull down menu.
2. Output - to the right of the input, the requested output coordinate system.
3. Input Coordinates - beneath the input and output coordinate system selection menus. They can be entered in either HMS and DMS format or decimal degrees.
4. **CALCULATE**, **VIEW OUTPUT**, **CLEAR** and **HELP** buttons - beneath the input coordinates. **CALCULATE** runs *precess* and **CLEAR** clears the screen. **VIEW OUTPUT** adds the command line output beneath the GUI output.
5. Results - below the buttons. Output from *precess*.

The web interface to *precess* is easy to use. However, there several features that are only available through the command line (CLI) version. A file of coordinates can be submitted for conversion through the CLI version. Conversions involving supergalactic coordinates are only available in the CLI version.

Example 1

Precess B1950 coordinates to J2000, and return the answer in decimal degrees.

Enter 17 34 18.3 in the input **RA** box, and -34 16 54.8 in the input **Dec** box. Make sure the input **Coordinate System** is B1950, and the output **Coordinate System** is J2000. Click **Calculate**. The result will appear in the output boxes (RA=264.405876, dec=-34.311042.)

Example 2

Find out which constellation the previous target belong to.

Enter the input coordinates as in the above example. Choose “constellation” from the output **Coordinates Format** pull-down menu. Hit **Calculate**. The answer **Sco** will appear in the output box **Constellation**.

Example 3

Convert Equatorial J2000 coordinates to Galactic Coordinates

Enter the input coordinates e.g RA=3 23 18.6, Dec=64 15 16.8. Choose “Galactic” from the output **Coordinate System** pull-down menu and “J2000” for the input **Coordinate System**. Hit **Calculate**. The output boxes will change to L2 and B2, and the answer is L2= 09 14 05.20 B2 =+06 04 55.55.

12.5.3 Running *precess* in Command-line mode

To run *precess* in command-line mode it must be installed on the users home machine. For instructions on how to download and install *precess*, see section 12.2. Type *precess* to run the program in interactive mode. This enters the *precess* **command level** which allows the user to set the program parameters. The command level prompt is: **Precess[Setup]>:**

To see a list of available commands, type **?** or **help**. The most usual command sequence is to use **from**, **to** and **convert**, which may be abbreviated **f**, **t** and **c**. **from** and **to** define the input and output coordinate

systems, and **c** enters the **processing level**. Typing **c** or **convert** puts the user in the processing level. A message explaining the coordinate input format and then the processing level prompt appears. The processing level prompt is the name of the input system's 'x-coordinate.' Type in the coordinates in the appropriate format, either both coordinates on the same line or x-coordinate on one line and y-coordinate on the next. In the latter case the user is prompted for the name of the y-coordinate at the beginning of the second line.

RA and Dec are assumed by default to be in the format hh mm ss.ss dd mm ss.ss, while other coordinate systems are assumed by default to be in decimal degrees.

To leave the processing level and return to the command level, type **q** or **quit** in response to the processing level prompt. **q** or **quit** issued at the command level will leave the program entirely.

There is one other command; **list** or **l** displays the current settings of the program.

Example 1

Precess equatorial coordinates from 1950 to 1986. Enter **f B1950 t B1986** in the command level to convert from B1950 coordinates to B1986 coordinates, then **c** to reach the processing level:

```
Precess[Setup]>: f B1950 t B1986
Precess[Setup]>: c
```

Then enter the B1950 coordinates to be converted:

```
RA (B1950):16 26 36.7 37 27 54.3
```

The output follows.

```
unix prompt > precess
----- Precess -----
You are now in setup mode.
Type "c" to enter conversion mode,
    "?" to list setup mode commands,
or   "q" to quit the program.
The default conversion is from B1950 to J2000.
Precess[Setup]>:f B1950 t B1986
Precess[Setup]>:c
Precess[Conversion mode]
```

Example: 15 05 19.71 -00 23 12.2

RA (B1950): 16 26 36.7 37 27 54.3

RA,Dec B1986.0 16 27 53.51 +37 23 10.23

RA,Dec J2000.0 00 02 33.43 +00 16 44.19

It is possible to convert a file of coordinates if the file is in a format that *precess* can read. Here is an example file format when the input system uses “hh mm ss.ss” format:


```
00 01 12.3 -00 02 23.4
02 59 59.9 23 12 22.1
02 23 0 11 23 12
23 48 48.23 -2 11 14.123
```

To transform this file from B1950 to galactic coordinates, type

```
precess t g:bfile:gfile
```

where *bfile* is the file and *gfile* is the output file, which will contain:

RA (B1950)	Dec (B1950)	L	B
00 01 12.30	-00 02 23.40	98.275	-60.331
02 59 59.90	23 12 22.10	158.172	-30.327
02 23 00.00	11 23 12.00	156.571	-45.016
23 48 48.23	-02 11 14.12	90.687	-60.963
23 48 48.23	-02 11 14.12	90.687	-60.963

The general syntax is

```
unix prompt> precess commands:infile:outfile
```

where *commands* is a string of *precess* commands separated by spaces, and the input and output files default to standard input and output. The **c** command is assumed automatically, as are **q** commands at the end, so *commands* usually consists of a **from/to** specification. The default is B1950 to J2000, so to convert the above file to J2000 would require

```
unix prompt> precess :bfile:jfile
```

Note the colons separating the absent first argument from the second (input file) argument. e.g. to go from B1979.0 to B1950.0 with input coordinates in a file *star.cat* and an output *star.cat.pr*:

```
unix prompt> precess f B1979 t B1950:star.cat : star.cat.pr
```

12.5.4 Available coordinate systems

Equatorial coordinates

Equatorial coordinates consist of a longitudinal Right Ascension (RA, α) and a latitudinal Declination (Dec, δ). The plane of zero declination is the

projection of Earth's equator onto the celestial sphere, and the zero of RA is marked by the intersection of the ecliptic (Earth orbital) plane with the equatorial plane. This definition depends on epoch because of precession; its practical implementation also depends on the set of fundamental reference stars used to measure coordinates. There are two fundamental frames of reference currently in use: the FK4 and FK5 systems. The FK4 system is tied to the equatorial coordinate system for Besselian epoch B1950.0, while the more accurate FK5 system is tied to the equatorial system for Julian epoch J2000.0. While the coordinate system in most widespread use among astronomers is the B1950.0 system of equatorial coordinates, the IAU have recommended that J2000.0 coordinates be used.

Note that since the FK4 and FK5 reference frames rotate relative to one another, the transformation from B1950 to J2000 affects not only the coordinates but the proper motions of stars. An object with zero proper motion in B1950 will have a nonzero proper motion in J2000 and vice versa. Since this program does not deal with proper motions, coordinate conversions have been adopted which assume that the object in question has zero proper motion in the J2000 system. Note further, however, that the difference between J2000 and B2000 is typically less than one arc second.

Galactic coordinates

Defined conceptually by the Galactic plane and the Galactic center, galactic longitude l and galactic latitude b are the IAU 1958 system, formerly called l_{II} and b_{II} . The system is defined in terms of B1950 equatorial coordinates as RA of ($l=0$) = 192.25 degrees, inclination of galactic equator to B1950 equator = 62.6 degrees, longitude of ascending node 33 degrees.

Galactic l,b		B1950 RA,Dec		J2000 RA,Dec	
0	0	17 42 26.58	-28 55 00.43	17 45 37.20	-28 56 10.22
0	+90	12 49 00.00	+27 24 00.00	12 51 26.28	+27 07 41.70
33.0	0	18 49 00.00	00 00 00.00	18 51 33.73	+00 03 38.13
123.0	+27.4	12 00.00 00	+90 00 00.00	12 01 16.85	+89 43 17.74

The J2000 north celestial pole is at $l=122.932$, $b=27.128$.

Supergalactic coordinates

With the advent of large scale structure studies, the supergalactic coordinate system introduced by de Vaucouleurs is coming into more widespread use. The supergalactic equator is conceptually defined by the plane of the

local (Virgo-Hydra-Centaurus) supercluster, and the origin of supergalactic longitude is at the intersection of the supergalactic and galactic planes. Supergalactic longitude and latitude SGL, SGB are defined by

SGL,SGB		Galactic l,b		J2000 RA,Dec		
0	0	137.37	0	02 49 14.43	+59 31 42.05	
0	+90	47.37	+6.32	18 55 00.98	+15 42 32.17	
90.0	6.32	0	+90	12 51 26.28	+27 07 41.70	

Ecliptic coordinates

Ecliptic coordinates are defined by the earth's orbital plane. The B1950 north ecliptic pole is at B1950 RA 18 00 00, Dec +66 33 15.

Ecliptic coordinates are weakly epoch dependent, so the user may wish to use a specific epoch to define the orbital plane rather than the default B1950.0. To select Besselian epoch Bxxxx, use the from/to option ECxxxx. Julian epochs are not provided. EC is equivalent to EC1950.

Constellations

B1950 coordinates are precessed to B1875.0 and compared with the Delporte (1935) constellation definitions.

12.6 *colden* - Calculate Neutral Hydrogen Column Density

12.6.1 Introduction

colden is an interactive program to evaluate the neutral hydrogen column density at a given direction on the sky. *colden* can be run over the WWW using a browser such as Netscape, or can be downloaded and run locally using the command-line interface (see Section 12.2).

12.6.2 Running *colden* over the World Wide Web

To access the web version of *colden*, follow these steps:

1. Open the *CXC* website, URL <http://asc.harvard.edu>
2. Click on the *Proposer* button in the navigation bar at the top of the page, and then click on *colden*.

Chandra Proposal Planning Toolkit [PIMMS](#) [Colden](#) [Process](#) [Dates](#)

Colden: Galactic Neutral Hydrogen Density Calculator

Coordinate System:

Dataset: ☒ **NRAD** ☐ **Gal** **Velocity Range:** **Low:** **High:**
Full -550.0 to 550.0 km/s

RA: decimal degrees or HH MM [SS.SS] **Dec:** decimal degrees or sDD MM [SS.SS]

Galactic L2: **B2:** **NH:** **Comments:**

Figure 12.6: *colden* Interface

The *colden* page is shown in Figure 12.6. **Input Parameters** to *colden* are:

1. the input coordinate system
2. Survey selection: NRAO/Bell (see Section 12.6.4)
 - if Bell is selected, the range of velocities over which the column density is to be integrated may be specified (default: full range). If *Restricted* is selected, boxes will appear for velocity range entry.
3. the input coordinates.
4. GUI Buttons:
 - *CALCULATE* runs *colden*. The results appear in the boxes *Galactic L2, B2, NH, Comments*
 - *VIEW OUTPUT*: displays the detailed output below the output boxes
 - *CLEAR*: clears the form
 - *HELP*: displays the help information below the output boxes

The *Comments* box can have the following entries:

Interpolated Value interpolated from four nearest measurement directions

At target Measurement in exactly the specified column direction

At closest point Measurement in observed direction closest to the specified column direction; the specified direction does not have four nearest measurement directions suitable for interpolation

Gain uncertain Specified column direction is less than 0.2 deg from the equator (B1950); measurements near the equator in the Stark, et al. ("Bell") survey (ApJ Suppl. 79, p77, 1992) may suffer from large gain fluctuations

Too far south - No value computed – Specified column direction is at least 40.0 deg south of the equator (B1950); the Stark, et al. ("Bell") survey (ApJ Suppl. 79, p77, 1992) used a Northern Hemisphere telescope

Example 1

Evaluate the column density at RA=06 28 34.6, Dec=3 37 45.8 in J2000 coordinates

Choose *J2000* from the input **Coordinate System** pull-down menu. The default velocity range is *Full* if Bell is selected. Enter the coordinates in the RA and Dec boxes, and click on *CALCULATE*. The column density ($61.22 \times 10^{20} \text{ cm}^{-2}$) and galactic coordinates are returned. A comment “interpolated” is in the comment box.

Example 2

Evaluate the column density at galactic coordinates L2=86.655, B2=40.979. Restrict the velocity range -200 to +100 km s^{-1}

Choose *Galactic* from the input *Coordinate System* pull-down menu. Click *Restricted* from the *Velocity Range* pull down menu. Enter -200.0 and 100.0 in the *Range* boxes, which will now be active. Enter 86.655 in the *L2* box, and 40.979 in the *B2* box, and click *CALCULATE*. The result ($N_H = 1.83 \times 10^{20} \text{ cm}^{-2}$) will appear in the output **N_H** box.

12.6.3 Running *colden* in Command-line mode

To run *colden* in command-line mode, it must be installed on the users home machine. For instructions on how to download and install *colden*, see section 12.2. Type *colden* to run the program in interactive mode. This enters the *colden* **command level** which allows the user to set the program parameters. The command level prompt is:

```
Colden[Setup]>:
```

To see a list of available commands, type **?** or **help**. The most usual command sequence is to use **data** to select the dataset (Bell or NRAO; see Section 12.6.4) and **convert** to enter the main calculation loop. These may be abbreviated **d** and **c**. Type **f** or **from** to select a new input coordinate system (B1950 is the default); this syntax is the same as for *precess*, described in section 12.5. Type **c** or **convert** to enter the processing level. There will be a message explaining the coordinate input format and then the processing level prompt. The processing level prompt is the name of the input system’s ‘x-coordinate.’ Type in the coordinates in the appropriate format, either both coordinates on the same line or x-coordinate on one line

and y-coordinate on the next. In the latter case the user will be prompted with the name of the y-coordinate at the beginning of the second line.

Example 1

Enter a pair of equatorial coordinates. Run colden (here we assume that the executable has been aliased to “colden”: see section 12.2). At the colden set-up prompt type **c** or **convert**:

```
Colden[Setup]>: c
```

and then enter the coordinates:

```
RA (1950): 02 20 20.1 -00 00 23
```

The output will look like this:

```
unix prompt> colden
----- Colden -----
You are now in setup mode.
Type "c" to enter conversion mode,
    "?" to list setup mode commands,
or   "q" to quit the program.
The default conversion is from B1950.
Colden[Setup]>:c
Data source: BELL
RA  (B1950)  Dec (B1950)   Galactic coords      NH (10**20 per cm**2)
                                -550.0 to   550.0 km/s

RA  (B1950):02 20 20.1 -00 00 23.
02 20 20.10 -00 00 23.00   165.463201 -54.914277  2.99 (Interpolated)
```

Example 2

Enter a pair of galactic coordinates Enter colden. In the set-up level specify that the coordinates are galactic (“ from g”), then type **c** to enter the processing level:

```
Colden[Setup]>: from g
Colden[Setup]>: c
```

Once in the processing level, enter the desired coordinates:

L: 97.74 -60.18

The output will look like this:

```
unix prompt> colden
----- Colden -----
You are now in setup mode.
Type "c" to enter conversion mode,
    "?" to list setup mode commands,
or   "q" to quit the program.
The default conversion is from B1950.
Colden[Setup]>:from g
Colden[Setup]>:c
Data source: BELL
L           B           Galactic coords      NH (10**20 per cm**2)
                                -550.0 to   550.0 km/s

L:97.74 -60.18
  97.740000 -60.180000  97.740000 -60.180000  2.82 (At closest point)
L:
```

RA and Dec are assumed by default to be in the format of Example 1, i.e. hh mm ss.ss dd mm ss.ss, while other coordinate systems are assumed by default to be in the format of Example 2, i.e. in decimal degrees.

colden supports two column density datasets; the Stark, et al., Bell Labs survey, and the Dickey and Longman 1992, dataset (see Section 12.6.4). The Bell survey data is velocity resolved. To select a velocity slice in the Bell data, use the **vlims vmin vmax** command at the command level. **vlims *** returns the velocity slice to its default, maximum range, -550 to +550 km/s.

The **P** command sets the output format: type **P0** (terse), **P1** (normal) or **P2** (verbose). There is one other command; **list** or **l** displays the current settings of the program.

To leave the processing level and return to the command level, type **q** or **quit** in response to the processing level prompt. **q** or **quit** issued at the command level will leave the program entirely.

Using *colden* on a file

It is possible to convert a file of coordinates if the file is in a format that *colden* can read. Here is an example file format when the input system uses “hh mm ss.ss” format:

```
00 01 12.3 -00 02 23.4
02 59 59.9 23 12 22.1
02 23 0 11 23 12
23 48 48.23 -2 11 14.123
```

To calculate NH for this file if the coordinates are B1950, using the Bell data (default) type

```
unix prompt> colden :bfile:gfile
```

where *bfile* is the file with coordinates and *gfile* is the output file. Please note that a space is required after “colden” and before the “:”. The general syntax is

```
unix prompt> colden commands:infile:outfile
```

where *commands* is a string of *colden* commands separated by spaces, and the input and output files default to standard input and output. The **c** command is assumed automatically, as are **q** commands at the end, so *commands* usually consists of a **data** or **vlims** specification. The default is B1950 coords and the Bell dataset. To use the NRAO dataset for a file with J2000 coordinates:

```
colden from J2000 data NRAO:bfile:jfile
```

Note the colons separating the absent first argument from the second (input file) argument. To select a velocity slice in the Bell dataset:

```
colden vlms -20 120:bfile:newfile
```

This syntax is also useful for interactive mode, to go directly into the processing level. For example:

```
colden from g data nrao list
```

where *list* command makes the program echo the choice of input and output system to the terminal prior to the start of processing.

Using *colden* for a single evaluation

The **eval** command evaluates a single position and exits. Example:

```
colden data nrao eval 14 11 30 20 11 10
```

12.6.4 Supported Datasets

There are two datasets supported:

- **Bell** is the Stark, et. al., Bell Labs survey. We have an early version of the spectra from 1984, and have not checked them in detail against the published (1992) FITS data; we hope to support the published version in the future. There are two data files, one integrated over velocity and one with the velocity-resolved spectra.

Note that the Stark et al data only covers $\delta > -40$ degrees.

- **NRAO** is the Dickey and Lockman (1990) all-sky interpolation of Stark et al and several other surveys. It is not velocity-resolved.

12.7 *dates* - Calendar Conversion Tool

12.7.1 Introduction

dates is an interactive calendar and time conversion tool. *dates* can be run over the WWW using a browser such as Netscape, or can be downloaded and run locally using the command-line interface (see Section 12.2).

12.7.2 Running *dates* over the World Wide Web

The *CXC* has written a WWW interface to *dates*. The default timescale is UTC (Coordinated Universal Time). To access *dates*, open the *CXC* website, URL <http://asc.harvard.edu> and click on the *proposer* button on the top navigation panel, and follow the *dates* link.

The *dates* page has three sections:

1. Input parameters - selection of input type (normal calendar, Julian Date, Modified Julian Date, day of year, or *Chandra* time (see Section 12.7.5)) and input value. Note that after selection of type, the formatting prompt next to the value entry box may change.
2. Command buttons - *CALCULATE*, *VIEW OUTPUT* produces an unformatted dialogue with the command line, *Clear* clears the screen, and *HELP*.
3. Results - output from *dates*; all 5 types of dates are computed and appear in their respective windows.

Example 1

Convert Gregorian (our normal) Calendar to Julian day

Select *Calendar* in the **Convert From** pulldown box. Enter the date in the input box. Allowed formats are “1997 Aug 28” or “1997 Aug 28 12:34:28.23.” Click on **OK**. The output is displayed in the “Results” boxes. In this case the Julian day is JD 2450689.0239378472, the Modified Julian Day is MJD 50688.5239378470, the day of year is DOY 240.52, and the *Chandra* time should be some large negative number of seconds.

Example 2

Convert Julian Day to Gregorian Calendar

Select *Julian* from the pulldown menu. Enter the date in the input **Date** box. The required format is the decimal value of the date to be converted, followed by up to 10 digits after the decimal point: e.g. 2450789.2674652. Click on **Calculate**. The output is displayed in the *Results* boxes. This Julian day corresponds to Gregorian date AD 1997 Dec 6 18:25:08.99.

Restrictions to capabilities of WWW Interface

The current interface does not include time conversion (e.g. convert Eastern Standard Time to Greenwich Mean Time); nor does it deal with dates earlier than the year one (so as to avoid complications of negative day numbers and BC vs AD, etc). The command-line version (see Section 12.7.3) does not have these restrictions.

12.7.3 Running *dates* in Command-line mode

To run *dates* in command-line mode it must be installed on the users home machine. For instructions on how to download and install *dates*, see section 12.2. To run the program in interactive mode, type ‘prop_dates’. This enters the *dates* **command level** which allows the user to set the program parameters. The command level prompt is:

```
----- Dates -----
You are now in setup mode.
Type ‘c’ to enter conversion mode,
    ‘?’ to list setup mode commands,
or   ‘q’ to quit the program.
The default conversion is from Gregorian calendar date to JD.
Dates [Setup]>:
```

To see a list of available commands, type **?** or **help**. The default input calendar is the Gregorian calendar, which is the usual civil calendar in the US and Europe. The default output calendar is the Julian Day number. The default input and output timescales are both UTC (Coordinated Universal Time), which is the usual scientific timescale. Type **f** or **from** to select a new calendar and timescale.

Example 1

Convert UTC date to greg(TAI), i.e. Gregorian Calendar, Coordinated Atomic Time

Run *dates* and type **to TAI** at the setup prompt:

```
Dates[Setup]>: to TAI
```

Type **c** or **convert** to enter the processing level. Type in the date in the appropriate format:

```
UTC: 1996 Dec 10 17:40:00
```

The output will look like this:

```
unix prompt> dates
----- Dates -----
```

```

You are now in setup mode.
Type "c" to enter conversion mode,
    "?" to list setup mode commands,
or   "q" to quit the program.
The default conversion is from Gregorian calendar date to JD.
Dates [Setup]>:to TAI
Dates [Setup]>:c
Dates [Conversion mode]
Enter "q" to return to setup mode
UTC:1996 Dec 10 17:40:00

```

```

-----
UTC          Tue AD 1996 Dec 10 17:40:00    UTC (Gregorian)
TAI          Tue AD 1996 Dec 10 17:40:30.00 TAI (Gregorian)
-----

```

Example 2

Convert Julian date to UTC

Run *dates* and type **f JD t UTC** at the setup prompt (from Julian day to UTC)

```
Dates[Setup]>: f JD t UTC
```

Type **c** or **convert** to enter the processing level. Type in the date in the appropriate format:

```
Julian Day:2450579.28125
```

The output will look like this:

```

hypatia-560: dates
----- Dates -----
You are now in setup mode.
Type "c" to enter conversion mode,
    "?" to list setup mode commands,
or   "q" to quit the program.
The default conversion is from Gregorian calendar date to JD.
Dates [Setup]>:f JD t UTC
Dates [Setup]>:c
Dates [Conversion mode]

```

Enter "q" to return to setup mode

Julian Day:2450579.28125

```
-----
Julian Day          JD 2450579.2812500000 UTC
Gregorian date      Sat AD 1997 May 10  18:45:00.00 UTC (Gregorian)
-----
```

12.7.4 Running *dates* on a file

The syntax for running *dates* on a file is:

```
dates commands:infile:outfile
```

If *infile* is present, *dates* enters batch mode and reads a series of dates from *infile*, converting each one and printing the output in *outfile* (which defaults to the terminal). If *commands* are missing, the default conversion of Gregorian date UTC to JD(UTC) is used. Example:

```
dates from EST to TAI:date_list.in:date_list.out
```

where *date_list.in* contains:

```
1993 Jun 30 06:00
1993 Jun 30 23:30
1993 Jul  1 00:30
1993 Jun 30 18:59:59
1993 Jun 30 18:59:60
1993 Jun 30 19:00:00
1993 Jun 30 23:59:59
1993 Jul  1 00:00:00
```

Then *date_list.out* will contain the same dates converted from Eastern Standard Time (EST) to International Atomic Time (TAI).

12.7.5 Supported Calendars and Timescales

The following calendars are supported:

Syntax	Calendar	Type	Output on
greg	Gregorian date	Gregorian calendar	
date	Gregorian date - simplified output	Gregorian calendar	
pack	Gregorian date in packed format	Gregorian calendar	
DOY	Gregorian date in packed format, day of year	Gregorian calendar	
JD	Julian Day Number	JD	
MJD	Modified Julian Day	JD	
days	Days since zero	JD	
time	Seconds since zero (Default: Chandra time)	Elapsed time	
GSD	Greenwich Sidereal Date	GSD	Yes
GST	Greenwich Sidereal Time	GSD	Yes
OS	Old Style Julian Calendar	Archaic: Julian proleptic	
roman	Roman calendar (post-Augustan)	Archaic: Roman	Yes
RF	French Revolutionary calendar	Archaic: French	Yes

Note that some calendars may only be used as the output system.

Timescales supported by default are:

Specifier	Timescale
UTC	Coordinated Universal Time
TT	Terrestrial Time (Ephemeris)
TDB	Barycentric Dynamical Time
TAI	Coordinated Atomic Time
UT1	Universal Time (output only)
GMST	Sidereal Time (output only)

The following additional timescales are defined as offsets to UTC:

Specifier	Timescale	Offset to UTC
MST	Moscow Summer Time	+0400
DMV	Moscow Decree Time	+0300
BST	British Summer Time	+0100
GMT	Greenwich Mean Time	+0000
EDT	Eastern Daylight Time	-0400
EST	Eastern Standard Time	-0500

CDT	Central Daylight Time	-0500
CST	Central Standard Time	-0600
MDT	Mountain Daylight Time	-0600
MST	Mountain Standard Time	-0700
PDT	Pacific Daylight Time	-0700
PST	Pacific Standard Time	-0800

12.7.6 Zero Points - Command-Line only

The **zero** command supports the special calendars **days** and **time**, which give elapsed time since a zero point. The default zero point is the zero-point of *Chandra* clock time, 1988 Jan 1. **zero** prompts for a date in the current input format. Thus one may define an alternate zeropoint by (this is only for the command-line version):

```
Dates [Setup]>: from JD; zero 2440000.5
Dates [Setup]>: from greg to days; convert
Gregorian date:1994 Aug 13
```

```
-----
Gregorian date          Sat AD 1994 Aug 13          UTC (Gregorian)
JD - 2440000.5          9577.000000000000
-----
```

This particular zero point is frequently used among the X-ray binary community.

Alternatively, one might define:

```
Dates [Setup]>: from greg; zero 1994 Jan 0.0
Dates [Setup]>: from greg to time; convert
Gregorian date: 1994 Aug 13 14:20:22.3
```

```
-----
Gregorian date          Sat AD 1994 Aug 13  14:20:22.30 UTC (Gregorian)
TIME(JD 2449352.5)      19491623.3
-----
```

which gives the true elapsed number of seconds since the given zero point.

12.7.7 Input Formats - Command-Line only

JD For the **JD**, **MJD** and **days** calendars, one must simply enter a numeric value. Only Julian days between about -2×10^9 and 2×10^9 (i.e. 5 million years BC to 5 million years AD) are supported.

greg The Gregorian calendar supports a variety of input formats. The standard form of the input for **greg** is the words “AD” or “BC”, followed by the year, the month name, the day, and the time of day with hours, minutes and seconds separated by colons. E.g.

AD 1993 Jun 30 23:59:60.234

In addition, the following formats may be used for specifying dates in the Gregorian calendar:

- For BC dates, the BC is mandatory; for AD dates, the AD may be omitted.
- We use the usual astronomical convention in which day 0 of a month is the last day of the preceding month. Thus May 0 is Apr 30.
- Month numbers may be used instead of month names: e.g. 1993 06 30 23 59 60.234.
- Alternate formats for the time are supported: colons may be omitted, spaces may be used instead, or the letters h,m,s:

23:59:60.234
 235960.234
 23 59 60.234
 23h59m60s.234

- For imprecise dates, trailing information may be omitted, as for example:

1993 Jun 30 23:59:60
 1993 Jun 30 23:59 or 1993 Jun 30 2359
 1993 Jun 30 23h
 1993 Jun 30
 1993 Jun
 1993

In these cases, the earliest possible date is assumed, so 1993 Jun means 1993 Jun 0 (i.e. 1993 May 31.0) and 1993 means 1993 Jan 0 (i.e. 1992 Dec 31.0). The intent is that if a **greg** to **JD** conversion is used, and the resulting **JDs** are sorted, they will come out with the imprecise dates first.

- Further forms of imprecise and uncertain dates are supported:

1993 Jun 30 23:59?	(Centiday)
1993 Jun 30?	(Approx day)
1993 Jun?	(Approx month)
1993 Q2	(2nd quarter of 1993)
1993?	(Approx year)
c. 1993, ca. 1993	(Approx year)
1990s	(Decade)
1990s?	(Approx decade)
20C, BC 17C	(Century)
20C?, ca. BC 17C	(Approx century)
BC 3M	(Millenium)

- Day of Year format supported on input:

1997 Day 104 14:20:32

date The **date** calendar is identical to Gregorian but suppresses the calendar name and the day of the week in its output.

DOY The **DOY** (Day of Year) format is a compact numeric format representing the year and day of year. The last three digits of the integral part of the number are taken to be the day of year; earlier digits are then assumed to be the year. If the year is less than 100, 1900 is automatically added. Examples:

DOY	greg
97212.324	1997 Jul 31 07:46:33.6
1997212.324	1997 Jul 31 07:46:33.6
2002004	2002 Jan 4 00:00
02004	1902 Jan 4 00:00
102004	102 Jan 4 00:00

The **DOY** calendar is the only way to get **DOY** values on output, but on input one may also use the **greg** calendar in the form 1997 Day 212 07:46

pack **pack** is a numeric format where the last 4 digits represent MM and DD, the earlier digits are then assumed to be the year. If the year is less than 100, 1900 is automatically added.

Examples:

pack	greg
970731.324	1997 Jul 31 07:46:33.6
19970731.324	1997 Jul 31 07:46:33.6
20020104	2002 Jan 4 00:00
020104	1902 Jan 4 00:00
1020104	102 Jan 4 00:00

time The elapsed time calendar, **time**, gives seconds since the zero point defined by the **zero** command. A numeric value must be entered. The default **zero** is *Chandra* time: the time tag on events in the *Chandra* data files, measured in seconds since 1998 Jan 1 00:00:0.0.

GSD, GST The Greenwich Sidereal Date is essentially JD(GMST), i.e. the Julian Day number for Greenwich Mean Sidereal Time. Calendar **GSD** outputs the result as a JD and fraction of day, while **GST** outputs the result as an integer day number and hh:mm:ss.sss of sidereal time.

OS The Old Style (**OS**) calendar, or Julian proleptic calendar, was the civil calendar in Italy until the 16th century, in England until the 18th century, and in Russia until the 1920s. It differs from the Gregorian (New Style) calendar in that century years are always leap years, i.e. every year divisible by 4 is a leap year.

The Old Style and New Style calendars were in agreement from AD 200 Mar 1 (JD 1794167.5) to AD 300 Feb 28 (JD 1830690.5). Input format for **OS** is the same as for **greg**.

roman The Roman imperial proleptic calendar implemented here is based on the Julian proleptic calendar. The Julian calendar date is converted to time since the founding of the city of Rome ('ab urbe condita,' AUC), and the days and months are converted to Roman imperial (post-Augustan) days and months. Leap days are handled by the insertion of a bissextile day, BIS-KAL. FEB, on Feb 23, between VI KAL MAR and V KAL MAR. The eponymous consuls are listed if the appropriate data file is in the path.

RF The calendar of the first Republique Francaise is supported.

12.7.8 Setup Commands - Command Line Only

The following commands can be used on the command line or in setup mode (i.e. after *dates* has been run)

Command	Short form	Syntax	Action
help	H, ?	H	Brief summary of commands
list	L	L/opt	Display internal program state
print	P	Pn	Set output format type
from	F	F spec	Define source calendar and timescale
to	T	T spec	Define destination calendar and timescale
zero	Z	Z date	Set reference date (Default: 1998 Jan 1)
eval	E	E date	Convert once and exit
convert	C	C	Enter interactive convert loop
do	D	DO date1;date2;step	Loop convert
quit	Q	Q	Exit program

Display commands

- **help** prints a brief command summary like the one above.
- **list** has several options. With no option, **list** displays the current conversion settings (from and to). List options are:
 - **list/conv** displays the current conversion settings in greater detail.
 - **list/cal** lists the available calendars, which may be selected with the **from** and **to** commands.
 - **list/ts** lists the available timescales, which also may be selected with the **from** and **to** commands.
 - **list/ct** and **list/tt** list the internally available calendar types and timescale types, useful mainly for debugging.
- **print n** or **Pn** sets the print mode to n, where n is one of the integers 0, 1, 2.
 - P2 is the default for interactive mode. Each conversion outputs four lines: a leading banner of dashes, the ‘from’ info (to check the program has parsed your input correctly), the ‘to’ info (the

result), and a trailing banner of dashes. Each ‘info’ gives the calendar followed by the value.

- P1 is the default for batch mode. A single line gives the from and to values side by side, and a header line is issued on entry to convert mode giving the **from** and **to** calendars.
- P0 is a concise mode which gives only the output value.

12.8 *ObsVis* – Observation Visualizer

The Observation Visualizer is a tool to aid observation planning allowing inspection of instrument fields-of-view (FOVs), observatory roll angle and target visibility.

ObsVis is GUI-based and may be down-loaded from our website, installed and run on a user’s own computer. It is available for the following operating systems: SUN Solaris 2.6 & 2.7, Linux Redhat 6.0 & 6.1 and Slackware 3.5. There is also a limited WWW capability available on the CXC web page in the Proposal Tools section.

ObsVis has three major features:

- **Instrument FOVs:** Displays the digital sky survey (DSS) image around a target of interest with the requested Chandra instrument FOV(s) overlayed. The instrument and observing parameters such as the roll angle, target offsets and gratings can be changed interactively allowing the user to investigate the optimum observing parameters, avoid confusing sources etc..
- **Observatory Roll angle:** Calculates the nominal roll angle as a function of time for the specified target position. This option is also available via the web at: *obsvis.harvard.edu*.
- **Target Visibility:** Calculates the visibility of the specified target as a function of time. This option is also available via the web at: *obsvis.harvard.edu*.

Short help *tooltips* are available for most GUI items and will appear when the cursor hovers over the selection/entry box for ~ 1 second.

12.8.1 Obtaining the *ObsVis* Software

To obtain the *ObsVis* software, follow these steps:

1. Open the *CXC* website, URL <http://asc.harvard.edu>
2. Click on the link on the left side of the *CXC* homepage to “Proposal Information,” or the “proposer” icon at the bottom of the page. Follow the links to “Observation Visualizer.”
3. Follow the instructions for downloading, installing and running the software

12.8.2 Getting Started with *ObsVis*.

The top level page (Figure 12.7) allows entry of the J2000 coordinates, target offsets and roll angle for a target of interest. Only the coordinates are required. For example if you enter:

RA: 12 18 57.8
Dec: 47 18 12.0
Name: NGC4258

and click on *DISPLAY BOTH*, the Roll/Visibility plot shown in Figure 12.8 will appear. The target name is used as a label but is not a required entry.

The figure shows two curves, the target visibility and the range of allowed roll angle as a function of Julian date. The target visibility is the average fraction of an orbit during which a target is observable. Because the detectors will not be operated while the spacecraft is in the radiation belts, the maximum visibility is $\approx 80\%$. This is reduced from the 85% shown due to additional ACIS CTI measurements on either side of the radiation belt passage. For targets in the ecliptic plane, the sun constraint causes visibility to drop to 0% for 3 month intervals. There is also a moon constraint which may affect the visibility.

The Digital Sky Survey image obtained after zooming out with *ds9* (click on “zoom” and then “out” twice) is displayed in Figure 12.9 for NGC4258. The default Chandra instrument field-of-view (FOV) is the ACIS instrument with ACIS-I at the aimpoint. The aimpoint is marked as a circle inside a box. All offsets and the roll angle default to 0.0.

FileOptions

RA(J2000):12:18:57.8

Dec(J2000):47:18:12.1

Target NameNCC4258

Roll(deg)0.0

Offset-Y(arcmin):0.0

Offset-Z(arcmin):0.0

Offset-SimZ(arcmin):0.0

Offset-SimZ(mm):0.0

Science Instrument FOV:ACIS-I-S

Grating:NONE

CLEAR FORM

DISPLAY Roll and Visibility

DISPLAY Field of View

DISPLAY BOTH

Figure 12.7: *ObsVis* target form.

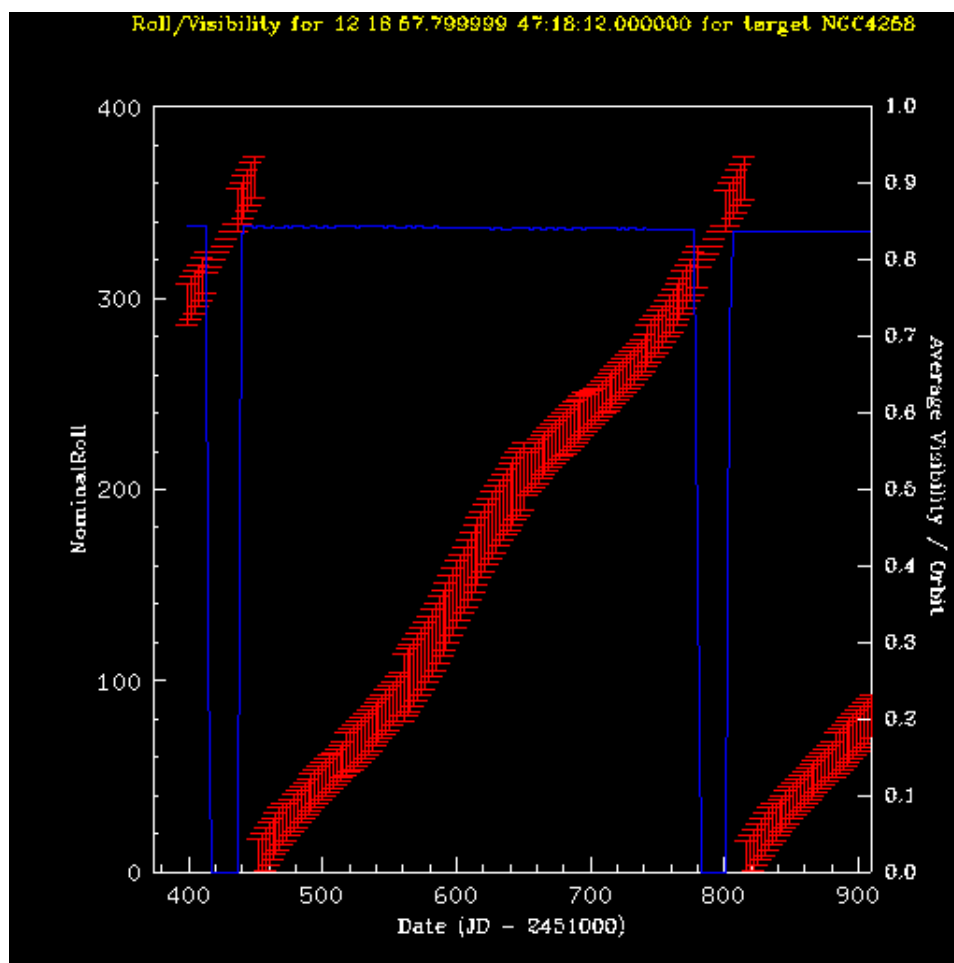


Figure 12.8: *ObsVis* Roll and Visibility Plot for NGC4258. Visibility is shown by the (blue) line and the range of allowed roll angle by the (red) vertical points.

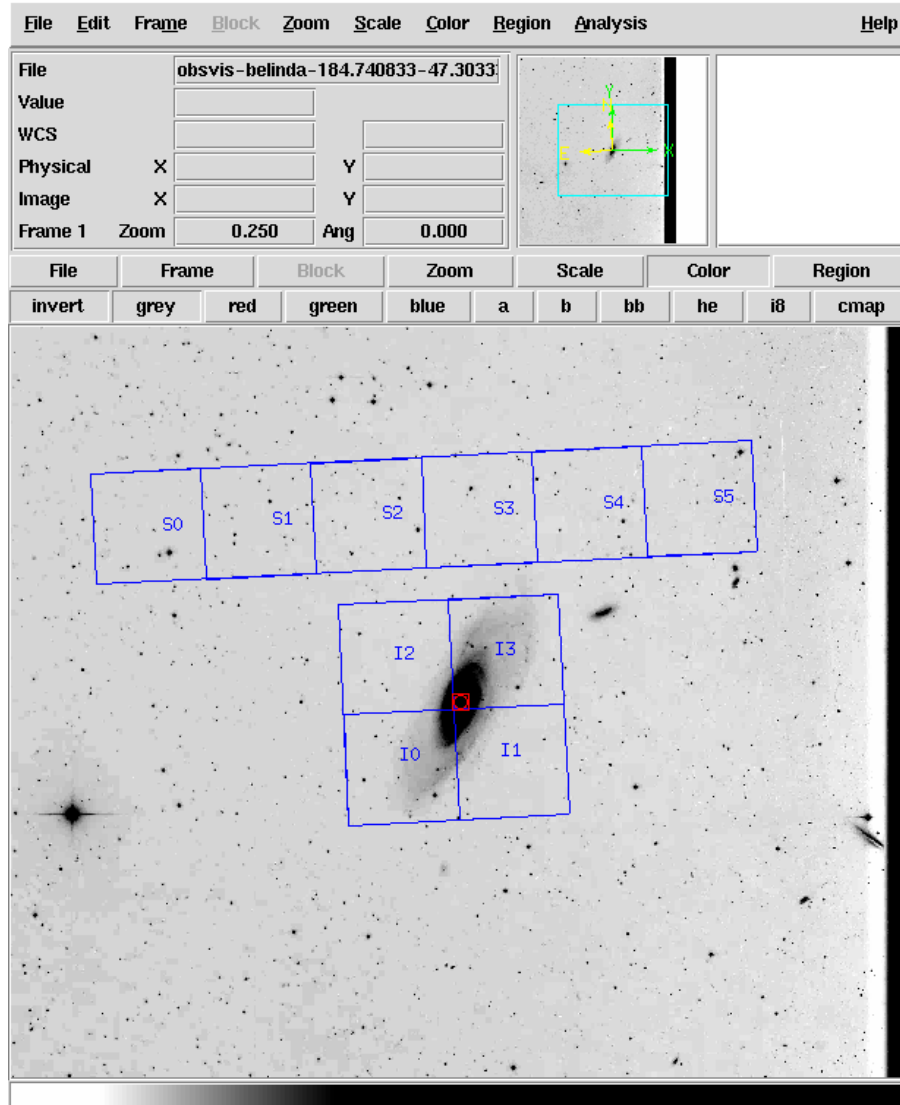


Figure 12.9: *ObsVis* Digital Sky Survey (DSS) image with ACIS-I (the default) FOV superposed for NGC4258. The image has been zoomed outwards by two steps using *ds9* to show the full ACIS-I plus ACIS-S FOV.

12.8.3 Setting the Observing Parameters

There are two locations for setting the parameters of a particular observation. The main *ObsVis* GUI allows specification of the coordinates, a name for labeling, as well as offsets and the roll angle since a user may wish to run *ObsVis* repeatedly when determining these parameters.

The Main *ObsVis* GUI

1. **Target Coordinates** – enter RA and Dec of target in hexadecimal coordinates, coordinate epoch (J2000 or B1950).
2. **Name** – the target name may be entered and is subsequently used to label the Roll/Visibility plot.
3. **Roll Angle** – rolls the instrument FOV around the aimpoint. It is measured in degrees west of north, valid range is $0 - 360^\circ$. Thus a positive value rolls the FOV clockwise on the *ds9* display.
4. **Target Offsets, (Offset-Y, Offset-Z)** – these parameters move the target away from the telescope aimpoint in the Y/Z direction. Both target position (red) and aimpoint (blue) will be marked on the resulting FOV display. The units are arcminutes, as required for input into RPS. A +ve Offset-Y moves the target towards lower-numbered ACIS chips (*e.g.* towards S2 on ACIS-S). A +ve Offset-Z offset moves the target down ACIS-I towards ACIS-S.
5. **SIM offset (Offset-SimZ)** – this is a motion of the SIM (Science Instrument Module) in the Z direction, moving the aimpoint (and the target) across the detector FOV. in *ObsVis* it is specified in arcminutes, however the value in mm is also displayed as the RPS form requires the offset to be specified in mm. A +ve SIM-Z offset moves the target and the telescope aimpoint in the direction from ACIS-I to ACIS-S.

Options: The Dates Dialog

The range of dates applied to the Roll/Visibility Plot may be changed by selecting *Start/End Dates* from the *Options* menu of the main *ObsVis* GUI (see Figure 12.10). The default range is: 1 Sept 2000 – 31 Dec 2001, which includes the expected ~ 1 year period for Cycle 2. Most users will wish to look at a whole year to get the big picture, the solar constraint is the same each year.

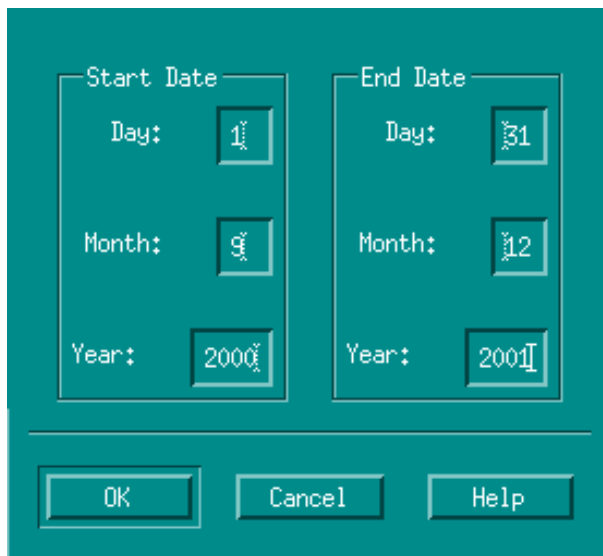


Figure 12.10: *ObsVis* Dates Dialog, accessed by selecting *Start/End Dates* in the *Options* menu of the main *ObsVis* GUI.

Options: The Parameters Dialog

The Parameters Dialog is reached by selecting *Parameters* from the *Options* menu of the main *ObsVis* GUI (see Figure 12.11). This Dialog allows the user to specify the instrument field of view, the grating spectrum overlay (if applicable), source catalogs and the size of the DSS image to be downloaded (default $120'' \times 120''$). **Note: For the new settings to be adopted, click *OK***

The various options are described in detail below.

- **Field of View** – the selected instrument FOV (default: ACIS-I) is superimposed on the Digital Sky Survey (DSS) image of the field centered at the target coordinates (with offsets and roll as specified on the main *ObsVis* GUI).
- **Grating Spectra** – the selected grating (default: NONE) dispersion pattern will be overlayed on the DSS image at the position of the target
- **Catalogs** – sources in the DSS image for the selected catalogs (default: NONE) will be labeled on the image. This selection currently includes:

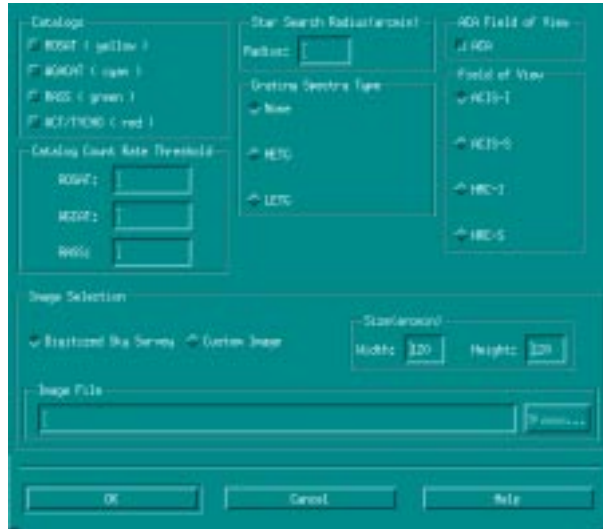


Figure 12.11: *ObsVis* Parameters Dialog, accessed by selecting *Parameters* in the *Options* menu of the main *ObsVis* GUI.

the ROSAT and WGAOAT X-ray source catalogs, the ROSAT All Sky Survey source list and the Tycho star catalog.

- **Search Radius** – the radius (default: 90') around the target position within which the catalog search is carried out.
- **Catalog Count Threshold** – the threshold above which to include sources in the first three catalogs may be set (default: 0.1 ct s⁻¹).
- **ACA Field of View** – the FOV of the Aspect Camera is overlaid on the DSS image if this option is selected (default: yes).
- **Image Selection** – By default a 120" × 120" section centered on the target coordinates is downloaded from the DSS CDROMs at CfA. The size may be modified by selecting the required width and height of the downloaded image. It is also possible to load a custom image into *ObsVis* on which the requested overlays will be placed, select *Custom Image*.
- **Image File** – If *Custom Image* is selected, the full path of the image file should be entered here.

12.8.4 Saving the *ObsVis* Output.

The current display may be printed or saved to a file by selecting *Print* from the “*File*” menu of SAO/DS9, selecting *File* and providing a filename in the menu which then appears.

The parameter settings set using the *Options* menu for *ObsVis* are saved when the application is exited and are automatically re-loaded when *ObsVis* is run again.

12.8.5 Known Bugs

Occasionally *ObsVis* hangs, usually this is during the download of a new image or a re-display of the FOV. If this occurs, we recommend exiting and re-starting the tool.

Chapter 13

Proposal Preparation and Submittal

This chapter discusses the details of filling in the proposal forms.

For Cycle 2, the following significant changes have been made:

- entire proposal is submitted electronically;
- Added **upload** button for science justifications;
- Added **postscript** button to return PostScript version of forms;
- Added standard list of institutions;
- Added Joint *Chandra/HST/NOAO* proposal?;
- Added Large Project option

13.1 Preparing the Proposal

The person considering the submission of a proposal for *Chandra* observing time should generally work through the following items.

- Decide on the science goal(s) to be pursued.
- Read the *Chandra* instrument descriptions.
- Choose the instrument that best achieves the science goal(s).
- Decide which target(s) best achieve the science goal(s).

- Determine if a specific target is a Cycle 2 target or has been observed or scheduled based on the Cycle 1 target list.
- Obtain the flux or the counting rate in a specific energy band from an observation of the target with a previous X-ray mission or from an estimate.
- Use PIMMS to generate an approximate *Chandra* count rate for the chosen instrument. Check the pileup warning if the chosen instrument is ACIS. If pileup will affect the science, explore approaches to mitigate it (Subarrays, Alternating Exposures, off-axis pointing).
- Use XSPEC to generate a simulated spectrum or MARX to generate a simulated event file.
- Check that the science goal(s) can be achieved by analyzing the simulated spectrum or event file.
- If a grating observation is desired, check that there are no other bright sources lying in the field-of-view (so that the dispersed spectrum of the other bright source does not fall onto the dispersed spectrum of the target). Specify a roll angle if necessary.
- Set the instrument parameters. For faint sources observed with ACIS ($< \sim 0.01$ counts frame $^{-1}$), this essentially means choosing the default Timed Exposure mode, the Faint Event Telemetry format, and choosing ACIS-I or ACIS-S as the aim point. If necessary, choose the chip that will be sacrificed if the “FEP0” problem recurs. For brighter sources, pileup probably should be mitigated.
- Fill in the proposal forms (e-mail or WWW version). Verify the forms. Generate a PostScript version of them.
- Construct the proposal text. Generate a PostScript version, including figures. See the detailed material in Appendix C of the *Chandra* NRA.
- Submit the proposal forms electronically. After receiving a proposal number, upload Postscript versions of the science justification and the proposal forms.

13.2 Submitting a Proposal

Electronic submission of proposal information (name, institution, targets, etc.) is required to reduce the overhead in processing the proposals. The scientific justification must also be submitted electronically. Paper copies of the proposal will only be accepted from individuals without access to the Internet. Those individuals should notify the *DO* well before the proposal deadline, stating the method to be used to submit the proposal. Contact information is listed in the Appendix.

To aid the proposer in submitting the required information electronically, a Remote Proposal Submission (RPS) system is available. RPS comes in two flavors: a WWW version (but only for browsers that support Forms) and an e-mail server. Each address is listed below.

RPS was first developed at the HEASARC, in the Laboratory for High Energy Astrophysics at NASA-GSFC. The Observation Cycle Group in the Data Systems Group of the *Chandra* Science Center adapted RPS for use by *Chandra*.

13.2.1 WWW version

The WWW version provides a form-based interface to the proposal processor. Links exist for help for each page of the form and for each parameter to be entered. Generic help for RPS is available at the top of the form.

Remember: the WWW version is stateless, which means nothing is done with the entries you have supplied UNTIL you, the user, clicks on one of the action buttons (such as saving the form). Be certain to save your form entries often. You can save the html file to your local disk and reload it. The section below contains specific help for each field of the RPS form.

The blue triangles (left side of first RPS page) toggle between a collapsed page (the initial appearance) and an expanded page. Note that starting with Cycle 2, each target will be enclosed in its own “pagelet”.

General Instructions for WWW RPS:

- Enter the proposal data into the RPS form.
- Save the proposal data often! For this, use the **SAVE** button on the RPS form. The form will be saved as an HTML file on a disk at the user’s site so it can be re-loaded at any time.
- Verify the proposal data for completeness and accuracy. Use the **VERIFY** button on the RPS form.

- Save the ‘verified’ proposal data to a local disk. Use the **SAVE** button on the RPS form.
- Generate the LaTeX file. Use the **LaTeX** button to generate a LaTeX file.
- Write the science justification. Generate a PostScript version (including figures) of the proposal.
- Submit the proposal to the *CXC*. Use the **SUBMIT** button on the RPS form which will appear **only after** the proposal has been successfully verified. Pressing this button should be done only once per proposal.
- **UPLOAD** PostScript versions of the proposal justification and the proposal forms by providing the full path name to the files when requested by RPS.

13.2.2 E-mail server

Instructions to use the e-mail server may be obtained by sending a blank e-mail message to:

`rps@head-cfa.harvard.edu`

(Note: Some UNIX mailers do not permit the transmission of an e-mail with no subject and no text; at least one character must be provided as either the subject or the text. It does not matter which character is used, or where it is placed.)

The response will be an ASCII file of instructions (about 1 page in length) that describes how to construct a mail file to obtain a blank version of the `parameter_field_name:answer` file, how to obtain a LaTeX version of the proposal forms, how to verify your entered answers, and how to submit the final version of the forms. The `name:answer` file, a plain ASCII file, may be edited with any editor.

The next section contains specific help for each field of the proposal form. It was designed to be used with the WWW version, however, the overall layout of the e-mail handler form matches that of the WWW form.

13.3 RPS Help: Specific Help for Fields of Cover and General Pages

RPS provides a facility for filling the *Chandra* Observation Request forms. Electronic submission of forms is required. Scientific justification is NOT submitted electronically. Proposals must also be submitted in hard copy (15 copies).

Short descriptions of each form and field are below. This file is ordered by form (Cover, General, Target, Constraint). Fields in this file are listed in the same order as found on the hardcopy forms, WWW forms, and the E-Mail handler forms.

13.3.1 COVER PAGE

Your personal details (name, address, telephone number, etc.) and the proposal name and number of targets.

- Principal Investigator Title
Your title (Dr, Ms, Mr, etc.) - up to 20 characters. This does NOT refer to one's job description (i.e., "postdoc").
- First Name
Your first name. 20 characters long at a maximum. Required.
- Middle Name or Initial
You may add another name or initials - up to 20 characters allowed.
- Last Name
Your last name. Up to 25 characters are allowed. Required.
- Department
Your department at your institute, up to 100 characters of it.
- Institute
Your institute, using up to 100 characters. Please copy/paste the institute name from the list (available from the RPS page; copy/paste using the *browser's* copy/paste capability).
- Street
The first line of your institute address, i.e., Street, any number within it, etc. Up to 30 characters.

- Mailstop The mailstop at your institute, if any. Maximum of 30 characters.
- City or Town Your Town / City. Up to 30 characters.
- State or Province
The name of the state or province of the institute. Up to 32 characters.
- Zip or Postal Code
The users post code, ZIP code or equivalent. Up to 10 characters.
- Country
The default is 'USA'. Up to 30 characters. Required. Below is the list of accepted country names (or abbreviations):

ARGENTINA	FINLAND	KOREA	SPAIN
AUSTRALIA	FRANCE	LATVIA	SWEDEN
AUSTRIA	GERMANY	LITHUANIA	SWITZ
BELGIUM	GREECE	MEXICO	TAIWAN
BRAZIL	HONGKONG	NETH	TURKEY
BULGARIA	INDIA	NORWAY	UK
CANADA	IRELAND	NZ	UKRAINE
CHILE	ISRAEL	PERU	USA
CHINA	INDONESIA	POLAND	
CZECH	IRAN	PORTUGAL	
DENMARK	ITALY	RUSSIA	
ESTONIA	JAPAN	S AFRICA	

If your country is not on this list, please contact the *DO* via the HelpDesk (asc.harvard.edu) or send email to usupporthead-cfa.harvard.edu.

- Telephone Number
Your telephone number, plus any extension. 15 characters allowed. Required.
- Fax Number
Your Fax number, if available. 15 chars.

13.3. RPS Help: Specific Help for Fields of Cover and General Pages 337

- Update address

If your address has changed since the last proposal round, you may request that our database be updated. This will CHANGE our database entry for you, rather than INSERT a "new" you.

- E-Mail Address

Your E-Mail address. Up to 50 chars. Required. An E-Mail receipt will be sent to this address within 24 hours of the electronic submission of your proposal.

- Large Project Rules?

For Cycle 2, Large Projects, defined as total exposure time >300 ksec are permitted. The project expects to award ~20% of the observing time to Large Projects. Details are in Appendix C of the NRA.

- Joint *Chandra*/HST *Chandra*/NOAO proposal?

HST: For Cycle 2, as an experiment, a small amount of observing time has been reserved in the programs of both HST and Chandra to be awarded by the review panels of the other observatory (HST: 100 orbits; Chandra: 400 ksec (the two amounts of time, when multiplied by the efficiencies of the observatories, are equal). This approach aims to reduce the "double jeopardy" inherent in proposing for simultaneous observations with both telescopes. Users may apply to HST and be awarded Chandra time and vice versa. Users who are submitting their proposal for consideration of joint Chandra/HST observations must set the flag to "Submit to Chandra". The "Submitted to HST" is used for proposers who sent their proposal to the HST review. The default is "no".

NOAO: Large Chandra proposals in Cycle 2 may also apply for NOAO time (on all telescopes except Gemini) to provide ground-based data which is required to meet the scientific goals of the proposal. NOAO has reserved up to 5% of the time on all telescopes except Gemini to be allocated by the Chandra TAC. Details of telescope/instrument combinations available at a given time are provided on the web at: <http://www.noao.edu/gateway/nasa/>. Proposers wishing to apply for NOAO time should select the "NOAO" option.

To apply for both NOAO and HST time select "HST+NOAO".

- Is there an E/PO component?

This item merely flags those proposals submitting a separate E/PO proposal (Education and Public Outreach). The flag is used for sorting. Default is “no”.

- Multi-telescope Observations

Are the *Chandra* observations to be coordinated with another observatory? If the answer is ‘yes’, you must flag the box and specify the other observatories in the ‘Telescopes’ box. If the other observatories are ground-based, just use ‘ground’ (note, however, that the scheduling of *Chandra* can not be dictated by ground-based observatories). Choices are: XTE, ASCA, SAX, HST, XMM, GRO, ground.

- Subject Category

The type of objects(s) to be viewed in the Proposal. Required. Enter one of the following categories:

Solar System and Misc.
 Normal Stars and WD
 WD Binaries and CV
 BH and NS Binaries
 SN, SNR and Isolated NS
 Normal Galaxies
 Active Galaxies and Quasars
 Clusters of Galaxies
 Extragalactic Diffuse Emission and Surveys
 Galactic Diffuse Emission and Surveys

- Observation Type

GO	General Observer
TOO	Target of Opportunity
Archive	Archive user
GTO	Guaranteed Time Observer
CAL	Calibration (<i>CXC</i> Only)

RPS is being used by all *Chandra* groups as the input to the observation database, so the *Observation Type* of a target is important. General Observers (GO’s) should choose one of ‘GO’, ‘TOO’, or ‘Archive’ as appropriate. The Observation Type of ‘Calibration’ is to be used

13.3. RPS Help: Specific Help for Fields of Cover and General Pages 339

only by the *CXC*. No proposal from non-*CXC* personnel can be accepted that requests a Calibration observation. You *must* be a member of a GTO team to use Observation Type of ‘GTO’.

- Proprietary Rights

The default is the standard 12 months for proprietary data rights. ‘No proprietary rights’ means that the data flows directly into the archive. Valid options are:

- S - Standard (12 months) (default)
- 1, 2, 3, 4, 6, or 9 months
- N - No proprietary rights

- Data Distribution Medium

Indicates the preferred distribution method for the PI’s data. Options are:

4GBDAT	4 GB 4 mm DAT
2GBDAT	2 GB 4 mm DAT
5GB8MM	5 GB 8 mm Exabyte
2GB8MM	2 GB 8 mm Exabyte
WWW Only	No other medium selected default to WWW access
CDROM zipped	650 MB CD-ROM with data compression
CDROM un-zipped	650 MB CD-ROM with no data compression

Note that for CD-ROMs, if ‘CD-ROM,unzipped’ is chosen and the data is too large to fit on the CD-ROM, the data will be zipped. If the data is too large to fit on a CD-ROM when zipped, the data will be sent on ‘4GB 4mm DAT’ tape. Required.

- Proposal Title

The title of the proposal up to 120 characters. Required.

- Abstract

800 characters maximum. Abstracts exceeding this limit will be truncated. Required.

NOTE: LaTeX Special Characters. The RPS processor will insert a ‘\’ (backslash) preceding all LaTeX special characters, such as \$,

%, #, and \ when generating the LaTeX file. When this file is run through the LaTeX processor, the special characters will be printed as they were entered. If these special characters are intended as LaTeX markups (i.e., a math environment delimited by dollar signs in the abstract field), the attached backslashes must be removed by editing the LaTeX file *before* the file is LaTeX'd. Note that making *any* changes elsewhere in the form will create a discrepancy between the electronically submitted proposal and the LaTeX form.

- Number of Targets

This entry is automatically filled in by RPS based upon the number of target pages.

- Total Time

This entry is automatically filled in by RPS based upon the sum of the exposures requested for each target.

13.3.2 GENERAL FORM

For details of any collaborators, etc. Up to 11 Co-Investigators are allowed. All fields are optional apart from the printed form requiring the name of an administrator at your Institution. The printed form must be signed by both the proposer and an administrator of her/his institution. If you are using the Web, a wide browser window will avoid form entry fields wrapping to new lines.

- Co-Investigator First Name

First Name for each Co-Investigator. 17 chars.

- Co-Investigator Last Name

Last Name for each Co-Investigator. 27 chars.

- Co-Investigator Institute

Institute for each Co-investigator. 60 chars. Again, use the 'copy and paste' capability of the browser.

- Co-Investigator E-Mail Address

E-Mail address for the Co-I Contact. 60 chars.

- Co-Investigator Country

The default is ‘USA’. Up to 10 characters. For non-US Co-Investigators, please read Appendix C of the NRA. The list of countries is included in the material above for the PI’s country.

- Is the first Co-I doing observing, rather than the PI?

Flag indicating if the first Co-I listed is also the person who will primarily carry out the observations. This should be used for PIs who may be difficult to reach and for situations when a graduate student or post-doc is to be considered the “real” PI. The default is ‘N’.

- Observing Investigator’s Telephone

Telephone number of the Observing Investigator. 24 chars.

- Name of Administrator

Name of administrator who will sign the form on behalf of the Institute of the PI. Up to 60 chars. Note that for the science review an actual signature is **not** required. Required.

- Administrative Authority

Post or Title of the administrator. 60 chars.

- Administrative Institute

Institute of the administrator. 60 chars.

13.4 RPS: Specific Help for Fields of TARGET FORM(S)

The section describes the details that need to be filled in for each different target. Starting with Cycle 2, each target is contained on its own page within the RPS form.

13.4.1 Parameters Required for All Targets, Regardless of Instrument

- Delete target?

RPS is stateless until a action button is used. To exclude a target, the deletion flag must be set to ‘yes’. The default position is ‘no’ and should remain that way unless the proposer intends to remove the target.

- Target Number

The number of the target. Since the number is used to show the Peer Review observing priority of one target relative to another, you may wish to change these around. However, the final proposal must contain a sequence of target numbers from 1 to the total number of primary targets. RPS will sort the final target list if the target numbers are not in numeric order. The user need not explicitly place the targets in numeric order but must assign the desired ordering.

- Target Name

The normal name for the object. Up to 20 characters. Required. Please use commonly accepted names for objects (if necessary, please use IAU-sanctioned name schemes) and put the object name first (e.g., NGC 4151, SN1987A, M31 Bulge Field A instead of “Field A of M31”).

- Solar System Object

The name of the Solar System Object to be observed, from the following choices: None, Earth, Moon, Mars, Jupiter, Venus, Saturn, Neptune, Pluto, Uranus, or Comet.

The default is ‘None’. Observations of moving solar system objects are done with a sequence of pointed observations, with the object moving through the field of view during each dwell period. The sequence of pointings will be derived from the object ephemeris to ensure that the object remains within 5' of the *Chandra* line-of-sight. Most solar system objects move slowly enough so that a single pointing will suffice. Should your observation be selected then the *CXC* will work with you to produce an observation that both meets your scientific objectives and optimizes the use of *Chandra*.

- Target Position Flag

Logical value indicating the observation is identified by a Target Name and RA and Dec value. The default is ‘Y’. This setting should NOT be changed unless: – the proposer will be observing a Solar System object, or – the proposer will be observing a generic TOO for which coordinates will be supplied at a later date.

- Right Ascension (R.A.)

The Right Ascension of the source in mandatory J2000 coordinate system. The standard format is HH MM SS.S - hours, minutes, seconds, separated by spaces. Alternatively, it may be entered as degrees

(DDD.DDDDDD), in which case it will be converted to sexagesimal during verification. The seconds may be entered as a real value with tenths (ie SS.S). Required.

- Declination

The declination of the source in mandatory J2000 coordinate system. The standard format is #DD MM SS.S - degrees, arcminutes, arcseconds, separated by spaces (# indicates an optional sign). Alternatively, it may be entered as degrees (DDD.DDDDDD), in which case it will be converted to sexagesimal during verification. If no sign is given it will be assumed to be positive. Required.

- Offset Pointing (Delta-Y/Delta-Z Offsets)

The user may wish to offset-point the observatory for a number of reasons, e.g., to reduce the effects of ACIS pile-up or to avoid HRC pore limits by blurring the image. Offset pointing is discussed in section 3.2. The default (zero offset) places the optical axis of the telescope at the specified target RA and Dec, to better than 30'' and thus at the aim point of the selected detector (with only one exception: ACIS-S: see below). Section 6.4 discusses the ACIS aimpoints in detail.

Specifying a nonzero offset moves the target coordinates off the optical axis and the image quality is reduced (see Figure 4.8). You can move the target position to a specific detector location by entering values for the Delta-Y and Delta-Z Detector Offsets in arcmin measured from the aim point — one along the y axis, and the other along the z axis. A positive Z offset moves the target from ACIS-I to ACIS-S. A positive Y offset moves the target from chip S3 towards chip S4 on ACIS-S. The ositive Z offset moves the target towards the readouts in ACIS-S (i.e. away from ACIS-I)(cf. Figure 3.1). Note the 180 degree differencebetween the Y/Z coordinates and the Delta-Y/Delta-Z coordinates.

For ACIS-S, the aim-point falls precisely on a node-node boundary. The extraction of spectra from such a location is complicated because the dither carries the target into chip regions with differing redistribution matrices. Other differences may exist. To reduce this impact, a small, 20'' offset will be added to **every** ACIS-S observation if no entry is made in the y-offset box. The 20'' offset has a negligible effect on the image quality (the diameter of the circle in which >90% of the

Table 13.1: Recommended SIM-Z offsets

Configuration	Mode	SIM z(mm)	SIM z (arcmins)	SIM z (motor steps)
HETG+ACIS-S	TE	-3	-1.02389	-1193
HETG+ACIS-S	CC	-4	-1.36519	-1591
LETG+ACIS-S	TE	-8	-2.73038	-3182
LETG+ACIS-S	CC	-8	-2.73038	-3182

encircled energy lies within $2''$ is $\sim 2'.4$ in size). If the proposer does *not* want the automatic offset, please enter “0.0” in the Y-offset box.

Since the offset moves the target position away from the aim point, the RA and Dec of the optical axis will lie somewhere on a circle centered at the target location. The RA and Dec of the optical axis will depend upon the spacecraft roll angle at the time of the observation. If the observer wants the optical axis at a particular RA and Dec with a YZ target offset, then the observer must specify a roll constraint.

All units are arcmins. The overall valid range is -50.0 to +50.0 for (y,z) offsets. Thus it is possible to specify an offset so large that the target is not imaged anywhere on the detector, so exercise caution. Furthermore, if the target is offset by more than 15 arcmins, then ghost images (see Chapter 4) from the target may be visible.

Finally, offsets are implemented in software by redefining the pointing position. This means that roll constraints apply at the new positions.

Any numeric value entered in the box will override the default values. For ACIS-S, enter 0.0 if the on-axis position is required.

- SIM Translation offset?

It is possible to move the Science Instrument Module in the Z direction. This moves the location of the focus on the instrument. Thus a target can be placed at a different Z position on the instrument and remain in focus. Units of Zsim are mm. The conversion is 1 arcmin = 2.93 mm. See Figure 1.2 for the definition of Z-sim motion.

Please note that $SIM - Z > -8mm$ for ACIS-S is not allowed due to flight problems

- Is the observation to be a raster scan?

The default is ‘N’. The observer is advised that for small spacecraft motions there is a more efficient way of moving *Chandra* called nudge

Table 13.2: Valid SIM-Z values by detector

Detector	Minimum	Maximum
HRC-S	-12.5439	61.3518
HRC-I	-61.3518	126.621
ACIS-S	-190.500	22.5685
ACIS-I	-22.5685	27.4739

mode. This mode is described in the Aspect System chapter of the Observatory Guide. This mode will be used if pointing positions are separated by 30 arcmins or less to take advantage of the reduced overhead possible with this mode. Should your observation be selected then the *CXC* will work with you to produce a raster that both meets your scientific objectives and optimizes the use of *Chandra*.

- Total Observing Time

The requested duration in kiloseconds for the observation. This is the TOTAL observing time, so for monitoring observations, this is the sum of all pointings. For example, for two observations of 40 kiloseconds each, specify 80 ksec as the Total Observing Time and 2 for the Number of Observations, in the Constraints Section.

- Is this a constrained observation ?

Yes/no value indicating whether the scheduling of the observation is constrained in any manner. The default is 'N'.

- Do you want optical monitor data for your target?

The proposer should be aware that the aspect camera (see Chapter 5) is NOT optimized for optical monitoring (the aspect camera is a 4-in (10 cm) telescope that images the defocused beam onto an array of 3x3 pixels, each pixel is 5 arcsec on a side), however one can use the camera to measure the instrumental ($\sim B+V+R$) magnitude of target objects. If the target is fainter than ~ 10 th mag, the aspect solution will be degraded by $\sim \sqrt{4/5}$. Very roughly, at an instrumental magnitude of 12.5 one can do $\sim 5\%$ differential photometry in 10 seconds, and at 15.0 one can do $\sim 15\%$ differential photometry in 200 seconds. Please see the aspect chapter for the limitations on the photometry and the expected signal-to-noise ratios.

The use of one of the guide-star channels as an optical monitor will be subject to approval by the peer review. The degradation of the

aspect solution may lower the usefulness of the archive of the field. The default is 'N'. This will be weighed with the scientific value of the optical data.

- V Magnitude of Target

Specify the V magnitude of the target if the use of the optical monitor is desired.

- Detector

Specifies which detector will be on the optical axis doing the observation. Specify one of ACIS-S, ACIS-I, HRC-S or HRC-I. See the HRC or ACIS chapters for the aim point locations.

The target coordinates, including any specified offsets, will be placed at the aim point of the selected detector. Note a user should use the offset parameters (above) to move the target away from the nominal aim point should this be desired.

- Grating

Specifies which grating to use. Options are NONE, HETG, and LETG. The default is NONE which specifies no grating (direct imaging). You should use ACIS-S with the HETG and HRC-S with the LETG, unless you make a case otherwise in your science justification.

- Count Rate

The Count rate box must be filled in by all users. For detectors without gratings, this count rate is the source count rate in counts per second. For ACIS-S+grating or HRC-S+grating, this count rate is the zero-order count rate in counts per second.

For variable sources, supply the maximum expected count rate. This will allow for consistency checking of requested observation mode(s). The PIMMS tool can be used to calculate count rate.

- 1st Order Count Rate

The 1st order count rate entry should be filled in ONLY for those GOs who choose to use ACIS-S+grating or HRC-S+grating. The units are counts per second.

- Total Field Count Rate

This item requests the count rate across the field of the detector. This rate should include the *total* background (see 6.10 for ACIS and 7.8 for the HRC) as well as nearby sources. Units are counts per second.

- Is target an extended source?

If the target is an extended source, set the flag to ‘Y’. The default is ‘N’.

13.4.2 HRC-S Parameters

Note that the Imaging mode of the HRC does not have any user-settable parameters, so the ‘HRC-S Parameter’ flag should remain ‘N’ if the user wants to use HRC-I.

For Cycle 2, the only user-settable parameter is a request to block the zero-order image when using HRC-S with the LETG.

- HRC-S Zero-Order Blocking

The spectrum’s zero order may be blocked if desired. The blocking is carried out with shutters (“butter” knives) within the HRC prior to the photon detection in the microchannel array.

13.4.3 ACIS Parameters

This sections contains the details for any observation which proposes to use the ACIS. ACIS has a large number of possible observing modes. The GO is urged to become familiar with each mode prior to specifying the details of the proposed observation.

13.4.4 ACIS Required Parameters

For faint sources ($\sim <0.01$ counts frame⁻¹), these are the ONLY parameters that must be set.

- Exposure Mode

The exposure mode for ACIS for which two choices are possible: Timed Exposure (TE) or Continuous Clocking (CC). The default is TE.

- Event Telemetry Format

Event Telemetry Format controls the packing of the data into the telemetry stream. The choices are Faint (TE,CC), Very Faint (TE),

Faint+Bias (TE), Graded (TE,CC). The default value is Faint. Very Faint and Faint+Bias ('VF' and F+B) may only be used for the 'TE' mode. ("Event Telemetry Format" is similar to "Bit Mode" for *ASCA*.)

A one-sentence description of the modes is:

- Very Faint: same as Faint, except event region is 5x5 pixels in size
 - Faint: returns (x, y) position of event, energy, time-stamp + values of pixels in the 3x3 event region
 - Faint+Bias: same as Faint, except the bias in a 3x3 event region is also returned (see Section 6.13.)
 - Graded: returns (x, y) position of event, energy, time-stamp + Grade of pixels in 3x3 event region
- Use standard 6 ACIS chips?

A 'yes' answer will activate the 6 standard ACIS chips appropriate to the chosen detector. Those chips are as follows:

ACIS-I = I0 - I3 + S2 + S3
 ACIS-S = S0 - S5
 ACIS-S(imaging) = I2,I3,S1-S4

If the GO must use fewer than the standard 6 chips or a non-standard set of chips, s/he MUST turn on those chips individually (see below).

- CCDs On

			I0	I1			
			I2	I3			
S0	S1	S2	S3	S4	S5		

The ACIS CCD chip layout is as pictured. ACIS can read out as many as 6 chips. The user is required to set the CCD chips to read. At least one chip must be set.

- Identify least significant chip (optional)

The Front End Processors carry out event detection. During the first 6 months of the mission, FEP0 generated numerous spurious events

that saturated telemetry. For a short-term solution, only 5 CCDs were read so that FEP0 was not used. A patch has been installed in the ACIS Flight software which has restored the use of FEP0. Should the problem re-occur we expect to lose only the top half of the chip associated with FEP0. In the event of further FEP0 problems the default is to continue observing in 6-chip mode. However, the user may optionally specify that they prefer to change to 5-chip mode, and choose which chip to drop. The default is NA (continue observing in 6 chip mode OR the observation only uses 5 or less chips)

Default chip assignments for FEP0 are given in Section 6.16.

13.4.5 ACIS Optional Custom Parameters:

The custom parameters are available so users can mitigate the effects of pileup or an overflow of telemetry.

ACIS Parameters that affect PILEUP:

- Use most efficient frame exposure time? OR
- CCD frame exposure time

The CCD frame exposure time is the fundamental unit for ACIS. It ranges from 0.2 to 10.0 seconds in .1 second increments. Responding with a 'Y' to the question 'Use most efficient frame exposure time?' allows the ACIS team to adjust the CCD frame time as necessary. The user may override that freedom by specifying a CCD frame time. Note that an entire CCD takes ~ 3 seconds to read (~ 3 millisec per row * 1024 rows), so a 0.2 second frame time has a small observing efficiency which the proposer must justify. The default frame time is 3.2 seconds. A shorter frame time can aid in mitigating pileup by a factor of up to ~ 8 . A shorter frame time is most easily achieved by the use of a Subarray.

- Subarray Type

A subarray is a reduced region of the CCDs (all of the CCDs that are turned on) that will be read. A reduced region may also help to reduce the effects of pulse pile-up. The first menu indicates whether the proposer intends to use the subarray capability by choosing 'None' or 'Use <X> Subarray' (where <X> = 1/8, 1/4, 1/2) or 'Use Custom Subarray.' The default is 'None'.

Table 13.3: Standard Subarrays

	ACIS-I		ACIS-S
Standard Size	Start Row	No. of Rows	Start Row
1/2	512	512	256
1/4	768	256	384
1/8	896	128	448

Note that the minimum Frame Time depends on the size and location of the subarray. See Chapter 6 of the *Proposers' Observatory Guide* (asc.harvard.edu) for more information.

The standard subarrays can be selected to avoid pileup approximately by the factor of the subarray size. The standard subarrays for ACIS-I use the values as listed in Table 13.4.5. For ACIS-S, the starting rows differ because of the different position of the aim-point relative to the readout node. Figure 6.20 of the *Proposers' Observatory Guide* contains an schematic of the locations of the default Subarrays.

– Subarray : Start Row

The starting row that will be read for processing. Valid range is 1 - 896 (since the minimum number of rows is 128).

– Subarray : Number of Rows

The number of rows that will be read for processing. Valid range is 128 - 1024.

- **Frame Time:** The exposure time for ACIS. Default is 3.2 sec. Can be set from 0.2 to 10.0s. An equation in section 6.12.1 of the ACIS chapter can be used to calculate the amount of time necessary to read out the custom number of rows specified above.
- **Use Alternating Exposure Readout?** Alternating Exposure Readout observation sets the number of SECONDARY exposures that will follow each primary exposure. If $n = 0$, only primary exposures are used. A deadtime will result from the short exposure since the electronics still require 3.2 sec to process the full frame. Therefore, to minimize the deadtime, the number of short exposures should be kept to a minimum. As a general example, consider the following two situations. If the user wants 10 3.2-sec exposures for every 0.2-sec exposure, the primary exposure time is 0.2, the CCD frame exposure time is 3.2

sec, and the number of secondary exposures is 10. The observational efficiency is 0.91. If the user wants 5 0.3-sec exposures for every 3.2-sec exposure, then the primary exposure time is 3.2, the CCD frame exposure time is 0.3 sec and the number of secondary exposures is 5. The efficiency for this case is 0.24. Note the minimum on the primary exposure is 0.2 sec. Times longer than 3.2 seconds are discouraged for Cycle 2 until operational experience exists.

An example might prove useful here. If the proposer wants to sample the image 4 times using an exposure of 0.3 sec, then the specified parameters are: $n = 4$; $T = 0.3$ sec

(the secondary exposure will be carried out at the default exposure time appropriate for the number of chips to be read and the number of lines per chip; if all 6 chips are to be read appropriate for the number of chips to be read and the number of lines per chip; if all 6 chips are to be read completely, this default time will be 3.2 sec).

The resulting exposure sequence will be carried out as follows:

0.3 sec, 3.2 sec, 3.2 sec, 3.2 sec, 3.2 sec, 0.3 sec, 3.2 sec, etc.

until the total requested observing time is used.

ACIS Parameters that affect TELEMETRY:

- Energy filter: Use Energy Filter

This parameter allows the user to filter every candidate event before packing into the telemetry stream. The filter applies to all of the active CCDs. The use of an event filter does NOT affect pulse pileup, but only reduces the telemetry. The default is 'N'.

- Energy filter: Low Threshold

The value of the threshold that will be applied in keV. Valid range is 0 - 10.

- Energy filter: Range

The range of the event amplitude in keV. Valid value is a single entry within the range of .1 - 15.

- Spatial Window: Use Spatial Window

This set of parameters allows the user to filter the data to reduce the telemetry load. The use of a Spatial Window does NOT affect the reading of the CCD, so there will be no impact on pulse pile-up. Spatial windows do reduce the telemetry.

The user can either *IN*clude the photons specified by the window bounds or *EX*clude the photons within the window bounds. The default is ‘N’ (i.e., *no* windows).

The user may specify up to 6 windows *per* CCD chip for a total of 36 windows in all. Space is provided in RPS for a total of 6 windows. If the user desires additional Spatial Windows, enter the following information into the ‘Additional Spatial Windows’ box (all information on one line, each field separated by white space):

```
chip number
window number
starting row
starting column
window width
window height
low energy threshold
energy range
```

where “chip” should be one of (I0, I1, I2, I3, S0, S1, S2, S3, S4, or S5), “window number” should be a serially increasing number, and the remaining parameters are listed below.

Spatial Windows can either Include all of the photons in the defined region or Exclude all of the photons in the defined region. The order in which windows are specified is significant if the windows overlap and are on the same chip. In this case the FIRST window specified takes precedence. For example, if one window excludes the top 2/3 of chip S2, and the next window includes the bottom 2/3, the first window will overlay the second, resulting in just the bottom 1/3 of S2 being telemetered. The order in which the windows are applied is the order in which they are entered on the RPS form.

– Spatial Window: Chip

Value indicating the chip to be used for this spatial window. Choices are I0, I1, I2, I3, S0, S1, S2, S3, S4, and S5.

- Spatial Window: Type
Spatial Windows can either INclude all of the photons in the defined region or EXclude all of the photons in the defined region. Options are: I - Include or E - Exclude.
- Spatial Window: Start row for window
The starting row that will be read. Valid range is 1 - 896.
- Spatial Window: Start column for window
The starting column that will be read. Valid range is 1 - 896.
- Spatial Window: Width of window
The Number of columns of the window that will be read. Valid range is 128 - 1024.
- Spatial Window: Height of window
The Number of rows of the window that will be read. Valid range is 128 - 1024.
- Spatial Window: Lower Threshold
The value for the lower discrimination threshold in keV. Valid range is 0.1 - 15.0.
- Spatial Window: energy range
The value for the energy range in keV. Valid value is a single entry within the range of 0.1 - 15.0.
- Definition for additional Spatial Windows?
Text box to specify additional Spatial Windows. Please specify additional Spatial Windows in the order requested.

General ACIS Parameters:

- Bias Request: Request separate bias (Y, N)

Bias frames (see Chapter 6.13) will be obtained periodically by the Operations staff as part of the overall maintenance and calibration of the instruments. The proposer may wish to request that a bias frame be obtained explicitly for her/his observation. The additional time must be justified in the proposal because it is an overhead that will reduce the time available for science observations. The cost is 1.5 ksec per request. The default is 'N'.

13.5 RPS: Help for Fields for Target CONSTRAINTS

This section contains the details for any time critical observation. The types of constraint are:

Window:	In a fixed time-window
Roll:	Requests a specific spacecraft attitude
Monitoring:	Samples at a given interval
Phase dependent:	Samples at a given phase
Uninterrupted:	Absolutely no interruptions

- Window Constraint

Indicates that the exact time of observation execution must be constrained within a time window. The start and end times must be given in UT (year, month, day, hour, minute). See the NRA document for the anticipated dates covered by the NRA period. The default is 'N'.

- Window Constraint: Start Year
The year to start in for time critical observations. Earliest valid entry is 1998.
- Window Constraint: Start Month
The month to start during for time critical observations. Specify as 01-12.
- Window Constraint: Start Day
The day to start on for time critical observations.
- Window Constraint: Start Hour
The hour to start at for time critical observations. Valid entries: 00-23.
- Window Constraint: Start Minute
The minute to start at for time critical observations. Valid entries: 00-59.
- Window Constraint: Stop Year
The year to end in for time critical observations. Earliest valid entry is 1998.
- Window Constraint: Stop Month
The month to end in for time critical observations. Specify as 01-12.

- Window Constraint: Stop Day
The day to end on for time critical observations.
- Window Constraint: Stop Hour
The hour to end for time critical observations. Valid entries are 00-23.
- Window Constraint: Stop Minute
The minute to end for time critical observations. Valid entries are 00-59

- Roll Constraint

Indicates whether the observation is to be carried out with a specific roll angle for the spacecraft. Default is 'No' (no roll constraint).

The spacecraft roll is the angle between celestial north and the spacecraft -Z (minus Z) axis projected on the sky. The roll angle is constrained as a function of time because power must be supplied by the solar cells. For any given time and target, there is a nominal roll angle for which the solar power arrays are aimed directly at the sun. A roll constraint translates directly into a constraint on the day and time when an observation may be carried out.

- spacecraft roll angle
The specific roll angle desired. It is measured in degrees *west* of north, and is measured from the aim point (not the center of the array). It should only be specified for cases in which a specific attitude is required to meet scientific objectives. Valid range is 0.0 - 360.
- roll tolerance
Measured in degrees. Defined as the half-range (assumed symmetric) that is acceptable for the specified roll angle.

- Monitoring Observation

Indicates whether the observation is to be made in several parts at fixed intervals but with no fixed starting time. The number of parts is specified on the Target Page in the 'Number of Observations' field. The default is 'N'.

- Number of Observations

Number of observations of the target. This will be one unless constraints are set. For monitoring observations this will give the number of parts into which the total exposure will be divided.

- Minimum Interval Between Observations

Minimum interval between monitoring observations. Units are days.

- Maximum Interval Between Observations

Maximum interval between monitoring observations. Units are days.

- Phase-Dependent Observation

A Phase-dependent observation requests coverage of a particular range of times of a periodic source, with those times specified in terms of the period of the source. The Epoch is the reference date given in MJD and the Period has units of days. The Minimum and Maximum Phase are the minimum and maximum orbital phase to be included. The “error” in the phase range indicates the precision with which the scheduling software must match the phase-specified schedule. The default is ‘N’ (no phase-dependent observation).

- Phase Dependent: Phase Dependent Epoch

For Phase Dependent observations, the reference date (MJD). The observations will be made at an integral number of Periods from this date. This date must be specified as close to the start of the observation cycle as possible. The reference date must be within 5 years of the current year.

- Phase Dependent: Phase Dependent Period

The period in days between phase dependant observations.

- Phase Dependent: Minimum Phase

Minimum orbital phase to be observed. Values must be between 0 and 1.

- Phase Dependent: Minimum Phase Error

The error on the minimum orbital phase. Values must be between 0 and 0.5. This parameter sets how precisely the phase range will be covered.

- Phase Dependent: Maximum Phase

Maximum orbital phase to be observed. Values must be between 0 and 1.

13.6. RPS: Help After Submitting: When You've Discovered A Mistake 357

- Phase Dependent: Maximum Phase Error

The error on the maximum orbital phase. Values must be between 0 and 0.5. This parameter sets how precisely the phase range will be covered.

- Uninterrupted Observation Required

Indicates that the science CAN NOT be done if the observation is interrupted in any manner. Use sparingly. This flag should, in general, NOT be used because the typical operating mode for *Chandra* will be one pointing per target until the allocated observing time has been expended (i.e., all observations are expected to be “uninterrupted”).

- Remarks Any relevant comments you wish to make regarding the Target. Up to 400 characters. The Remarks are attached as the last page of the proposal.

13.6 RPS: Help After Submitting: When You've Discovered A Mistake

If, after submitting the forms and uploading the justification, you discover a mistake (more than just a typo in the justification) and you want to re-submit, then you should follow the following steps:

13.6.1 Mistake Discovered BEFORE the Proposal Deadline

- Correct the error.
- Go through the submit process as if you had not submitted before
- Send the *DO* a notice (using HelpDesk on the WWW form) that you have re-submitted.

Once a proposal arrives, it is scanned to see if it may duplicate a previously-received proposal. Proposals that appear to be duplicates are then flagged for the attention of a member of the *DO*. The proposal with the most recent date and time is accepted as the “final” proposal.

13.6.2 Mistake Discovered AFTER the Proposal Deadline

- If the item is critical to the success of the potential *observation* (for example, incorrect coordinates), please inform the *DO* as soon as possible.

- Late changes in the Science Justification are not allowed. However, some typographical or numerical errors can be misleading, and corrections of such can be sent to *CXC DO* in a letter of explanation. If appropriate, this letter will be included in material sent to the Peer Review. Note that a long list of corrections to a careless submission cannot be accepted since this would be *de facto* a late-proposal submission.

Part III

Appendices

Appendix A

Help and Contact Information

A.1 Contact Information

The Proposal Review is organized by the *CXC DO*. Questions should be sent to *DO* staff via the form on the *CXC* webpage. Go to the *CXC* homepage and click on the “HelpDesk” link at the bottom of the page. The URL for the *CXC* home page is

<http://asc.harvard.edu/>

The *CXC* can also be contacted via email, but the WWW form above is preferred. The email address is:

usupport@cfa.harvard.edu

A.2 The *CXC* Website

All proposal material is available from the *CXC* Website. Updates and news items are regularly posted here, and proposers are urged to check the “Announcements Box” and the “What’s New” page for the latest information.

The material most relevant to proposers is in the following sections:

User Documents - links to *CXC* documents. Includes postscript, PDF and HTML versions of the *Proposers’ Observatory Guide*. Also other *Chandra* technical documents.

Proposer - includes links to the RPS and the proposal preparation tools. The Proposal tools include:

1. *PIMMS* - calculate *Chandra* count rates
2. *dates* - a routine to convert times and dates between different calendars
3. *colden* - a routine to retrieve the neutral hydrogen density at a given RA and Dec.
4. *precess* - allows conversion between different astronomical coordinate systems and precession of equatorial coordinates.
5. *MARX* - simulates *Chandra* images and event files.
6. *ObsCat* - allows users browse the *Chandra* Observing Catalog.
7. *ObsVis* - the *Chandra* Observation Visualizer. Allows interactive display of instrument and telescope field of view on a star field. Calculates allowed roll angles.

The “Proposer” section also has links to responses required for simulations.

Newsletters - an archive of *CXC* Newsletters in HTML.

Other useful background material includes an overview of the *Chandra* Observatory, a list of *Chandra*-related web sites, and detailed calibration information. *Chandra* calibration data is publically available and can be accessed from the *Chandra* Data Archive. Finally, *Chandra* data can be analyzed using *CIAO* (Chandra Interactive Analysis of Observations). *CIAO* is available from the “Data Analysis” link in the top navigation bar.

A.3 The HelpDesk Form

We are using commercial Helpdesk software to track your requests and problems. Click on “HelpDesk” and the HelpDesk form will appear. You must fill in the “user login” box with first initial, lastname; e.g. gwashington, alincoln. You must select a category. You must state or describe the problem or request. Information in other fields is helpful but not mandatory. To send, click on the “Submit Ticket” button at the bottom.

A.4 Software Available for Proposers

Software available for proposal planning is summarized in A.2, and instructions for use are given elsewhere in this Guide. *ObsCat* is written in

JAVA, and hence is a web-based tool. No command line version is available. However a lot of information is available from the *CXC* target pages (asc.harvard.edu/targets/) Command-line versions are available for *PIMMS*, *colden*, *precess*, *dates*, *MARX* and *ObsVis*. These routines can be obtained via FTP from the *CXC* FTP site:

`asc.harvard.edu`

XSPEC will be used to analyze simulated *Chandra* data by many proposers, including output from the *MARX* simulator. It is available from the HEASARC at:

`http://heasarc.gsfc.nasa.gov/docs/xanadu/xanadu.html`

The Remote Proposal Submission (RPS) software, originally written by the High Energy Astrophysics Science Archive Center at NASA Goddard Space Flight Center, has been modified to accept *Chandra* proposals. The WWW interface to RPS can be accessed from the *CXC* website, or instructions for using the email server can be obtained by sending a blank email to rps@head-cfa.harvard.edu. Electronic submission of proposal information is required.

A.5 Documents for Proposers

The main reference documents for writing *Chandra* proposals are the NASA Research Announcement (NRA), The NRA contains instructions for proposal preparation and submission, and the deadline for proposal submission. It is available from the *CXC* website as well as NASA Headquarters (<http://www.hq.nasa.gov/>). The *Proposers' Observatory Guide* is a reference manual for the *Chandra* satellite, containing detailed descriptions of the telescope, Science Instruments and Gratings, as well as an overview of Science Operations and the aspect system. It also contains the information required to astronomers write a proposal - for example, effective areas for the mirror-instrument combinations and examples of how to run the proposal planning software. The *Proposers' Observatory Guide* is available from the *CXC* website (<http://asc.harvard.edu>) in HTML, postscript and PDF format. A hardcopy can be obtained via the *CXC* HelpDesk. Other useful material can be found in back issues of the *CXC* Newsletter.

A.6 CXC DO Staff

- Dr. Fred Seward, fseward@cfa.harvard.edu

- Dr. Belinda Wilkes, bwilkes@cfa.harvard.edu
- Dr. Andrea Prestwich, aprestwich@cfa.harvard.edu
- Dr. Nancy Evans, nevans@cfa.harvard.edu

Appendix B

Acronym List

This list is a superset of acronyms and abbreviations used in this document.

ACA Aspect Camera Assembly

ACACAL ACA Calibration Data

ACIS AXAF CCD Imaging Spectrometer

ACIS-I ACIS Imaging array

ACIS-S ACIS Spectroscopic array

ADC Analog-Digital Conversion

ADU Analog to Digital Unit

AO Announcement of Opportunity

ARM Alignment Reference Mirror

ASC AXAF Science Center

ASCA also known as Asuka, Astro-D - Japanese X-ray satellite

ASCDS ASC Data Analysis System

ASCII American National Standard Code for Information Exchange

ASPQUAL Aspect Solution Quality Indicators

AUC ‘ab urbe condita’

AXAF Advanced X-Ray Astrophysics Facility

BI Back-illuminated

BST British Summer Time

CC Continuous Clocking

CCD Charge Coupled Device

CCDM Communication, Command, and Data Management

CCMD Continuous Clock Mode

CDT Central Daylight Time

CGCD Crossed Grid Charge Detector

CoI Co-Investigator

COLDEN Calculate Neutral Hydrogen Column Density

CR Cosmic Ray

CSS Coarse Sun Sensor

CST Central Standard Time

CTE Charge Transfer Efficiency

CTI Charge Transfer Inefficiency

CXC Chandra X-ray Center

CXCDS Chandra X-ray Center Data Systems

CXO Chandra X-ray Observatory

Dec Declination	GO General Observer
DMV Moscow Decree Time	GSD Greenwich Sidereal Date
DO Director's Office	GSFC Goddard Space Flight Center
DOY Day of Year	GSPROPS Guide Star Properties
DSN Deep Space Network	GST Greenwich Sidereal Time
E/PO Education and Public Outreach	GTO Guaranteed Time Observer
EC Ecliptic Coordinates	GUI Graphical User Interface
EDT Eastern Daylight Time	GYROCAL Gyro Calibration Data
EIPS Electron Impact Point Source	HEASARC High Energy Astrophysics Science Archive Research Center
EPHIN Electron Proton Helium In- strument	HEG High Energy Grating
ESA Earth Sensor Assembly	HESF High Energy Suppression Filter
EST Eastern Standard Time	HESS HETG Support Structure
FI Focal Plane Instrumentation (Front- Illuminated)	HETG High Energy Transmission Grating
FIDPROPS Fiducial Light Properties	HETGS HETG Spectrometer
FITS Flexible Image Transport System	HP Hewlett-Packard
FLA Fiducial Light Assemblies	HPD Half Power Diameter
FOV Field of View	HQ Headquarters
FPSI Focal Plane Scientific Instru- ments	HRC High Resolution Camera
FPX Focal Plane X	HRI High Resolution Imager
FPY Focal Plane Y	HRMA High Resolution Mirror As- sembly
FSS Fine Sun Sensor	HST Hubble Space Telescope
FTA Fiducial Transfer Assembly	ICD Interface Control Document
FTS Fiducial Transfer System	IDS Interdisciplinary Scientist
FUV Far-UV	IPI Instrument Principal Investigator
FWHM Full Width Half Maximum	IPS Integral Propulsion System
GESS Grating Element Support Struc- ture	IRAF Image Reduction and Analysis Facility
GMST Greenwich Mean Sidereal Time	IRU Inertial Reference Unit
GMT Greenwich Mean Time	

ISAS Institute of Space and Astronautical Science	NMM Normal Maneuver Mode
IUE International Ultraviolet Explorer	NPM Normal Pointing Mode
IUS Inertial Upper Stage	NRA NASA Research Announcement
JD Julian Day	NRAO National Radio Astronomy Observatory
JOVE Joint Venture (NASA/Universities)	OBA Optical Bench Assembly
JPL Jet Propulsion Laboratory	OBSCAT Observing Catalog
KSC Kennedy Spaceflight Center	OBSVIS Observation Visualizer
LESF Low-energy Suppression Filter	OCC Operations Control Center
LETG Low Energy Transmission Grating	OFLS Off-line System
LETGS LETG Spectrometer	ONLS On-line System
LGA Low Gain Antenna	OS Operating System (Old Style)
LRF Line Response Function	PCAD Pointing Control and Attitude Determination
LSF Line Spread Function	PDR Preliminary Design Review
MARX Model of AXAF Response to X-rays	PDT Pacific Daylight Time
MCP Micro Channel Plate	PH Pulse Height
MDT Mountain Daylight Time	PHA Pulse Height Amplifier (or Amplitude)
MEG Medium Energy Grating	PI Principal Investigator
MIT Massachusetts Institute of Technology	PIMMS Portable Interactive Multi-Mission Software
MJD Modified Julian Date	PPM Positions & Proper Motions
MSFC Marshall Space Flight Center	PSF Point Spread Function
MST Mountain Standard Time (Moscow Summer Time)	PSPC Position Sensitive Proportional Counter
MUPS Momentum Unloading Propulsion System	PST Pacific Standard Time
NASA National Aeronautics and Space Administration	PSU Pennsylvania State University
NASCOM NASA Communication system	QE Quantum Efficiency
	RA Right Ascension
	RCS Reaction Control System
	RCTU Remote Command and Telemetry Unit

RF	Republique Française	VCDU	Virtual Channel Data Unit
RfO	Requests for Observations	VETA	Validation Engineering Test Article (mirror)
ROSAT	Roentgen Satellite	WORM	Write-Once-Read-Many (times) storage device
RPS	Remote Proposal Submission	WWW	World-Wide Web
RRC	Retroreflector Collimator	XRCF	X-ray Calibration Facility
RWA	Reaction Wheel Assembly	XRS	X-Ray Spectrometer
SAO	Smithsonian Astrophysical Observatory	XSPEC	X-ray Spectral fitting package
SI	Science Instrument	XTE	X-ray Timing Explorer
SIM	Scientific Instrument Module	XUV	Extreme Ultraviolet
SMF	Software Maintenance Facility		
SN	Space Network		
SNR	Supernova Remnant		
SOHO	Solar and Heliospheric Observatory		
SOP	Standard Operating Procedure		
SOURCE	Science Operations and User Research Central Exchange		
STSCI	Space Telescope Science Institute		
TAI	International Atomic Time		
TBD	To Be Determined		
TBR	To Be Reviewed		
TDB	Barycentric Dynamical Time		
TE	Timed Exposure		
TOO	Target of Opportunity		
TS	Telescope System, or Telescope Scientist		
TT	Terrestrial Time		
UT	Universal Time		
UTC	Universal Time Coordinated		
UV	Ultraviolet		